Spring 2018

Simplified, Alternative Formulation of Numerical Simulation of Proton Exchange Membrane Fuel Cell

Russell L. Edwards
Old Dominion University

SIMPLIFIED, ALTERNATIVE FORMULATION OF NUMERICAL SIMULATION OF PROTON EXCHANGE MEMBRANE FUEL CELL

by

Russell L. Edwards
B.S. M. E. June 1993, University of Cincinnati
M. Eng. June 2005, The Pennsylvania State University

A Dissertation Submitted to the Faculty of
Old Dominion University in Partial Fulfillment of the
Requirements for the Degree of

DOCTOR OF PHILOSOPHY
MECHANICAL ENGINEERING

OLD DOMINION UNIVERSITY
May 2018

Approved by:

_____
Dr. Ayodeji O. Demuren (Advisor)

_____
Dr. Miltiadis Kotinis (Member)

_____
Dr. Sandeep Kumar (Member)

ABSTRACT

SIMPLIFIED, ALTERNATIVE FORMULATION OF NUMERICAL SIMULATION OF PROTON EXCHANGE MEMBRANE FUEL CELL

Russell Louis Edwards
Old Dominion University
Advisor: Dr. Ayodeji O. Demuren

Three-Dimensional proton exchange fuel cell (PEMFC) operation in steady-state is simulated with computational fluid dynamics / multiphysics software that is based upon the finite-element method. PEMFC operation involves the simultaneous simulation of multiple, interconnected physics involving fluid flows, heat transport, electrochemical reactions, and both protonic and electronic conduction. Modeling efforts have varied by how they treat the physics occurring within and adjacent to the membrane-electrode assembly (MEA). Several approaches treat the MEA as part of the computational domain, solving multiple, and coupled conservation equations via the CFD approach within the 3 regions of the MEA. The thickness dimensions of the 3 regions of the MEA can be 2 orders of magnitude less than the features of the neighboring flow channels. Though this approach has been commercialized, the computational costs are quite high, due to the presence of large numbers of high-aspect ratio cells within the thin MEA. Research into the underlying physical phenomena, such as water transport, has also progressed, suggesting that various modeling errors may undermine many previous approaches. Other approaches treat the MEA as an interface, where they avoid these difficulties, but lose the ability to predict catalyst layer losses. This study develops an upgraded interface formulation where coupled water, heat, and current transport behaviors of the MEA are modeled analytically. Improving upon previous work, catalyst layer losses can now be modeled accurately without the ad-hoc changes in model chemical kinetic parameters. The interface model is developed considering only thru-plane variation, based upon varied fundamental research into each of the relevant physics. First, the model is validated against differential cell data with high and low humidity reactants. Validation continues with full 3-D test cases

with different current levels and inlet conditions. Distributed data of current density are used to show model agreement with experimental data.

ACKNOWLEDGEMENTS

I would like to thank Dr. Ayodeji O. Demuren for his encouragement and guidance during this research. His advice for the latter stages of this research about writing and revising the dissertation has been valuable. His independent study course in combustion and fuel cells was, undoubtedly, the most beneficial course for this research. I would like to express my thanks to Dr. Miltiadis Kotinis for his introduction to working with the open-source CFD package OPENFOAM, even though I was unable to implement this work with it.

In addition, I would like to thank Dr. Orlando Ayala for his helpful insights into working with COMSOL and developing models with that software. His reviews of the various model stages have proven helpful in eliminating a great deal of uncertainty.

I would like to thank Dr. Kevin Cooper of Scribner Associates for his brief input by phone when conducting fuel cell experiments (that eventually were used in separate published work). Dr. Cooper recommended very helpful references that led to the most important and necessary simplifications of the interface model contained herein.

I gratefully acknowledge the financial support of the National Science Foundation Marine Engineering Scholarship at Old Dominion University. Additionally, I would like to thank the Mechanical and Aerospace Engineering Department for their support through research and teaching assistantships.

I would like to express sincere thanks to all of my friends and extended family for their help, encouragement, guidance, and support during the course of this research. In particular, my parents who gave advice rooted in their own past doctoral program, and who took the time to review and improve my writing, my sister for her endless positivity, and to Lori Wright for her companionship through the long and dry researching and writing process.

NOMENCLATURE

Roman Symbols

A	cross-sectional area	m^2
$A_{-CL,Pt}$	electrochemically available catalyst area (ECSA)	m^2_{Pt} /g_{Pt}
a_W	water diffusion constant for ionomer	$=1.67 \times 10^{-9}$ m/s
c_f	fixed charge site concentration	mol m^{-3}
c_p	gas mixture heat capacity	J kg^{-1} K^{-1}
c_W	water concentration	mol m^{-3}
$C_{p,i}$	species molar heat capacity	J mol^{-1} K^{-1}
D_{ik}	binary diffusivity of species pair i-k	m^2 s^{-1}
$\tilde{D}_{ik}$	multicomponent Fick Diffusivity matrix	m^2 s^{-1}
D	diffusion coefficient	
d	mean pore diameter size	m
dS	entropy change of ORR reaction	=44 J mol^{-1} K^{-1}
E_c^{rev}	ORR activation energy; zero overpotential	=67 kJ mol^{-1}
EW	ionomer dry equivalent weight	kg (mol SO_3^-)$^{-1}$
F	Faraday's constant	=96,487 C eq^{-1}
f_v	volume fraction of water within ionomer	-
IC	mass ratio of dry ionomer to carbon in catalyst layers	-
I	operating current density	A m^{-2}
$I_{0,-}$	superficial exchange current density of - electrode	A cm^{-2}
I_x	crossover current density	A m^{-2}
$i_{0,-}$	specific exchange current density of reaction - on Pt catalyst	A cm^{-2}_{Pt}
$\vec{\mathbf{J}}_e$	electronic current flux vector	A m^{-2}
$\vec{\mathbf{J}}_{io}$	ionic current flux vector	A m^{-2}
$\vec{\mathbf{J}}_T$	thermal flux vector	W m^{-2}
$\vec{\mathbf{J}}_w$	water flux vector within ionomer	mol m^{-2}
k	mass transfer coefficient	m s^{-1}
L	surface loading	mg cm^{-2}
M	molecular weight of gas mixture	kg mol^{-1}
M_i	molecular weight of species i	kg mol^{-1}
$\vec{\mathbf{N}}_i$	mass flux vector – species i	kg m^{-2} s^{-1}
$N_{i,j}$	normal mass flux – species i location j	kg m^{-2} s^{-1}
n_d	electro-osmotic drag coefficient	-
Ptc	weight percent Pt/Carbon in catalyst powder	-

p	gas pressure	Pa
p_i	gas partial pressure of species i	Pa
$\dot{Q}$	superficial heat source	W m^{-2}
R	universal gas constant	=8.314 J mol^{-1} K^{-1}
R_{Ω}	high-frequency resistance	Ω m^2
R_{Ohm}	ohmic resistance	Ω m^2
R^{H^+}	protonic resistance of -	Ω m^2
R^{e^-}	electronic resistance of -	Ω m^2
$\mathbb{RH}$	relative humidity	-
T	temperature	K
t	time	s
t	thickness	m
$\vec{u}$	velocity vector	m s^{-1}
V	voltage	V
$\mathbb{V}$	molar volume	m^3 mol^{-1}
W	MEA water content	mol m^{-2}
x_i	mole fraction species i	-

Greek Symbols

α	relative humidity	-
δ	pseudo time-step	s
ε	porosity volume fraction	-
κ	thermal conductivity	W m^{-1} K^{-1}
ρ	density of gas mixture	kg m^{-3}
λ	water uptake (non-dimensionalized)	mol H2O (mol $SO3^-$)$^{-1}$
η	overpotential, anode or cathode	V
Θ_{xCL}	ratio: thermal resistance of ACL/ CCL to that of membrane	-
θ	ratio: protonic resistance / kinetic resistance	-
χ_{CCL}	resistance correction factor	-
Φ	potential field	V
ζ	stoichiometric flow ratio	-
σ	conductivity	S m^{-1} or Ω^{-1} m^{-1}
μ	viscosity of gas	Pa s or kg s^{-1} m^{-1}
ω_i	mass fraction of species i	-
υ	charge transfer coefficients	-
η	kinetic overpotential	V
$\%_i$	species imbalance of species i	-

Superscripts

$\mathbb{C}$	conduction	assessed from conduction effects
$\mathbb{D}$	diffusional	assessed from diffusional effects
eff	effective	effective porous medium diffusivity
eq	equilibrium	from equilibrium water uptake

e^-	electronic	referring to electronic conduction
$\mathbb{FV}$	finite-volume	from finite volume solution
F	free-space	free-space diffusivity
H^+	protonic	referring to ionic conduction
$\mathbb{III}-\mathbb{P}$	3-point	from 3-point approximate solution
$\mathbb{OP}$	operating	operating parameters of model
$\mathbb{S}$	swollen	altered value after water uptake
sheet	sheet	sheet resistance of ACL / CCL
K	Knudsen	referring to Knudsen diffusion
M	molecular	referring to molecular diffusion
100% RH	100% humidity	referring to saturated humidity
*	reference value	reference T, P conditions

Subscripts

A	anode-side	anode region bordering MEA
a	absorption	water absorption into ionomer
a	anodic	charge transfer coefficient
ACL	anode catalyst layer	referring to that layer of MEA
C	cathode-side	cathode region bordering MEA
C	carbon	referring to carbon material
CCL	cathode catalyst layer	referring to that layer of MEA
c	cathodic	charge transfer coefficient
cell	cell	cell value; cathodic-anodic
coll	collector	referring to the current collector
con	consumed	species consumption by reaction
ch	channel	referring to inlet channel
d	desorption	water desorption from ionomer
dV	volume change	fractional volume change
e	electronically conductive phase	
Gas	gaseous volume fraction	referring to gaseous space
GDL	gas diffusion layer	referring to that layer of PEMFC
H_2	hydrogen	referring to hydrogen species
H_2O	water	referring to water species
i	species index	referring to species i
Io	ionically conductive phase	referring to ionomer material
in	inlet	referring to flow inlet
k	kinetic	referring to kinetic effects
loss	loss	referring to voltage losses
MEA	membrane-electrode assembly	referring to the entire MEA
MEM	membrane	referring to that layer of MEA
N_2	nitrogen	referring to nitrogen species
O_2	oxygen	referring to oxygen species
OC	open-circuit	thermodynamic or reversible cell voltage
Ohm	ohmic	referring to total ohmic resistance
out	outlet	referring to flow outlet
prod	produced	species production by reaction
Pt	platinum	referring to platinum material
SAT	saturation	saturated state
T	thermal	referring to heat transport
V	void volume fraction	referring to void space
w	water	water dissolved in ionomer
x	crossover	referring to crossover
$\perp$	plane-perpendicular	through-plane direction
=	plane-parallel	in-plane directions
μ	chemical potential	referring to chemical potential
0	reference value	
1	MEA; ACL-membrane interface	anode side of membrane
2	MEA; membrane midpoint	middle of membrane thickness
3	MEA; CCL-membrane interface	cathode side of membrane

TABLE OF CONTENTS

LIST OF TABLES

LIST OF FIGURES

1 INTRODUCTION

1.1 Background

Polymer electrolyte membrane or proton exchange membrane (PEM) fuel cells are electrochemical energy conversion devices that produce electrical energy from the chemical energy present in hydrogen fuel. Water and fractional waste heat are the byproducts. The PEMFC has been used in automotive, marine, and portable electronics applications where it develops useful electric voltage at high efficiency, without creating the pollutants associated with combustion. They exhibit high efficiency at relatively low operating temperatures, with efficiency reaching as high as 60% when used for electrical energy conversion and 80% when there is co-generation of electrical and thermal energy.

Recent decades have seen technological advances. As achievable levels of power density have increased, costs have declined. The suitability of PEM fuel cells is typically ascertained in light of their power density, cost per kilowatt, and durability (a lifetime of operation in hours). Power density, or current density, has increased beyond 1 A/cm^2 over a decade ago. The durability and cost have been the major barriers to commercialization. The major focus of fuel cell cost reduction and performance improvement strategies is said to be on the issues of (i) heat and water management and (ii) new material development [1].

Goals relating to durability are typically expressed in terms of a lifetime of several thousand operating hours. Material degradation of key components has been studied extensively, and typically limits durability. Performance typically degrades gradually over time. The choice of cell design and operating conditions will typically influence some vectors of performance degradation, such as membrane degradation, or the reduction of effective catalyst surface area with aging.

Water and thermal management are fundamentally intertwined problems which will influence the durability, performance, and efficiency of a PEM fuel cell. The reactant gases are commonly highly humidified even though the device produces water in operation. The humidification is done to ensure high conductivity and efficiency from the water-absorbing (PEM) membrane at the heart of the fuel cell. When water can't be removed from the flow channels quickly enough, the formation of liquid water occurs and often leads to 'flooding' where liquid water accumulates and blocks the access of the reactant gases to the catalyst sites. The slight temperature rises predicted through the device's heat generation will have a substantial impact upon evaporation and reaction rates within the device. Accordingly, interest from the automotive industry in low-humidity operation with thin (~ 30 μm) membranes has been noted.

The computational fluid dynamics (CFD) approach is used for PEMFC design and simulation. Early pioneering work was isothermal and only 1-dimensional. It was helpful in establishing the fundamental models and relationships, but is generally thought to be inadequate in analyzing 3-dimensional flow effects that interact with electrochemical reactions of the PEMFC. Later models account for 3-dimensional effects that many analytical solutions will neglect or not consider. This approach has been successfully commercialized; however the computational costs remain quite high. The PEMFC is a multi-scale problem. Simulation of even greatly simplified PEMFC flow field designs had been reported in the literature benefitting from advances in parallel computing. Costs are driven by the requirements of meshing / discretizing the flow channels (~ 2×10^{-3} m thickness) simultaneously with the extremely thin catalyst layers (~$1\text{-}2 \times 10^{-5}$ m) and membranes (~$3\text{-}20 \times 10^{-5}$ m) that comprise the membrane-electrode assembly (MEA)[2].

Other approaches omit the thin MEA from the computational domain, treating the MEA as an interface, separating the anode and cathode flow domains. The MEA can be treated as a reacting wall, with consumption / production source terms on either side to mimic its operation. This approach may entail less computational cost. It has been criticized in the literature, however, for lacking the capability to model reaction rates and losses occurring within the thin porous catalyst layers, detailed water distribution in the membrane, and the important transient effects linked to these phenomena.

Most recent commercially-available CFD models differ first in terms of the effects they will consider. The state of a model (steady-state, transient), its dimensionality (0-D to 3-D), and the nature of the model approach (theoretical, empirical) distinguish most efforts according to what information they seek. Discrete physics of the PEMFC can be included or ignored, such as heat transport (isothermal vs. non-isothermal), electronic conduction, gas density changes (variable-flow vs constant-flow), and liquid water accumulation effects (single-phase vs multiphase).

Models considering similar state, dimensionality, and effects (physics) will then differ, primarily, in how they treat the MEA. The physics of the MEA include water transport, heat transport, gaseous diffusion, and the kinetics of the reactions occurring in the anode and cathode. A multitude of subsequent studies have improved the understanding of each area from the time when CFD models were first being developed and refined (2000-2007). Some widely-used modeling assumptions have been called into question by direct experimental evidence. Many analytical approaches to model catalyst layer operation have been published.

CFD models haven't put most of these new findings into practice, and tend to continue using transport property data from the 1990's. The objective of this work is to re-formulate the interface approach to represent the MEA, accurately modeling the relevant physics (including catalyst layer losses), for steady-state problems. The application of judiciously-chosen simplifying assumptions, newly-refined water-transport physics within the MEA, and membrane water storage mechanism leads to development of a new interface representation of the MEA for use in the CFD approach. The new interface representation incorporates the capabilities missing from prior efforts.

1.2 PEM Fuel Cell Fundamentals

This section is intended to present the fundamental operating principles of the PEM fuel cell. In its most basic definition, a fuel cell is an electro-chemical energy conversion device that converts a supplied fuel to electrical energy (and heat) continuously, for as long as reactants are supplied to its electrodes. A fuel cell converts the initial chemical energy of the reactants (the fuel and oxidizer), into

electrical energy. Fuel cells are classified according to type by the technology used in the electrolyte. This work focuses on the Polymer Electrolyte Membrane, aka Proton Exchange Membrane (PEM) fuel cell. Older sources also refer to the technology as the Solid Polymer Electrolyte (SPE) fuel cell.

The basic components of the PEM fuel cell can be explained by means of a cut-away diagram in Figure 1.1. The left side is the negative, or anode terminal, and the right side the positive, or cathode terminal. Electrical connection to an external circuit is made via the electrically conductive current collector plates. Both current collector plates typically have gas flow channels that direct the flow of the hydrogen fuel within the anode side, and the oxygen or air oxidizer on the cathode side. The fuel and oxidizer, collectively referred to as reactants, are typically supplied in carefully metered amounts as pressurized, humidified gas streams.

Collector plates serve first as the electric terminals of the cell. In a stack arrangement they will connect the cells electrically. They contain flow channels to distribute the humidified gases over the surface of the anode and cathode. Collector plates have been made from graphite and various metals to have the desired electrical conductivity and resistance to corrosion.

Gas diffusion layers (GDL) contact both sides of the MEA. These provide electronic and heat conduction between the collector plates and the MEA. They are highly porous in order to allow the gases in the flow channels to diffuse through to the MEA. The diffusion media typically is made of carbon cloth or carbon paper materials, with thicknesses~ 150-400 um typical.

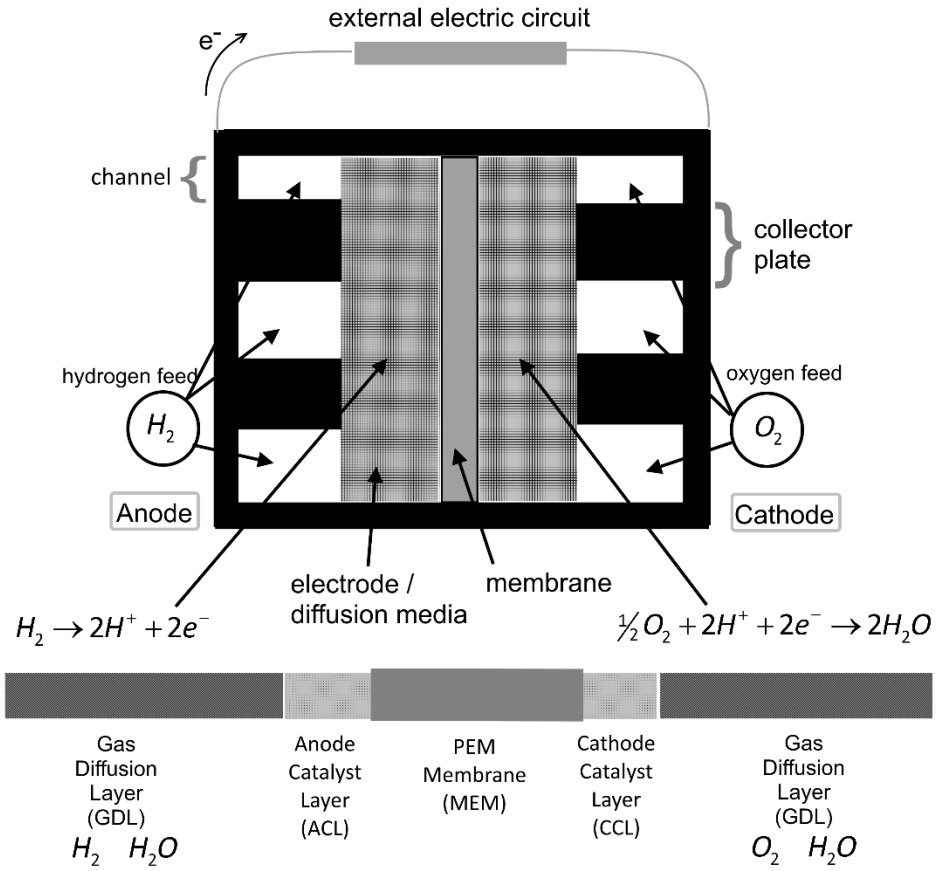

Figure 1.1. Introductory cutaway schematic of a single-cell PEMFC

Catalyst layers are attached to both the anode (ACL) and cathode (CCL) side of the central polymer electrolyte membrane (PEM). These are porous structures consisting of three phases. Fine catalyst particles of platinum (Pt) or an alloy thereof provide the reaction sites distributed throughout the CL thickness. These are supported on complex structures of carbon particles that provide electronic conduction within the catalyst layers. This carbon-supported platinum catalyst (often denoted as PT/C) technology creates a large number of active catalyst sites and a catalytic surface area much greater than the planar electrode surface area, so that the reaction can proceed at a feasible rate. A dispersed electrolyte phase serves, likewise, to allow protonic conduction to the reaction sites. The remainder void volume consists of pores to allow for gas permeation. Typical thicknesses are 5-15 μm.

The electrolyte membrane serves to separate the two respective gas flows. The membrane must, according to its function, be highly conductive of the protons while simultaneously non-conductive for electrons in order to avoid short circuiting the external electrical circuit. Nafion has been the common benchmark material. It absorbs water, possibly 40% or more by weight, when in contact with humidified gases, and when so hydrated, becomes proton-conductive. Protonic conductivity rises significantly with water content, allowing the device to operate efficiently. Thicknesses available range from .001" (25 μm) to .007" (175 μm). Thinner membranes have been more popular for some time.

Coupled chemical reactions occur on opposite sides of the planar catalyzed membrane. Convective and diffusive transport of reactant gases occurs within separated flow channels on both the anode (Hydrogen fuel/ negative terminal) and cathode (Air/ positive terminal) sides. Each gas permeates through a gas diffusion layer (GDL) and reaches the respective anode and cathode catalyst layers where the corresponding electrochemical reactions occur. Operation requires conduction of protons through the central membrane (PEM), as well as conduction of electrons through the GDL, graphite flow field plates, and an external electrical circuit.

The device typically removes product heat through convection, with the reactants, as well as conduction, through the GDL and collector plates. Separate, additional dedicated cooling channels might assist ordinary conduction in the removal of excess heat in large, high power density stacks. Contact resistances between the diffusion media and current collector plates are thought to be important for simulating the heat and current conduction physics. Water removal occurs through reactant flow channels, as vapor or liquid water droplets.

At the anode, hydrogen is oxidized in the hydrogen oxidation reaction (HOR) into its constituent protons (H^+) and electrons (e^-). The HOR occurs at reaction sites (catalyst particles) distributed through the thickness of the anode catalyst layer (ACL) where diatomic hydrogen is split into two protons and two electrons:

$$H_2 \rightarrow 2H^+ + 2e^- \tag{1.1}$$

The protons produced by this reaction move through the thickness of this membrane to reach the cathode catalyst layer (CCL) under the influence of the electric field. Electrons reach the CCL through the external circuit, and oxygen gas reaches the CCL by diffusing through the diffusion media. At reaction sites, distributed through the thickness of the CCL, the oxygen reduction reaction (ORR) consumes oxygen, protons, and electrons, creating water as the reaction product:

$$O_2 + 4H^+ + 4e^- \rightarrow 2H_2O \tag{1.2}$$

The product water hydrates the membrane, and will leave the cell through the reactant gas streams. Water movement within the membrane depends on operating conditions. Both anode and cathode gas streams exchange water with the MEA, and remove product water from the device.

The performance, or device efficiency, of a PEM fuel cell is typically assessed through a voltage measurement conducted over a range of current densities, known as a polarization curve or characteristic curve. The curve is typically explained (empirically fit) by computing an ideal, thermodynamic, voltage and then subtracting estimates of various polarizations (losses) from it.

Performance losses within the PEMFC have been the subject of a tremendous deal of research. Losses are typically described according to well-known categories of loss mechanisms, and will likely vary spatially within a given cell. The major categories of losses with the PEMFC are activation (or kinetic), ohmic, and mass transport (or concentration) polarizations.

Activation losses describe the voltage drop required to drive both the anode and cathode chemical reactions at rates greater than equilibrium. Also known as activation polarization, kinetic losses tend to dominate the voltage drop occurring in the PEMFC at low current densities. Activation losses occurring from the ORR occurring in the CCL tend to be more significant. These losses are described by models of electrochemical kinetics, and are greatly influenced by catalyst-site temperature, gas composition, and the effective catalyst site surface area, itself dependent upon the complex catalyst layer composition.

Ohmic losses with the PEMFC are ‘iR’ type losses. These tend to dominate the voltage drop occurring in the PEMFC at mid-range current densities. Thus the measured voltage curve becomes nearly

linear with current. Relatively minor ohmic losses come from electronic conduction losses within PEMFC components and contact resistances. Primary measurable ohmic losses come from the ionic resistance of the membrane, which is centrally dependent upon its state of hydration and temperature. The use of thin membranes helps to minimize ohmic losses.

Mass transport, or concentration, losses occur at high current density operation. These arise from the inability to supply reactants to the reaction sites at the required rate(s). When reactant consumption levels grow large enough, gas transport limitations develop in the diffusion media and catalyst layers. These arise through the normal effective diffusivity of the GDL media and catalyst layers, and are further exacerbated if liquid water accumulates and blocks the pores of the GDL used for gas diffusion. Mass transport losses arise from reduced reactant compositions at the reaction sites within the catalyst layer(s). With the inability to supply reactants at the required rate(s), the voltage curve turns down precipitously near a limiting current value.

1.3 Survey of Previous Work – Experimental

The earliest experimental studies of the PEM fuel cell typically involved measuring the polarization curve, the fundamental test of a PEM fuel cell, where voltage is plotted as a function of the average current density of the device. The polarization curve is measured under delineated test conditions such as cell temperature, and reactant gas flow rates and humidity levels. As voltage levels are synonymous with efficiency, such comparisons have direct merit.

In these zero-dimensional (0-D) models, the measured curve was compared against the thermodynamic voltage, and several mechanisms of voltage losses assessed from the measured data. The polarization curve can usually be fitted with a number of empirical functions that estimate the open-circuit voltage, along with average values of the different loss effects[3] [4] such as gas crossover, kinetic losses, ohmic losses, and mass transport effects. One example of this approach illustrated how the shape of the curve indicates different fundamental loss mechanisms, where one loss mechanism was clearly dominant in various current density ranges [5]. The 0-D models weren’t predictive models but served as

fits of, and analysis of, the experimental data. Laurencelle et al. showed the application of experimental data to fit a polarization curve equation [6]. Cooper et al [7] show the settled state of these "characterization" equations; these analysis and fitting procedures aren't likely to experience significant further advancement.

Experimental work described here is that used to validate CFD models. Distributed diagnostic measurements have been developed to provide benchmark data for fuel cell model validation. The term distributed diagnostics refers to the efforts to measure local spatial variations in temperature, current, cell resistance or conductivity, species concentration, etc. These tools are ideally used to validate multi-dimensional models. Local polarization curves have been produced [8] from a small portion of a segmented cell.

Current mapping is commonly used as a term to describe distributed current density measurement. Distributed current density measurements were identified as key to understanding fuel cell systems [9], where very small cells were found to have nearly uniform current distribution, and larger area cells have gradients of current density, oxygen concentration, humidity, water flooding, and/or temperature. The measurement techniques began with magnetic loop arrays that are embedded in the current collector plates [10] [11]. This technique has the advantage of being done independently of cell operation, but can only be used with a single cell: it is not compatible with fuel cell stacks. Other approaches involved using segmented cells: individual cells that were electrically isolated from each other. These segmented cells could provide spatial resolutions near the size of a single gas channel[12].

Some of the segmented approaches have been criticized in that a segmented MEA will disrupt the current distribution reaching the current collectors, thus giving a measurement that isn't representative of the intended measurement: the un-segmented MEA. Rather, the work of Mench and Wang [9] uses an un-altered MEA with an electrically segregated (segmented) flow field.

Validation of models can typically be done via local polarization curves, or presentation of the current distribution data presented along the direction of the flow path [8]. Global curves may show good agreement, but the detailed distribution data may not be completely satisfactory.

Distributed temperature and species measurements have been used for evaluating model agreement. Attempts to measure the thru-membrane temperature profile have involved embedding thermocouples In the diffusion media of a PEMFC [13], as well as embedding micro thermocouples between two layers of membrane sheets [14, 15]. Temperature measurements were plotted at discrete points along the length of the serpentine flow path. This work showed that commonly used isothermal assumptions are not well justified at high current densities, as temperatures varied as much as 10°C within the electrolyte.

Developments in the measurement of species distribution used a gas chromatograph to measure the mol fractions of the various species present in the gas channels of an operating PEMFC [16]. This allowed an experimental verification of the water vapor mole fraction in the PEMFC flow fields, though measurements could only be taken steady-state. Measurements could be taken about every 2 minutes, but this technique was not workable with the presence of liquid water. Later in 2005, this same group had combined in-situ measured data of species distribution, current distribution, and measured high frequency resistance distribution. Measurement capabilities had nearly reached real-time (1 s per point) [17].

1.4 Survey of Previous Work – Specialized and Electrochemical

Reactant crossover measurement is relevant to PEMFC modeling because the reactant crossover reduces the open-circuit cell voltage (OCV) by a noticeable amount from the reversible voltage or 'Nernst' value. There are several methods to determine gaseous reactant (hydrogen) crossover through the proton exchange membrane. Accounting for crossover can be done by adding a crossover current to the model for kinetic losses or with an arbitrary reduction in the OCV of a fuel cell. The crossover is usually unresolved; that is assumed to be spatially uniform over the area of the MEA.

The in-situ electrochemical methods for measuring crossover include cyclic voltammetry (CV) [18] and Linear sweep voltammetry (LSV) [7]. Crossover can be measured directly, and levels of 1-2 mA/cm2 are thought to be typical. LSV can also detect the presence of an internal short through the presence of a positive slope of the current / potential curve.

Active Surface Area Measurement typically uses CV in fuel cell studies to measure the electrochemically active surface area (ECSA) of catalyst layers. ECSA testing is used to evaluate the performance of catalysts, modifications to catalyst layer microstructure(s) and/or catalyst loading, and the presence of adsorbed surface poison. CFD models use either ECSA or exchange current density estimates to calculate kinetic losses of both the anode and cathode[19] [20]. They are often not known precisely, and have been treated as parameters which are adjusted to align model predictions with experimental data.

Typically, area values are reported with respect to the catalyst loading. Values of around 50 m^2/g Pt [4], with ordinary platinum catalysts, are reported in well-designed PEMFC cathodes. ECSA values have been seen, experimentally, to drop with decreasing humidity and/or ionomer volume fraction [21], and most CFD models have failed to account for this.

Ohmic Losses in the PEMFC are comprised of ionic resistance losses (from the electrolyte), electronic contact resistances between components, and bulk electronic resistance. Test equipment is now commonly available to make in-situ ohmic resistance measurements on an operating PEMFC. The most common in-situ methods are the current-interrupt and high frequency resistance (HFR) methods. These produce the sum of (i) electronic resistances, and (ii) ohmic resistances arising in the membrane of a

PEMFC [22]. The two methods were nearly equivalent and have been frequently used for kinetics research and as a validation aid.

It is typically desired to separate the ohmic resistance components. Electronic resistances might be implicitly assumed to be negligible, or may be measured separately (ex-situ) within a 'dummy' cell (one where the MEA has been removed). This latter procedure was used in kinetics research [19, 20, 23]. The previously-mentioned in-situ methods do not address, or include, catalyst layer ionic and electronic resistances. Further research has been focused on experimentally assessing ionic resistance losses in catalyst layers[24]. Ionic conduction losses have been shown to be significant, while electronic conduction losses within PEMFC catalyst layers have frequently been considered negligible[20, 25].

Diffusional Losses in Catalyst Layers have been investigated. In an operating PEMFC, reactant gases must move through some portion of the thickness of each catalyst layer to reach the available reaction sites. This process was thought to be dominated by diffusion instead of pressure-driven flow[4], and so significant experimental and modeling research has been invested into determining diffusional gas transport models applicable to the catalyst layer structures. As hydrogen has a greater diffusional coefficient, and anode losses aren't typically as significant, most effort has focused on oxygen diffusion through CCL structures.

Key early works investigated the microstructure of catalyst layers, finding that there existed two distinct pore size distributions with the typical CL structures, and that pore sizes were between the nanometer and sub-micrometer size [26, 27]. The larger pores tended to partially fill with ionomer, dropping effective oxygen diffusion coefficient as ionomer loading increased [28] and influencing the performance of the MEA.

Several modeling works have tended to greatly overestimate effective oxygen diffusion coefficients in PEMFC catalyst layers. Estimates of effective values reached 0.1-0.3 $cm^2\ sec^{-1}$ at 80°C, to justify ignoring these diffusional losses[29, 30]. Experimental measurements of effective diffusion coefficients were given in 2005 to be 0.006-0.007 $cm^2\ sec^{-1}$ at 80°C[31] when a typical CL structure was evaluated. In 2010, measured effective diffusion coefficients dropped from 0.024-0.001 $cm^2\ sec^{-1}$ at 80°C

as ionomer loadings and humidity were increased [32]. Later measurements, in 2011, found 0.002 cm^2 sec^{-1} at 80°C[33]. The Bruggeman correction, which was commonly used for estimating effective diffusion coefficients of porous catalyst layers, was found to under estimate catalyst layer tortuosity[32, 33].

Pore size distributions within the CL structures were found to be similar in size to the mean free path of oxygen molecules. Inaccessible pores were present, which reduced the porosity by 20-60% from the value which was expected based purely on density-based calculations. Oxygen diffusion was found to take place within the "transition region" where both Knudsen and molecular diffusion must be taken into account[33]. By 2012, experimental measurements at 0%RH were shown to be consistent with such a model of diffusion, when porosity and tortuosity effects were properly assessed[34]. The presence of inaccessible pores in the CL structures served to reduce porosity and the effective diffusion coefficient.

Intensive, pore-scale models have also developed these findings. These models are intended to serve as a valid analytical basis for macrohomogeneous models, providing effective transport properties. They computationally reconstruct catalyst layer microstructures and then devise effective transport properties. The choice of pore-scale models chosen (referred to as a reconstruction algorithm) did not substantially affect the effective transport properties that these models were to predict[35]. It was more important to account for the reduced porosity[36] resulting from Nafion loading.

Electrode Kinetic parameter estimation research has progressed. Both anode and cathode electrodes are expected to continue utilizing the current carbon-supported platinum (Pt/C) technology[37]. CFD models require kinetic data to estimate voltage or efficiency losses occurring in these reactions. Each follows Butler-Vollmer kinetics [4, 38], where the reaction rate is described by two parameters: (i) exchange coefficients and (ii) exchange current density. Many CFD models have tended to present kinetic values without clear justification, treating these as free parameters which are adjusted to produce agreement between model and experimental data. Kinetic model parameters, such as exchange current density, have come to be discussed in terms of the electrochemically active surface area (ECSA), which is

then related to catalyst loading. The trend among higher-quality works is to use kinetic model parameters devised with consideration of ACL/CCL composition.

The hydrogen oxidation reaction (HOR) occurring in the anode is quite facile (rapid). Under these conditions, the Butler-Vollmer relations simplify to linear kinetics[4]. Voltage losses are typically very small, often too small to measure. When they have been investigated, it has been for seemingly academic reasons, or for investigating a possibility to lower the anode platinum catalyst loading, saving cost, without significantly degrading performance[39]. Estimates of the HOR kinetics parameters available in 2007 were collected and showed variations of orders-of-magnitude. Neyerlin et al. presented HOR kinetics parameters from a H2 pump test [23], arguing that the prior rotating-disk electrode (RDE) experiments were compromised by unacknowledged mass transport limitations. Butler-Volmer model parameters were only determined from experimental data to within a factor of 2. Durst et al. offered more precise kinetic data estimates and developed temperature-dependence as well[37].

The oxygen reduction reaction (ORR) occurring in the cathode is much slower and voltage (efficiency) losses from it more substantial. Under these conditions, the Butler Vollmer relations reduce to Tafel kinetics[4, 38], where a Tafel slope, reaction order, and exchange current density are required. Substantial work has gone into cathode catalyst layer development and the characterization of the cathode ORR reaction. The cathode reaction follows Tafel kinetics with reaction order (with respect to oxygen concentration) of about 0.5[40]. There has been a substantial disagreement in modeling the cathode reaction between much older and more recent works. Experimental work combined with intensive micro-scale modeling was able to explain how previous experiments produced kinetic data with double the theoretically-correct Tafel slope due to undiagnosed ionic conduction losses in the cathode catalyst layer and un-realized gas diffusion limitations[41]. The suggestion of these and later workers is that older rotating disk electrode (RDE) kinetic experiments and the derived data is in some doubt.

Wang presented calculations in 2007 showing how the oxygen concentration levels, temperature, and ionic conductivity within typical cathode catalyst layers could be considered uniform[30]. Ionic conductivity, however, was still highly hydration-dependent.

Neyerlin and Gu [19] improved the ohmic-loss compensation techniques to better measure in-situ ORR kinetic data. Later work extended the technique to account for incomplete catalyst layer utilization[20]. Incomplete catalyst layer utilization occurs under high current density and/or low humidity operation when effective catalyst layer resistances become significantly large. Wang and Feng [29] expanded the analytical solutions used by Neyerlin and Gu[19]. By 2009, Liu and Murphy verified the correctness of these solutions by testing a range of varying electrode compositions with differing humidity [24]. The ionomer volume fraction of about 0.13 (I/C >0.6), and relative humidity of 30%[42], were thresholds for good performance and usage of the analytical solution for cathode catalyst layer performance. These limits seem to accommodate most typical catalyst layer compositions.

With recognition/compensation of appropriate catalyst layer resistance, a model of ORR kinetics could be devised that is consistent across different operating conditions. Experimentally-determined ORR kinetics were found to be almost independent of humidity and electrode composition and Pt catalyst loading. The remaining loss, attributed to humidity variation in typical operational conditions, can be explained by the experimentally-observed shift in ECSA from humidity alone [21]. Thus, a model of ORR kinetics was put together that is consistent and viable across different operating conditions and catalyst layer compositions.

CFD models that don't account for cathode catalyst layer resistances can still match experimental polarization data fairly well, and even while operating at low humidity conditions where catalyst layer losses should be large enough to introduce significant error. These models can match experimental V-I data by doubling the Tafel slope of the ORR[43] and then treating the exchange current density as a free parameter of the problem: it is chosen to match the experiment in question without connection to the underlying CCL catalyst loading.

Water Transport in PFSA Membranes has been an area of fundamental investigation. Water Transport models mostly follow two very distinct modeling approaches: the hydraulic model of Bernardi and Verbrugge [44] and the 'diffusive' approach of Springer and Zawodzinski of Los Alamos National Laboratory[45]. The latter approach is used by most CFD models. By 2008, the diffusive approach was

the de-facto model in commercial software[46]. Many works reported membrane water transport property values devised mostly ex-situ. These have had the goal of measuring water sorption, membrane conductivity, water diffusion coefficients, and electro-osmotic (EO) drag coefficients following the 'diffusive' model framework. The intention was that CFCD models would be more useful and accurate with appropriate transport parameters (property values).

The 'diffusive' approach begins with determination of an equilibrium water uptake value. Zawodzinski and Neeman [47] measured equilibrium water uptake curves from membranes exposed to humidified gas and liquid water. They developed empirical fit for water content as a function of water activity (relative humidity) based upon weight gain data for selected membranes. This was followed with data from both liquid water uptake and vapor phase uptake [48]. Hinatsu et al. refined the apparatus for these measurements and reported water uptake data by Nafion with liquid through a range of temperatures, as well as the vapor-equilibrated uptake curve through 80 °C [49]. Another apparatus improvement was reported by Jalani et al. [50]. Onishi et al. examined water uptake in more detail, raising the possibility that the prior water uptake data was dependent upon "thermal history" [51], and that many water uptake studies might have been influenced by these effects. Kusoglu then investigated the influences of constraint and compression upon water uptake[52]. The previous water uptake curves were mostly empirical in nature, with expressions made to fit the experimental data.

Membrane ionic conductivity was investigated by early authors, and a strong water content dependence was both expected and found [48] in 1993, with conductivity exhibiting linear dependence on water content at 30 °C. Halim and Buchi also conducted conductivity measurements using AC impedance measurements of liquid-equilibrated membranes. They found similar activation energies for multiple membranes and that the variation of conductivity with temperature follows the Arrhenius law [53]. The early relationships still appear to be in use in CFD models; however later work has proposed relationships in which membrane ionic conductivity takes a somewhat different form [51, 54].

The membrane water transport model of Springer requires a self-diffusion coefficient of water, and an electro-osmotic drag coefficient (representing the number of water molecules carried with each

proton that crosses the membrane). Both are temperature and water content dependent. Attempts to measure these parameters have generated much disagreement between various groups and authors. The earliest work may be from 1991 where Zawodzinski used pulsed field gradient spin-echo 'H NMR measurements of 'H intradiffusion coefficients in Nafion 117 membranes (in the absence of a water concentration gradient)[47]. Measures of electro-osmotic drag were also reported as being 2.5 (liquid-equilibrated membrane) and 0.9 (vapor-equilibrated membrane). Motupally et al. reported permeation experiments to measure water diffusion in 2000[55]. This correlation is used in a substantial number of models for the diffusion coefficient. Note that this work assumes the validity of the equilibrium assumption: water uptake data from equilibrated membranes is used to assign water content values on opposite sides of a membrane during permeation experiments. The experiment limited itself to one particular membrane thickness.

A multitude of approaches have been used to attempt measurement of electro-osmotic drag. A hydrogen pumping cell can be used to measure electro-osmotic drag[56]. The transport parameters, however, were subject to a great amount of disagreement in the methods used and results obtained[57]. By 2007, there was general agreement that the resulting water content profile in thin (50 μm) membranes was nearly linear and anode dryout was not expected in the thin membranes[56].

Membrane Water Content Imaging technologies have been refined. Some of these works have aspired to validate the membrane water transport models in-situ. Buchi and Scherer made membrane resistance measurements with an operating fuel cell with a known, thick composite membrane. Membrane resistance was found to increase greatly with current density and attributed this to drying out of the anode side of the membrane [58]. Later work used distributed local resistance measurements from evenly spaced increments between anode and cathode[59]. Drying out effects could clearly be seen where the membrane resistances increased at the anode side as current density increased. The effect was more pronounced with thicker membranes and less noticeable in the thinner ones. The characteristic dry out of the anode side was shown deriving from the non-linearity of the water transport in the membrane,

explained as the variation of the diffusion coefficient with water content. However, only a qualitative agreement of diffusive models with the experimental data could be shown[60].

Further sorption/ de-sorption (wetting and drying) experiments, performed on Nafion membranes, were used to investigate water transport. Nafion membranes had very flat water content profiles as they gained or lost water; the rate of water redistribution within the membrane was found to be much faster than the water loss. It was also seen that the uptake of water is an order of magnitude faster in the presence of liquid water, compared to water vapor. In both liquid/vapor cases the sorption kinetics are controlled by the transfer process at the membrane surface[61, 62]. Water content equilibrium values were seen to match the previously determined sorption curves determined by gravimetric tests[63]. Imaging done during permeation and operational fuel cell experiments utilizing micro-Raman spectroscopy found the presence of significant interfacial resistance, which was influenced by temperature and humidity. The local water content at the edges of the membrane was not in equilibrium with the water activity in the gas phase during these permeation experiments. In all cases, equilibrium water content slowly re-established when water flux ceased, and linear water content profiles were observed in steady operation with membranes less than 100 μm in thickness[63, 64].

Examinations of water content imaging, during permeation experiments, with X-ray microtomography also suggested the presence of an interfacial resistance to water transport[65]. Operational PEMFC water content imaging measurements with the MRI technique captured the anode-side depletion of water as current density increased[66]. In-2010, Tsushima was able to perform MRI measurements with operating PEMFC at higher realistic operating temperatures, and the technique (environmental MRI or EMRI) was extended beyond most of the earlier work limited to room-temperature measurements[67]. This work showed linear water profiles developing as the membrane hydration levels increased. They inferred that the diffusion coefficient of water in Nafion was maximum at dimensionless water contents as low as 3-5[65], as originally reported by the Los Alamos workers[47].

Experimental efforts into water content imaging are many and varied, however different workers and techniques have inferred the presence of an interfacial resistance to transport present in operational

fuel cell MEA's. This calls into question the assumption of equilibrium of water content (between the gaseous phase and the membrane water content) employed with most membrane water transport models. That equilibrium assumption has been widely employed in most CFD models.

Non-Equilibrium Water Transport in PFSA Membranes was introduced around 2004 by Chen et al [68] and Berg et al [69]. They modeled non-equilibrium membrane water uptake rates. The concept of this work was establishing a model of water transport in the membrane that was not based on equilibrium absorption from the adjoining water vapor. Instead, the rate of absorption / desorption of water into / from the membrane was driven by a gap or jump in the water content level between the actual water content and that determined by the equilibrium sorption values. By 2007 Majsztrik et al conducted a more thorough series of sorption, desorption, and permeation experiments, finding that diffusion was only one of the three resistances to water sorption (interfacial resistance, diffusion, and membrane swelling to accommodate water uptake)[70]. Which resistance was the controlling one was said to vary with humidity, sample thickness, and temperature. Monroe, Romero et al [71] did another group of water permeation experiments and claimed interfacial resistance limits the overall water transfer rates when membrane thickness is less than a critical value of about 300μm. State-of-the-art membranes are about 30-100 μm.

Ge et al developed mass transfer coefficients which were not constant, but rather were dependent on the local volume fraction of water at the membrane edges [72]. The diffusion coefficient was also modeled as being dependent on the water volume fraction in the membrane (which is water content dependent). This group later determined the electro-osmotic drag coefficient as well [57] with measurements in an operational fuel cell. They compared measured and calculated resistance from the membrane to validate the model. The agreement was highly precise over different thicknesses and a range of current densities. The membrane property values (correlations) produced were reasonably consistent with prior works. This work neglected catalyst layer effects and losses, and still required meshing and solving conservation equations throughout the membrane. This work also relied heavily upon the water uptake data of Hinatsu et al. [49], which was later called into question [51].

Additional experimental investigations of interfacial water transport resistance have been pursued[73]. Adachi et al noted significant interfacial resistance in membranes less than 200 μm in thickness [74]. The presence of catalyst layers, on both sides of the membrane, were found to not change water permeation significantly[75], and so it was suggested that membrane water permeation experiments could be correlated to those of an operating PEMFC.

Transport in diffusion layers (GDL) has been advanced. Their function is to provide a path for electronic conduction into the current collector plates; to allow gases and liquid water to move into/from the catalyst layers; and to offer some structural support. Each GDL can incorporate either a single diffusion media (DM) or can be a composite structure combining the above with a 'micro porous layer'. Specialized source terms are added to the momentum equation in this region, and diffusion coefficients through porous media as well. Electrical and thermal transport must be properly accounted for.

Gas transport in porous materials are typically characterized by their porosity, tortuosity and permeability. The macrohomogeneous models commonly treat the diffusion layers as isotropic[76]. Two nearly equivalent approaches exist for modeling gas transport in these porous materials [31, 77]. The porous nature of gas diffusion media tends to slow gas diffusion, and so the gas-phase diffusion coefficients are modified into "effective" values by accounting for the porosity and tortuosity of these media. It is typically done with Bruggeman correction. Pressure-driven flow and convection is modeled with Darcy's law. Computational works might not use the permeability values supplied by manufacturers, however, because the properties are expected to change under GDL compression. Mench also describes how catalyst and microporous layers (MPL) need to take into account both molecular and Knudsen diffusion[4].

Electronic conduction in the GDL is often neglected in earlier published CFD models because the commercially available carbon papers have good electrical conductivity. Electron conduction was seen to have significant effects altering the current density distribution in the second and third dimensions of a PEMFC model [78, 79]. Properties of the electronically conducting phase will be needed, such as the electrical conductivity of that solid phase. It is commonly recognized that these GDL materials do not

have an isotropic electronic conductivity: higher values occur in the in-plane than the through-plane direction [38, 76].

The thermal conductivity of diffusion media might be similarly anisotropic, though most early work seems to treat the GDL as isotropic. Attempts to measure thermal conductivity of GDL materials seem to have intensified post 2005 when more effort was put into non-isothermal fuel cell modeling. Burford and Mench developed an estimate of thermal conductivity of the diffusion media from in-situ micro-thermocouple measurements [14, 15]. Soon afterward, several research groups began to use ex-situ direct measurement methods to determine the thermal conductivity of fuel cell materials, particularly the diffusion media. Measurements included thermal conductivity of the GDL media itself, along with its temperature and compression dependence; and also a contact resistance which was itself compression dependent. Khandelwal and Mench found the thru-plane thermal conductivity for a common carbon paper between 1-2 W/m K, which decreases with temperature due to the presence of a carbonized thermosetting resin used as a binder[80]. They found thermal conductivity affected by the presence of added PTFE in the GDL as well. They also noted the presence of a significant thermal contact resistance which asymptotically reached its lowest limiting value with compression pressure of about 2 MPa. Hysteresis is observed in the contact resistance due to the compression and deformation and breakage of the fibers in the media. Models describing the thermal conductivity of porous materials have been compared with this experimental data[81]. Another work examined thru-plane thermal conductivity and contact resistance of GDL materials with varying compression and levels of liquid water[82]. Each changed conductivity significantly. Sadeghi made additional measurements showing an air-pressure dependence. At low gas pressures, the surface contact resistance became greater than internal conduction losses[83]. Finally, Teertstra et al showed that the thermal anisotropy of the GDL materials, with in-plane thermal conductivity levels 10 x those in the thru-plane direction[84].

1.5 Survey of Previous Work – Computational

The focus now turns to the level of the fuel cell modeling level. Previous computational studies of three-dimensional PEM fuel cell performance are reviewed in this section. Competing global approaches to modeling fuel cells commonly diverge in the area of modeling the MEA (also known as the "fuel cell sandwich"). The literature contains many competing approaches. These works might model a single flow channel of a PEMFC, a single fuel cell model, or even a complete stack. This section is intended to describe some of the more fundamental classifications of computational work seeking to model the operation of a PEM fuel cell. CFD models are then typically characterized by being transient or steady state; combined with their scale and dimensionality; a description as isothermal/non-isothermal and single-phase / multiphase in its treatment of the presence of liquid water.

Computational work is easily divided by scales into microscopic and macroscopic models. Microscopic models are those that seek to model transport on the length scales of the microstructure of the material involved. This is called the "pore" level. These models require detailed information about the material microstructure and are more computationally expensive. Macroscopic models tend to average over this level, employing the continuum assumption. The CFD models considered here are macroscopic models. In employing the continuum assumption, the exact details of material microstructure are neglected. The important sub-regions of the fuel cell such as diffusion layers, membrane, and catalyst layers are handled this way. Diffusion layers are commonly considered as randomly oriented porous structures that are described by a porosity and permeability. In examining catalyst layers, a porosity (volume fraction) and surface area per unit volume might be considered.

Dimensionality separates models generally where 0-D models are those with no dimensionality; they are essentially only empirical relations devised to fit the polarization curve V-I data and thus model its steady-state performance with a single equation. These models have some value in determining the kinetic parameters of a fuel cell (area-averaged resistance, exchange current density). That allows the separation of various loss mechanisms for inspection. These 0-D models lack predictive capability and aren't useful in optimizing fuel cell designs. 1-D models consider the direction through the MEA

exclusively. These make up the majority of early modeling work. 2-D models additionally consider the direction downstream, or down the flow channel, and 3-D models consider effects in the cross-flow direction. Some works have varying dimensionality by region.

Isothermal models are those that do not consider the presence of temperature gradients within the fuel cell, and thus, do not account for heat transfer. Isothermal models can consider temperature effects, but simply treat temperature as an input to the problem. This assumption is fairly commonly used in CFCD.

Discrepancies in the treatment of liquid water are also common. The simplest approach to the treatment is the single-phase approach where the total water amount is considered without regard to whether it is in vapor or liquid form. The gas and liquid share the same velocity as they are in the same fluid mixture. Two-phase models model the treatment of liquid water presence by predicting a liquid saturation. Saturation values greater than zero characterize flooding and reduce the diffusion coefficients in the gas phase. This area has been the focus of a tremendous amount of effort in using CFD to model the PEMFC and is considered critical[85]. However, Single-phase models are generally considered valid as long as the saturation value of liquid within the GDL is kept small. These models are then recognized as appropriate for low-current density and low humidity operation where liquid water won't accumulate[76].

Computational fluid dynamics (CFD) models typically use the finite-volume method for solving fluid dynamics problems involving both single and two-phase flow. Incorporating electrochemical effects is typically done with an add-on electrochemistry module available as a part of many commercial software packages.

The supposedly first major group of CFD models were produced by the University of Miami Researchers. This original single-phase model had a variable water content in the membrane and temperature variation (the energy equation), but was only two-dimensional [86]. It was then expanded to three dimensions[87]. Later models by Liu and colleagues incorporated the multiphase mixture formulation of Wang [88, 89].

Another research group from the University of South Carolina published several papers (models) derived using the commercial CFD package FLUENT with its user-coding capability. These followed the general approach of the diffusive models of Springer. The membrane has variable water content, and water transport in the membrane was due to electro-osmotic drag and diffusion. The coefficients for each of these behaviors were primarily functions of water content, as is the membrane conductivity, following empirical property correlations that originated in the earlier Springer work [77, 90]. Later work added 2-phase water treatment[91]. Membrane and catalyst layers were not actually part of the computational domain: i.e. these regions were not meshed. The MEA in this work was treated as an interface, with no actual thickness, between the anode and cathode flow-fields. The water transport and ohmic potential drop across the membrane are treated using some simplifying linear approximations. Calculations then established the water flux and ohmic drop between the anode and cathode and created source terms on both sides of the interface to produce (i) reactant consumption / product creation, (ii) water flux, and (iii) ohmic loss.

The key simplifying relationship is the assumption that a linear water content profile exists across the membrane between anode and cathode values. Anode and cathode water content values were treated as Dirichlet boundary conditions: found as boundary conditions determined by the sorption isotherms based upon the humidity in the gas-phase of the adjoining cells. Water diffusion and EO drag are then based upon the lesser water content value or an average. Catalyst layer conduction losses aren't considered. With those approximations, source terms for species production and consumption could be calculated in the cells adjoining the MEA 'interface', as well as current density and the ohmic drop across the MEA. Thus a solution was had without meshing the membrane and catalyst layers, but at the expense of ignoring some important effects.

Sui and Djilali compared converged numerical solutions of water flux to the membrane transport equations to the approximate ones employed by Shimpalee and co-workers[92]. They claim that errors became large when there were large gradients in water content present (when unequal humidity levels present at the anode / cathode side). Errors were said to arise from the diffusion term, and were greater in

the thinner membranes rather than the thick ones (diffusion is stronger in relation to electro-osmotic drag in the thinner membranes). Mazumder followed this work and showed that the linear water content becomes the correct solution for the case of diffusion dominating drag effects in the membrane; i.e. for thin membranes [93].

The research group from Pennsylvania State University Electrochemical Engineering Center (ECEC) has also developed and refined CFD modeling. Their works introduced a single-domain approach that utilizes a single set of governing equations that apply to all sub-regions of the fuel cell, avoiding the use of interfacial boundary conditions at the boundaries between the different fuel cell sub-regions[94, 95]. These works were isothermal and single-phase, and didn't contain the detailed MEA submodel that was later employed in modeling water transport. Um and Wang later built a detailed MEA submodel where the water content distribution within the membrane is resolved. The spatial variations of ionic resistance and reaction rate within the catalyst layer were seen[96]. This work is isothermal, ignores electrical resistance in the device, and is a "constant flow" model where the mass source term in the continuity equation is neglected.

Comparisons of constant and variable flow models followed[97]. Constant flow models make two simplifying assumptions. They neglected the mass source term in the continuity equation and also set the gas density in the momentum equation to be constant. This has the effect of decoupling the solution of the flow field from the remaining governing equations (species, energy, and potential fields) and accelerating the calculations. They found that the gas density and velocity in the anode will experience large changes of about 50%, and that the flow decelerates. The anode HOR reaction was sufficiently facile that the overpotential from that reaction didn't change by more than about 15%, and was negligibly small to begin with. Water distribution and current density distributions were seen to remain similar. Cathode density and velocity didn't change as much because of the large percentage of inert nitrogen present in air, limiting velocity changes. Mass consumption terms impacted the flow field by reducing the pressure drop in a serpentine PEMFC. One calculation examined a PEMFC fed pure hydrogen and air[77].

Electron transport or current conduction losses are sometimes neglected in the published CFD models. Those that do take these losses into account must solve the charge conservation equation for the electronic phase. This gives two charge transport equations. One potential equation describes the electrolyte, or ionic phase, and another potential equation describes the solid, or electronic phase. If the electron transport equation is to be solved, additional capabilities become available. This allows the incorporation of electrical contact resistances between adjoining materials that were found to be significant experimentally [19], as well as the implementation of a boundary condition of total current, instead of cell voltage. Fuel cell stack modeling becomes possible with a total current boundary condition where the cells are connected in series and must therefore share the same current. Meng and Wang [78] examined the current density results with a model that both accounted for and ignored these losses (called "lateral resistance") in the GDL diffusion media. The patterns of current density produced were seen to differ substantially in the cross-flow channel direction. Simulation with a total current boundary condition followed [79]. They concluded that overall or global polarization curves were insufficient for validation of CFD models, and that distributed current density data were needed.

Non-Isothermal models consider heat transport and solve an additional conservation of energy equation. While isothermal models are common, non-isothermal models will solve the energy equation to gain a predicted temperature distribution and its effect on the performance of the PEMFC. Thermal management is intertwined with the water management topic through the temperature effect whereby the membrane water content depends on the relative humidity of gases and the saturation pressure of the gases is an exponential function of temperature. Bvumbe et al. [98] described the types and location of heat generation in the MEA. Early models that threat the MEA as an interface would only treat the heat generation globally [91]. Berning et al. set the prototype for thermal management establishing the heating terms among the various loss mechanisms[99]. The catalyst layers contain reversible and irreversible heat terms, and joule heating (ohmic heating) takes place in the membrane. Temperature distributions then depend on the thermal boundary conditions of the model, as well as the thermal properties (i.e. thermal conductivities) of various materials such as the diffusion layer and bipolar plates.

Some works using the CFD approach use simplified assumptions that might introduce modeling error. Berning et al. used a water transport model within the MEA which ignores water diffusion within the membrane[99]. They assume the membrane to be fully humidified, and the catalyst layers to be infinitesimally thin, precluding the treatment of catalyst layer losses due to dryout. The model of Mazumder and Cole [100, 101] similarly omitted diffusion or electro-osmotic drag in the membrane phase, and so this probably ignores water transport. The design and optimization-oriented CFD models of Grujicic and Chittajallu similarly assume a constant membrane hydration [102], as does the entire book of Al-Baghdadi [103]. By assuming the constant membrane hydration, they can essentially ignore the transport of water and assume a constant ohmic loss in the PEMFC membrane. They are constitutionally incapable of capturing the experimentally-observed reduction in membrane ohmic resistance (water gain) at low humidity and high current operation. Likewise, the increase in membrane ohmic resistance with high current density, under high humidity conditions, cannot be seen with these techniques.

In 2011, Pourmahmoud et al. [104] detailed the mesh requirements while utilizing the single-domain approach with a commercial CFD code. This approach meshes the MEA (thin membrane and catalyst layers), requiring a large number of cells with high skew ratio. Altogether, about 60 cells minimum must be used in the MEA through-plane direction, with about 20 gridpoints to cover the channel width and ~100 points in the flow direction. There are about 20-60 channels in the complete flow field, yielding something near 6 million points to model even a single small fuel cell [105]. These MEA cells have a very high aspect ratio, which negatively impacts the solution convergence [46]. Wu et al. investigated MEA meshing requirements as well [106]. An overly-fine computational mesh (used in the through-plane direction) caused the system to become unstable. The number of nodes used in the in-plane directions had much less effect on model stability.

The fundamental size mismatch between the thicknesses and dimensions of the different sub-regions of the PEMFC drive the high computational cost, even in 2005[2]:

> “CFD modeling is computationally demanding especially for three dimensional models. Because the geometric dimensions of the various fuel cell regions

> range several orders of magnitude, the models require very small elements to capture the details with accurate resolution."
>
> "For example, the typical anode and cathode catalyst layer thickness of PEM fuel cells are on the order of 10–20 μm, however, the height and width are 10–20 cm requiring at least a million elements for even a small 7 cm by 1 cm section of a fuel cell…. The computational cost of CFD modeling an entire cell is large and we are not yet able to simulate an entire fuel cell stack. However, the interactions between cells in a stack are critical for water and thermal management since the cells located at the middle section of the stack will require extra means of cooling."
>
> "Considering the computational cost of CFD modeling of PEM fuel cells, using a three-dimensional fuel cell stack model is not practical in most computing environments."

They then proceed to develop a 2-D model to reduce the computing cost and perform component optimization.

Later CFD models proceeded to focus on multiphase effects, modeling diffusion in microporous layers, without revisiting the difficulties with the modeling of the MEA layer. One example is Schwarz and Beale [107].

Several researchers have started developing multiscale approaches. Multiscale approaches first utilize a CFD model for the largest scales of the problem, the macroscopic scales, where problems of heat and mass transfer are solved. But it is also desired to model water transport throughout the fine, small-scale structure of catalyst layers. Effective transport properties throughout catalyst layer structures are not simply determined and must be found with detailed account for microstructural effects, such as pore filling, as one example[108]. The effects of very fine catalyst layer structure (of too small a scale to be resolved by the macroscopic CFD model) on PEMFC performance is being handled by mesoscale models.

1.6 Summary of Literature Review

PEMFC Modeling approaches seem mostly uniform in the treatment of laminar flows of gas mixtures. They are much less uniform in how they approach the modeling of the MEA, the heart of the device. There are several conflicting approaches and assumptions used in modeling the MEA. The

experimental and computational works can agree on several general conclusions, though there are several conflicting approaches and assumptions used in PEMFC modeling.

Modeling the behavior of the PEMFC with computational fluid dynamics requires understanding the intertwined physics of heat, water, and charge transport in the MEA. Fundamentally different approaches have been used to analyze thermal, water, and charge transport, however some consensus is emerging. Several commercially available software packages have converged on the "de-facto" standard approach started by the work of Springer and colleagues at Los Alamos National Labs (LANL). This approach treats water transport with the single-phase diffusion-based approach where water flux is governed by electro-osmotic drag and diffusion.

New developments in in-situ fuel cell experiments, and advanced imaging techniques with in-situ and ex-situ experiments, have called into question the validity of the MEA water transport models of many CFD modeling efforts. Most models use equilibrium uptake curves to form Dirichlet boundary conditions between gas humidity in the diffusion media (flow domain) and catalyst layer ionomer water uptake (the MEA). These relationships are used in modeling water transport within the MEA, in most of the CFD models, employing Springer's approach. A number of researchers investigating the behavior of the ionomer materials have found an "interfacial resistance" to water transport. Other models are reportedly compromised by assuming that water production takes place within the vapor phase of the cathode catalyst layer, as opposed to within the ionomer. Most models haven't incorporated the physics of membrane expansion with water uptake. The effective diffusivity, of common catalyst layer constructions, has only been validated against extensive experimental data relatively recently.

There appear to be 2 main methodological approaches. Existing approaches may incorporate the MEA into the computational domain, or treat it as an interface. The former method is used by single-domain approaches. These approaches numerically solve multiple conservation equations through the membrane and catalyst layers, in concert with the ordinary flow conservation equations in the gas channels. Because the catalyst layers are typically 1-2 orders of magnitude thinner than the gas channels,

this approach entails adding large numbers of thin, high-aspect ratio cells to the problem, increasing the computational costs.

The interface approach avoids adding large numbers of high-aspect ratio cells to the problem, but shortcomings have been noted. So far, it is fundamentally incapable of modeling hydration-related transients within the MEA, or changes in ohmic resistance of a differential cell caused by altering current loads. The approach has not yet meaningfully considered catalyst layer losses in either steady-state or transient operation; kinetic model parameters have been treated as free parameters, chosen without regards to platinum catalyst loading levels.

Modeling errors in water transport, central to PEMFC operation, may remain in both approaches.

Previous work has suggested the availability of simplifications to modeling the processes taking place in the MEA. Water and charge transport through the MEA has been shown to be primarily 1-D in nature. Lateral diffusion of water vapor in the gas phase adjacent to the MEA is known to be much higher than that in the catalyst layers. Modeling efforts comparing the 2-D and 1-D MEA approaches have found equivalent results.

Multiple groups have studied catalyst layer losses; they have found that these losses derive principally from ionic conduction losses. Gas concentration levels, temperature, and water content levels are claimed to be nearly constant, in the thru-plane direction, for typical constructions. Analytical solutions have been published for these simplified cases, which don't appear to have been adapted to CFD application.

Interface approaches to the modeling of the PEMFC have not been updated to incorporate the newly-available data. In particular, extensive experiments examining the physics of water transport have not been incorporated. Membrane expansion with water uptake hasn't been considered. The interfacial resistance to water transport has been similarly neglected. Recent experiments have connected catalyst-layer ionomer water content and varying exchange-current density. Most interface approaches haven't considered such a connection. Re-consideration of most CFD models, in light of subsequently-published experimental measurements of the underlying physic(s), is in order.

1.7 Objectives of the Current Study

The main objectives of the current study are to address perceived possibilities for modeling PEMFC operation with 3-D CFD, with appropriate physics capabilities, but at greatly reduced cost compared to the current dominant approaches, which entail meshing the exceedingly thin MEA.

This work upgrades the interface approach to modeling MEA behavior by applying updated physics to the problem from newly-published experimental findings. It then incorporates simplifications and analytical representations of the relevant physics. The Interface model is updated to include correct models of both HOR and ORR kinetics, as well as water transport. A new approximate water transport scheme has been devised that allows for membrane hydration changes with current levels.

The particular objectives of the current study are listed as follows:

(i) Develop an upgraded interface model for the simulation of the MEA under steady-state conditions. The model should incorporate newly-published physics of the MEA and address the missing capabilities of the previously-developed interface approach. Specifically, the interface approach should add capabilities of (i) modeling water storage, and (ii) modeling catalyst layer losses.

(ii) Validate the existing and upgraded interface models against published data from differential cell experiments. Demonstrate the performance improvements.

(iii) Conduct benchmark simulations with the upgraded interface formulation. Develop a numerical formulation of the upgraded interface approach to show the case of a validated benchmark data with distributed current, temperature, species fraction, and water content data as available.

The organization of this dissertation is outlined below. Chapter 2 presents the mathematical formulation of the problem. It presents the basic principles of operation of the PEMFC, the governing equations of flow for the device, and the interface model is developed with its inputs (boundary conditions) from the governing equations. The numerical formulation of the governing equations of flow is presented in Chapter 3. Verifications of the MEA interface model's approximate treatment of water transport are presented in chapter 4. The approximate solution is compared to well-resolved finite-volume solutions. Discrepancies in the results are catalogued with respect to membrane thickness,

humidity boundary conditions, and current density. Interface models are validated against experimental, differential cell data in chapter 5.

Chapter 6 examines 3-D test cases and employs the upgraded interface approach to these problems. Chapter 7 gives a summary and examines some opportunities for future work.

2 MATHEMATICAL FORMULATION

The mathematical formulation is described as follows. First, an overview of the common simplifications and assumptions employed is presented in section 2.1. The relevant conservation equations for the 3-D domains are described in 2.2. These include the conservation of mass, momentum, species, energy, and charge (or current). The 2-D MEA interface model follows in 2.3. Boundary conditions and operating conditions are defined in 2.4. Finally, initial conditions are given in 2.5.

2.1 Simplifications and Assumptions

The reactant gas streams are treated as laminar flows of concentrated multi-species ideal gas mixtures. They occur in the respective anode and cathode flow domains, which have free-flow channel and porous flow (diffusion layer) regions. The anode mixture consists of hydrogen (H2), water vapor (H2O), and possibly some inert. The cathode mixture consists of either humidified air or humidified oxygen, consisting of a mixture of oxygen (O2), water vapor (H2O), and possible nitrogen (N2). These flows can be modeled with conventional inflow, outflow, and pressure boundary conditions.

The MEA serves to separate the two gas streams. It is modelled as a collection of variables and boundary conditions to determine wall fluxes of the various quantities into the two flow (computational) domains. It creates a current density flux boundary condition for the electronic current conservation physics. It creates mass flux boundary conditions for the reactants and product water species and a corresponding mass flow boundary condition for the continuity equation. There are also heat flux boundary conditions that apply to the conservation of energy equation.

The MEA formulation makes use of several simplifying assumptions. Nafion ionomer is assumed where the equivalent weight is known. In order to develop analytical representations of catalyst

layer losses, the compositions (volume fractions) of the ACL / CCL are assumed to be uniform throughout their thickness. A carbon-supported catalyst is presumed and porosity relations from particular catalyst materials are employed. Variations of ECSA, with humidity, are assumed known and are not modeled intensively here. The representation of anode losses depends on the given model of HOR kinetics and may not be rigorously valid with greatly reduced PT catalyst loadings. Estimates of the bounds of validity are given.

2.2 Governing Equations of Flow and Reaction

This section attempts to describe and categorize the governing relationships, or equations, used in the 3-D anode and cathode domains in this model of a PEM fuel cell with computational fluid dynamics. The relations consist of (1) fluid dynamics (2) heat transfer and (3) current conduction.

2.2.1 Basic Gas Mixture Relations:

Several basic gas mixture relations apply to the anode and cathode gas flows that are commonly used in PEM fuel cell modeling. These flows are assumed to be single-phase ideal gas mixtures; liquid water isn't considered outside of the MEA. The flows are compressible and laminar. In the porous diffusion media, the Brinkman equations solve for fluid velocity. The solid and fluid phases are assumed to be in thermodynamic equilibrium. Ideal gas mixture relations are detailed in appendix A.1 .

2.2.2 Single Phase Conservation Equations

This section presents the single-phase governing equations of a PEMFC model, which will necessarily vary by region. The various computational subdomains or regions of the PEM fuel cell are described in Figure 2.1 with a cut-away view representing the cross-section of a single channel on each side. The divisions mirror the major components of the device. The MEA is drawn as a line because it is approximated as a 2-dimensional interface, of zero thickness, within the 3-D geometry that interacts with the anode and cathode as a collection of boundary conditions, with its own storage of variables.

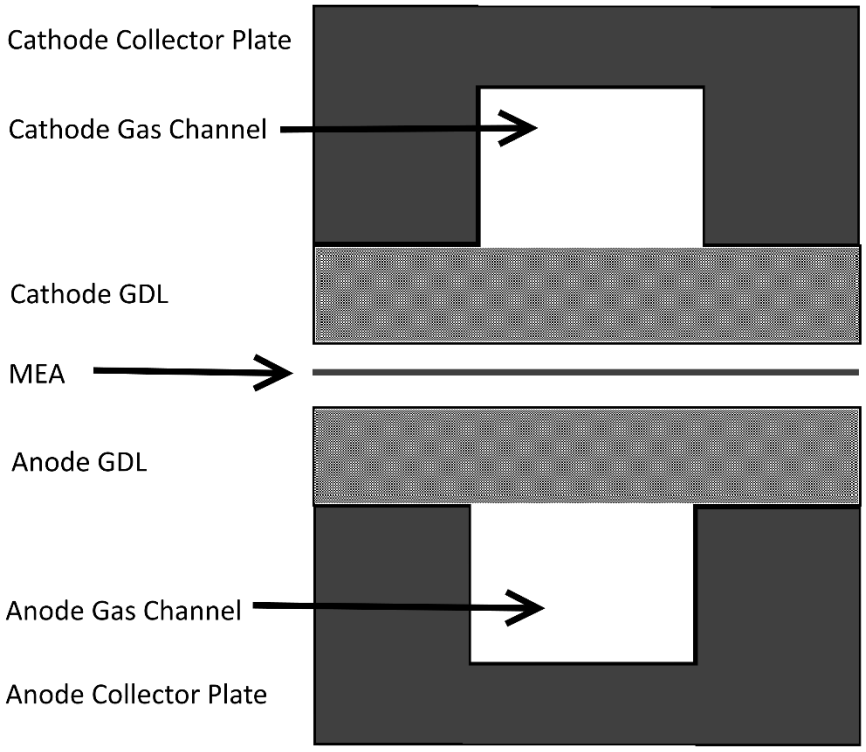

Figure 2.1. Regions and Computational Domains of the PEMFC

Gas flows occur in the free flow regions of the anode and cathode gas channels and also in the porous regions of the gas diffusion layers (GDL). The GDL have a porosity ε, which is the fraction of a control volume occupied by gas, between zero and 1. Porosity is zero in pure solid regions (the collector plates) and unity in the free flow regions. Physical properties of the fluid are volume averages taken over the volume of the pores. The density and viscosity of the fluid in the porous regions are those same properties that can be measured experimentally in a free flow region and so all properties are continuous with those in the adjacent free flow. The flow velocity in the porous regions is defined as a superficial volume average, or Darcy velocity. This average over a unit volume (entire volume comprising both solid matrix and pore) defines velocity as the volume flow rate per area of the porous medium. When defined this way, the fluid velocity is continuous at gas channel (free flow region)-GDL (porous flow region) boundaries.

The continuity and momentum equations in eq. (2.1) and eq. (2.2) below, taken together, are known as the Brinkman equations.

$$\nabla\bullet\left(\rho\vec{\mathbf{u}}\right)=0 \tag{2.1}$$

$$\frac{\rho}{\varepsilon^2}\left(\vec{\mathbf{u}}\bullet\nabla\vec{\mathbf{u}}\right)=-\nabla p+\nabla\bullet\left[\frac{\mu}{\varepsilon}\left\{\nabla\vec{\mathbf{u}}+\left(\nabla\vec{\mathbf{u}}\right)^T-\frac{2}{3}\left(\nabla\bullet\vec{\mathbf{u}}\right)\overline{\overline{\mathbf{I}}}\right\}\right]-\overline{\overline{\mathbf{K}}}^{-1}\mu\vec{\mathbf{u}} \tag{2.2}$$

where μ (kg m^{-1} s^{-1}) is the dynamic viscosity of the mixture, $\vec{\mathbf{u}}$ is the mass-average velocity vector (m s^{-1}) in the Cartesian coordinate system, $\overline{\overline{\mathbf{K}}}$ is the permeability tensor of the porous medium.

The conservation of species equations are applied to the same domains and represent mass flux from convection and diffusion. Temperature-driven diffusion is assumed to be insignificant. The cathode gas has three species (oxygen=1, water=2, and nitrogen=3) and the anode uses two species (hydrogen=1, water=2). The cathode relationships are in eq. (2.3) where $\tilde{D}_{ik}$ (i, k=1,2,3) are the multicomponent Fick Diffusivities, the components of the multicomponent Fick diffusivity matrix, which are needed to solve the problem. These are symmetric, i.e. $\tilde{D}_{ik}=\tilde{D}_{ki}$. The multicomponent Fick Diffusivities are determined from the multicomponent Maxwell-Stefan diffusivities D_{ik}, which are, for low-density gas mixtures, the binary diffusivities for the same species pairs.

$$\begin{aligned}\nabla\bullet\left(\rho\vec{\mathbf{u}}\omega_1\right)&=\nabla\bullet\left[\rho\omega_1\sum_k\tilde{D}_{1k}\left(\nabla x_k+\frac{\nabla p}{p}\left(x_k-\omega_k\right)\right)\right]\\ \nabla\bullet\left(\rho\vec{\mathbf{u}}\omega_2\right)&=\nabla\bullet\left[\rho\omega_2\sum_k\tilde{D}_{2k}\left(\nabla x_k+\frac{\nabla p}{p}\left(x_k-\omega_k\right)\right)\right]\\ \omega_3&=1-\omega_1-\omega_2\end{aligned} \tag{2.3}$$

$$\frac{x_i x_k}{D_{ik}}=-\omega_i\omega_k\frac{\sum_{j\neq i}\left(\mathrm{adj}B_i\right)_{jk}}{\sum_{j\neq i}\tilde{D}_{ij}\left(\mathrm{adj}B_i\right)_{jk}},\quad \left(B_i\right)_{kj}=\tilde{D}_{kj}-\tilde{D}_{ij},\quad i\neq j \tag{2.4}$$

The term $\left(\text{adj}B_i\right)_{jk}$ is the jk[th] component of the adjoint of the matrix B_i. Solving eq. (2.4) creates several algebraic expressions for the elements of the multicomponent Fick Diffusivity matrix $\tilde{D}_{ik}$, which can be solved directly for binary and ternary systems.

The multicomponent Maxwell-Stefan Diffusivities D_{ik} are the binary diffusivities for each of the species pairs, estimated in eq. (2.5) with an empirical relationship originating from kinetic gas theory. Here D_{ij} has units of (m^2 s^{-1}), temperature T (K), P absolute pressure (Pa), M_i molar mass (kg mol^{-1}), and v_i molar diffusion volumes of the species (m^3 $mole^{-1}$). The relevant data are below in Table 2.1.

$$D_{ij} = 3.16x10^{-8}[\text{Pa m}^2\text{s}^{-1}]\frac{T^{1.75}\,[\text{K}^{-1}]}{P\left(v_i^{1/3}+v_j^{1/3}\right)^2}\left[\frac{1}{M_i}+\frac{1}{M_j}\right]^{1/2} \tag{2.5}$$

Table 2.1. Data for estimating binary diffusivities for gas species pairs.

Species	Molecular mass (kg mol^{-1})	Diffusion volume (m^3 $mole^{-1}$)
O2	.032	$16.6x10^{-6}$
N2	.028	$17.9x10^{-6}$
H2	.002	$7.07x10^{-6}$
H2O	.018	$12.7x10^{-6}$

In the GDL domains, the solid matrix of the porous material serves to reduce the volume available for diffusion. Effective diffusivities are modeled for the porous domains in eq. (2.6).

$$\tilde{D}_{ij}^{eff} = \tilde{D}_{ij}\varepsilon^{3/2} \tag{2.6}$$

The heat equation assumes a single temperature field throughout the anode and cathode domains. The temperature field denoted T is modeled within solid domains (the current collector plates), fluid domains (the flow channels), and porous flow domains (the diffusion media, or GDL). Thermal equilibrium among the different phases is assumed. The heat equation is eq. (2.7) where ρ (kg m^{-3}) is the fluid density, c_p (J kg^{-1} K^{-1}) is the gas mixture heat capacity at constant pressure, and $\vec{\mathbf{u}}$ (m s^{-1}) is the

fluid velocity field. Q (W m^{-3}) represents resistive heat generation. The term k_{eff} (W m^{-1} K^{-1}) represents the effective thermal conductivity of the domain. In the flow channels it refers to the thermal conductivity of the gas mixture k, in the collector plates it refers to the solid material's conductivity and in the porous domains it is the effective thermal conductivity of the combined solid-fluid system, which is found by a volume average of the thermal conductivity of the solid phase of the GDL, k_{GDL}, and that of the gas mixture, k in (2.8).

$$\nabla \bullet \left(\rho c_p \vec{\mathbf{u}} T - k_{eff} \nabla T \right) = Q \tag{2.7}$$

$$k_{eff} = \left(1 - \varepsilon\right) k_{GDL} + \varepsilon k \tag{2.8}$$

The thermal conductivity of the GDL material is strongly anisotropic, with in-plane ($k_{GDL,=}$) and thru-plane ($k_{GDL,\perp}$) values. It is represented by a tensor as eq. (2.9).

$$k_{GDL} = \begin{bmatrix} k_{GDL,=} & 0 & 0 \\ 0 & k_{GDL,=} & 0 \\ 0 & 0 & k_{GDL,\perp} \end{bmatrix} \tag{2.9}$$

Significant thermal contact resistances have been recognized as occurring at the current collector plate and the GDL. At other component interfaces, such contact resistances are commonly ignored [109]. Thermal contact resistance between multiple layers of GDL was found to be negligible [82], and the contact resistance with solid plates (R_{ct}) was found to be about 1-1.5x10^{-4} m^2 K/W at typical cell compaction pressures.

The conservation of electronic current equation must be solved in the electronically-conductive domains, namely the collector plates and GDL. Voltage losses arising from electronic conduction have been ignored in many models; thought to be insignificant due to the high electrical conductivity of the respective materials. However, contact resistance losses between the GDL and collector plate have been found to be significant [38]. The electrical conductivity of GDL materials has also been found to be highly anisotropic. A rudimentary effort here attempts to address these issues.

Electric current flows in the solid, or electronically-conductive (e) phase of the GDL and the collector plates. Current flux $\vec{\mathbf{J}}_e$ in eq. (2.10) (A m^{-2}) is represented as the flow of positive charges in the direction of reduced electrical potential, in the presence of an electric field $\vec{\mathbf{E}}$ (V m^{-1}), and current must be conserved as eq. (2.11), where Φ_e is the scalar electric potential and σ_e (S m^{-1}) the electrical conductivity. The electrical conductivity of the current collector plate (CCL) is isotropic, but that of the GDL is a tensor: it has separate in-plane ($\sigma_{e,=}$) and thru-plane ($\sigma_{e,\perp}$) values as eq. (2.12).

$$\vec{\mathbf{J}}_e = \sigma_e \vec{\mathbf{E}} = \sigma_e(-\nabla\Phi_e) \tag{2.10}$$

$$\nabla \bullet \vec{\mathbf{J}}_e = 0 \tag{2.11}$$

$$\sigma_e = \begin{bmatrix} \sigma_{e,=} & 0 & 0 \\ 0 & \sigma_{e,=} & 0 \\ 0 & 0 & \sigma_{e,\perp} \end{bmatrix} \tag{2.12}$$

Resistivity data has been published for GDL materials. Thru-plane resistivity values of .08 (Ω cm) and in-plane resistivity values of .006 (Ω cm) have been reported as typical [38]. Current collector plates are commonly made from graphite, or metals. These materials have much lower resistivity (greater conductivity) and hence the voltage losses in these components are often not a great concern.

Electrical contact resistance between the gas diffusion media and the current collector plate were found to be significant and highly influenced by the cell assembly pressure (contact force). Carbon cloth and carbon fiber papers were reportedly measured as 2-3 Ωcm^2 at full compaction pressure.

Resistive heating gives a minor volumetric heat source Q (W m^{-3}) from the dissipation of electrical energy within the conductive GDL and CCL domains described by eq. (2.13).

$$Q = \vec{\mathbf{J}}_e \bullet \vec{\mathbf{E}} \tag{2.13}$$

The collected conservation equations represent 8(anode) or 9(cathode) scalar equations for the same number of unknown variables to be solved for. The continuity and momentum equations represent pressure p and the three velocity components of velocity $\vec{\mathbf{u}}$. The conservation of species equations represent 2 scalar mass fractions in the anode domain, with variables $\omega_1 = \omega_{H2}$ and $\omega_2 = \omega_{H2O}$. In the

cathode domain, the conservation of species equations represent 3 scalar mass fractions, with variables $\omega_1 = \omega_{O2}$ and $\omega_2 = \omega_{H2O}$, and $\omega_3 = \omega_{N2}$. The conservation of energy equation contains 1 equation for the scalar variable T (temperature) and the remaining conservation of electronic current equation contains the scalar voltage variable Φ_e.

2.3 Governing Equations of MEA Interface

The MEA is represented as a 2-dimensional interface; a zero-thickness layer that separates the anode and cathode computational domains. The MEA computational routine accesses the solution variables at the surface of each domain and produces fluxes into each of the physics. This section explains the mathematics of the upgraded interface model being used to replicate the operation of a Nafion-based membrane electrode assembly (MEA) installed in a PEM fuel cell. The role of the interface model in multi-domain approaches has been to approximate all the externally relevant behavior of the MEA (i.e. current generation, reactant consumption, water permeation, heat generation, etc.) by boundary conditions on both sides of the interface [76].

A variety of focused research into the distinct physics of the MEA is needed in order to create this interface model. The following sections explain the different areas of physics which are needed. Distinct physics operate exclusively within the MEA, which are not used in the larger 3-dimensional model, and this information is needed to determine input/output behavior. Then, the later sections show how the interface model inputs are used to determine the outputs. Model results are validated against differential cell data in chapter 5.

2.3.1 Interface Model: Schematic

Figure 2.2 shows an interface schematic with typical thickness dimensions added. The anode contains hydrogen, water vapor, and inert nitrogen species, while the cathode is modelled as a mixture of oxygen, water vapor, and inert nitrogen. The interface takes as boundary values the anode (A) and cathode (C) solution variables from the GDL. The interface replaces the MEA, containing the anode catalyst layer (ACL), membrane (MEM) and cathode catalyst layer (CCL) regions, in the center portion of the figure, and substitutes sources, acting as boundary conditions.

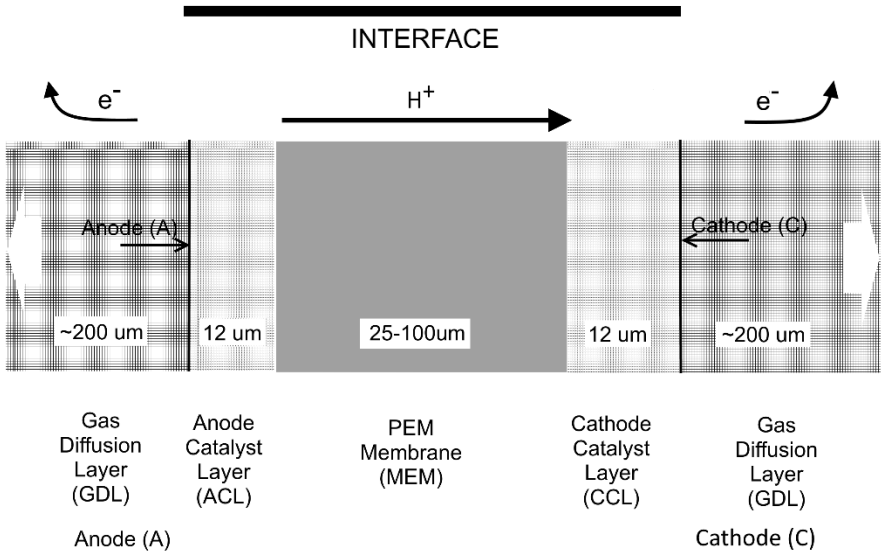

Figure 2.2. Schematic of hte MEA interface model

2.3.2 Interface Model: Inputs and Outputs

The MEA is represented as a 2- dimensional or planar mesh in contact with the anode and cathode flow domains in Figure 2.3. It tabulates the inputs and outputs from the proposed interface model that interact with the overall conservation equations. Inputs include gas pressure, temperature, mole fractions, and voltage from the adjacent anode and cathode cells within the gas diffusion layer (GDL). The mole fractions of the species present (water and the reactants: hydrogen, oxygen, and nitrogen) are used to calculate humidity and thermodynamic voltage similarly to the previous works.

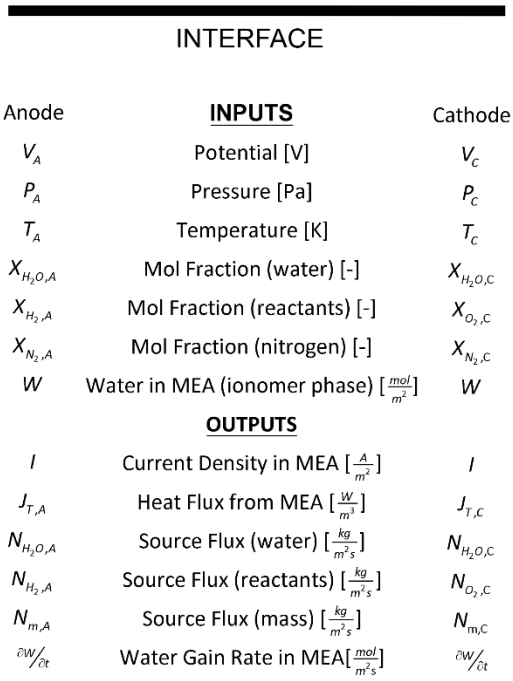

Figure 2.3. Inputs and Outputs of MEA interface model

The interface model outputs estimates of current density, heat sources, reactant fluxes, water fluxes, and the water gain rate of the ionomer phase of the MEA. The thermal source terms $J_{T,A}$ and $J_{T,C}$ represent waste heat generation, occurring in the MEA, due to fuel cell losses. The total heat generation is split between anode and cathode. Stoichiometric relationships require reactant mass consumption $N_{H_2,A}$ and $N_{O_2,C}$ at the anode and cathode boundaries, respectively, with a fixed relationship to the current density I. Convective boundary conditions are used to calculate water mass flux $N_{W,A}$ and $N_{W,C}$ of the anode and cathode. The processes are listed in Figure 2.4 by their simplest equation forms. Moving from left to right, the output groups are described in brackets{}; the next column gives their defining equations; and the third column gives their key terms with those term's principal dependencies, which are indicated by output groups {} and a numbered list (1-8) of inputs / internal variables.

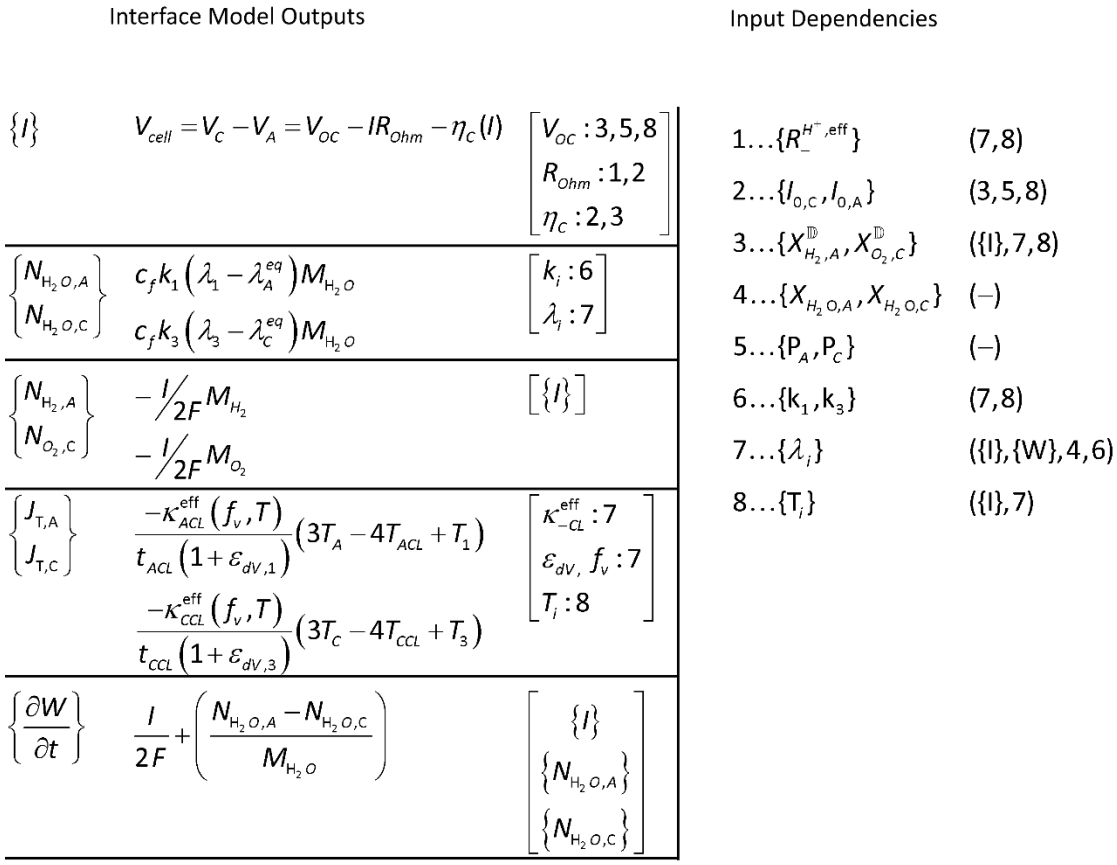

Figure 2.4. Interface model outputs and their dependencies

The top of the figure indicates the dependence of current density on ohmic resistance R_{Ohm} , and that variable's formulation from ionic resistances $R_{ACL}^{H^+,\text{eff}}$, $R_{CCL}^{H^+,\text{eff}}$, and $R_{MEM}^{H^+}$ from the catalyst layers and membrane, respectively. These resistances depend on { λ_i , T_i }, the local water content and temperature profiles of the MEA, respectively. A great of coupling/ interdependency is involved through combined temperature and humidity effects.

The water content of the MEA is kept as a scalar variable W, the spatially-integrated water content through the thickness of the ionomer phase of the MEA. A water gain rate is calculated as part of the computations and W is subsequently adjusted to reach its unique equilibrium. As water content W nears its equilibrium value, the water gain/loss rate will lessen. Experimentation with the calculations has

found that there is a unique equilibrium point with a given set of inputs; a steady-state solver can determine the equilibrium values of W by solving eq. (2.14)

$$W^{i+1} = W^{i} + {\partial W}/{\partial t}\,\delta \tag{2.14}$$

The remainder of this chapter shows the background and formulation of the interface model. After presenting the necessary background, the various sections are assembled.

2.3.3 Interface Model: Composition of the MEA

The basic material composition of the MEA is described before proceeding with the rest of the model development. The MEA consists of the following regions: anode catalyst layer, membrane, and cathode catalyst layer, denoted by ACL, MEM, and CCL, respectively. Appendix B.1 covers the details of the MEA composition.

2.3.4 Interface Model: Ionomer-Phase Water Uptake

Ionomer equilibrium water uptake from humidified gases is modeled with reference to water activity, or gas humidity at both anode (α_a) and cathode (α_c) side adjacent cells. Appendix B.2 covers the background of water transport within the MEA with greater detail. Water uptake is non-dimensional λ (mol H_2O/mol $SO3^-$), the number of water molecules per acid site within the ionomer, which normalizes water uptake for any equivalent weight. Water uptake from Nafion membranes in contact with liquid water has been observed at $\lambda = 22$ water molecules per acid site, while uptake from the vapor phase ranges from $\lambda = 1-2$ (10% RH) to $\lambda = 14-16$ (100% RH) [110].

Water concentration of dissolved water in the ionomer, C_w (mol H_20 m^{-3}), is related to the dimensionless water content λ expressed as (2.15) where c_f is the concentration of fixed charge sites (mol $SO3^-$ m^{-3}), a constant for a given membrane and independent of water content. As a result of water sorption, the membrane phase then expands and is considered a mixture of the two phases: dry membrane and water. The volume fraction of water within the ionomer phase, f_v, is described as the ratio of water volume to the sum of membrane and water volume in the hydrated ionomer in (2.16). The terms $\mathbb{V}_w$ and

$\mathbb{V}_{lo}$ represents the molar volume of water (m^3 mol^{-1}) and the ionomer, respectively. A corresponding fractional increase in volume of the hydrated ionomer phase, ε_{dV}, compared to the dry volume, is described by eq. (2.17) [24].

$$C_w = c_f \lambda = \frac{\rho_{lo}}{EW}\lambda \tag{2.15}$$

$$f_v = \frac{\lambda \mathbb{V}_w}{\mathbb{V}_{lo} + \lambda \mathbb{V}_w} = \frac{\lambda\left(M_w / \rho_w\right)}{(EW/\rho_{lo}) + \lambda\left(M_w/\rho_w\right)} \tag{2.16}$$

$$\varepsilon_{dV} = \frac{\mathbb{V}_w}{\mathbb{V}_{lo}}\lambda = \frac{M_w \rho_{lo}}{EW \rho_w}\lambda \tag{2.17}$$

The volume increase of the hydrated ionomer with water uptake is assumed to increase its thickness. The swollen membrane thickness is eq. (2.18).

$$t_{MEM}^{\mathbb{S}} = t_{MEM}\left(1+\varepsilon_{dV}\right) = t_{MEM}\left(1 + \frac{M_w \rho_{lo}}{EW \rho_w}\lambda\right) \tag{2.18}$$

2.3.5 Interface Model: Ionomer-Phase Water and Current (Ion) Transport

The membrane is almost entirely impermeable to gases, but allows absorption, desorption, and permeation of water. Thus, only water and protonic current needs to be considered within the membrane. The consumption of hydrogen and oxygen reactants is accounted for by boundary fluxes from the gas diffusion layer (GDL) regions of the computational domain. The inert species nitrogen has zero-flux conditions at the interfaces.

Water and current transport within the membrane are assumed to occur only in the thru-plane direction and are treated with the common, de-facto standard phenomenological approach of Springer et al [45], using only macroscopic calculations. This approach was used by all commercial CFD codes (as of 2008)[46]. The flux forms are shown in eq. (2.19). The flux of water $\vec{\mathbf{J}}_w$ (mol m^{-2} s^{-1}) occurs due to electro-osmotic drag from the protonic current density $\vec{\mathbf{J}}_{lo}$ (A m^{-2}) and diffusion from the spatial gradient

in water content λ. The current density $\vec{\mathbf{j}}_{lo}$ represents protons (H+) moving through the membrane under the influence of the gradient of the electric potential field of the ionic phase Φ_{lo} and conservation of current requires $\vec{\mathbf{j}}_{lo}$ satisfy $\nabla \cdot \vec{\mathbf{j}}_{lo} = 0$. When restricted to the thru-plane direction only, current density must be constant through the thickness of the membrane.

$$\vec{\mathbf{j}}_{W} = n_d \frac{\vec{\mathbf{j}}_{lo}}{F} - c_f D_W \nabla \lambda \quad \vec{\mathbf{j}}_{lo} = -\sigma_{lo} \nabla \Phi_{lo} \tag{2.19}$$

The three values n_d, D_W, and σ_{lo} are transport properties obtained from experiment, analytical arguments, or theoretical considerations. They have been found to exhibit water content and temperature dependence. Property variation makes this problem inherently non-linear and the degree of property variation with changes in water content was said to be substantial[93]. The electro-osmotic drag coefficient, n_d (-), represents the number of water molecules dragged from anode to cathode along with each migrating proton. Typical approximate values have been reported as 0.6-1.0 for vapor-equilibrated membranes and 2-2.5 for liquid-equilibrated membranes[57] . The diffusion coefficient of water in the Nafion membrane phase, D_W ($m^2\ s^{-1}$), is also a complex function of temperature and water content. This work will use the methodology of Ge et al. [72] where the diffusion coefficient was found to be between 2-10 x 10^{-10} $m^2\ s^{-1}$, varying with water content and temperature. The ionic conductivity of the ionomer σ_{lo}, (S m^{-1} or $\Omega^{-1}\ m^{-1}$), is also very much water-content and temperature dependent. Typical values range from 2-20 S m^{-1}, with the greatest conductivity being in liquid-equilibrated membranes [20, 53, 54].

These properties are re-formulated with the best available published data Appendix B.3 .

2.3.6 Interface Model: Gas-Phase Transport in Catalyst Layers

Gas transport losses within the anode and cathode catalyst layers are considered in this section. Hydrogen and oxygen reactants are consumed through the thicknesses of anode and cathode porous catalyst layers (electrodes). Reaction rates will vary with depth through the catalyst layer, however the distribution of reaction rates is predominantly shaped by conduction losses in the catalyst layer's ionomer [29, 30] and not by normally-occurring variations in reactant gas concentration. The reactant mole fractions at the outer edge of the ACL and CCL, $X_{H_2,A}$ and $X_{O_2,C}$ are adjusted to diffusion-corrected values $X^{\mathbb{D}}_{H_2,A}$ and $X^{\mathbb{D}}_{O_2,C}$ at the location of average reaction current density as seen in eq. (2.20) and eq. (2.21). The normal current density is I (A m^{-2}), $t^{\mathbb{D}}_{ACL}$, $t^{\mathbb{D}}_{CCL}$ (m) represent the effective gas diffusion lengths within each catalyst layer and $D^{\text{eff}}_{H_2,\text{ACL}}$, $D^{\text{eff}}_{O_2,\text{CCL}}$ are the effective catalyst layer diffusion coefficients.

$$X^{\mathbb{D}}_{H_2,A} = X_{H_2,A} - \frac{I}{2F}\frac{t^{\mathbb{D}}_{ACL}}{D^{\text{eff}}_{H_2,\text{ACL}}}\frac{RT_{ACL}}{P_A} \tag{2.20}$$

$$X^{\mathbb{D}}_{O_2,C} = X_{O_2,C} - \frac{I}{4F}\frac{t^{\mathbb{D}}_{CCL}}{D^{\text{eff}}_{O_2,\text{CCL}}}\frac{RT_{CCL}}{P_C} \tag{2.21}$$

The details of formulating an effective diffusion coefficient from the ACL and CCL composition are in Appendix B.4 .

2.3.7 Interface Model: Kinetic Losses in Catalyst Layers

The interface model treats kinetic losses, also referred to as activation losses, in the anode and cathode catalyst layers. Kinetic losses are the losses (voltage losses) required to drive the chemical reactions at the rate (current density) required. Separate formulations are developed here to describe the anode and cathode kinetics. Anode kinetics typically aren't that important to a PEMFC model as the hydrogen oxidation reaction (HOR) is quite facile, with a large exchange current density. Cathode kinetics are very important to PEMFC modeling and the subject of a great deal more research. The oxygen reduction reaction (ORR) occurring at the cathode is a source of major voltage loss with currently available practical PEMFC catalyst configurations.

Anode losses are examined first. Anode kinetics follow the general Butler-Volmer (BV) model. The ideal BV model pre-supposes an anode catalyst layer (ACL) without ohmic resistance or gas diffusion losses[4, 111] in eq. (2.22), where I (A m^{-2}) refers to the cell current and $I_{0,A}$ refers to the superficial exchange current density for the HOR occurring at the anode electrode (explained below). The term η_A refers to the kinetic or activation overpotential at the anode (V): the voltage loss. The terms υ_a and υ_c are the anodic and cathodic charge transfer coefficients, respectively. These are fundamental constants describing the reaction, which are not supposed to change with operating conditions such as temperature, humidity, etc [23, 37]. They are not appropriately used as adjustable parameters in a given problem. The superficial exchange current density $I_{0,A}$ is the dominant parameter in the BV equation to be influenced / optimized, influencing the voltage loss. Exchange current density depends on gas temperature, pressure, and reactant concentration (mole fraction). It also depends on electrode morphology, the catalyst type, and the aging / degradation of the catalyst layer. It is known to be an exponentially-increasing function of temperature.

$$I = I_{0,A}\left[\exp\left(\frac{\upsilon_a F}{RT_{ACL}}\eta_A\right) - \exp\left(\frac{-\upsilon_c F}{RT_{ACL}}\eta_A\right)\right] \tag{2.22}$$

The HOR reaction is facile; the exchange current density can reach ~20 times or more the size of the maximum operating current density at typical operating conditions. The bracketed term must necessarily be small as well and so the arguments to the exponential terms are typically less than 0.15. With this limitation, the linearized BV equation in eq. (2.23) can represent the losses of the HOR[4, 111].

$$\eta_A = \frac{RT_{ACL}}{\left(\upsilon_a + \upsilon_c\right)F}\frac{I}{I_{0,A}} \tag{2.23}$$

Several sources indicate that the reaction is symmetric, i.e. $\upsilon_a = \upsilon_c$ [3, 37, 38, 111]. Sources indicate that $\upsilon_a = \upsilon_c = 0.5$ and thus $\upsilon_a + \upsilon_c = 1$ [4, 37, 111]. Other sources indicate that $\upsilon_a = \upsilon_c = 1$ and thus $\upsilon_a + \upsilon_c = 2$ [3, 38]. Focused experiments [23] claimed that both values of the charge transfer coefficients could fit the experimental data. As of 2015, Durst et al. showed that $\upsilon_a + \upsilon_c = 1$ could fit measurements performed over a range of temperatures [37].

The details of formulating $I_{0,A}$ (A m^{-2}), the superficial exchange current density for the HOR occurring at the anode electrode, are in Appendix B.5

Cathode kinetic losses are examined next. BV kinetics simplify to Tafel kinetics when modeling the ORR occurring at the CCL. With very low exchange current density, and without significant conduction or diffusional losses, Tafel kinetics follows eq. (2.24) [19] where the term η_C (V) refers to the purely kinetic or activation overpotential of the ORR at the cathode. I (A m^{-2}) refers to the cell current as before and I_x the crossover current density (which represents a small amount of hydrogen permeation "crossover" from the anode through the membrane into the cathode). The superficial exchange current density $I_{0,C}$ refers to the superficial exchange current density for the ORR occurring at the cathode electrode. Exchange current density for the ORR taking place on platinum catalyst depends on gas temperature, pressure, reactant concentration (mole fraction), electrode morphology, and the catalyst type. It is known to be an exponentially-increasing function of temperature. The term υ_c is the cathodic charge

transfer coefficient, which was found experimentally to be unity for the ORR when ohmic losses were correctly accounted for[19]. The Tafel slope indicated is 70 mV/decade at 80 °C (with υ_c=1).

$$\eta_C = \frac{RT_{CCL}}{\upsilon_c F}\ln\left[\frac{I+I_x}{I_{0,C}}\right] = \underbrace{\frac{2.303\,RT_{CCL}}{\upsilon_c F}}_{\text{Tafel Slope}}\log\left[\frac{I+I_x}{I_{0,C}}\right] \tag{2.24}$$

Experimental works have shown considerable disagreement in measuring the Tafel slope. Some works have reported "double Tafel slopes" where the values consistent with υ_c=1 are reported at low current densities together with a doubled Tafel slope (consistent with υ_c=0.5) at greater current densities. This apparent doubling of the Tafel slope can be caused by the presence of un-recognized transport losses in the CCL (i) from conduction in the electrolyte phase, or (ii) from diffusive losses in the gas phase[19]. Prior CFD models, utilizing the Interface approach, have typically not been able to model catalyst layer losses in rigorous fashion. In order to match experimental data, several works modeling low humidity operation employed doubled, or nearly doubled, Tafel slopes[43] [112] to match the experimental data. In the present model, the cathodic charge transfer coefficient υ_c=1 and does not change with current level, humidity, or other factors.

The details of formulating $I_{0,C}$ (A m^{-2}), the superficial exchange current density for the ORR occurring at the cathode electrode are in Appendix B.6 .

2.3.8 Interface model: Calculation of Water Transport

The interface needs to calculate a MEA hydration and temperature profile. Approximate heat and water transport equations must be solved within the MEA in order to estimate ohmic resistances, effective catalyst layer losses, and current density. The interface model iteratively calculates (i) a water content profile, (ii) current density, and (iii) a temperature profile.

Figure 2.5 shows a profile schematic to explain the water and heat transport equations. An approximate water content profile $\lambda(z)$ is assumed to be a second order polynomial determined by three unknown values $(\lambda_1 \quad \lambda_2 \quad \lambda_3)$ occurring at the ACL-membrane interface (anode side), midpoint, and CCL-membrane interface (cathode-side) of the membrane. The equilibrium water uptake of the anode, λ_A^{eq}, and cathode λ_C^{eq}, are found from the water uptake curves, using the water activity and temperature of the anode and cathode gases. The water contents of the ionomer in the ACL, λ_{ACL} and CCL, λ_{CCL}, are assumed uniform throughout the respective catalyst layers, with values of λ_1 and λ_3.

The water transport model employs convective boundary conditions of water absorption and desorption. The MEA can gain or lose water content. The water content profile utilizes 3 equations: 2 values of its slope, at points 1 and 3, in addition to the integrated water content (W), at pseudo steady-state conditions. The pseudo-steady-state assumption involves ignoring water content distribution variations within the ionomer of the MEA, to represent hydration level by an overall MEA water content.

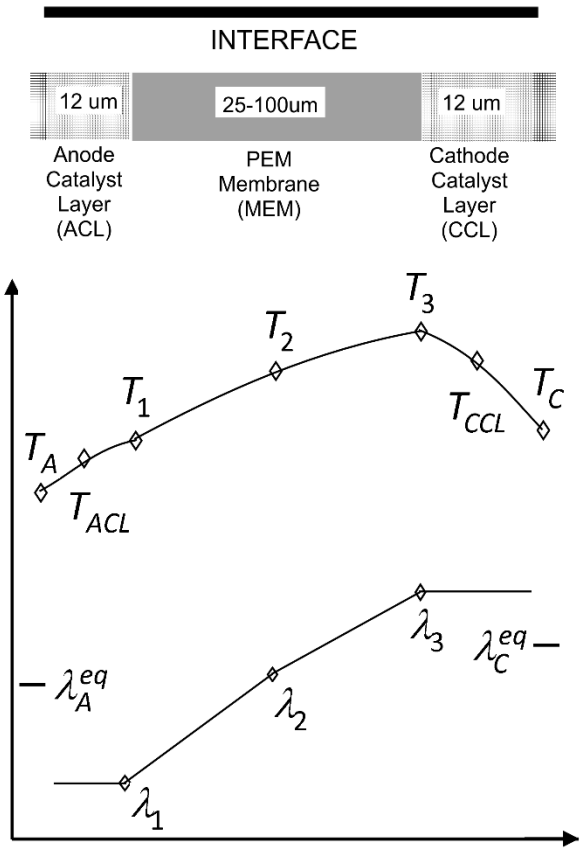

Figure 2.5. Temperature and water content profile schematic of proposed interface model

The water transport model employs convective boundary conditions of water absorption and desorption. The MEA can gain or lose water content. The water content profile utilizes 3 equations: 2 values of its slope, at points 1 and 3, in addition to the integrated water content (W), at pseudo steady-state conditions. The pseudo-steady-state assumption involves ignoring water content distribution variations within the ionomer of the MEA, to represent hydration level by an overall MEA water content.

A thick MEA can experience non-linear anode dry out effects at high current density [58, 59]. The approximate solution, to be presented, predicts anode dryout but not the highly-nonlinear effects. It is intended to model thin membrane behavior (1-2 micron thickness) but not thick membranes (3-7 microns), as shown in the verification material contained within chapter 4.

The water contents are found by assembling three equations to solve for the three unknown water contents. The first equation relates the MEA water content W to the three water content values. The MEA water content W (mol m^{-2}) is represented as a lumped parameter value for each cell of the interface. During steady-state operation, the value of W must be such that the water gain rate $\partial W / \partial t = 0$. When W is less than the steady-state value, the water gain rate is positive; the converse occurs as well. The overall water content of the ionomer phase, integrated through the thickness of the MEA can be presented as eq. (2.25), which simplifies to eq. (2.26).

$$W = \int_{z=-t_{ACL}}^{z=t_{MEM}+t_{CCL}} \varepsilon(z)\lambda(z)\,dz = \left(c_f \varepsilon_{ACL,Io} t_{ACL}\right)\lambda_1 + \frac{c_f t_{MEM}}{6}\left[\lambda_1 + 4\lambda_2 + \lambda_3\right] + \left(c_f \varepsilon_{CCL,Io} t_{CCL}\right)\lambda_3 \qquad (2.25)$$

$$\left(c_f t_{MEM} + 6c_f \varepsilon_{ACL,Io} t_{ACL}\right)\lambda_1 + \left(4c_f t_{MEM}\right)\lambda_2 + \left(c_f t_{MEM} + 6c_f \varepsilon_{CCL,Io} t_{CCL}\right)\lambda_3 = 6W \qquad (2.26)$$

The second equation examines the slope in the water content profile at z=0, the ACL-membrane interface. There is water flux to/from the ionomer by absorption or desorption from the anode gas stream, according to the absorption / desorption kinetics previously given. The water flux within the membrane should be identical, being driven by the combination of electro-osmotic drag and back diffusion. The absorption flux (positive) or desorption flux (negative) is presented as eq. (2.27) and the water flux within the ionomer phase at z=0 is written as eq. (2.28) using a three-point estimate of the slope at z=0.

$$\begin{aligned} \lambda_A^{eq} > \lambda_1: &\quad J_{W,A} = k_a(f_v, T_{ACL}) c_f (\lambda_A^{eq} - \lambda_1) \\ \lambda_A^{eq} < \lambda_1: &\quad J_{W,A} = k_d(f_v, T_{ACL}) c_f (\lambda_A^{eq} - \lambda_1) \end{aligned} \qquad (2.27)$$

$$J_{W,A} = n_{d,1}\frac{I}{F} - c_f D_{W,1}\left.\frac{d\lambda}{dz}\right|_{z=0} = n_{d,1}\frac{I}{F} - \frac{c_f D_{W,1}}{t_{MEM}}\left[-3\lambda_1 + 4\lambda_2 - \lambda_3\right] \qquad (2.28)$$

The expression simplifies to eq.(2.29). The transport properties (drag coefficient $n_{d,1}$, diffusion coefficient $D_{W,1}$, and mass transfer coefficient $k_{a|d}$) are evaluated at the water content and temperature of the ACL-membrane interface (λ_1, T_{ACL}).

$$\left(\frac{-3c_f D_{W,1}}{t_{MEM}}\right)\lambda_1 + \left(\frac{4c_f D_{W,1}}{t_{MEM}}\right)\lambda_2 - \left(\frac{c_f D_{W,1}}{t_{MEM}}\right)\lambda_3 = n_{d,1}\frac{I}{F} - J_{W,A} \qquad (2.29)$$

The third equation sets the slope in the water content profile at $z = t_{MEM}$, the CCL-membrane interface. There is a water flux within the membrane driven by electro-osmotic drag and back diffusion. Product water is produced in the ionomer phase of the CCL by the ORR. To the right of the CCL-membrane interface, there is desorption or absorption flux into or from the cathode gas stream. The desorption flux (positive) or absorption flux (negative) is presented as eq.(2.30) where the water volume fraction term uses λ_3 as the water content. The water flux within the ionomer phase at $z = t_{MEM}$ is written as eq.(2.31) using a three-point estimate of the slope at $z = t_{MEM}$.

$$\begin{aligned} \lambda_3 > \lambda_C^{eq}: \quad & J_{W,C} = k_d(f_v, T_{CCL}) c_f (\lambda_3 - \lambda_C^{eq}) \\ \lambda_3 < \lambda_C^{eq}: \quad & J_{W,C} = k_a(f_v, T_{CCL}) c_f (\lambda_3 - \lambda_C^{eq}) \end{aligned} \tag{2.30}$$

$$J_{W,C} = n_{d,3} \frac{I}{F} - c_f D_{W,3} \left. \frac{d\lambda}{dz} \right|_{z=t_{MEM}} = n_{d,3} \frac{I}{F} - \frac{c_f D_{W,3}}{t_{MEM}} \left[3\lambda_3 - 4\lambda_2 + \lambda_1 \right] \tag{2.31}$$

Water production by the ORR also occurs here. If interfacial resistance to water transport is incorporated into modeling efforts, a decision needs to be made as to where water creation occurs: in the ccl gaseous phase, ionomer phase, or directly as liquid. The extensive investigations of Wu, Berg, and Li [106, 113] have explained that water creation takes place in the ionomer phase and lamented that many prior modeling efforts were compromised by treating product water creation as if it occurred in the gaseous phase.

The flux into the cathode, by electro osmotic drag and diffusion, is added to the product water creation, and set equal to desorption / absorption flux exiting the cathode into the cathode gas stream. Equating the water fluxes $J_{W,C}$ yields eq. (2.32), where k_3 is evaluated as an absorption or desorption coefficient according to the relative values of λ_C^{eq} and λ_3. This expression simplifies to(2.33), where, again, the coefficients of diffusion ($D_{W,3}$) and electro-osmotic drag ($n_{d,3}$) are evaluated at the water content and temperature of the CCL-membrane interface (λ_3, T_{CCL}).

$$\underbrace{n_{d,3}\frac{I}{F}-c_f D_{W,3}\left.\frac{d\lambda}{dz}\right|_{z=t_{MEM}}}_{\text{flux into CCL by EO drag / diffusion}}+\underbrace{\frac{I}{2F}}_{\text{production in the CCL}}=\underbrace{J_{W,C}}_{\text{desorption flux entering cathode gas stream}} \tag{2.32}$$

$$\left(\frac{c_f D_{W,3}}{t_{MEM}}\right)\lambda_1-\left(\frac{4c_f D_{W,3}}{t_{MEM}}\right)\lambda_2+\left(\frac{3c_f D_{W,3}}{t_{MEM}}\right)\lambda_3=\left(0.5+n_{d,3}\right)\frac{I}{F}-J_{W,C} \tag{2.33}$$

Together there is a system of 3 equations and 3 unknowns to solve for the water contents in eq. (2.34). The solution updates $\begin{pmatrix}\lambda_1 & \lambda_2 & \lambda_3\end{pmatrix}$. The current density ($I$) is updated in a subsequent step. After the water content profile is calculated, the molar flux of water into the anode, $J_{W,A}$, and out of cathode , $J_{W,C}$, (mol m^{-2}s^{-1}) can be updated from the water content profile of the MEA as eq.(2.35).

$$\begin{bmatrix}\frac{3c_f D_{W,1}}{t_{MEM}} & -\frac{4c_f D_{W,1}}{t_{MEM}} & \frac{c_f D_{W,1}}{t_{MEM}}\\ 6c_f\varepsilon_{ACL,lo}t_{ACL}+c_f t_{MEM} & 4c_f t_{MEM} & 6c_f\varepsilon_{CCL,lo}t_{CCL}+c_f t_{MEM}\\ \frac{c_f D_{W,3}}{t_{MEM}} & -\frac{4c_f D_{W,3}}{t_{MEM}} & \frac{3c_f D_{W,3}}{t_{MEM}}\end{bmatrix}\begin{Bmatrix}\lambda_1\\ \lambda_2\\ \lambda_3\end{Bmatrix}=\begin{Bmatrix}J_{W,A}-n_{d,1}\frac{I}{F}\\ 6W\\ \left(0.5+n_{d,3}\right)\frac{I}{F}-J_{W,C}\end{Bmatrix} \tag{2.34}$$

$$\begin{aligned}J_{\mathrm{W},A}&=c_f k_1\left(\lambda_A^{eq}-\lambda_1\right)\\ J_{\mathrm{W,C}}&=c_f k_3\left(\lambda_3-\lambda_C^{eq}\right)\end{aligned} \tag{2.35}$$

The water gain rate within the MEA, $\partial W/\partial t$ (mol m^{-2} s^{-1}), is found by applying conservation of mass principles to the water in the ionomer phase. In eq.(2.36), the first term represents water production due to the ORR; which takes place in the ionomer phase. The next term represents water flux into the anode and the final term water flux out of the cathode.

$$\frac{\partial W}{\partial t}=\frac{I}{2F}+J_{\mathrm{W},A}-J_{\mathrm{W,C}} \tag{2.36}$$

2.3.9 Interface Model: Calculation of MEA Resistances

In the previous section, a three-point MEA water content profile was described. Ohmic losses within the interface are calculated from the hydration-dependent conductivities. The volume fraction of water within the ionomer is given by eq.(2.37) and the corresponding fractional increase in volume of the hydrated ionomer phase, ε_{dV} , is given by eq.(2.38). Values of the ionic conductivity $\sigma_{lo,1-3}$ can be calculated as described in section 2.3.5.

$$f_v = \frac{\lambda\left(M_w/\rho_w\right)}{\left(EW/\rho_{lo}\right)+\lambda\left(M_w/\rho_w\right)} \tag{2.37}$$

$$\varepsilon_{dV} = \frac{M_w \rho_{lo}}{EW \rho_w}\lambda \tag{2.38}$$

The membrane proton conduction resistance $R_{MEM}^{H^+}$ (Ω m^2) is calculated by an approximate integration of the three conductivity values. Volumetric swelling in the membrane is treated as occurring purely in the thru-plane direction (in thickness); membrane thickness swells with water content at the center at the membrane as eq. (2.39).

$$R_{MEM}^{H^+} = \int_0^{t_{MEM}^{\mathbb{S}}} \frac{1}{\sigma_{lo}} dz = \frac{t_{MEM}\left(1+\varepsilon_{dV,2}\right)}{6}\left(\frac{1}{\sigma_{lo,1}}+\frac{4}{\sigma_{lo,2}}+\frac{1}{\sigma_{lo,3}}\right) \tag{2.39}$$

The effective cathode catalyst layer resistance $R_{CCL}^{H^+,\text{eff}}$ (Ω m^2) is derived from an analytical solution that is also greatly hydration-dependent. The effective conduction thickness $t_{CCL}^{\mathbb{C}}$ and diffusion thickness $t_{CCL}^{\mathbb{D}}$ sum to the swollen cathode catalyst layer thickness. These items are detailed in Appendix B.7 .

The effective anode catalyst layer resistance $R_{ACL}^{H^+,\text{eff}}$ (Ω m^2) modeled by an analytical solution which accounts for both kinetic and ohmic losses simultaneously. This is detailed in Appendix B.8 .

The MEA might contain some electronic conduction resistances as well. The term $R_{cnt}^{e^-}$ (Ω m2) refers to electronic contact resistances which may be present. This term is treated as a humidity-

independent, but assembly-pressure dependent, term to represent contact resistances between the gas diffusion media (GDL) and ACL/CCL (catalyst layers). When comparing the interface model directly to experimental data, additional bulk resistances must be included in the electronic resistance term. Electronic bulk conduction losses will occur outside of the interface (MEA) region, and these may be accounted for in $R_{cnt}^{e^-}$. Bulk electronic conduction losses occur in the anode and cathode diffusion media and the conductive flow field plates. Electronic contact resistances can also be found between the diffusion media and flow field plates. These resistances are also treated as temperature and humidity independent; they are a constant for a given cell assembly.

In-situ / on-line resistance measurements are commonly made simultaneously with voltage and current readings in the operating PEMFC. A high frequency resistance (HFR) measurement produces R_{Ω} (Ω m^2) that is the sum of the membrane protonic resistance and the electronic resistances present [22] as eq. (2.40). The HFR measurement is commonly used for model validation of water transport modeling efforts, because the HFR measurement contains a first component that has membrane water-content dependence and a second component that has been found to be constant for a given cell assembly. Catalyst layer resistances are not included in these measurements.

$$R_{\Omega} = R_{MEM}^{H^+} + R_{cnt}^{e^-} \tag{2.40}$$

The total ohmic resistance within the interface, R_{Ohm} (Ω m^2), is the sum of HFR resistance and effective catalyst layer resistances as eq. (2.41).

$$R_{Ohm} = R_{\Omega} + R_{ACL}^{H^+,\text{eff}} + R_{CCL}^{H^+,\text{eff}} = R_{cnt}^{e^-} + R_{MEM}^{H^+} + R_{ACL}^{H^+,\text{eff}} + R_{CCL}^{H^+,\text{eff}} \tag{2.41}$$

With these resistances known, the following section has the possibility to develop the voltage-current relationship for the interface.

2.3.10 Interface Model: Polarization Curve and Current Estimation

This section describes the voltage-current relationships in the interface model. Established voltage and current relationships are used to produce an updated estimate of current density with the Newton-Rhapson technique.

The cell voltage is the difference between anode and cathode potential levels at the interface locations. Cell current is the previously-described current density. The cell voltage is then treated as the ideal/reversible voltage minus various voltage losses.

The thermodynamically-determined open circuit, ideal, or reversible voltage can be calculated from established thermodynamic relationships. The relationship used in this work was given by Liu et al.[24]. The reversible cell voltage V_{OC} is eq. (2.42). The reversible cell voltage can be seen to be a function of cathode temperature (T_{CCL}), hydrogen partial pressure ($X^{\mathbb{D}}_{H_2,A} P_A$), oxygen partial pressure ($X^{\mathbb{D}}_{O_2,C} P$), and cathode humidity α_C.

$$V_{OC} = 1.229 - 0.000846\left(T_{CCL} - 298\right) + \frac{RT_{CCL}}{2F}\ln\left(\frac{X^{\mathbb{D}}_{H_2,A} P_A}{101,300}\right) + \frac{RT_{CCL}}{4F}\ln\left(\frac{X^{\mathbb{D}}_{O_2,C} P_C}{101,300}\right) - \frac{RT_{CCL}}{2F}\ln\alpha_C \quad (2.42)$$

The interface model is then to calculate the current density given the anode and cathode voltage levels V_C and V_A among the inputs. The cell voltage V_{cell} in eq. (2.43) is defined as the ideal open-circuit voltage minus the various losses[20]. The definition of the open-circuit voltage already has taken into account some reduction in the oxygen and hydrogen mole fractions due to mass-transfer (diffusional) losses within the catalyst layers.

$$V_{cell} = V_C - V_A = V_{OC} - IR_{Ohm} - \eta_C \quad (2.43)$$

The iR-free or kinetic voltage V_k describes the cell voltage in the absence of ohmic losses. Recalling that the ACL combined kinetic and ohmic losses have been incorporated into the ohmic resistance term R_{Ohm}, the kinetic voltage is described as eq. (2.44). The kinetic voltage is formed analytically by subtracting cathode kinetic losses η_C from the thermodynamically-determined open-circuit

voltage V_{OC}. Experimentally, it is formed by adding the measured cell voltage V_{cell} to a correction for ohmic losses IR_{Ohm}.

$$V_k = V_{OC} - \eta_C \approx V_{cell} + IR_{Ohm} \tag{2.44}$$

The voltage loss V_{loss} is defined as a simple re-arrangement to give eq. (2.45), which is the voltage-current relationship of the interface, where the current density I needed to satisfy this relationship is sought, but is not known. An implementation of the Newton-Rhapson root-finding method to solve for the current density I^{new} was found sufficiently stable for use here. The procedure initializes $I = I_x$ and then calculates an updated estimate of the operational current density I^{new} using eq. (2.46). All terms in the equations are updated with each new current density estimate.

$$V_{loss} = V_{OC} - V_{cell} = IR_{Ohm} + \frac{RT_{CCL}}{1F}\ln\left[\frac{I + I_x}{I_{0,C}}\right] \tag{2.45}$$

$$I^{new} = I + \frac{V_{loss} - IR_{Ohm} - \frac{RT_{CCL}}{1F}\ln\left[\frac{I + I_x}{I_{0,C}}\right]}{R_{Ohm} + \frac{RT_{CCL}}{1F}\frac{}{I + I_x}} \tag{2.46}$$

2.3.11 Interface Model: Calculation of Temperature Profile

This section describes the calculation of the MEA temperature profile and heat fluxes from the MEA into the anode and cathode diffusion media. Several terms from the interface model were given temperature dependence. The interface takes as inputs the temperatures from the opposite sides of the MEA and outputs heat fluxes to the anode and cathode computational domains. A simultaneous solution of the 7 temperature values (5 unknowns) is developed to produce a steady-state temperature profile and the needed heat fluxes into the anode and cathode flow domains.

A 1-D temperature profile estimates the temperature rise in the MEA in Figure 2.5. Temperatures T_A and T_C are taken as Dirichlet boundary conditions from the 3D simulation; thermal contact resistance is thought to be minimal. Heat generation within the regions of the MEA has been detailed [114]; it occurs predominantly within the CCL. Hence, the maximum internal MEA temperature is drawn as skewed to the cathode side. Some experimental results reported that the cathode was 0.9 K higher in temperature than the anode and the overall temperature rise was about 5 K from membrane surface to (outer) collector plate [13].

This section applies a general heat transport equation to the MEA. The thermal conductivities and heat generation terms of each region of the MEA are collected. Convective effects within the MEA are ignored, following similar work[115]. Heat transport in the thru-plane direction occurs by conduction, with the thermal conductivity being hydration-dependent. The regions of the MEA are thought to be isotropic and thermal contact resistances between the layers of the MEA are thought to be negligible [98].

In earlier interface models, a thermal source term was created at the cathode GDL/MEA interface based upon the (estimated) overall efficiency of the device [116]. This current model divides the heat flux between anode and cathode, but does not go into excessive detail examining the spatial distribution of heat generation within catalyst layers.

The temperature profile calculations are detailed in Appendix B.9 .

2.3.12 Interface Model: Boundary Conditions

With the iterative scheme of the previous section having converged on a current density estimate, and the water content profile of the MEA having been determined, the interface model produces its outputs to the 3-D computational domains: the overall solution scheme. Boundary conditions on the anode and cathode side of the MEA represent current density, heat flux, water flux, reactant consumption, and water gain rate.

The interface model takes as inputs the voltages from the opposite sides of the MEA, and outputs a current density I from eq. (2.46). Heat fluxes $J_{T,A}$ and $J_{T,\mathrm{C}}$ are given by (B.67). The water flux and reactant terms are given in eq.(2.47), where the convention is that positive fluxes denote mass / species entering the respective 3-D computational domains. The water gain rate in eq. (2.36) increments the MEA water content.

$$\begin{aligned} N_{\mathrm{H}_2,A} &= -\frac{I}{2F}M_{H_2} & N_{O_2,\mathrm{C}} &= -\frac{I}{4F}M_{O_2} \\ N_{\mathrm{H}_2O,A} &= -J_{\mathrm{W},A}M_{\mathrm{H}_2O} & N_{\mathrm{H}_2O,\mathrm{C}} &= J_{\mathrm{W},\mathrm{C}}M_{\mathrm{H}_2O} \\ N_{m,A} &= N_{\mathrm{H}_2,A} + N_{\mathrm{H}_2O,A} & N_{m,\mathrm{C}} &= N_{O_2,\mathrm{C}} + N_{\mathrm{H}_2O,\mathrm{C}} \end{aligned} \tag{2.47}$$

2.3.13 Interface Model: Iterative Operation

This section describes the iterative operation of the interface model to estimate the correct current density, water content, water content profile (and hence ohmic resistances), temperature profile, boundary (species) fluxes, and thermal fluxes that were described. The main variables of the iterative routine are given in Table 2.2. There are six principal variables of interest that are solved for. Other variables, such as ohmic resistances, are derived from these.

Table 2.2. Principal interface variables for iterative solver.

Symbol	Description
$\{ \lambda_1 - \lambda_3 \}$	Water content profiles
$\{ J_{W,A}, J_{W,C} \}$	Water fluxes
$\{ W \}$	Water content of the ionomer phase of the MEA
$\{ I \}$	Current density
$\{ T_{ACL}, T_1 - T_3, T_{CCL} \}$	Temperature profile
$\{ J_{T,A}, J_{T,C} \}$	Thermal fluxes

First, the water content profile $\lambda_1 - \lambda_3$ is determined. Given water contents, volume fractions within the ionomer are calculated. Water transport parameters are determined for the ionomer phase. The water transport equations are then formulated and solved with the most recent estimates of current density and the other solution variables. The water fluxes are updated, followed by the MEA water gain rate.

Second, ohmic resistances are re-assessed. With the newly-updated water content values and the previous current density estimate, the effective membrane, anode, and cathode resistances can be formulated.

Third, diffusional adjustments representing mass-transfer resistances within the catalyst layers are calculated as in section 2.3.6. The anode and cathode effective gaseous diffusion coefficients have water-content dependence. These are re-calculated with the updated water contents. The diffusion-corrected oxygen and hydrogen mole fractions are then calculated using the updated gaseous diffusion coefficients in addition to the most recent current density estimate.

Fourth, the current density estimate is updated as described in section 2.3.10. The above revised estimates of ohmic resistances, kinetics (with reduced, diffusion-corrected reactant mole fractions), and open-circuit voltage are used.

Fifth, the approximate temperature profile and thermal fluxes are determined as described in section 2.3.11. The slight temperature rise in the MEA impacts the water transport scheme through the temperature-dependent convective boundary conditions, exchange-current density, and water vapor saturation pressure.

Finally, source terms are calculated as described in section 2.3.12. The anode and cathode water fluxes $J_{W,A}$ and $J_{W,C}$ are updated, but with relaxation (~ 0.5) to ensure stability and convergence. The water content variable W is updated, utilizing the estimates of the water content profile, current density, and temperature profile. The water gain rate will approach zero as the water content nears its equilibrium value. Meaningful steady-state, or equilibrium, is reached only when the water gain rate $\partial W / \partial t$ goes below a tolerance such as .00005 mol m^{-2} s^{-1}.

The convergence of the algorithm was assessed with two criteria: current density and water gain rate. Verification cases produced convergence of the MEA current density { I } to within ~ 1% within a few (~5) iterations.

2.4 Operating and Boundary Conditions

Boundary and initial conditions for the 3-D PEMFC model are needed in order to make this problem mathematically well-posed. Operating conditions are described first, as boundary and initial conditions will derive from them. Next, boundary conditions are developed. Initial conditions are given in the subsequent section. To illustrate the boundary conditions with the simplest geometry possible, a single-channel cell is chosen for illustrative purposes.

2.4.1 Operating Conditions

Operating conditions for a typical single-cell case are listed in Table 2.3. Operating parameters derive from typical, practical, representative experimental conditions. Anode and Cathode gas streams are supplied at the operating temperatures as humidified reactant streams (gas mixtures) with specified stoichiometric ratio. As the bottom entries of the table suggest, the operating temperature of the anode / cathode collector plates is typically the same as the temperature at which gases are supplied. It is typically monitored at the interior or exterior of the collector plate(s) and is a control set-point. Experimentally, the operating cell voltage and current density are not independent, one can be controlled for and the other is measured to form the polarization curve.

Table 2.3. Operating conditions and parameters for single cell.

Parameter:		Symbol:		Unit:	
Operating cell voltage		$V_{cell}^{\mathbb{OP}}$		V	
Average operating cell current density		$I_{cell}^{\mathbb{OP}}$		A m^{-2}	
MEA area (length x width)		A_{MEA}		m^2	
Anode:			Cathode:		
Parameter:	Symbol:	Unit:	Parameter:	Symbol:	Unit:
Operating pressure	$P_A^{\mathbb{OP}}$	Pa	Operating pressure	$P_C^{\mathbb{OP}}$	Pa
Flow inlet area	$A_{A,ch}$	m^2	Flow inlet area	$A_{C,ch}$	m^2
Stoichiometric flow ratio	$\zeta_A^{\mathbb{OP}}$	-	Stoichiometric flow ratio	$\zeta_C^{\mathbb{OP}}$	-
Relative humidity	$\mathbb{RH}_A^{\mathbb{OP}}$	%	Relative Humidity	$\mathbb{RH}_C^{\mathbb{OP}}$	%
Inlet temperature	$T_A^{\mathbb{OP}}$	K	Inlet temperature	$T_C^{\mathbb{OP}}$	K
Cell temperature	$T_A^{\mathbb{OP}}$	K	Cell temperature	$T_C^{\mathbb{OP}}$	K

2.4.2 Fluid Flow Boundary Conditions

Boundary conditions are now developed using a single-channel cell for illustrative purposes. Boundary conditions must be specified at all external boundaries of the computational domains and there are also internal boundary conditions for some equations. Figure 2.6 shows a cutaway schematic used to illustrate the various boundary conditions.

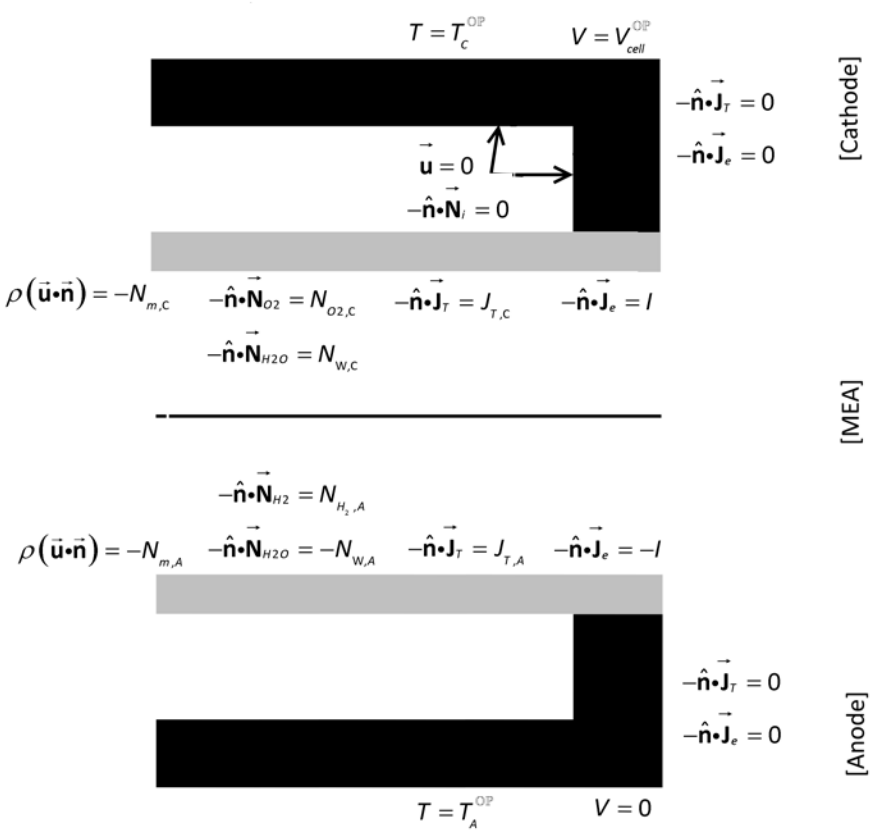

Figure 2.6. Boundary condition schematic for single cell

Inflow and outflow fluid flow boundary conditions are used. Inlet values of normal fluid velocity are specified in eq. (2.48) for both the anode and cathode flow channels that create a constant overall operating stoichiometric flow ratio of $\zeta_A^{\mathbb{OP}}$ and $\zeta_C^{\mathbb{OP}}$ for the anode and cathode, respectively. The term

$I A_{MEA}$ is the total current (A) and the remaining terms are mole fraction, temperature, and pressure values evaluated at the inlet, or as defined by operating conditions. At the outlets, the common pressure boundary condition is used. The calculation domains utilize reference pressures of $P_A^{\mathbb{OP}}$ and $P_C^{\mathbb{OP}}$, and dynamic pressures are set to zero at the outlet boundaries.

$$u_{\mathrm{A,in}} = \zeta_A^{\mathbb{OP}} \frac{I A_{MEA}}{2F} \frac{1}{x_{H_2,in}} \frac{RT_A^{\mathbb{OP}}}{P_A^{\mathbb{OP}}} \frac{1}{A_{A,ch}}$$
$$u_{\mathrm{C,in}} = \zeta_C^{\mathbb{OP}} \frac{I A_{MEA}}{4F} \frac{1}{x_{O_2,in}} \frac{RT_C^{\mathbb{OP}}}{P_C^{\mathbb{OP}}} \frac{1}{A_{C,ch}} \tag{2.48}$$

The default fluid flow boundary condition is the wall boundary condition, assuming laminar flow, the fluid velocity is set to zero as $\vec{\mathbf{u}} = 0$. At the inner walls of the flow channel, and the outer (left and right-side) edges of the GDL, the fluid velocity is constrained to zero. At the MEA interface, a reacting wall boundary condition is used. The mass-average flow velocity in the adjoining cells of the anode flow domain is set to the Stefan velocity as eq. (2.49) and the flow velocity in the cathode flow domain as eq.(2.50).

$$\rho\left(\vec{\mathbf{u}}\bullet\vec{\mathbf{n}}\right) = -N_{m,A} = \frac{I}{2F} M_{H_2} + c_f k_1 \left(\lambda_A^{eq} - \lambda_1\right) M_{H_2O} \tag{2.49}$$

$$\rho\left(\vec{\mathbf{u}}\bullet\vec{\mathbf{n}}\right) = -N_{m,C} = \frac{I}{4F} M_{O_2} + c_f k_3 \left(\lambda_C^{eq} - \lambda_3\right) M_{H_2O} \tag{2.50}$$

2.4.3 Species Equation Boundary Conditions

Inflow and outflow boundary conditions are used. Species mass or mole fractions are specified for both anode and cathode flow channel inlets. The anode mole fractions of water and hydrogen species are specified as eq. (2.51). The three cathode mole fractions are specified similarly. If the cathode uses humidified air, for example, the molar ratio of oxygen to nitrogen (for dry air) of 0.21 / 0.79 leads to eq. (2.52).

$$x_{H_2O,in} = \mathbb{RH}_A^{\mathbb{OP}} \frac{P_{SAT}(T_A^{\mathbb{OP}})}{P_A^{\mathbb{OP}}} \quad x_{H_2,in} = 1 - x_{H_2O,in} = 1 - \mathbb{RH}_A^{\mathbb{OP}} \frac{P_{SAT}(T_A^{\mathbb{OP}})}{P_A^{\mathbb{OP}}} \tag{2.51}$$

$$x_{H_2O,in} = \mathbb{RH}_C^{\mathbb{OP}} \frac{P_{SAT}(T_C^{\mathbb{OP}})}{P_C^{\mathbb{OP}}} \quad x_{O_2,in} = 0.21\left(1 - x_{H_2O}\right) \quad x_{N_2,in} = 0.79\left(1 - x_{H_2O}\right) \tag{2.52}$$

The default boundary condition for the species equations is the no flux boundary condition, representing a boundary where no mass flows in or out of the computational domain. At the inner walls of the flow channel, and the outer (left and right-side) edges of the GDL, the species flux is constrained to zero in eq. (2.53).

$$-\hat{\mathbf{n}} \bullet \vec{\mathbf{N}}_i = -\hat{\mathbf{n}} \bullet \left(\rho \vec{\mathbf{u}} \omega_i + -\rho \omega_i \sum_k \tilde{D}_{ik} \left(\nabla x_k + \frac{\nabla p}{p} \left(x_k - \omega_k \right) \right) \right) = 0 \tag{2.53}$$

At the MEA interface, a reacting wall boundary condition is used. In the anode domain, on that side of the interface, an inward flux of hydrogen is defined as eq. (2.54) and the water flux is accounted for by the mass constraint (the boundary condition for the Stefan velocity).

$$-\hat{\mathbf{n}} \bullet \vec{\mathbf{N}}_{H_2} = -\hat{\mathbf{n}} \bullet \left(\rho \vec{\mathbf{u}} \omega_{H_2} + -\rho \omega_{H_2} \sum_k \tilde{D}_{H_2-k} \left(\nabla x_k + \frac{\nabla p}{p} \left(x_k - \omega_k \right) \right) \right) = -\frac{I}{2F} M_{H_2} \tag{2.54}$$

In the cathode domain, on that side of the MEA interface, boundary conditions for the fluxes of oxygen and water species are given in eq. (2.55) and (2.56).

$$-\hat{\mathbf{n}} \bullet \vec{\mathbf{N}}_{O_2} = -\hat{\mathbf{n}} \bullet \left(\rho \vec{\mathbf{u}} \omega_{O_2} + -\rho \omega_{O_2} \sum_k \tilde{D}_{O_2-k} \left(\nabla x_k + \frac{\nabla p}{p} \left(x_k - \omega_k \right) \right) \right) = -\frac{I}{4F} M_{O_2} \tag{2.55}$$

$$-\hat{\mathbf{n}} \bullet \vec{\mathbf{N}}_{H_2O} = -\hat{\mathbf{n}} \bullet \left(\rho \vec{\mathbf{u}} \omega_{H_2O} + -\rho \omega_{H_2O} \sum_k \tilde{D}_{H_2O-k} \left(\nabla x_k + \frac{\nabla p}{p} \left(x_k - \omega_k \right) \right) \right) = -N_{H_2O,A} = -c_f k_1 \left(\lambda_A^{eq} - \lambda_1 \right) M_{H_2O} \tag{2.56}$$

2.4.4 Energy Equation Boundary Conditions

Gas temperatures are specified at the flow inlets as in eq. (2.57). At the flow outlets, the common outflow boundary condition is applied to the gradient of the temperature T as eq. (2.58). The vertical outer edge also employs an insulating or symmetry temperature boundary condition.

$$T_{\text{A, in}} = T_A^{\mathbb{OP}} \quad T_{\text{C, in}} = T_C^{\mathbb{OP}} \tag{2.57}$$

$$\nabla T \bullet \hat{\mathbf{n}} = 0 \tag{2.58}$$

Temperature boundary conditions are also applied to the outer top and bottom edge of the current collector plates, which are the desired cell temperatures $T_A^{\mathbb{OP}}$ or $T_C^{\mathbb{OP}}$. The boundary conditions require that all heat produced in the MEA is removed from the computational domains by the reactant gas streams or conduction through the collector plate top and bottom horizontal surfaces.

At the MEA interface, the heat generated within the MEA, from the various losses, is split between the anode and cathode computational domains as eq. (2.59).

$$-\hat{\mathbf{n}}\bullet\vec{\mathbf{J}}_T = J_{T,A} \quad -\hat{\mathbf{n}}\bullet\vec{\mathbf{J}}_T = J_{T,C} \tag{2.59}$$

2.4.5 Current Conservation Boundary Conditions

The current conservation equation employs Voltage boundary conditions on the collector plate bottom (anode) and top (cathode) horizontal surfaces, which are the 0 and $V_{cell}^{\mathbb{OP}}$, respectively. The vertical outer edge employs an insulating or symmetry voltage boundary condition of eq. (2.60). At interfaces between the GDL and current collector, there is a contact impedance boundary condition of eq. (2.61), representing the electrical contact resistance of the surface contact, where R_s is the surface impedance (Ohm m^2) and $\vec{\mathbf{J}}$ the current density (A m^{-2}). The subscripts GDL and coll refer to voltage on either side of the contact resistance.

$$\hat{\mathbf{n}}\bullet\vec{\mathbf{J}}_e = 0 \tag{2.60}$$

$$\hat{\mathbf{n}}\bullet\vec{\mathbf{J}}_{GDL} = \frac{1}{R_s}\left(V_{GDL} - V_{coll}\right) \quad \hat{\mathbf{n}}\bullet\vec{\mathbf{J}}_{coll} = \frac{1}{R_s}\left(V_{coll} - V_{GDL}\right) \tag{2.61}$$

At the MEA interface, a normal current density boundary condition of eq. (2.62) is applied to both computational domains. The current density convention represents the current density vector as positive charges moving towards a lower potential. The current density of electrons entering into the anode domain is equivalent to that of positively-charged particles exiting the domain. Similarly, the current density of electrons exiting the cathode domain into the MEA is equivalent to that of positively-charged particles entering the domain.

$$-\hat{\mathbf{n}}\bullet\vec{\mathbf{J}}_e\Big|_A = -I \quad -\hat{\mathbf{n}}\bullet\vec{\mathbf{J}}_e\Big|_C = I \tag{2.62}$$

2.5 Initial Conditions

A set of initial conditions for all of the solution variables are needed to serve as a starting point for solver iterations. This section will list the initial conditions for the anode and cathode flow domains, followed by the MEA solution variables.

In the anode flow domain, initial conditions for the mixture specification are given as those from the inlet boundary condition as in eq. (2.63). The dynamic pressure and velocity fields are initialized as zero. The temperature field is initialized as $T_A^{\mathbb{OP}}$. The voltage field in the anode electronic conduction domain is initialized as zero, the ground boundary condition.

$$x_{H_2} = x_{H_2,in} \quad x_{H_2O} = x_{H_2O,in} = 1 - x_{H_2,in} \tag{2.63}$$

In the cathode flow domain, initial conditions for the mixture specification are given as those from the inlet boundary condition as in eq. (2.64). The dynamic pressure and velocity fields are initialized as zero. The temperature field is initialized as $T_C^{\mathbb{OP}}$. The voltage in the cathode electronic conduction domain is initialized as $V_{cell}^{\mathbb{OP}}$, which is the voltage boundary condition.

$$x_{O_2} = x_{O_2,in} \quad x_{H_2O} = x_{H_2O,in} \quad x_{N_2} = 1 - x_{O_2,in} - x_{H_2O,in} \tag{2.64}$$

Initial conditions for the MEA solution variables are also needed. Initial values for the water content profile are determined from the water uptake function $\lambda\left(\mathbb{RH}_A^{\mathbb{OP}}, T_A^{\mathbb{OP}}\right)$ as in eq. (2.65). The anode and cathode water flux values $J_{W,A}$ and $J_{W,C}$ are initialized as zero. The MEA area-specific water content W is initialized using the water uptake function in eq. (2.66). The MEA current density I is initialized as $I = I_x$, the crossover current density. The temperature profile values are initialized as $T_A^{\mathbb{OP}}$.

$$\{\lambda\} = \begin{Bmatrix} \lambda_1 \\ \lambda_2 \\ \lambda_3 \end{Bmatrix} = \begin{Bmatrix} \lambda\left(\mathbb{RH}_A^{\mathbb{OP}}, T_A^{\mathbb{OP}}\right) \\ \lambda\left(\mathbb{RH}_A^{\mathbb{OP}}, T_A^{\mathbb{OP}}\right) \\ \lambda\left(\mathbb{RH}_A^{\mathbb{OP}}, T_A^{\mathbb{OP}}\right) \end{Bmatrix} \tag{2.65}$$

$$\{W\} = c_f\left(t_{ACL}\varepsilon_{ACL,Io} + t_{MEM} + t_{CCL}\varepsilon_{CCL,Io}\right)\lambda\left(\mathbb{RH}_A^{\mathbb{OP}}, T_A^{\mathbb{OP}}\right) \tag{2.66}$$

3 NUMERICAL FORMULATION

In the previous chapter, the governing equations of flow and reaction, as well as the MEA interface modeling were described. The boundary conditions at the MEA interface serve to link the computational domains of the anode and cathode. This chapter describes the numerical method employed to solve the system of equations.

A single-channel co-flow PEMFC test-case is shown for simplicity. It is a computationally-efficient means of demonstrating the coupled solution domains. The next section explains the computational methodology, where conservation equations and solver variables are described within each region. The third section documents the solution algorithm. A flow diagram of the overall solution procedure is presented, in addition to the solver settings in each of the steps. The last section examines convergence criteria of this model.

3.1 Computational Domains

The representative mesh for the dingle channelis pictured in Figure 3.1. There are essentially 3 computational domains for this problem. The lower 3-D anode domain is connected to the upper 3-D cathode domain via the MEA interface model. The anode and cathode operate in a co-flow arrangement. The meshes for the anode and cathode include the flow channel regions, as well as the porous gas diffusion layer (GDL), and the solid, highly conductive current collector plates. About 7900 domain elements and 4900 boundary elements (353,873 degrees of freedom) are used in the base case mesh.

Figure 3.1. Single-Channel PEMFC computational domains and meshes

This model was created with geometrical and operating parameters listed in Table 3.1 and Table 3.2, respectively. The gas input compositions are detailed in Table 3.3. The MEA compositions are detailed in Table 3.4.

Table 3.1. Geometrical and physical parameters of single-flow channel numerical model.

Parameter:	Anode:	Cathode:
Width of gas channel	0.8 mm	0.8 mm
Width of rib	0.8 mm	0.8 mm
Height of channel	1 mm	1 mm
Height of GDL	500 μm	500 μm
Height of current collector plate	0.5 mm	0.5 mm
Length of flow channel	2.0 cm	2.0 cm
Porosity of GDL	0.4	0.4
Permeability of GDL	$1.2x10^{-11}$ m^2	$1.2x10^{-11}$ m^2
Electrical conductivity of GDL (thru-plane)	1250 S/m	1250 S/m
Electrical conductivity of GDL (in-plane)	10000 S/m	10000 S/m
Electrical conductivity of CCL	40000 S/m	40000 S/m
Electrical contact impedance (GDL-CCL)	4 mΩ cm^2	4 mΩ cm^2
Thermal conductivity of GDL(thru-plane)	17 W/(m K)	17 W/(m K)
Thermal conductivity of CCL (in-plane)	1.7 W/(m K)	1.7 W/(m K)

Table 3.2. Operating conditions and parameters of single-flow channel numerical model

Parameter:		Symbol:			Value:	
Operating cell voltage		V_{cell}^{OP}			0.87-0.76 V	
Average operating cell current density		I_{cell}^{OP}			0.030, 0.044, 0.063, 0.1, 0.2, 0.3, 0.5, 0.75, 1.0, 1.25, 1.5 A cm^{-2}	
MEA area (length x width)		A_{MEA}			5 cm^2	
Anode:			Cathode:			
Parameter:	Symbol:	Value:	Parameter:		Symbol:	Value:
Operating pressure	P_A^{OP}	149.09 kPa	Operating pressure		P_C^{OP}	149.09 kPa
Flow inlet area	$A_{A,ch}$	unknown	Flow inlet area		$A_{C,ch}$	unknown
Stoichiometric flow ratio	ζ_A^{OP}	1.2	Stoichiometric flow ratio		ζ_C^{OP}	2.5
Relative humidity	$\mathbb{RH}_A^{OP}$	100 %	Relative Humidity		$\mathbb{RH}_C^{OP}$	100 %
Inlet temperature	T_A^{OP}	353.15 K	Inlet temperature		T_C^{OP}	353.15 K
Cell temperature	T_A^{OP}	353.15 K	Cell temperature		T_C^{OP}	353.15 K

Table 3.3. Gas input compositions of single-flow channel numerical model

Gas Input Compositions 80°C temperature 101 kPa reactant partial pressures 100% RH	Anode V_A =0	p_{H_2} =101 kPa	p_{H_2O} =47.79 kPa	p_{N_2} =0 kPa	p_A =149.09 kPa
		$x_{H_2,A}$ =0.679	$x_{H_2O,A}$ =0.320	$x_{N_2,A}$ =0.0	
	Cathode V_C =0.66-0.90	p_{O_2} =101 kPa	p_{H_2O} =47.8 kPa	p_{N_2} =0 kPa	p_C =149 kPa
		$x_{O_2,C}$ =0.679	$x_{H_2O,C}$ =0.320	$x_{N_2,C}$ =0.0	

Table 3.4. MEA compositions of single-flow channel numerical model

Membrane	Ionomer equivalent weight	EW	1100	g / equiv or g / mol SO_3^-
	Thickness (dry)	t_{MEM}	$22x10^{-6}$	m
	Crossover current density	I_x	10	A / m^2
Anode Catalyst Layer	Platinum loading	$L_{ACL,Pt}$	0.35	mg_{Pt} / cm^2
	Pt/C mass ratio	Ptc_{ACL}	50	%
	Ionomer to carbon ratio	IC_{ACL}	1.4	-
	Thickness (dry)	t_{ACL}	$12x10^{-6}$	m
	Available catalyst area	$A_{ACL,Pt}^{100\%RH}$	50	m^2_{Pt} / g_{Pt}
	Specific exchange current density	$i_{0,ACL}^*$	0.24	A / cm^2_{Pt}

Cathode Catalyst Layer	Platinum loading	$L_{CCL,Pt}$	0.5	mg_{Pt} / cm^2
	Pt/C mass ratio	Ptc_{CCL}	50	%
	Ionomer to carbon ratio	IC_{CCL}	1.4	-
	Thickness (dry)	t_{CCL}	$18x10^{-6}$	m
	Available catalyst area	$A_{CCL,Pt}^{100\%RH}$	50	m^2 / g_{Pt}
	Specific exchange current density	$i_{0,CCL}^{*}$	$2x10^{-8}$	A / cm^2_{Pt}
Electronic Resistance	Cell electronic resistance	$R_{cnt}^{e^-}$	0.011	$\Omega\ cm^2$

3.2 Computational Methodology

The conservation equations and solver variables within each region of the model are described here. The conservation equations applicable to the 3-D anode and cathode domains are straightforward versions of the standard conservation equations already presented. The 2-D MEA domain is coupled to both of these 3-D domains and presents boundary conditions for each of the physics considered.

3.2.1 Overall Approach

Conservation equations for energy, current, and fluid flow are solved in the 3-D anode and cathode computational domains. Inside the thin MEA, only through-plane variation is considered. The membrane tends to very thin in comparison to the flow channel dimensions, or the thickness of the diffusion layers. Elementary scaling arguments have been employed to suggest that all heat, water, and current transport within the membrane is 1-dimensional, occurring only in the thru-plane direction. Previous numerical computations showed that no more than 4% of variation could be attributed to incorporation of in-plane transport of water and heat [46].

In the proposed model, current and energy conservation occur outside of the MEA in fully 3-dimensions. Boundary normal current density and normal heat fluxes are determined by the interface model, and then applied to the anode and cathode domains.

Flow and water transport take on a different character inside and outside of the MEA. In the anode and cathode, fully 3-dimensional fluid flow with variable species mass fractions occurs. The mass fractions of the reactants and water are the most immediately relevant solution variables. Inside the MEA, a 1-dimensional governing equation for the water content is solved, using the non-dimensional water content λ which was introduced. The MEA produces fluxes of hydrogen, oxygen, and water that influence the anode and cathode fluid flows. Implementation of the solution strategy of this work requires multiple couplings between the anode and cathode domains with the MEA domain between them.

3.2.2 Anode

In the anode, the continuity and momentum equations are solved for the mixture velocity in eq. (2.1) and pressure in eq. (2.2) in the flow channel and gas diffusion layer (GDL) domains. The conservation of species equations in eq. (2.3) are also solved in the same flow domains for the species mass fractions $\{\omega_i\}$ where the species are denoted (hydrogen=1, water=2).

The conservation of energy equation in eq. (2.7) is solved for temperature $\{T\}$ in the fluid and solid (collector plate) domains. The conservation of electronic current equation in eq. (2.11) is solved for electronic potential $\{\Phi_e\}$ inside of the electronically-conductive domains, namely the GDL and the current collector.

3.2.3 Cathode

The same set of equations are solved for the cathode, except that different species are utilized. There are three species mass fractions $\{\omega_i\}$ denoted as (oxygen=1, water=2, nitrogen=3).

3.2.4 Membrane-Electrode Assembly

Within the MEA, the first group of solver variables contains the strongly-coupled water transport and current density physics. The water content profile $\{\lambda_1, \lambda_2, \lambda_3\}$ (-) is solved for via a system of 3 equations and 3 unknowns as a coefficient form boundary partial differential equation (PDE) derived from eq. (2.34). Fully converted to steady-state, the system can be expressed as eq (3.1) below. This form is compatible with the iterative solvers COMSOL employs, avoiding a zero on the diagonal of the second equation.

$$\begin{bmatrix} c_f k_1 + \frac{3c_f D_{W,1}}{t_{MEM}} & -\frac{4c_f D_{W,1}}{t_{MEM}} & \frac{c_f D_{W,1}}{t_{MEM}} \\ \frac{-c_f(3D_{W,1}+D_{W,3})}{t_{MEM}} & \frac{c_f(4D_{W,1}+4D_{W,3})}{t_{MEM}} & \frac{-c_f(D_{W,1}+3D_{W,3})}{t_{MEM}} \\ \frac{c_f D_{W,3}}{t_{MEM}} & -\frac{4c_f D_{W,3}}{t_{MEM}} & c_f k_3 + \frac{3c_f D_{W,3}}{t_{MEM}} \end{bmatrix} \begin{Bmatrix} \lambda_1 \\ \lambda_2 \\ \lambda_3 \end{Bmatrix} = \begin{Bmatrix} c_f k_1 \lambda_A^{eq} - n_{d,1}\frac{I}{F} \\ (n_{d,1}-n_{d,3})\frac{I}{F} \\ \left(0.5+n_{d,3}\right)\frac{I}{F} + c_f k_3 \lambda_C^{eq} \end{Bmatrix} \tag{3.1}$$

The MEA water content { W } (mol m^{-2}) of eq. (2.25) is solved for as a boundary ordinary differential equation (ODE) or differential algebraic equation (DAE). A user-defined variable { W_2 } is created in eq. (3.2) to hold the incremented water content profile. It is the sum of the current value of { W }, defined in the prior equation, and an incremental water gain within the MEA, expressed in the right-most term. The water content { W } is then simply adjusted against { W_2 } in eq. (3.3).

$$W_2 = \frac{c_f}{6}\left[\left(t_{MEM} + 6\varepsilon_{ACL,lo}t_{ACL}\right)\lambda_1 + \left(4t_{MEM}\right)\lambda_2 + \left(t_{MEM} + 6\varepsilon_{CCL,lo}t_{CCL}\right)\lambda_3\right] + \left[\frac{I}{2F} + J_{W,A} - J_{W,C}\right]\delta t \quad (3.2)$$

$$\frac{\partial W}{\partial t} = 0 = W - W_2 \quad (3.3)$$

The anode / cathode molar fluxes of water { $J_{W,A}$, $J_{W,C}$ } (mol m^{-2}s^{-1}) are a paired boundary ODE. These were defined in eq. (2.35) and could be adjusted against those definitions. A more stable approach was found, which is numerically equivalent, in eq. (3.4) and eq. (3.5). These redundant solver variables were needed to ensure solution stability, as the calculations have frequently diverged when these water flux boundary conditions were used directly. Relaxation can be applied to these water flux variables by the COMSOL iterative solver.

$$\frac{\partial J_{W,A}}{\partial t} = 0 = J_{W,A} - \left[n_{d,1}\frac{I}{F} + \frac{c_f D_{W,1}}{t_{MEM}}\left(3\lambda_1 - 4\lambda_2 + \lambda_3\right)\right] \quad (3.4)$$

$$\frac{\partial J_{W,C}}{\partial t} = 0 = J_{W,C} - \left[(n_{d,3} + 0.5)\frac{I}{F} + \frac{c_f D_{W,3}}{t_{MEM}}\left(-\lambda_1 + 4\lambda_2 - 3\lambda_3\right)\right] \quad (3.5)$$

The current density { I } (A m^{-2}) is solved for as another boundary ODE. The current density is not estimated directly from the equation of the polarization curve in eq. (2.45). Instead, an available iterative scheme is used. First, the cathode (purely kinetic) voltage loss η_C is estimated in eq. (3.6) as a user-defined variable. It represents the overall voltage loss occurring in the interface, minus the anode loss η_A, minus the ohmic losses occurring in the MEA. Another user-defined variable { I_2 } in eq. (3.7)is created

to update the current density, based upon the estimate η_C. The current density { I } is then simply adjusted against { I_2 } in eq. (3.8).

$$\eta_C = V_{OC} - \left(V_C - V_A\right) - \eta_A - I(R_{cnt}^{e^-} + R_{MEM}^{H^+} + R_{CCL}^{H^+,\text{eff}}) \tag{3.6}$$

$$I_2 = 2I_{0,C}\sinh\left(\frac{\upsilon F}{RT_{CCL}}\eta_C\right) \tag{3.7}$$

$$\frac{\partial I}{\partial t} = 0 = I - I_2 \tag{3.8}$$

The second group of solver variables, within the MEA, contains the heat transfer physics. The temperature profile { T_i } or { $T_{ACL}, T_1, T_2, T_3, T_{CCL}$ } [K] within the MEA is solved for as another coefficient form boundary PDE as was previously given in eq. (B.65). The boundary heat fluxes coming from the MEA into the anode { $J_{T,A}$ } and cathode { $J_{T,C}$ } computational domains (W m^{-2}) are solved for as another boundary ODE. These are simply adjusted against their definitions, defined from the temperature profile, in eq.(3.9) and eq. (3.10).

$$\frac{\partial J_{T,A}}{\partial t} = 0 = J_{T,A} - \frac{-\kappa_{ACL}^{\text{eff}}\left(f_v, T\right)}{t_{ACL}\left(1+\varepsilon_{dV,1}\right)}\left(3T_A - 4T_{ACL} + T_1\right) \tag{3.9}$$

$$\frac{\partial J_{T,C}}{\partial t} = 0 = J_{T,C} - \frac{-\kappa_{CCL}^{\text{eff}}\left(f_v, T\right)}{t_{CCL}\left(1+\varepsilon_{dV,3}\right)}\left(3T_C - 4T_{CCL} + T_3\right) \tag{3.10}$$

3.3 Solution Algorithm

The system of coupled physics equations and boundary conditions are discretized and then solved iteratively by the Galerkin finite element method in the commercial software package COMSOL multiphysics 5.1[117]. Quadratic Lagrange shape functions were used for all variables. The number of iterations that was required varied. Higher current densities required more iterations.

The PEMFC problem includes solving for multiple interacting groups of physics. The electrochemical kinetics of the MEA interact with conduction effects from outside of the MEA to determine the operating current density. Flow physics interact with the species consumption terms from reactant consumption. Temperature variations also influence the problem. While the reaction rates are temperature-dependent, this is not the source of difficulty that might be expected. Rather, the temperature-dependent humidity effects have a significant influence on this problem through the water transport physics of the MEA. With the several interacting physics, the fully coupled system may be difficult to solve due to the lack of reasonable starting guesses for each participating physics. Here, the reaction rates will strongly interact with the fluid flow. Therefore, reasonable starting guesses of the fluid velocity are needed.

A staged solution schemes is used to improve solution convergence. Partial solutions, of a limited collection of problem physics, are solved sequentially. Each stage of the scheme can use the prior converged solution to provide improved initial values for the iterative solution process.

The staged solution scheme used here is shown in Figure 3.2. The first stage solves for the anode and cathode flows, where each flow is described as a solution for pressure $\{p\}$, velocity $\{\vec{u}\}$, and compositions through the species mass fractions $\{\omega_i\}$. Temperatures and electrical potentials are solved for in the zero current state. Approximate solutions for the MEA temperature profile $\{T_i\}$ and boundary heat fluxes $\{J_{T,A}, J_{T,C}\}$ are produced. The current density and water fluxes remain at their initial (zero) values. In the first stage, there is no reaction or species consumption, and the gas compositions are essentially uniform throughout each of the flow domains. Electrical potentials and MEA water contents

are solved only to get initial values for the next stage. These include the water content profile $\{\lambda_1, \lambda_2, \lambda_3\}$ (-) and the water content $\{W\}$.

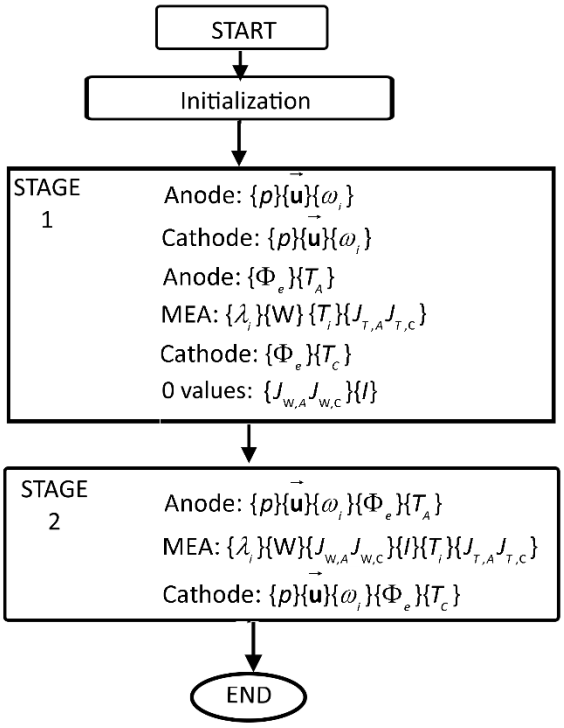

Figure 3.2. The staged solution scheme

The second stage introduces water transport physics and current conduction. These include water fluxes $\{J_{W,A}, J_{W,C}\}$ and current density $\{I\}$. The complete problem is solved in the second stage.

Both stages of the solution scheme use a segregated solving approach. The different contributing physics are solved sequentially. The solution process is divided into steps, where each step employs a linear system solver in concert with a nonlinear method which performs damped iterations of Newton's method.

A flow diagram representing the solution algorithm of the first stage is shown in Figure 3.3. The software-generated default solver configuration was modified somewhat. The segregated solver first solves for the anode and cathode flows; this is represented in the figure by the pressure and velocity variables $\{p\}$ and $\{\vec{\mathbf{u}}\}$. This is followed by a step solving the species transport equations: computing

the mass fractions of water vapor, oxygen, nitrogen (if included), and the MEA water contents. Step 3 solves the temperature fields and the MEA temperature profile in the absence of current generation. Step 4 solves for the electrical potentials to create the most appropriate initial value possible.

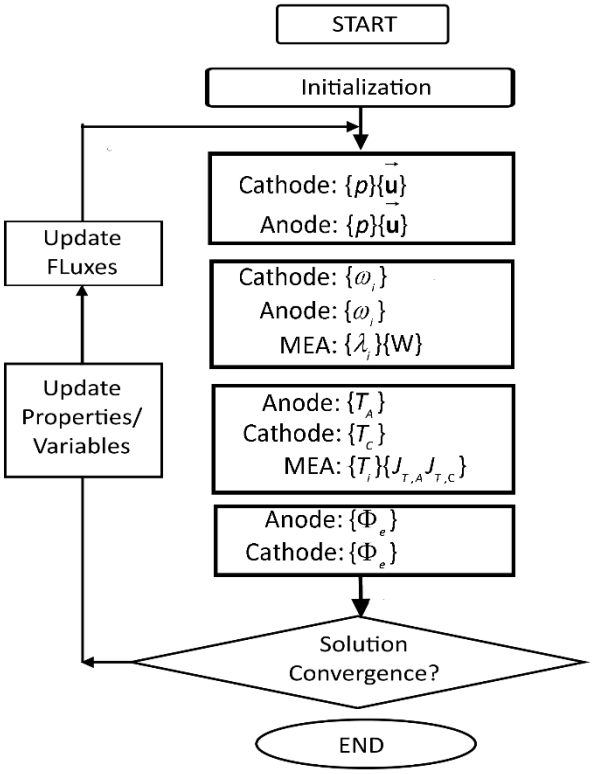

Figure 3.3. Flow diagram of the first stage solution scheme

The segregated solution algorithm of the second stage is shown in Figure 3.4. The current conservation physics are solved first in the sequence; step 1 solves for the 3-D electric potential fields { Φ_e } of the anode and cathode conductive domains in concert with the 2-D MEA current density. Step 2 solves the heat transfer physics. This includes for the 2-D temperature profile of the MEA { T_i } as well as the MEA heat fluxes { $J_{T,A}$, $J_{T,C}$ } and the 3-D energy equation in the anode and cathode domains { T_A , T_C }.

Step 3 ties together the variables of the water transport physics. In the 2-D MEA domain, the water content, water content profile, water fluxes are solved together. These water contents are

principally coupled to the humidity of the adjacent gas streams, and so the mass fractions of the water species and non-reacting nitrogen are solved in this step as well. Steps 4 and 5 solve for the cathode and anode gas flows, as was done earlier in the first stage. As indicated, the procedure is to be repeated until convergence.

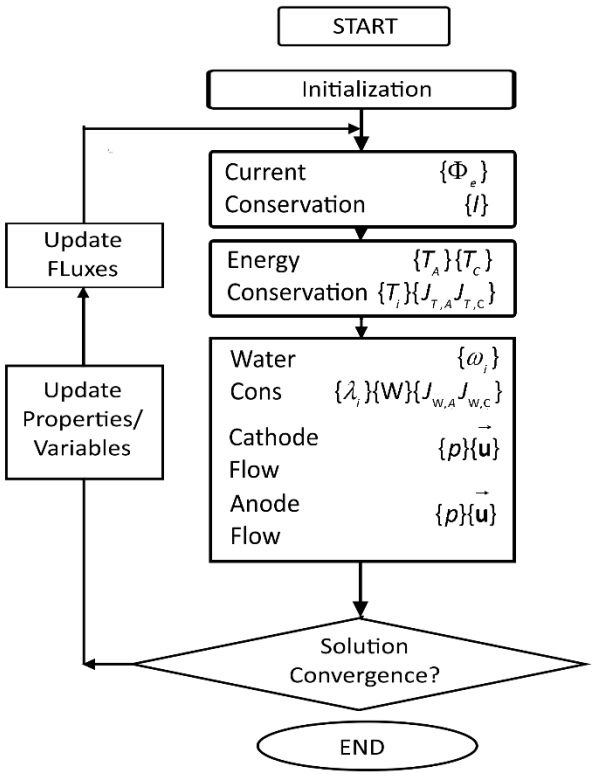

Figure 3.4. Flow diagram of the second stage solution scheme

Table 3.5 lists some of the solver settings of the first stage solution scheme. Within the anode and cathode 3-D domains, the GMRES iteratuive solver with geometric multigrid preconditioner and Vanka pre/postsmoother is used to solve for the fluid flow variables. The species mass fractions and MEA water contents use the SOR line pre/post smoother. A hybrid setup is also described for the temperatures and heat fluxes. One iteration of each is performed with damping factor of 0.7 applied to the damped Newton iterations.

Table 3.6 lists some of the solver settings of the third stage solution scheme. Steps 1, 2, and 3 employ hybridized preconditioners. Step 1 solves the total current conduction physics, solving for the electrical potentials in the 3-D domains and MEA current density together. Step 2 solves the total heat transfer physics similarly. Step 3 combines the water transport physics of the MEA with the water mass fractions in the 3-D domains.

Table 3.5. Solver Settings for the first stage segregated solution scheme.

1: Flow $\{ p , \vec{\mathbf{u}} \}$ Anode and Cathode	Non-linear Solver:	Termination: by	iterations:	1
		Nonlinear Method:	fixed damping:	0.7
	Linear Solver	Type: Iterative	Solver:	GMRES
			Preconditioning:	Left
		Preconditioner: Geometric Multigrid 2 levels, V-cycle	Vanka Smoother:	2 iterations
			Block Solver:	Direct
			Main iterations:	#2 (0.8 relaxation)
			Secondary iterations:	#2 (0.5 relaxation)
2: Mass Fractions $\{ \omega_i , \lambda_i \}$ Anode and Cathode	Non-linear Solver	Termination: by	iterations:	1
		Nonlinear Method:	fixed damping:	0.7
	Linear Solver	Type: Iterative	Solver:	GMRES
			Preconditioning:	Left
		Preconditioner: Geometric Multigrid 2 levels, V-cycle	SOR Line Smoother:	2 iterations
			Main iterations:	#2 (0.2 relaxation)
			Line based on Mesh:	Coupled multivariable method
			Secondary iterations:	#1 (0.4 relaxation)
3: Thermal $\{ T_A , T_C , J_T \}$	Non-linear Solver	Termination: by	iterations:	1
		Nonlinear Method:	fixed damping:	0.7
	Linear Solver	Preconditioner: Geometric Multigrid 2 levels, V-cycle	SOR smoother: T_A , T_C	SOR / SORU solver
			Iterations:	#2 (0.5 relaxation)
			Direct Preconditioner: J_T	PARDISO solver
			Algorithm:	Nested dissection multithreaded
4: Potential $\{ \Phi_e \}$	see 3	-	SOR smoother: Φ_e	SOR / SORU solver
			Iterations:	#2 (0.5 relaxation)

Table 3.6. Solver Settings for the second stage segregated solution scheme.

1: Anode / Cathode: $\{\Phi_e\}$ MEA: $\{I\}$	Non-linear Solver:	Termination: by	Iterations:	2
		Nonlinear Method:	Fixed damping:	0.7
	Linear Solver:	Type: Iterative	Solver:	GMRES
			Preconditioning	Left
		Preconditioner: Geometric Multigrid 2 levels, V-cycle	SOR smoother: Φ_e	SOR / SORU solver
			iterations:	#2 (0.5 relaxation)
			Direct Preconditioner: I	PARDISO solver
			Algorithm:	Nested dissection multithreaded
2: Anode / Cathode: $\{T_A, T_C\}$ MEA: $\{J_{T,A}, J_{T,C}\}$ $\{T_i\}$	Non-linear Solver:	Termination: by	Iterations:	1
		Nonlinear Method:	Fixed damping:	0.7
	Linear Solver:	Solver: GMRES	Preconditioning:	Left
		Preconditioner: Geometric Multigrid 2 levels, V-cycle	SOR smoother: T_A, T_C, T_i	SOR / SORU solver
			Iterations:	#2 (0.5 relaxation)
			Direct Preconditioner: J_T	PARDISO solver
			Algorithm:	Nested dissection multithreaded
3: Anode / Cathode: $\{p, \vec{\mathbf{u}}\}$ $\{\omega_i\}$ MEA: $\{\lambda_i\}\{W\}$ $\{J_W\}$	Non-linear Solver	Termination: by	Iterations:	3 / tolerance
		Nonlinear Method:	Automatic damping:	
	Linear Solver	Iterative	Solver	GMRES
			Preconditioning:	Left
		Preconditioner: Geometric Multigrid 2 levels, V-cycle	Vanka smoother: $p, \vec{\mathbf{u}}$	2 iterations
			Block Solver:	Direct
			Main iterations:	#2 (0.8 relaxation)
			Secondary iterations:	#2 (0.5 relaxation)
			SOR Line smoother: ω_i	2 iterations
			Main iterations:	#2 (0.2 relaxation)
			Line based on mesh	Coupled multivar method
			Secondary iterations:	#1 (0.4 relaxation)
			Direct Preconditioner: λ_i	PARDISO solver
			Algorithm:	Nested dissection multithreaded
		Preconditioner: Jacobi $\{J_W\}$	Iterations:	#1 (0.4 relaxation)

3.4 Convergence Criteria

Convergence criteria were developed by both residuals and species balance criteria. The coupled groups of equations are solved iteratively and convergence of the solution was deemed attained when the relative error in the solution and residuals of each field was less than 10^{-4}.

The overall species balances are also monitored as indications of the convergence of the solution. Species balances are assembled for the hydrogen, oxygen, and water species, based upon their mass consumption. The species balances are a means of verifying that the results are physically meaningful. In all simulations, the values of the species imbalance were less than 0.1%.

The mass flow rate $\dot{m}$ (ks s^{-1}) of hydrogen, oxygen, and water species entering (in) the computational domains can be calculated by eq. (3.11), (3.12), and (3.13).

$$\dot{m}_{H_2,\text{in}} = M_{H_2} \iint_{inlet} \frac{p}{RT} u_{A,in} x_{H_2} \tag{3.11}$$

$$\dot{m}_{O_2,\text{in}} = M_{O_2} \iint_{inlet} \frac{p}{RT} u_{C,in} x_{O_2} \tag{3.12}$$

$$\dot{m}_{H_2O,\text{in}} = M_{H_2O} \left[\iint_{inlet} \frac{p}{RT} u_{C,in} x_{H_2O} + \iint_{inlet} \frac{p}{RT} u_{A,in} x_{H_2O} \right] \tag{3.13}$$

Mass flow rates leaving (out) the computational domains can be calculated by eq. (3.14), (3.15), and (3.16).

$$\dot{m}_{H_2,\text{out}} = M_{H_2} \iint_{outlet} \frac{p}{RT} u_{A,\text{out}} x_{H_2} \tag{3.14}$$

$$\dot{m}_{O_2,\text{out}} = M_{O_2} \iint_{outlet} \frac{p}{RT} u_{C,\text{out}} x_{O_2} \tag{3.15}$$

$$\dot{m}_{H_2O,\text{out}} = M_{H_2O} \left[\iint_{outlet} \frac{p}{RT} u_{C,\text{out}} x_{H_2O} + \iint_{outlet} \frac{p}{RT} u_{A,\text{out}} x_{H_2O} \right] \tag{3.16}$$

The mass flow rates of hydrogen and oxygen that are consumed (con) can be found by integrating the current density of the MEA as in eq. (3.17) and eq. (3.18).

$$\dot{m}_{H_2,\text{con}} = \frac{M_{H_2}}{2F} \iint_{MEA} I\,dA \tag{3.17}$$

$$\dot{m}_{O_2,\text{con}} = \frac{M_{O_2}}{4F} \iint_{MEA} I\,dA \tag{3.18}$$

$$\dot{m}_{H_2O,\text{prd}} = \frac{M_{H_2O}}{2F} \iint_{MEA} I\,dA \tag{3.19}$$

The species balance criteria (%) for hydrogen, eq.(3.20), oxygen, eq.(3.21), and water, eq. (3.22) are given below. Smaller values indicate better mass conservation by the overall model.

$$\%_{H_2} = \left| 1 - \frac{\dot{m}_{H_2,\text{con}} + \dot{m}_{H_2,\text{out}}}{\dot{m}_{H_2,\text{in}}} \right| \tag{3.20}$$

$$\%_{O_2} = \left| 1 - \frac{\dot{m}_{O_2,\text{con}} + \dot{m}_{O_2,\text{out}}}{\dot{m}_{O_2,\text{in}}} \right| \tag{3.21}$$

$$\%_{H_2O} = \left| 1 - \frac{\dot{m}_{H_2O,\text{out}}}{\dot{m}_{H_2O,\text{in}} + \dot{m}_{H_2O,\text{prd}}} \right| \tag{3.22}$$

4 VERIFICATION OF THE NUMERICAL MODEL

In this chapter, aspects of the numerical formulation are verified. First, the numerical formulation of the MEA water content profile is evaluated. The 3-point, or parabolic, water content approximation is compared to a solution obtained by the finite-volume method. Next, a mesh-independence study is performed to ensure that the solutions obtained are independent of grid size or mesh details. Checks are developed to ensure fundamental mass and species balances.

4.1 Verification of Membrane Water Transport Formulation

The MEA interface model has as its purpose to compute the local behavior of the MEA. Local behavior includes the estimation of local current density, reactant consumption, water production, and heat generation. The thru-plane water content distribution is needed to determine the membrane ohmic resistance and catalyst layer losses. These voltage losses are centrally-dependent upon ionomer conductivity; and ionomer conductivity is principally influenced by water content. Water transport within the MEA must be evaluated, and fluxes into the anode and cathode gas streams (computational domains) determined. Verification of the MEA interface model involves comparing solutions of this water / current transport problem. Solutions developed using the finite-volume technique with high-accuracy are compared with the approximate 3-point solution being put forward in this work.

4.1.1 Introduction and Dimensionality

The membrane water transport scheme is subjected to a verification exercise. The 1-dimensional approximate analytical representations of water and current transport are intended to reduce solution complexity and cost associated with discrete, numerical solutions. These schemes need to accurately reproduce the ohmic resistance and boundary water fluxes under variable operating conditions. Questions

then arise about scheme accuracy. Thereforre, the approximate analytical water and current transport scheme is compared against 1-dimensional finite volume numerical solutions.

Following the methodology of some earlier works, these 1-dimensional approximate analytical solutions (for the membrane water content profile) are compared to the finite-volume method, and discrepancies assessed[92]. The prior findings serve as methodological examples for a verification activity. The goal of this section is to verify the 3-point approximate analytical 1-D water transport solution. This is done by comparison to a solution, of the same water / current transport model, created from the finite volume method at fine mesh density.

4.1.2 Development of 1-D Finite-Volume Solution

For the purposes of the verification exercises, this section presents a 1-dimensional finite-volume solution for the present model of membrane water transport. It is not part of the numerical model. In the interface model, the water transport solution determines the distribution of non-dimensional water content λ throughout the membrane thickness. From this distribution, ionic conductivity, the MEA resistance(s), current density, and water flux into the anode and cathode are determined.

Transport properties, such as diffusion coefficient and electro-osmotic drag coefficient, and the boundary conditions for water absorption and desorption, are themselves dependent on λ, making this problem deeply non-linear. The diffusion coefficient, as well as absorption and desorption parameters, are piecewise continuous functions of water content. As such they are not differentiable and finite volume methods have been identified as appropriate for solution [93].

The 1-dimensional computational domain(s) and boundary conditions are shown in Figure 4.1. The domain spans from the ACL / membrane interface at z=0 to the membrane / CCL interface at $z = t_{MEM}$ in geometry which is un-expanded by MEA water uptake (swelling). Convective boundary conditions are described by absorption / desorption coefficients k_1 and k_{M+1}, with equilibrium water uptake values λ_A^{eq} and λ_C^{eq} determined by the anode and cathode relative humidity boundary conditions. The 3-point solution uses water content values λ_{1-3}, while the finite volume solution uses evenly

distributed values $\lambda_1 - \lambda_{M+1}$ where M is the number of cells (M=8 shown). For this verification exercise, uniform temperature is assumed. The current density I (A/m^2) will be treated as if it is a known input, from the 3-point solution, and listed.

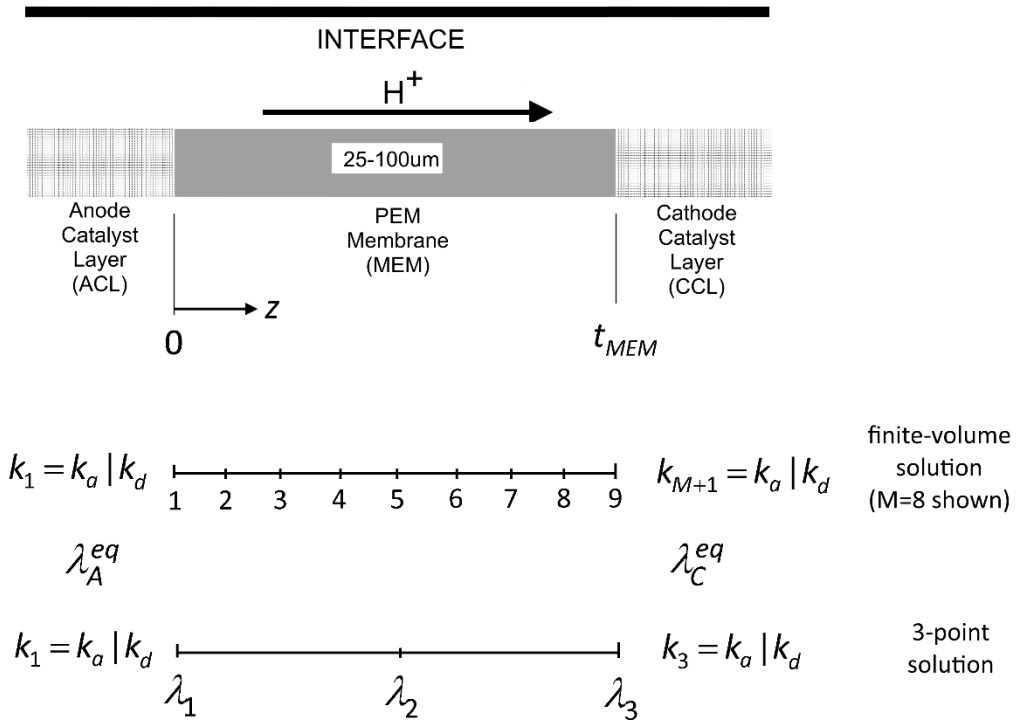

Figure 4.1. 1-D computational domain and boundary conditions for membrane water transport model

The phenomenological model of water transport in Nafion membrane was described in section 2.3.5. The current density I (A m^{-2}) will be treated as if it is a known input to the finite-volume solution. The steady-state solution is now developed with central-differencing applied to both terms, on a uniformly-spaced grid. For an interior node (2-8 pictured above), there are no water generation sources, and mass conservation leads to eq. (4.1), where L/R indicates evaluation at a point midway between the node and its left or right-side neighbor. The terms are described eq.(4.2) in terms of node i .

$$\left[n_d \frac{I}{F}\right]\Big|_L - \left[c_f D_w \frac{d\lambda}{dz}\right]\Big|_L = \left[n_d \frac{I}{F}\right]\Big|_R - \left[c_f D_w \frac{d\lambda}{dz}\right]\Big|_R \tag{4.1}$$

$$[n_d \frac{I}{F}]\Big|_L = \frac{(n_{d,i-1} + n_{d,i})}{2}\frac{I}{F} \qquad [n_d \frac{I}{F}]\Big|_R = \frac{(n_{d,i} + n_{d,i+1})}{2}\frac{I}{F}$$
$$[c_f D_w \frac{d\lambda}{dz}]\Big|_L = c_f \frac{(D_{w,i-1} + D_{w,i})}{2}\frac{(\lambda_i - \lambda_{i-1})}{\Delta z} \quad [c_f D_w \frac{d\lambda}{dz}]\Big|_R = c_f \frac{(D_{w,i} + D_{w,i+1})}{2}\frac{(\lambda_{i+1} - \lambda_i)}{\Delta z} \tag{4.2}$$

After simplification, the equations for these interior nodes have the form of eq. (4.3).

$$\left(-\frac{c_f(D_{w,i-1} + D_{w,i})}{2\Delta z}\right)\lambda_{i-1} + \left(\frac{c_f(D_{w,i-1} + 2D_{w,i} + D_{w,i+1})}{2\Delta z}\right)\lambda_i - \left(\frac{c_f(D_{w,i} + D_{w,i+1})}{2\Delta z}\right)\lambda_{i+1} = \frac{n_{d,i-1} - n_{d,i+1}}{2}\frac{I}{F} \tag{4.3}$$

At point 1 (the membrane / ACL interface), the water flux by absorption/ desorption from the anode is balanced by flux towards the interior of the membrane in eq. (4.4). This can be simplified to eq. (4.5).

$$c_f k_1(\lambda_A^{eq} - \lambda_1) = [n_d \frac{I}{F}]\Big|_R - [c_f D_W \frac{d\lambda}{dz}]\Big|_R \tag{4.4}$$

$$\left(k_1 c_f + \frac{c_f(D_{w,1} + D_{w,2})}{2\Delta z}\right)\lambda_1 - \left(\frac{c_f(D_{w,1} + D_{w,2})}{2\Delta z}\right)\lambda_2 = k_1 c_f \lambda_A^{eq} - \frac{(n_{d,1} + n_{d,1})}{2}\frac{I}{F} \tag{4.5}$$

At point M+1 (the membrane / CCL interface), the flux from the interior of the membrane, combined with production of water from the cathode reaction, is balanced by absorption / desorption flux from the cathode. This is depicted in eq. (4.6). This can be simplified to eq. (4.7).

$$[n_d \frac{I}{F}]\Big|_L - [c_f D_W \frac{d\lambda}{dz}]\Big|_L + \frac{I}{2F} = c_f k_{M+1}(\lambda_{M+1} - \lambda_C^{eq}) \tag{4.6}$$

$$-\left(\frac{c_f(D_{w,1} + D_{w,2})}{2\Delta z}\right)\lambda_M + \left(k_{M+1}c_f + \frac{c_f(D_{w,M} + D_{w,M+1})}{2\Delta z}\right)\lambda_{M+1} = k_{M+1}c_f\lambda_C^{eq} - \left(\frac{(n_{d,M} + n_{d,M+1})}{2} + \frac{1}{2}\right)\frac{I}{F} \tag{4.7}$$

The entire system of equations can be shown as eq. (4.8), where λ_i refers to $\lambda_2 \ldots \lambda_M$. This equation was solved iteratively for $\lambda_1 \ldots \lambda_{M+1}$. Iterations were carried out until the L2 residual of the above simultaneous equations reached below 10^{-14}.

$$\begin{bmatrix} k_1 c_f + \dfrac{c_f(D_{w,1}+D_{w,2})}{2\Delta z} & -\dfrac{c_f(D_{w,1}+D_{w,2})}{2\Delta z} & 0 \\ \cdots & \cdots & \cdots \\ -\dfrac{c_f(D_{w,i-1}+D_{w,i})}{2\Delta z} & \dfrac{c_f(D_{w,i-1}+2D_{w,i}+D_{w,i+1})}{2\Delta z} & -\dfrac{c_f(D_{w,i}+D_{w,i+1})}{2\Delta z} \\ \cdots & \cdots & \cdots \\ 0 & -\dfrac{c_f(D_{w,M}+D_{w,M+1})}{2\Delta z} & \left(k_{M+1}c_f + \dfrac{c_f(D_{w,M}+D_{w,M+1})}{2\Delta z}\right) \end{bmatrix} \begin{Bmatrix} \lambda_1 \\ \cdots \\ \lambda_i \\ \cdots \\ \lambda_{M+1} \end{Bmatrix}$$

$$= \begin{Bmatrix} k_1 c_f \lambda_A^{eq} - \dfrac{(n_{d,1}+n_{d,1})}{2}\dfrac{I}{F} \\ \cdots \\ \dfrac{n_{d,i-1}-n_{d,i+1}}{2}\dfrac{I}{F} \\ \cdots \\ k_{M+1}c_f\lambda_C^{eq} - \left(\dfrac{(n_{d,M}+n_{d,M+1})}{2}+0.5\right)\dfrac{I}{F} \end{Bmatrix} \tag{4.8}$$

With the water contents known, the objectives of the MEA routine can be produced. The membrane resistance $R_{MEM}^{H^+}$ is calculated from these values using trapezoidal integration in eq. (4.9). The membrane water gain rate, water production, anode, and cathode fluxes are calculated by relations similar to those already given from the 3-point model. The water gain rate in eq. (4.10)was found to be vanishingly small, below 10^{-10}.

$$R_{MEM}^{H^+} = \int_0^{t_{MEM}^S} \frac{1}{\sigma_{lo}} dz = \sum_{i=1}^{M} \frac{\Delta z}{2}\left(\frac{1+\varepsilon_{dV,i}}{\sigma_{lo,i}} + \frac{1+\varepsilon_{dV,i+1}}{\sigma_{lo,i+1}}\right) \tag{4.9}$$

$$\frac{\partial W}{\partial t} = \underbrace{\frac{I}{2F}}_{\text{production}} + \underbrace{k_1 c_f(\lambda_A^{eq}-\lambda_1)}_{\text{flux entering MEA from anode anode gas stream}} - \underbrace{k_{M+1}c_f(\lambda_{M+1}-\lambda_C^{eq})}_{\text{flux leaving MEA into cathode gas stream}} \tag{4.10}$$

With this solution in hand, it is possible to compare key items from the 3-point and finite volume formulations. Namely:

(i) Water content values λ_i from each solution

(ii) Membrane resistance $R_{MEM}^{H^+}$

(iii) Anode water flux $J_{w,A} = \frac{N_{H_2O,A}}{M_{H_2O}} = c_f k_1 \left(\lambda_A^{eq} - \lambda_1 \right)$

(iv) Cathode water flux $J_{w,C} = \frac{N_{H_2O,C}}{M_{H_2O}} = c_f k_{M+1} \left(\lambda_{M+1} - \lambda_C^{eq} \right)$

The last two items are linked by eq. (4.10), so only items (i), (ii), and (iii) are used for comparison in the following development where the 3-point and finite volume solutions are compared.

4.1.3 Grid Independence of the 1-D Finite Volume Solution

Mesh refinement studies were undertaken of this 1-dimensional finite volume solution to ascertain what sort of mesh density was necessary for grid-independent solutions for this isothermal, steady-state water transport problem. Figure 4.2 shows spatial profiles of λ for cases used in the experimental validation of section 5.2. Equal Relative humidity levels of (i) 60% and (ii) 100% were both examined at a temperature of 80 °C, dry membrane thickness of 22 μm, current density of 1.5 Acm^{-2}. In both cases, comparisons were made with 4, 8, and 16 uniform grids. The left-most and right-most points represent the equilibrium water content levels determined solely from humidity-based water uptake curves. The discontinuities result from the convective absorption / desorption boundary conditions.

There does not appear to be any meaningful variation between the solutions. This is because the water content profiles in Figure 4.2 are relatively flat and nearly linear, consistent with the experimental water content imaging results reported by multiple works[63, 64, 70].

Table 4.1 lists the water flux and membrane resistance values from this case. It is apparent that the solution becomes grid-independent with only a few nodes (4-8) for these cases. The solution at 16 points is considered converged.

The finite volume solution has been shown to be consistent for these cases at 25 μm thickness. A fine mesh is not needed because the water content profiles are nearly linear. The calculation results reflect the previous experimental observations of nearly linear water content profiles [56, 118] under typical operating conditions, with the usage of thin MEA's.

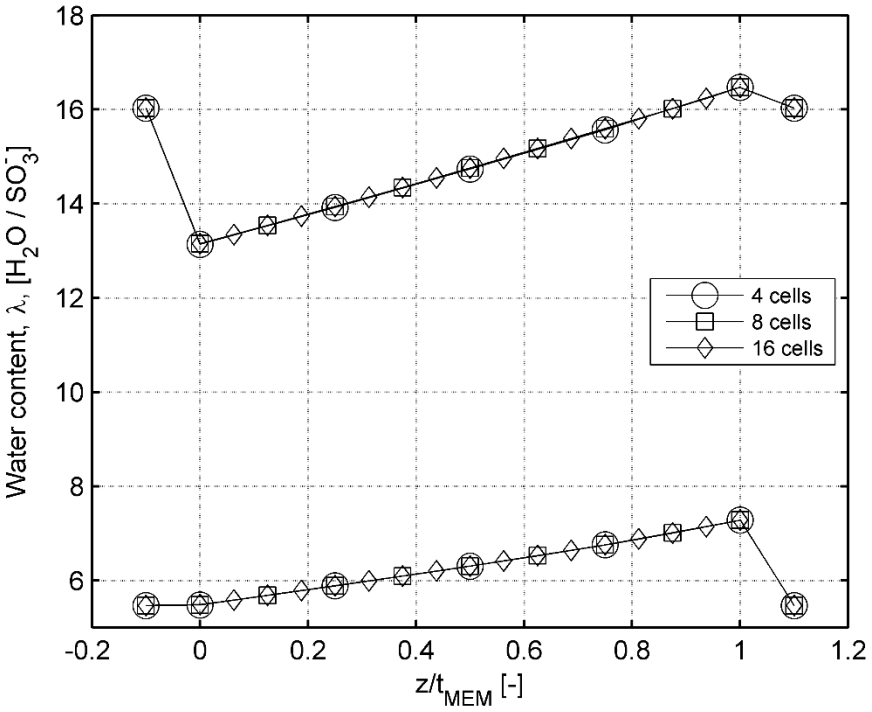

Figure 4.2. Water content profiles at 25 μm thickness for I=1.5 A/cm2 with 60%RH (bottom) and 100%RH (top) with multiple mesh densities

Table 4.1. Water flux and membrane resistance values for I=1.5 A cm^{-2} from equal humidity validation cases with multiple mesh densities.

100% RH, T=80 °C, t_{MEM}=22 μm, I=1.5 A cm^{-2}					
Number of cells	Water production (mol m^{-2} s^{-1})	Anode water flux (mol m^{-2} s^{-1})	Cathode water flux (mol m^{-2} s^{-1})	Water Gain Rate (mol m^{-2} s^{-1})	Membrane Resistance (Ω cm^2)
4	0.0793	0.0786	0.1579	~1 x10^{-15}	.0206
8	0.0793	0.0783	0.1576	~1 x10^{-15}	.0206
16	0.0793	0.0783	0.1576	~1 x10^{-15}	.0206
60% RH, T=80 °C, t_{MEM}=22 μm, I=1.5 A cm^{-2}					
Number of cells	Water production (mol m^{-2} s^{-1})	Anode water flux (mol m^{-2} s^{-1})	Cathode water flux (mol m^{-2} s^{-1})	Water Gain Rate (mol m^{-2} s^{-1})	Membrane Resistance (Ω cm^2)
4	0.0793	-0.0005	0.0788	~1 x10^{-15}	.0625
8	0.0793	-0.0005	0.0787	~1 x10^{-15}	.0624
16	0.0793	-0.0005	0.0787	~1 x10^{-15}	.0624

The same analysis is repeated at 100 μm thickness in Figure 4.3. The maximum realistic current density is reduced to 1.0 A cm^{-2} for the reasons as will be explained in the following section. Somewhat larger variations in water content and lower anode-side water content levels are seen. Table 4.2 lists the water flux and membrane resistance values from this case. It is apparent that the solution becomes grid-independent with only a few nodes (4-8) for these cases. The solution at 16 points is considered converged. In conclusion, no greater mesh density is necessary to produce a grid-independent solution.

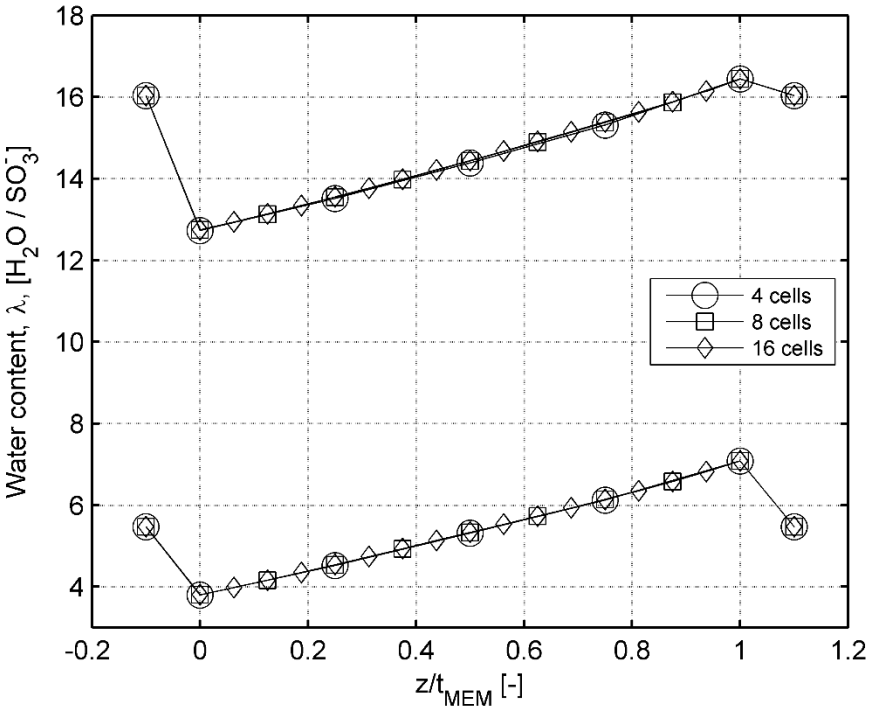

Figure 4.3. Water content profiles at 100 μm thickness for I=1.0 A/cm2 with 60%RH (bottom) and 100%RH (top) with multiple mesh densities

Table 4.2. Water flux and membrane resistance values for I=1.5 A cm^{-2} from equal humidity validation cases with multiple mesh densities.

100% RH, T=80 °C, t_{MEM}=88 μm, I=1.0 A cm^{-2}					
Number of cells	Water production (mol m^{-2} s^{-1})	Anode water flux (mol m^{-2} s^{-1})	Cathode water flux (mol m^{-2} s^{-1})	Water Gain Rate (mol m^{-2} s^{-1})	Membrane Resistance (Ω cm^2)
4	0.0518	0.0878	0.1397	~1 x10^{-15}	0.0841
8	0.0518	0.0875	0.1393	~1 x10^{-15}	0.0839
16	0.0518	0.0874	0.1392	~1 x10^{-15}	0.0839
60% RH, T=80 °C, t_{MEM}=22 μm, I=1.0 A cm^{-2}					
Number of cells	Water production (mol m^{-2} s^{-1})	Anode water flux (mol m^{-2} s^{-1})	Cathode water flux (mol m^{-2} s^{-1})	Water Gain Rate (mol m^{-2} s^{-1})	Membrane Resistance (Ω cm^2)
4	0.0518	0.0167	0.0685	~1 x10^{-15}	0.3885
8	0.0518	0.0166	0.0685	~1 x10^{-15}	0.3813
16	0.0518	0.0166	0.0684	~1 x10^{-15}	0.3795

4.1.4 Comparison 3-Point and Finite Volume Solutions

This section produces comparisons between the finite-volume and 3-point solutions. The two cases examined in the previous section, from the experimental validation in Chapter 5.2, are produced here first. Figure 4.4 shows spatial profiles of λ for both cases. Equal Relative humidity levels of (i) 100% and (ii) 60% were both examined at a temperature of 80 °C, current density of 1.5 A/cm^2. A dry membrane thickness of 22 μm is listed because that dry thickness will swell to its nominal value of 25 μm at 50% RH. The left and right-most points represent the equilibrium water content levels determined solely from the water uptake curves. There is little variation between the two different solutions.

Table 4.3 lists the water flux and membrane resistance values from these cases. The differences in the 3-point and finite-volume solutions are very minor. At 60% RH, the relative error in the anode flux appears large only because the flux is calculated to be very near zero. Relative error in the water gain rate is controlled by the solution tolerance(s) and isn't meaningful here.

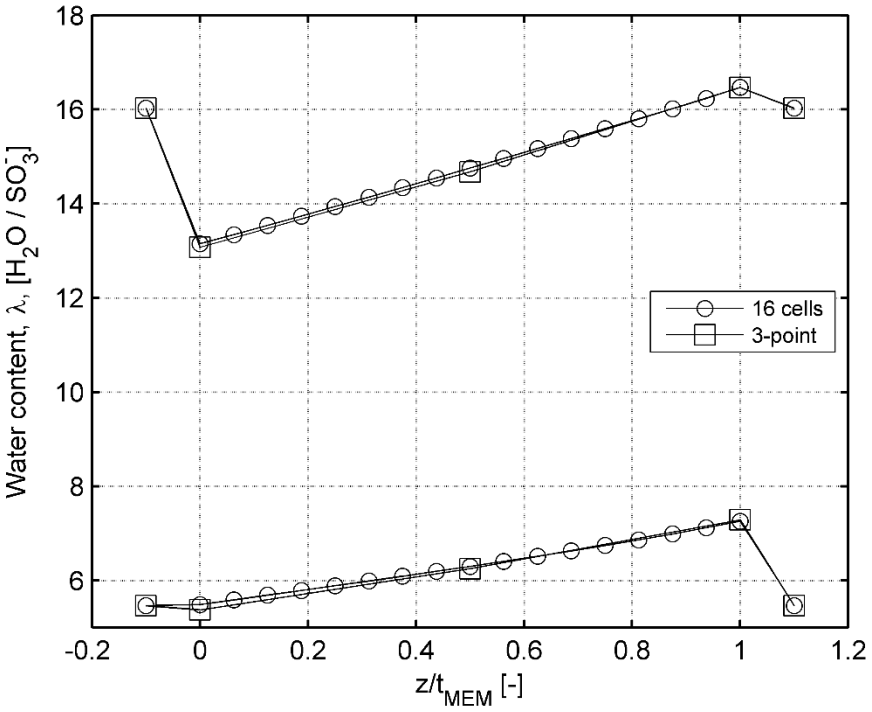

Figure 4.4. Water content profiles for I=1.5 A/cm2 with 60%RH (bottom) and 100%RH (top) from the 3-point and finite-volume solutions

Table 4.3. Water flux and membrane resistance values for I=1.5 A cm^{-2} from equal humidity validation cases from the 3-point and finite-volume solutions.

100% RH, T=80 °C, t_{MEM}=22 μm, I=1.5 A cm^{-2}					
Number of cells	Water production (mol m^{-2} s^{-1})	Anode water flux (mol m^{-2} s^{-1})	Cathode water flux (mol m^{-2} s^{-1})	Water Gain Rate (mol m^{-2} s^{-1})	Membrane Resistance (Ω cm^2)
16 cell	0.0793	0.0783	0.1576	6.6 $x10^{-15}$	.0206
3-point	0.0793	0.0799	0.1592	-8.28 $x10^{-6}$	.0207
relative error(-)	0	0.0204	0.0102	N/A	0.0053
60% RH, T=80 °C, t_{MEM}=22 μm, I=1.5 A cm^{-2}					
Number of cells	Water production (mol m^{-2} s^{-1})	Anode water flux (mol m^{-2} s^{-1})	Cathode water flux (mol m^{-2} s^{-1})	Water Gain Rate (mol m^{-2} s^{-1})	Membrane Resistance (Ω cm^2)
16 cell	0.0782	-0.0005	0.0775	5.5 $x10^{-15}$	.0625
3-point	0.0782	0.0012	0.0794	-6.7 $x10^{-6}$	.0636
relative error(-)	0	-2.76	0.0238	N/A	0.0187

Next, the finite-volume and 3-point solutions are compared across a range of current densities. In Figure 4.5, water content profiles of λ, with a dry membrane thickness of 22 μm, are seen for (i) 0.1 A cm^{-2}, (ii) 0.5 A cm^{-2}, (iii) 1.0 A cm^{-2}, and (iv) 1.5 A cm^{-2}. Equal Relative humidity levels of both 100% and 60% are examined at a temperature of 80 °C. Circles indicate the 3-point solutions and lines indicate the finite volume solutions. There is consistent agreement at this thickness of 22 μm.

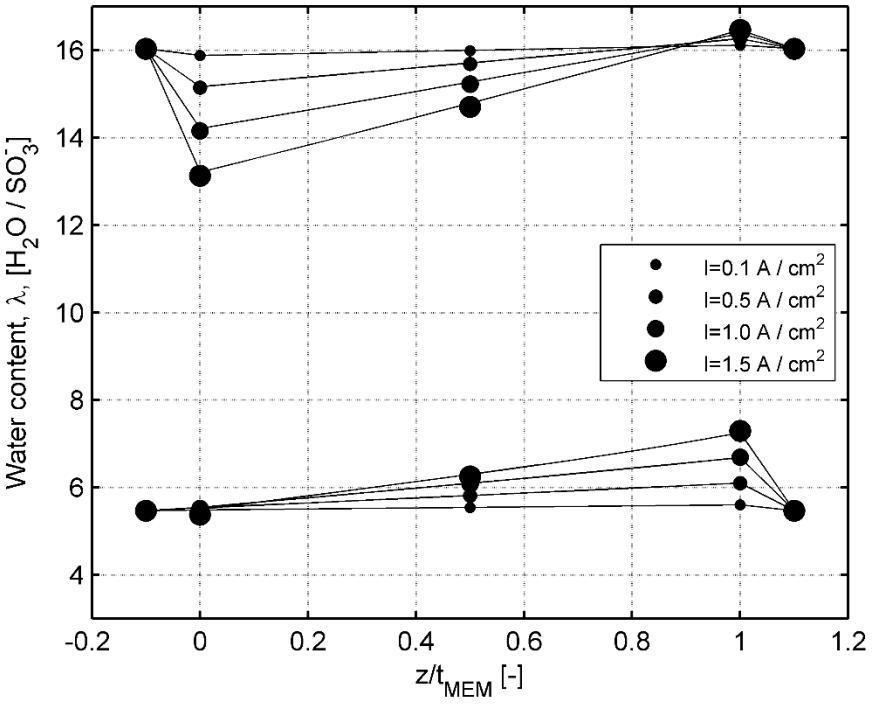

Figure 4.5. Water content profiles with indicated current density at 60%RH (bottom) and 100%RH (top), from 3-point and finite-volume solutions, at nominal thickness of 25 μm

In Figure 4.6, the dry membrane thickness is increased to 44 μm, and the same results are presented. At the highest current density, the 60% RH calculations lines produced by the finite volume solutions begin to show some curvature and slight discrepancies between the two solution methods begin to develop.

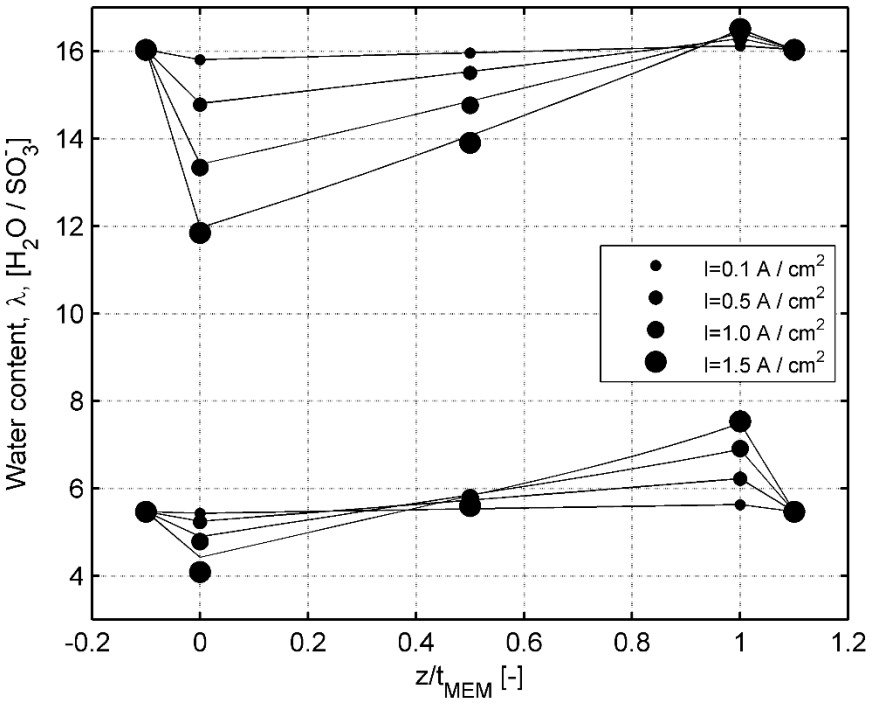

Figure 4.6. Water content profiles with indicated current density at 60%RH (bottom) and 100%RH (top), from 3-point and finite-volume solutions, at nominal thickness of 50 μm

In Figure 4.7, the dry membrane thickness is doubled again to 88 μm and the same results are presented. With increased thickness and elevated current density, ohmic losses are greatly increased. The maximum realistically attainable current density, with the catalyst loading prescribed, is reduced to about 1.0 A cm^{-2}. The discrepancies between the two solution methods become more plainly visible. Some amount of separation between the lines and filled circles emerges.

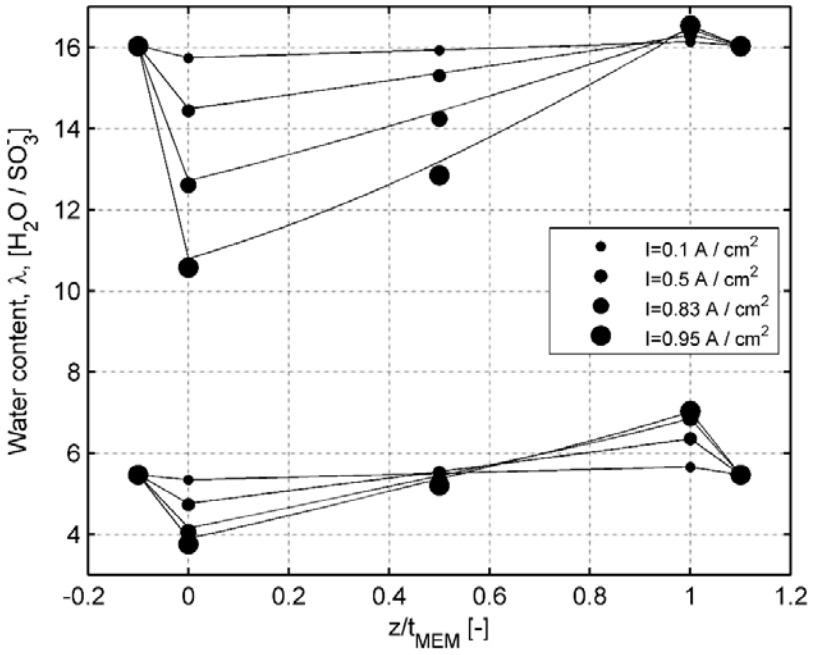

Figure 4.7. Water content profiles with indicated current density at 60%RH (bottom) and 100%RH (top), from 3-point and finite-volume solutions, at nominal thickness of 100 μm

The anode water fluxes resulting from the previously-presented solutions are compared with each other. In Figure 4.8, the water fluxes, from each solution, at each thickness, are compared directly. Good 1:1 agreement is seen with a few outliers observed at low levels; there doesn't appear to be any systematic difference. In Figure 4.9, resistances are compared for all of the same calculations. The cell voltage was not allowed to drop below 0.3V in these calculations, so the thickest membrane was evaluated with reduced maximum current. Lines represent the finite volume calculations, while points represent the 3-point method. Discrepancies start becoming noticeable for the thickest membranes at maximum current density. The relative error in the resistance is examined directly in Figure 4.10. The lines are nearly vertical where the relative error increases with current density and the thicker membranes (50 μm and 100 μm) produce greater levels of relative error than the thinnest (25 μm) one. The 3-point technique reaches a maximum 2% relative error approximating the 25 μm membrane, while greater errors near 10% appear in approximating the 50 μm and 100 μm membranes.

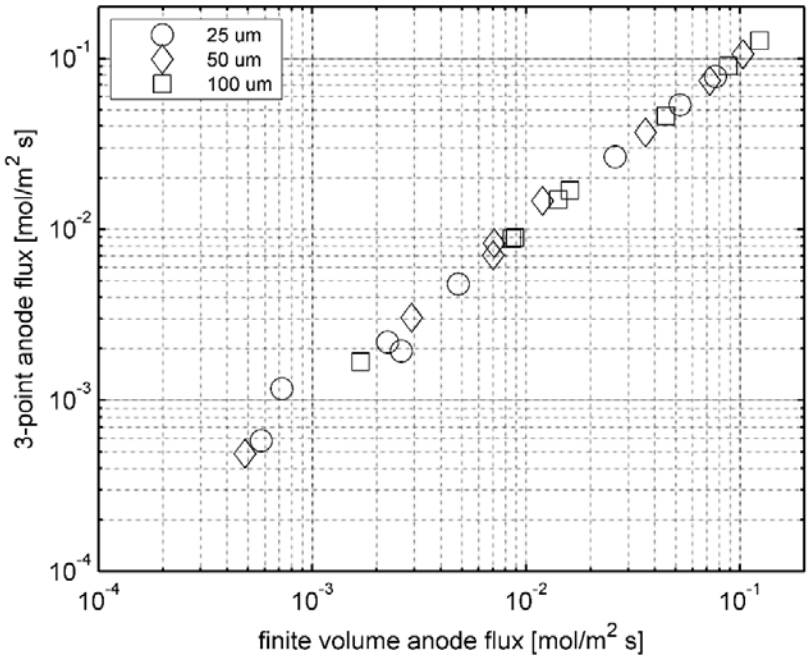

Figure 4.8. Comparison of water flux values, computed at the anode, from 3-point and finite-volume solutions, at nominal thicknesses of 25, 50, 100 μm

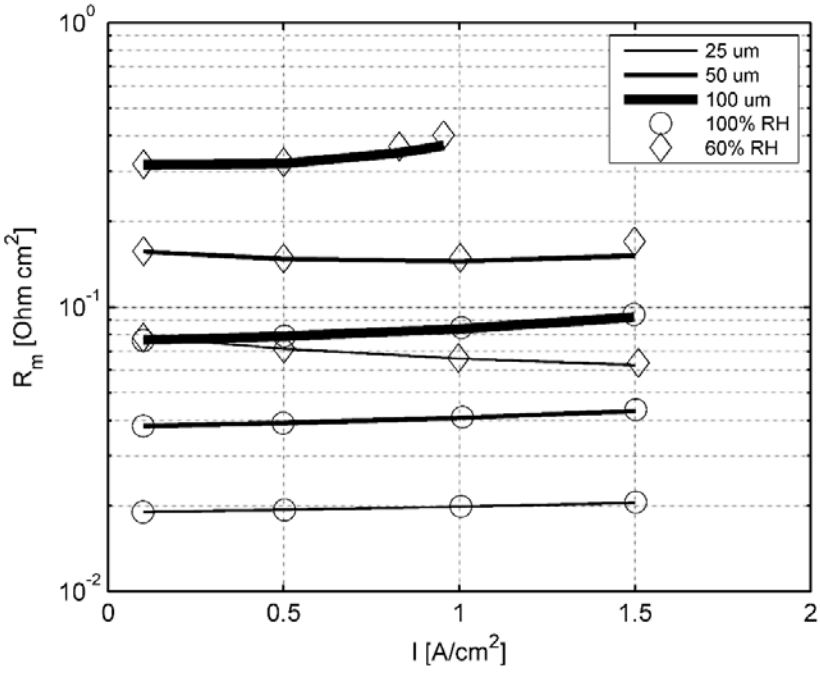

Figure 4.9. Comparison of resistance from 3-point (symbols) and finite-volume (line) solutions, at nominal thicknesses of 25, 50, 100 μm

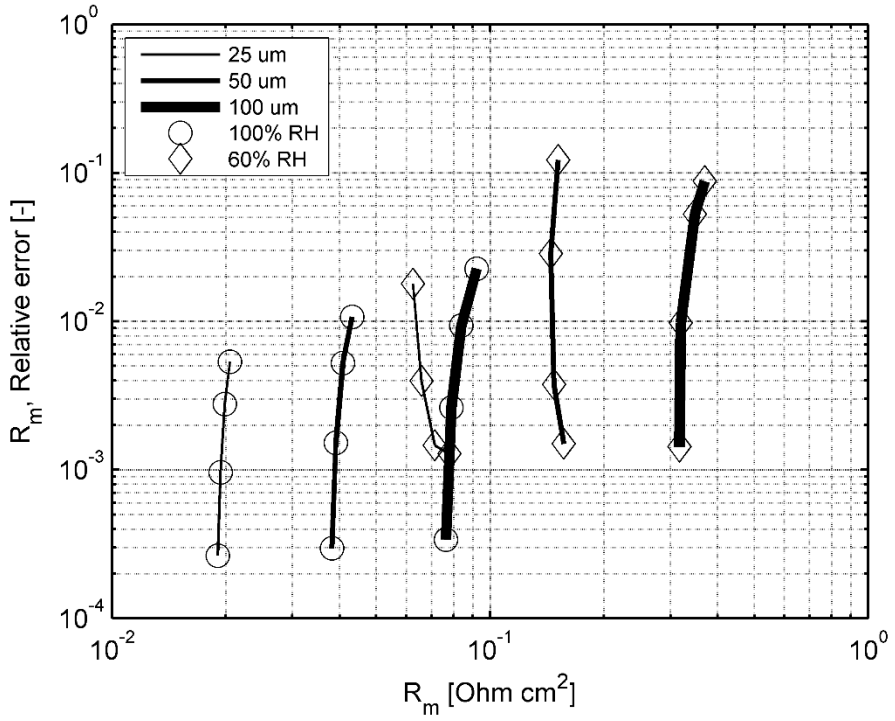

Figure 4.10. Relative error in resistance from 3-point (point) solutions, at nominal thicknesses of 25, 50, 100 μm

4.1.5 Systematic Examination of Approximation Errors

A systematic examination of how approximation errors change due to the humidity boundary conditions is presented. In the prior results, approximation errors were shown where equal anode / cathode humidity levels were assumed at 60% RH and 100% RH, respectively. Potentially, any combination of anode and cathode humidity levels could be encountered and so the approximation errors that will be introduced into the rest of the model must be assessed.

The water content profile solutions are used to calculate the water fluxes into the anode and cathode computational domains, as well as membrane resistance $R_{MEM}^{H^+}$, which is used in estimating the device's current density. Both anode and cathode side fluxes could be determined, but as they are directly related to each other, only the anode flux $J_{w,A}$ is examined here. The discrepancies of the 3-point method

were seen to grow with current density and membrane thickness. It is plausible, however, that humidity levels could reach any combination of values within reason (~ 0.3 – 1.0). A systematic assessment is therefore carried out at each thickness with current density held fixed near 1.0 A/cm^2. When this wasn't possible (certain simulations of the thickest membrane), cell potential was limited to 0.3 V and a reduced current density was used. Membrane equivalent weight was constant at 1100 g / mol SO_3^-.

Contours of water flux $J_{w,A}$ under these conditions are shown in Figure 4.11. Finite volume solutions are shown in the left column while 3-point solutions are shown in the right column. The rows indicate increasing thickness from 25 μm at the top, to 50 μm in the middle row, and 100 μm in the bottom row. It can be seen that the fluxes initially appear identical (25 μm). Noticeable discrepancies develop at bottom (100 μm), with the biggest differences occurring at low anode / high cathode humidity combinations. These are the conditions which create the greatest anode-cathode differences of membrane water content, and, hence, transport properties (electro-osmotic drag coefficient and the diffusion coefficient). Sui and Djilali had a similar finding [92].

Contours of membrane resistance $R_{MEM}^{H^+}$ are shown under the same conditions in Figure 4.12. The same trend is observed, where the resistance contours in the bottom row (100 μm) become noticeably distorted.

Relative errors in the anode water flux are computed as in eq. (4.11) by defining a relative error based on the maximum flux possible. This is defined as the sum of the water flux and water production terms. The term $J_{w,A}^{\mathbb{FV}}$ is the accepted finite-volume solution, $J_{w,A}^{\mathbb{III}-\mathbb{P}}$ the approximate 3-point solution, and $I/(2F)$ the water production. Figure 4.13 shows the relative error defined in this way for the same three membrane thicknesses. The error is under 2% in the thinnest membrane and small for high anode humidity in all cases. Discrepancies are concentrated at combinations of low anode humidity and high cathode humidity, as was previously noted.

$$\varepsilon\left[J_{w,A}^{\mathbb{III}-\mathbb{P}}\right]=\frac{J_{w,A}^{\mathbb{III}-\mathbb{P}}-J_{w,A}^{\mathbb{FV}}}{\left|J_{w,A}^{\mathbb{FV}}\right|+\frac{I}{2F}} \tag{4.11}$$

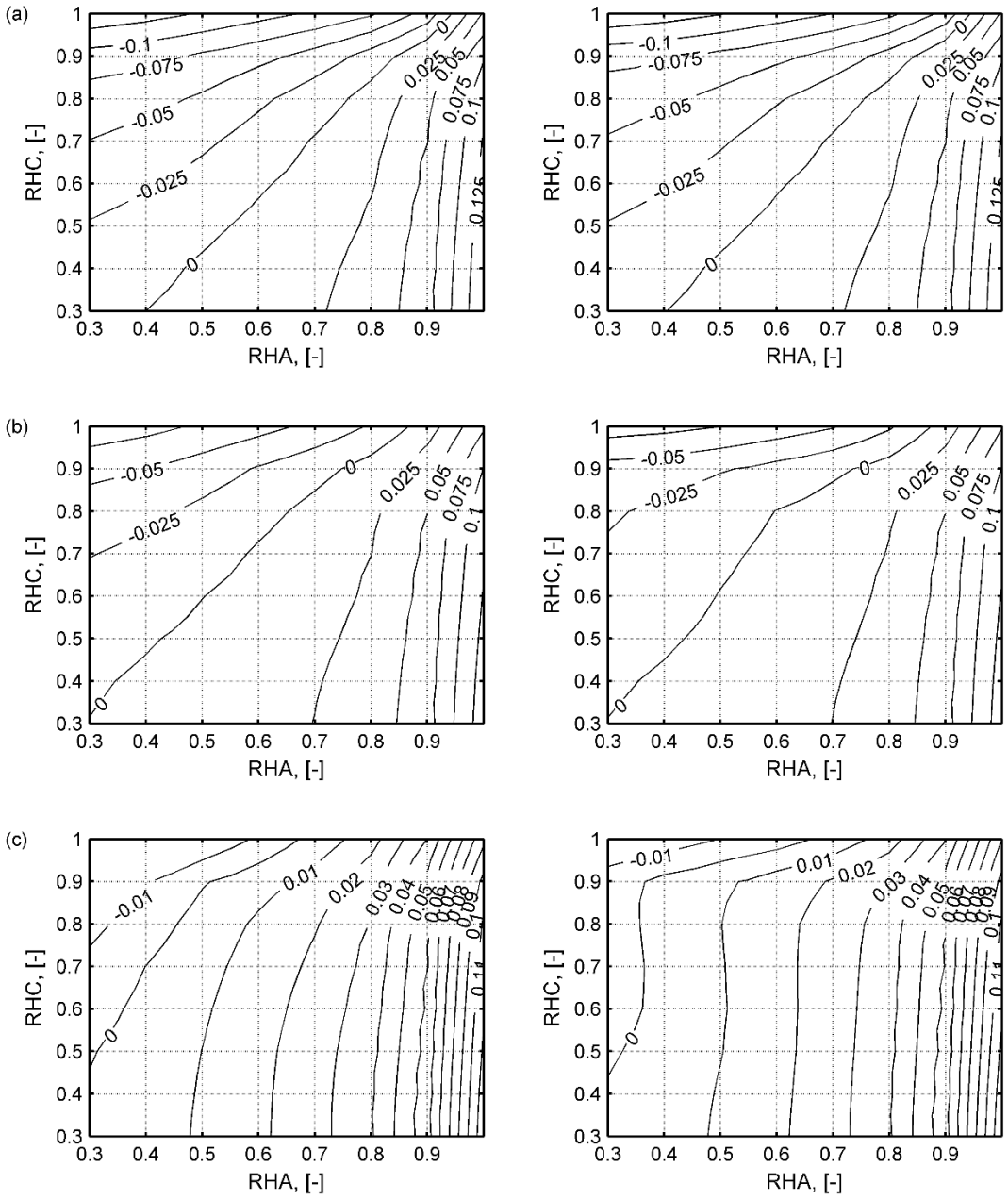

Figure 4.11. Contours of anode water flux (mol m-2 s-1) from finite-volume (left) and 3-point (right) solutions, at nominal thicknesses of (a) 25, (b) 50, and (c) 100 μm

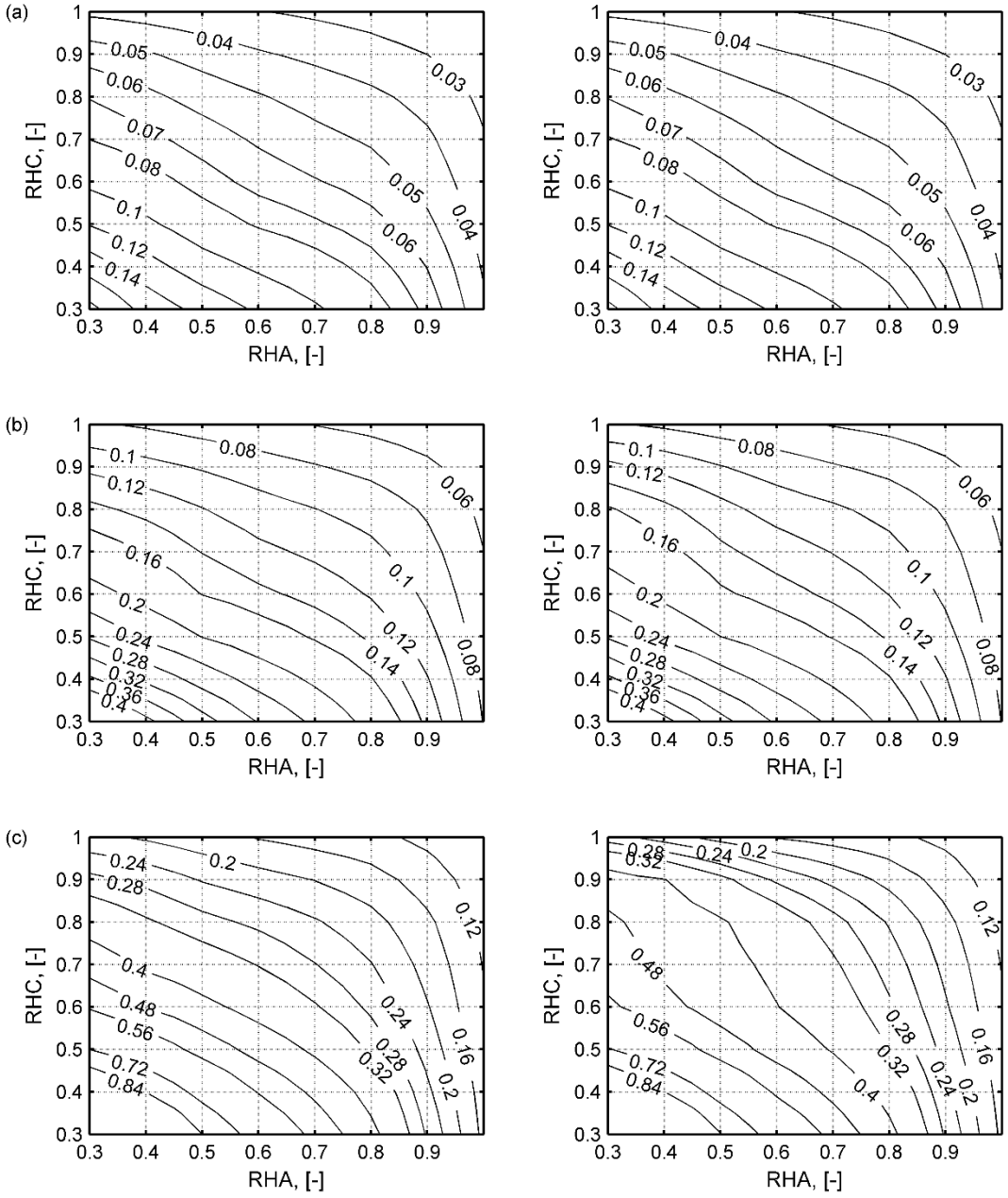

Figure 4.12. Contours of membrane resistance from finite-volume (left) and 3-point (right) solutions, at nominal thicknesses of (a) 25, (b) 50, and (c) 100 μm

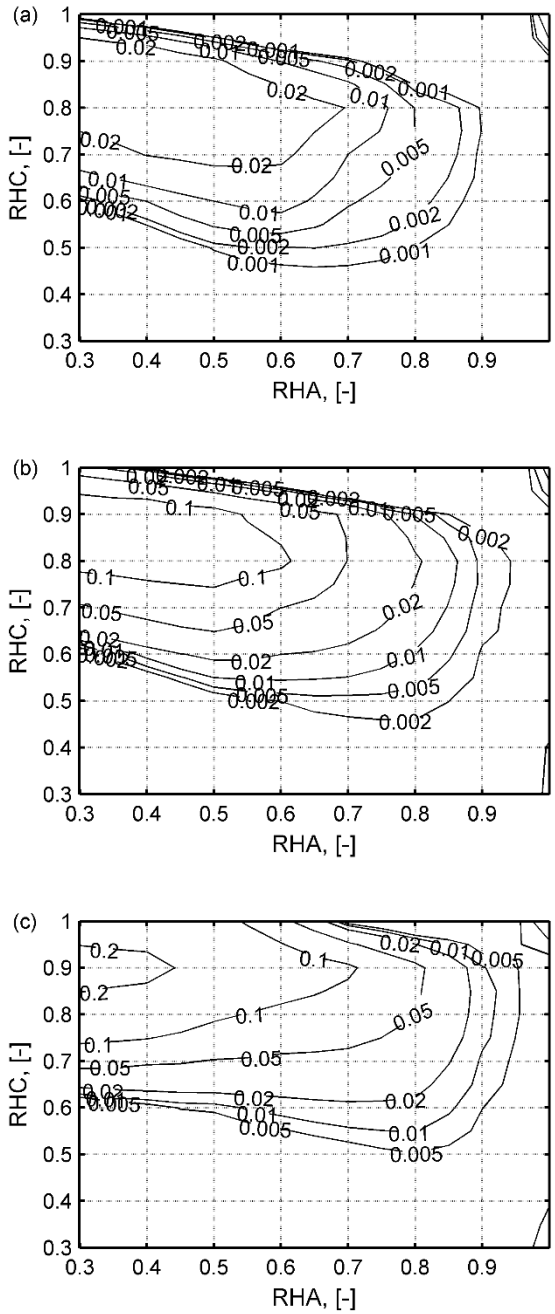

Figure 4.13. Contours of relative error in anode water flux from the 3-point solution, at nominal thicknesses of (a) 25, (b) 50, and (c) 100 μm

Relative errors in the computed membrane resistance are computed as in eq. (4.12), where $R_{MEM}^{H^+,\mathbb{III}-\mathbb{P}}$ is the resistance computed from the 3-point solution and $R_{MEM}^{H^+,\mathbb{FV}}$ is computed from the finite volume method. The discrepancies in Figure 4.14 exhibit the same trends. Discrepancies stay below 1% for the thin membrane case (part (a)), while they rise to 5% (part (b) and even 20-30% (part (c) when the membrane thickness is increased.

$$\varepsilon\left[R_{MEM}^{H^+,\mathbb{III}-\mathbb{P}}\right]=\frac{R_{MEM}^{H^+,\mathbb{III}-\mathbb{P}}-R_{MEM}^{H^+,\mathbb{FV}}}{R_{MEM}^{H^+,\mathbb{FV}}} \tag{4.12}$$

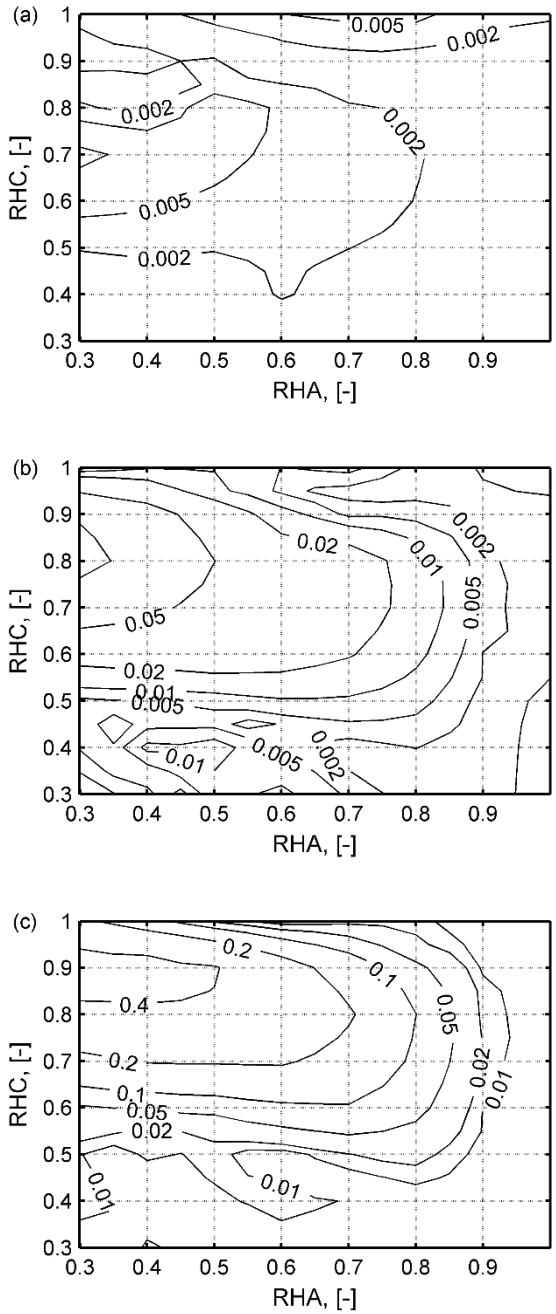

Figure 4.14. Contours of relative error in membrane resistance from the 3-point solution, at nominal thicknesses of (a) 25, (b) 50, and (c) 100 μm

4.1.6 Conclusions

The interface model, described in Chapter 3, utilizes an iterative, approximate analytical solution to determine the water content profile in the MEA. It was claimed that the simplified approach would be valid for thin membranes such as 1 micron thickness, but suffer degraded accuracy when used with thicker (~3-4 micron) membranes. The degree of accuracy was not quantitatively established. This section set out to quantify these approximation errors and develop guidelines for effective use of that interface model.

Water and charge transport schemes used to model the MEA behavior have used 1-dimensional schemes since some of the earliest PEM fuel cell models were developed [91]. Numerical experiments have suggested that this is a valid simplification to the problem because of the underlying physics [72]. The finite volume solution technique was found to be appropriate for solution of the 1-D water transport scheme in the MEA. Approximate analytical solutions were evaluated against these solutions used as benchmarks [92]. The approximate solution proposed here is, therefore, assessed against the 1-D finite volume solution technique with the same model of water transport.

First, a finite volume solution to the water transport model was developed using second-order central differencing discretization. Then the finite volume formulation was shown to be consistent. Under the typical conditions of operation, it was seen that as few as 4-8 nodes were necessary to get grid independence at thicknesses of 25 and 100 μm.

Comparisons of the 3-point and finite-volume solutions followed. Water content profiles were virtually indistinguishable for modeling the thinnest 25 μm membrane; relative error levels were seen reaching ~2% when maximum current density loads were applied.

The disagreements tended to grow as membrane thickness and current density increased. Relative errors in water flux were substantial when large differences in anode / cathode water content were present. When solving the same problem with thicker membranes, relative error levels associated with the 3-point solution grew to reach ~ 10%. Discrepancies were largest with thick membranes operating at the highest current densities.

Lastly, discrepancies of the 3-point method were assessed with regard to the principal outcomes of the water content profile. Membrane resistance and the anode-side water flux were calculated with systematic variation of the anode and cathode humidity boundary conditions. Current density was held fixed near 1.0 A cm^{-2}. Contours of relative error levels were generated, which again showed maximum error levels increasing with the membrane thickness. Relative errors remained under 2% when modeling the 25 μm membrane. At 50 μm thickness, relative errors remained under about 10% for each output. Relative errors grew to 20-40% when modeling the 100 μm membrane; this 3-point method is not recommended for use at that thickness. The suitability of this 3-point approximation technique for use with thin membranes has thus been established.

4.2 Verification of Grid Independency

4.2.1 Purpose of Grid independency

Generally, CFD solutions have a solution accuracy that improves with the fineness of the grid upon which they are employed. Accuracy and solution convergence depends upon the model(s) of physical phenomena used, discretization schemes (or shape functions), and solution routines. Numerical tests, for grid-independency, are typically performed to ensure that the solutions are not influenced by the particulars of the grid used.

This section seeks to provide evidence that the model results are independent of the computational mesh. The grid-independency study focuses on the meshes within the anode and cathode domains, as well as the 2-D mesh of the MEA. The results of some successively refined meshes are compared. Results are calculations of current density within the MEA. The results should change by less than a satisfactory tolerance as the grid size is reduced.

4.2.2 Computational Domains

A limited, typical single-channel PEMFC co-flow arrangement model is used to demonstrate that the model as presented will converge to a consistent, grid-independent solution with some level of sufficiently fine mesh refinement. The computational domains and meshes are presented in Figure 4.15. Mesh 1 holds 7920 domain elements and 4944 boundary elements. Mesh 2 holds 27392 domain elements and 12032 boundary elements. The mesh includes the anode domain (bottom) and cathode domain (top). The detached 2-D middle surface is the MEA, which interacts with the computational domains through prescribed fluxes of current, heat, and species consumption.

Geometrical and physical parameters of the demonstration model are presented in Table 4.4. Operating conditions and parameters for this model are shown in Table 4.5. The simulation is run with constant stoichiometric ratios, at target average current density of 0.5 A/cm^2. Cathode voltage is solved for in order to reach that target.

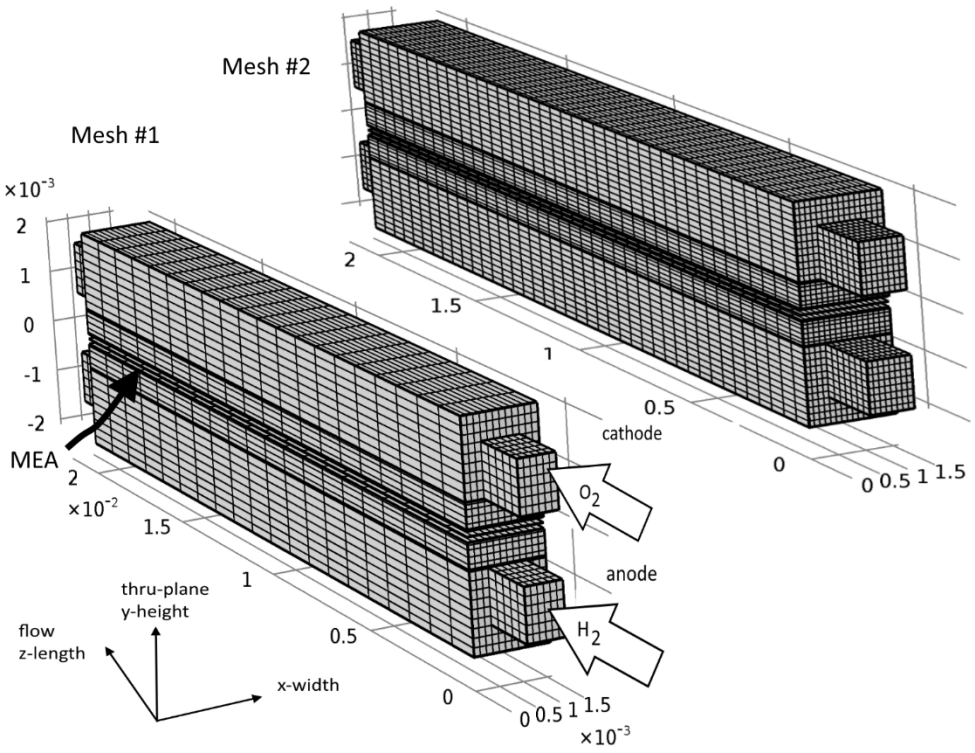

Figure 4.15. Single-channel PEMFC computational domains and meshes for grid-independence study

The compositions of the anode and cathode gas streams are given in

Table 4.6. The gas streams are humidified hydrogen and oxygen, respectively, with 60% RH. The MEA composition is detailed in Table 4.7. This composition is from the validation work in section 5.2.

Table 4.4. Geometrical Parameters of the single-channel PEMFC.

Gas Channel	Gas channel width (x)	W_{ch}	0.8	mm
	Gas channel height (y)	H_{ch}	1.0	mm
	Fuel cell length (z)	L_{ch}	20	mm
Shoulder	Shoulder width	W_{sh}	0.4	mm
	Shoulder height	H_{sh}	1.5	mm
GDL	thickness	H_{GDL}	500	μm
	density	ρ	1950	kg m^{-3}
	porosity	ε	0.78	-
	permeability	$\overline{\overline{\mathbf{K}}}$	10^{-15}	m^2
	in-plane thermal conductivity	$k_{GDL,=}$	17	W m^{-1} K^{-1}
	thru-plane thermal conductivity	$k_{GDL,\perp}$	1.7	$(\Omega\ m)^{-1}$

	in-plane electrical conductivity	$\sigma_{e,=}$	10000	$(\Omega\ m)^{-1}$
	thru-plane electrical conductivity	$\sigma_{e,\perp}$	1250	$(\Omega\ m)^{-1}$
Collector Plates	top height	H_{CCL}	1.5	mm
	thermal conductivity	k_{CCL}	44.5	$W\ m^{-1}\ K^{-1}$
	electrical conductivity	σ_e	$4x10^{06}$	$(\Omega\ m)^{-1}$
	thermal contact resistance	R_{cnt}^{T}	$1.5x10^{-4}$	$m^2\ K^1\ W^{-1}$
	electrical contact resistance	$R_{cnt}^{e^-}$	4.0	$m\Omega\ cm^2$

Table 4.5. Operating conditions and parameters of the single-channel PEMFC.

Parameter:		Symbol:			Value:
Operating cell voltage		$V_{cell}^{\mathbb{OP}}$			(solved for) V
Average operating cell current density		$I_{cell}^{\mathbb{OP}}$			0.5 A/cm^2
MEA area (length x width)		A_{MEA}			32 mm^2
Anode:			Cathode:		
Parameter:	Symbol:	Value:	Parameter:	Symbol:	Value:
Operating pressure	$P_A^{\mathbb{OP}}$	202.65 kPa	Operating pressure	$P_C^{\mathbb{OP}}$	202.65 kPa
Flow inlet area	$A_{A,ch}$	0.8 mm^2	Flow inlet area	$A_{C,ch}$	0.8 mm^2
Stoichiometric flow ratio	$\zeta_A^{\mathbb{OP}}$	4	Stoichiometric flow ratio	$\zeta_C^{\mathbb{OP}}$	4
Relative humidity	$\mathbb{RH}_A^{\mathbb{OP}}$	60 %	Relative Humidity	$\mathbb{RH}_C^{\mathbb{OP}}$	60 %
Inlet temperature	$T_A^{\mathbb{OP}}$	353.15 K	Inlet temperature	$T_C^{\mathbb{OP}}$	353.15 K
Cell temperature	$T_A^{\mathbb{OP}}$	353.15 K	Cell temperature	$T_C^{\mathbb{OP}}$	353.15 K

Table 4.6. Gas input compositions of anode and cathode of the single-channel PEMFC.

80°C temperature 101 kPa reactant partial pressures 100% RH	Anode V_A = ground	p_{H_2} =174 kPa	p_{H_2O} =28.6 kPa	p_{N_2} =0 kPa	p_A =202.65 kPa
		$x_{H_2,A}$ =0.8588	$x_{H_2O,A}$ =0.1412	$x_{N_2,A}$ =0.0	
	Cathode V_C = (variable)	p_{O_2} =36 kPa	p_{H_2O} =47.8 kPa	p_{N_2} =0 kPa	p_C =202.65 kPa
		$x_{O_2,C}$ =0.1804	$x_{H_2O,C}$ =0.1412	$x_{N_2,C}$ =0.6785	

Table 4.7. MEA compositions of anode and cathode of the single-channel PEMFC.

Membrane	Ionomer equivalent weight	EW	1100	g / equiv or g / mol SO_3^-
	Thickness (dry)	t_{MEM}	22×10^{-6}	m
	Crossover current density	I_x	10	A / m^2
Anode Catalyst Layer	Platinum loading	$L_{ACL,Pt}$	0.35	mg_{Pt} / cm^2
	Pt/C mass ratio	Ptc_{ACL}	50	%
	Ionomer to carbon ratio	IC_{ACL}	1.4	-
	Thickness (dry)	t_{ACL}	12×10^{-6}	m
	Available catalyst area	$A_{ACL,Pt}^{100\%RH}$	50	m^2_{Pt} / g_{Pt}
	Specific exchange current density	$i^*_{0,ACL}$	0.24	A / cm^2_{Pt}
Cathode Catalyst Layer	Platinum loading	$L_{CCL,Pt}$	0.5	mg_{Pt} / cm^2
	Pt/C mass ratio	Ptc_{CCL}	50	%
	Ionomer to carbon ratio	IC_{CCL}	1.4	-
	Thickness (dry)	t_{CCL}	18×10^{-6}	m
	Available catalyst area	$A_{CCL,Pt}^{100\%RH}$	50	m^2 / g_{Pt}
	Specific exchange current density	$i^*_{0,CCL}$	2×10^{-8}	A / cm^2_{Pt}
Electronic Resistance	MEA electronic resistance	$R^{e^-}_{cnt}$	0.011	$\Omega\ cm^2$

4.2.3 Results

The current density distributions obtained from this simulation with each mesh are shown in Figure 4.16. The results have been widened for clarity to allow easy comparison. The centerline results in Figure 4.17 show only a slight difference at the downstream end (y/L ~1).

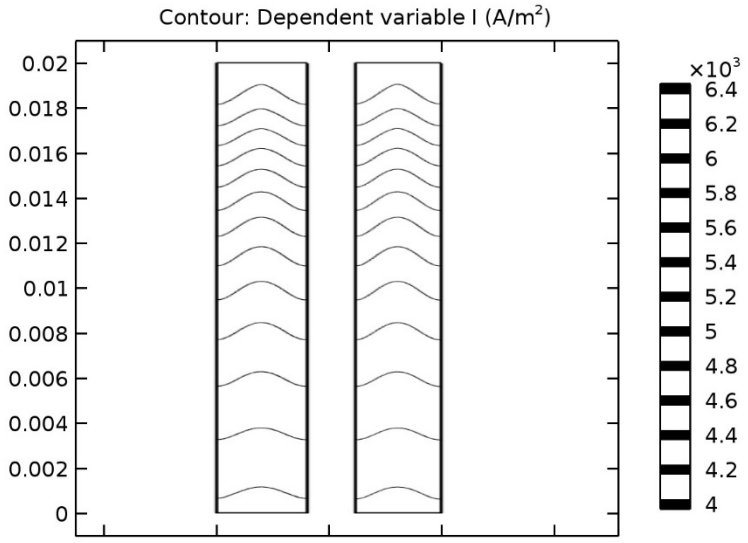

Figure 4.16. Enlarged current contours for mesh 1 (left) and mesh 2 (right)

Species conservation data are shown in Table 4.8 and Table 4.9. The mass flow rates are consistent between meshes. Imbalance levels of each species are seen to diminish with increasing mesh refinement, with levels capped at around 0.02%.

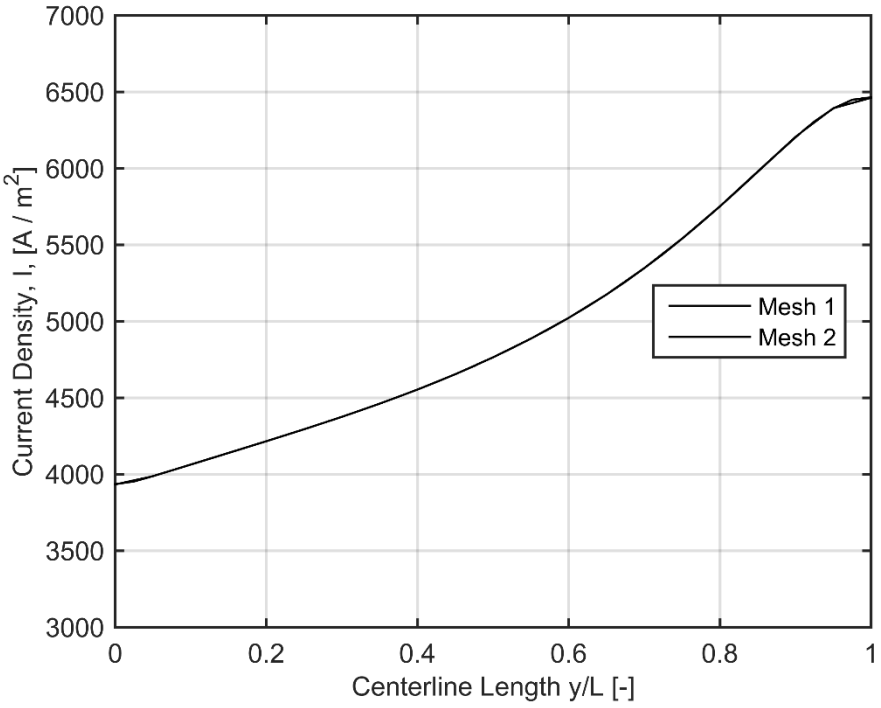

Figure 4.17. Centerline current density with mesh 1 and mesh 2

Table 4.8. Reactant species balance calculations.

H2	Inlet (kg/s x10^{-9})	Outlet (kg/s x10^{-9})	Consumption (kg/s x10^{-9})	Imbalance (x10^{-4})
Mesh 1	6.66	5.00	1.65	-2.11
Mesh 2	6.66	4.99	1.65	-1.48
O2	Inlet (kg/s x10^{-7})	Outlet (kg/s x10^{-8})	Consumption (kg/s)	Imbalance (x10^{-5})
Mesh 1	1.06	9.28	1.33	4.61
Mesh 2	1.06	9.29	1.33	2.20

Table 4.9. Water species balance calculations.

H2O	Inlet (A) (kg/s x10^{-7})	Outlet (A) (kg/s x10^{-8})	Production (kg/s x10^{-8})	Imbalance (x10^{-5})
Mesh 1	9.79	1.34	1.49	-1.87
Mesh 2	9.79	1.34	1.49	-5.48
H2O	Inlet (C) (kg/s x10^{-8})	Outlet (C) (kg/s x10^{-8})		
Mesh 1	4.67	5.80		
Mesh 2	4.67	5.80		

4.2.4 Conclusions

The distributed current density results and species balance calculations were compared on a base case mesh and one which was refined from the base case. Refinement of the mesh showed insignificant change in the current density solution. The solution reactant flow rates were insignificantly affected by further mesh refinement. Species imbalance figures began at sufficiently low levels (~0.02%), and decreased with greater mesh refinement. The model has been shown to converge to a physically meaningful result.

5 VALIDATION OF INTERFACE MODEL

In this chapter, the Non-Equilibrium Interface Model of membrane-electrode assembly (MEA) behavior is validated through the use of previously published experimental datasets. The interface model is designed to simulate the externally-observable behavior of the MEA with an approximate analytical solution. That solution considers only effects in the thru-plane direction and ignores variations of input parameters (properties) in the planar directions, treating those conditions as locally uniform. The model is validated against differential cell data, which were intended to be compatible with the model's simplifying assumptions.

Linked problems of water transport, current transport, energy transport, diffusional transport through the catalyst layers, and the fundamental kinetic relationships are described by this iterative scheme.

The interface model is intended to simulate the localized behavior of a larger device, but here is validated against a small-area PEMFC with spatially-uniform flow conditions. Validation takes place with the comparison to experimental data from differential cells with well-defined MEA compositions. As discussed by Oberholzer and Boillat[119], there is particular value in comparison to differential cell data. Differential cell data can re-produce the local conditions that might occur in a larger, economically-viable device (known as a technical cell). Complications arising from the variation of temperature, humidity, reactant concentration, and other factors along the direction of gas flow can be avoided. The differential PEMFC is built with small planar dimension (i.e. 0.5 cm^2) and operated with gas flows of very high stoichiometry (10-100). The intention is to create aforementioned conditions as uniform as possible within the anode and cathode.

With uniform conditions within the anode and cathode gas streams, model predictions are compared against measurements of cell ohmic resistance and the several voltage components. The voltage components are generally divided and described according to their respective loss mechanisms. Kinetic losses of the cathode's ORR reaction are presented as the first loss mechanism. Some discrepancies exist in the treatment of these losses. Ohmic losses of the membrane are the second loss mechanism. Cell ohmic resistance measurements reflect changes in hydration levels of the membrane. Ohmic losses associated with the ACL and CCL are also assessed. The measured cell voltage is shown with and without correction for high-frequency resistance (HFR).

An existing interface model is included for comparison to the proposed interface model. The widely-used approach of Shimpalee and co-workers [120] was formerly implemented in commercial CFD software. Complications arise, however, because certain parameters used in the model have varied. A model developed for automotive applications (with 75% RH) is used [112]. That work, however, utilizes a model of kinetic losses in the Cathode ORR that contradicts more detailed, focused, experimental kinetics investigations [20]. A second additional implementation of that work with the better treatment of cathode kinetics is also included. It incorporates the same kinetic relationships developed for the Non-Equilibrium Interface Model.

These two existing models use Dirichlet water content boundary conditions, derived from Nafion equilibrium water uptake curves. Hence, they are referred to as Equilibrium Interface Model(s) within this chapter. That approach has been criticized for the very approximate treatment of water transport in the MEA and also for neglecting important catalyst layer losses. These validation sections, with differential cell data, provide an illustration of these issues applied to a particular MEA construction. These issues have been rectified in the Non-equilibrium Interface Model.

The purpose of the present chapter is to (i) show comparison of the non-equilibrium interface model with experimental data (with utilization of the necessary simplifications in the analytical interface model) and (ii) compare and contrast results from the various interface models.

5.1 Validation of Voltage and Cathode Kinetics Relationships

The first verification step involves comparing model predictions to experimental data from the differential cell experiments of Neyerlin et al. [19] (published in 2006). This work was chosen because it included complete information about catalyst layer composition(s) with a differential cell experiment. These experiments were performed in order to determine the best representation of cathode catalyst layer losses, at least under fully-humidified conditions. It developed a representation of ORR kinetics (through the exchange current density) with carbon-supported platinum catalyst (Pt/C) technology, which is a common, but not the only, catalyst in use.

The authors explicitly made the assumption that diffusional losses within the PEMFC, and anode kinetic losses, could be neglected. This assumption considers that the gas pressures, temperatures, and composition (mole fractions) at the inlet(s) of the anode and cathode are unchanged throughout the entire differential cell.

5.1.1 Experimental Conditions

Operating conditions are shown in Table 5.1. Humidified hydrogen and oxygen were used as reactant gases. The gases were 100% humidified at T=60°C. Oxygen partial pressures were reported as 101 kPa (Case 1) and 175 kPa (Case 2). Hydrogen and oxygen partial pressures were identical. The saturation pressure of water vapor is 19.767 kPa at 60°C and therefore the total pressures are 120.767 and 194.767 kPa, respectively. Constant gas flow rates of 2000 sccm for both oxygen and hydrogen feeds were used, guaranteeing minimum stoichiometric ratios of 11.4 (anode) and 22.8 (cathode) at the largest current density of 0.5 A/cm^2. The uniformly high humidity and stoichiometric ratio of the gas flows creates spatially-uniform water and current distribution within the plane of the MEA, creating the sought-after differential cell flow condition.

Table 5.1. Operating conditions and parameters from the kinetics validation experiment.

Parameter:		Symbol:			Value:
Operating cell voltage		$V_{cell}^{\mathbb{OP}}$			0.87-0.76 V
Average operating cell current density		$I_{cell}^{\mathbb{OP}}$			0.03, 0.05, 0.1, 0.2, 0.3, 0.5 A cm^{-2}
MEA area (length x width)		A_{MEA}			50 cm^2
Anode:			Cathode:		
Parameter:	Symbol:	Value:	Parameter:	Symbol:	Value:
Operating pressure	$p_A^{\mathbb{OP}}$	case 1: 120.8 kPa case 2: 194.8 kPa	Operating pressure	$p_C^{\mathbb{OP}}$	case 1: 120.8 kPa case 2: 194.8 kPa
Flow inlet area	$A_{A,ch}$	unknown	Flow inlet area	$A_{C,ch}$	unknown
Stoichiometric flow ratio	$\zeta_A^{\mathbb{OP}}$	11.4 (min)	Stoichiometric flow ratio	$\zeta_C^{\mathbb{OP}}$	22.8 (min)
Relative humidity	$\mathbb{RH}_A^{\mathbb{OP}}$	100 %	Relative Humidity	$\mathbb{RH}_C^{\mathbb{OP}}$	100 %
Inlet temperature	$T_A^{\mathbb{OP}}$	333.15 K	Inlet temperature	$T_C^{\mathbb{OP}}$	333.15 K
Cell temperature	$T_A^{\mathbb{OP}}$	333.15 K	Cell temperature	$T_C^{\mathbb{OP}}$	333.15 K

The mol fractions of hydrogen/oxygen, water vapor, and inert nitrogen are calculated from their respective partial pressures, as part of an ideal gas mixture. The relevant gas pressures and mole fractions settings are shown below in Table 5.2.

Table 5.2. Gas input compositions of anode and cathode.

Case 1: 60°C temperature 101 kPa reactant partial pressures 100% RH	Anode V_A =0	p_{H_2} =101 kPa	p_{H_2O} =19.77 kPa	p_{N_2} =0 kPa	p_A =120.77 kPa
		$x_{H_2,A}$ =0.8363	$x_{H_2O,A}$ =0.1637	$x_{N_2,A}$ =0.0	
	Cathode V_C =0.76-0.88	p_{O_2} =101 kPa	p_{H_2O} =19.77 kPa	p_{N_2} =0 kPa	p_C =120.77 kPa
		$x_{O_2,C}$ =0.8363	$x_{H_2O,C}$ =0.1637	$x_{N_2,C}$ =0.0	
Case 2: 60°C temperature 175 kPa reactant partial pressures 100% RH	Anode V_A =0	p_{H_2} =175 kPa	p_{H_2O} =19.77 kPa	p_{N_2} =0 kPa	p_A =194.77 kPa
		$x_{H_2,A}$ =0.8985	$x_{H_2O,A}$ =0.1015	$x_{N_2,A}$ =0.0	
	Cathode V_C =0.79-0.9	p_{O_2} =175 kPa	p_{H_2O} =19.77 kPa	p_{N_2} =0 kPa	p_C =194.77 kPa
		$x_{O_2,C}$ =0.8985	$x_{H_2O,C}$ =0.1015	$x_{N_2,C}$ =0.0	

The differential cell was formed by two graphite serpentine flow fields compressing the respective anode and cathode diffusion media (DM) and MEA between them. A Teflon gasket was utilized to seal the perimeter. The diffusion media were carbon fiber paper substrates (Toray, Inc.) subsequently hydrophobized with polytetrafluoroethylene (PTFE) and given an un-described surface treatment. Their thickness and composition isn't further described because that work assumes the absence of oxygen diffusion losses in these DM.

Table 5.3. MEA compositions compiled from the prior work.

Membrane	Ionomer equivalent weight	EW	800	g / equiv or g / mol SO_3^-
	Thickness (dry)	t_{MEM}	22×10^{-6}	m
	Crossover current density	I_x	5	A / m^2
Anode Catalyst Layer	Platinum loading	$L_{ACL,Pt}$	0.2	mg_{Pt} / cm^2
	Pt/C mass ratio	Ptc_{ACL}	47	%
	Ionomer to carbon ratio	IC_{ACL}	1	-
	Thickness (dry)	t_{ACL}	6×10^{-6}	m
	Available catalyst area	$A_{ACL,Pt}^{100\%RH}$	53	m^2_{Pt} / g_{Pt}
	Specific exchange current density	$i_{0,ACL}^{*}$	0.24	A / cm^2_{Pt}
Cathode Catalyst Layer	Platinum loading	$L_{CCL,Pt}$	0.2	mg_{Pt} / cm^2
	Pt/C mass ratio	Ptc_{CCL}	47	%
	Ionomer to carbon ratio	IC_{CCL}	1	-
	Thickness (dry)	t_{CCL}	6×10^{-6}	m
	Available catalyst area	$A_{CCL,Pt}^{100\%RH}$	53	m^2 / g_{Pt}
	Pt-Specific exchange current density, reference value	$i_{0,CCL}^{*}$	2×10^{-8}	A / cm^2_{Pt}
Electronic Resistance	Cell electronic resistance	$R_{cnt}^{e^-}$	0.034	Ω cm^2

Table 5.3 shows the MEA composition. The membrane has 800 equivalent weight (EW) Nafion ionomer, with a nominal thickness of 25 μm (which is quoted at 50% RH). A dry thickness of 22 μm is used as that corresponds to a swollen membrane thickness of 25 μm at 50% RH. The rate of hydrogen permeation gas crossover to the cathode was measured and used for calculations, though the crossover

values were not individually disclosed. Experiments at high temperature and pressure reportedly produce greater levels of crossover, which can be converted to an equivalent crossover current density. A crossover current density of 0.5 mA/cm^2 was assumed here.

The anode catalyst layer (ACL) has platinum loading of 0.2 $mgPt/cm^2$. It was made from carbon-supported PT catalyst with 47% Pt/C mass ratio. The ionomer-to-carbon ratio was set as 1.0 in the model, which yielded nearly the ionomer volume fraction of 0.2 which was claimed by the original work. The cathode catalyst layer (CCL) has the same composition.

An estimate of the purely electronic resistances within the differential PEMFC was created experimentally. A dummy cell was created from the differential PEMFC when the MEA was removed and the device reassembled. Electrical resistance measurements of the dummy cell were used to estimate the PEMFC electrical resistances. These consist of various contact resistances between components, as well as bulk electronic conduction losses. The contact resistances between the diffusion media (GDL) and flow fields (FF) were said to be an order of magnitude larger than MEA-GDL and DM-DM contact resistances. Hence, a single electrical resistance value from the dummy cell is supplied; it is thought a reasonably accurate estimate of the electronic resistance of the PEMFC during all states of operation. The electronic conduction losses are considered constant, independent of temperature and humidity effects. The supplied electronic resistance value (0.030 $\Omega\ cm^2$) was adjusted upward, slightly, to (0.034 $\Omega\ cm^2$) compensate for the contact resistances between the GDL and MEA, which was not measured in the dummy cell's resistance measurement.

To compare the differential cell data with the predictions of these interface models, a key adjustment needs to be made. The electronic resistance term $R_{cnt}^{e^-}$, that would ordinarily apply only to the conduction losses within the MEA and contact resistances between the GDL and MEA, now incorporates all of the electrical resistances of the differential cell. That is, the electronic resistance term for the MEA is now, for the purposes of this comparison, incorporating electrical resistances from other components of the PEMFC, allowing a comparison.

5.1.2 Comparison of Results

The published experimental and kinetic voltage values were re-created with the aid of a plot digitizer software package and compared against output from the different interface models. Plots of kinetic voltage data are used to assess cathode kinetics. An explanation of how these values were derived for the interface model calculations and experiment, follows.

The polarization curve of the interface model is shown in eq. (5.1). It consists of an ideal cell potential V_{OC}, thermodynamically determined, minus the various losses. The term V_{cell} is the measured cell voltage (between anode and cathode terminals), V_{OC} is the ideal cell potential determined from thermodynamic arguments, I is the current density, η_C is the cathode kinetic over-potential, $R_{cnt}^{e^-}$ the electronic contact resistances and bulk conduction resistances, $R_{MEM}^{H^+}$ the hydration-dependent membrane ionic conduction resistance, and $R_{ACL}^{H^+,\text{eff}}$ and $R_{CCL}^{H^+,\text{eff}}$ the hydration-dependent effective conduction resistances within the respective catalyst layers.

$$V_{cell} = V_{OC} - \eta_C - IR_{cnt}^{e^-} - IR_{MEM}^{H^+} - R_{ACL}^{H^+,\text{eff}} - R_{CCL}^{H^+,\text{eff}} \tag{5.1}$$

The interface models calculate kinetic voltage as the ideal cell potential minus anode and cathode losses according to eq. (5.2). Anode losses were insignificant compared to those of the cathode and diffusional losses were not predicted to be very significant.

$$V_k = V_{OC} - IR_{ACL}^{H^+,\text{eff}} - \eta_C \tag{5.2}$$

Experimental values were arrived at as follows. Measurements were reported for the cell voltage $V_{cell} = V_C - V_A$, current density I, crossover current density I_x, high-frequency resistance R_Ω (HFR), and electronic resistance $R_{cnt}^{e^-}$ measured from an empty "dummy cell". To compensate for the cell's ohmic losses, they calculated the iR-free voltage or kinetic voltage from the measurements. The kinetic voltage in eq. (5.2) was found experimentally by adding the measured cell voltage to an ohmic correction IR_{Ohm}

(accounting for protonic conduction losses in the membrane and cathode catalyst layers and also electronic resistances) as in eq. (5.3).

$$V_k = V_{OC} - IR_{ACL}^{H^+,\text{eff}} - \eta_C \tag{5.3}$$

The ohmic correction R_{Ohm} was the sum of the high-frequency resistance R_Ω (HFR) and an experimental *estimate* of the effective cathode catalyst layer resistance $R_{CCL}^{H^+,\text{eff}}$ as in eq.(5.4).

$$R_{Ohm} = R_\Omega + R_{CCL}^{H^+,\text{eff}} = R_{cnt}^{e^-} + R_m^{H^+} + R_{CCL}^{H^+,\text{eff}} \tag{5.4}$$

The original work assumed that the average membrane conductivity measured by the high-frequency resistance measurement could be used to describe the average conductivity of the ionomer phase of the cathode catalyst layer. With knowledge of the thickness of each region (t_{MEM} and t_{CCL}) and the ionomer volume fraction of the CCL, $\varepsilon_{CCL,Io}$, the effective cathode catalyst layer resistance is eq., (5.5) where it is assumed that the tortuosity of the ionomer conduction network in the CCL electrode is unity. The factor of 1/3 arises because under conditions of full catalyst utilization, the effective CCL resistance is 1/3 the electrode sheet resistance.

$$R_{CCL}^{H^+,\text{eff}} = \left(\frac{1}{3}\right)\frac{R_\Omega - R_{cnt}^{e^-}}{\varepsilon_{CCL,Io}}\frac{t_{CCL}}{t_{MEM}} \tag{5.5}$$

With these substitutions, the experimental equation for kinetic voltage V_k becomes eq. (5.6).

$$V_k = V_{Cell} + I\left[R_\Omega + \frac{1}{3}\frac{R_\Omega - R_{cnt}^{e^-}}{\varepsilon_{CCL,Io}}\frac{t_{CCL}}{t_{MEM}}\right] \tag{5.6}$$

Figure 5.1 shows the results modeled kinetic voltage values and ohmic-resistance-corrected measured voltage values from the experiment. Neglecting anode losses ($IR_{ACL}^{H^+,\text{eff}}$), and diffusional losses, the kinetic voltage can be expressed with a single Tafel slope representing the cathode kinetic losses (η_C) as eq. (5.7), where υ_C, the cathodic transfer coefficient, was found to be unity[19], [19], giving a Tafel slope of ~70 mV/decade at 80 °C.

$$V_k = V_{OC} - 2.303\frac{RT_C}{\upsilon_c F}\log_{10}\left[\frac{I + I_x}{I_{0,C}}\right] \tag{5.7}$$

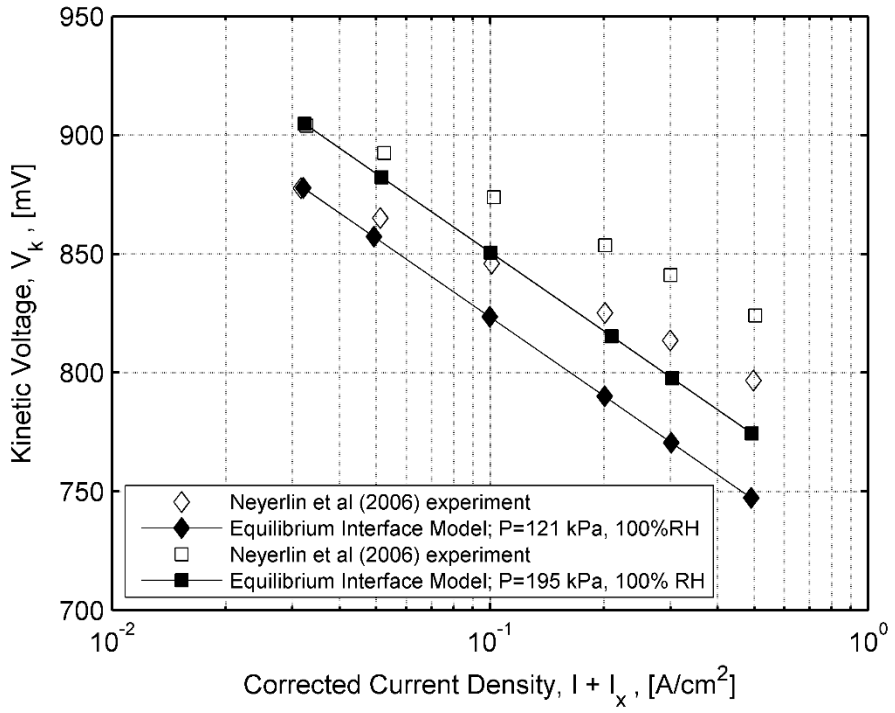

Figure 5.1. Measured and modeled kinetic (iR-free) cell voltage from the equilibrium interface model with un-modified Tafel slope

The Equilibrium interface approach used $\upsilon_c = 0.6$, giving a Tafel slope of 117 mV/decade at the same temperature[116]. The difference in Tafel slope produces the chief distinction apparent in the results. The different Tafel slopes of these interface models serve to distinguish the kinetic voltage results of each in the next section.

The equilibrium interface model yields poor agreement with experiment when examining the kinetic voltage data. The catalyst layer activity, or exchange current density $I_{0,C}$ was chosen to match the first data point; the published work doesn't describe how the exchange current densities were arrived at. The disagreement between model and experiment is obviously due to the model of cathode kinetics using

an incorrectly high Tafel slope. The Tafel slope can be adjusted by choosing various values of the (previously-described) cathodic charge transfer coefficient υ_c : it was 0.5 in 2009[43] and 0.6 in 2007[112].

When the kinetics model is altered so υ_c =1, Figure 5.2 shows the equilibrium interface model can show good agreement with the experimental kinetic voltage results if a suitable choice(s) of exchange current density $I_{0,C}$ is made for each of the two cases. Variations due to changes in catalyst loading or MEA water content were never described in this group's modeling work. No clear explanation has been found about how this parameter might be determined, other than to produce agreement with experimental data.

The results of the non-equilibrium interface model are shown in Table 5.4. Each polarization curve has 6 points, where current density was varied from 0.030 to 0.500 (A/cm^2). The individual voltage, current, water content, and water gain rate values produces by the non-equilibrium model are shown. The interface model iteratively adjusts MEA water content, W , by a simple implementation of Euler's method, such that the water gain rate in the MEA, $\partial W/\partial t$, approaches zero, with a maximum value (tolerance) of 5 x 10^{-5} mol s^{-1} m^{-2} , indicating the water content has reached equilibrium. W decreases somewhat with current density from anode dryout, where anode-side water contents within the MEA are reduced by the action of electro-osmotic drag within the membrane.

Table 5.4. Calculated cell voltage, current, and water content of the non-equilibrium interface model.

		V_{Cell} (V)	I (A/cm^2)	W (mol/m^2)	$\partial W/\partial t$ (mol/s/m^2)
Case 1: 60°C temperature 101 kPa reactant partial pressures 100% RH	1	0.877	0.032	0.9228	5 x 10^{-5}
	2	0.861	0.052	0.9222	-3.3x 10^{-5}
	3	0.838	0.103	0.9201	-3.8x 10^{-5}
	4	0.810	0.212	0.9149	-4.1x 10^{-5}
	5	0.791	0.317	0.9092	-3.2x 10^{-5}
	6	0.761	0.531	0.8965	-1.5x 10^{-5}
Case 2: 60°C temperature	1	0.899	0.033	0.9229	3.1 x 10^{-5}
	2	0.884	0.053	0.9223	-2.0 x 10^{-5}

175 kPa reactant partial pressures 100% RH	3	0.862	0.102	0.9206	-3.5×10^{-5}
	4	0.835	0.203	0.9160	-4.2×10^{-5}
	5	0.816	0.307	0.9107	-3.5×10^{-5}
	6	0.785	0.528	0.8982	-1.7×10^{-5}

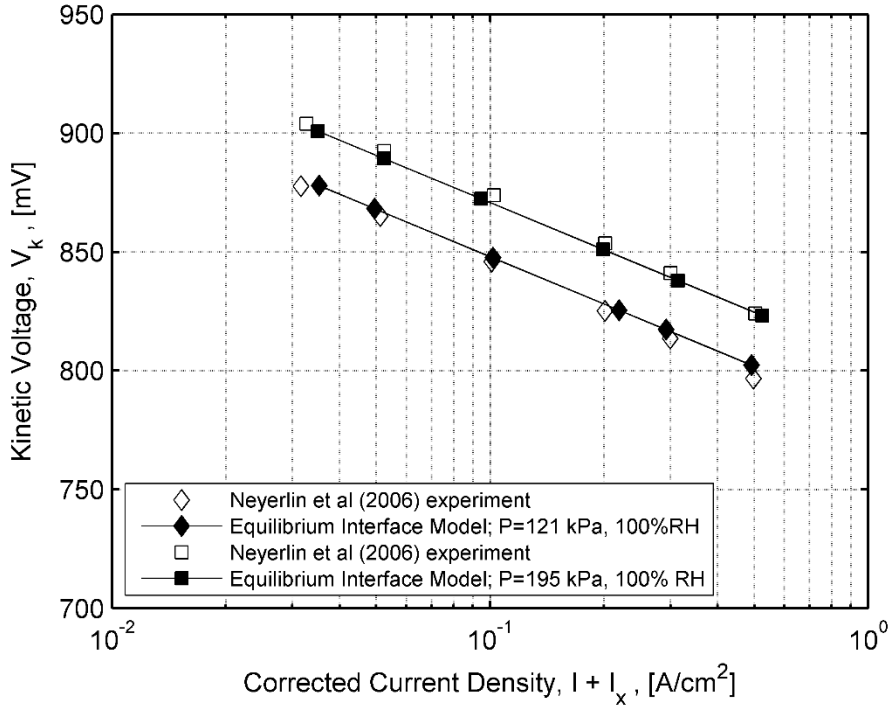

Figure 5.2. Measured and modeled kinetic (iR-free) cell voltage from equilibrium interface model with modified Tafel slope

The agreement seen in Figure 5.3 between the newly-developed non-equilibrium interface model, and experiment, was produced with a single correct set of kinetic values ($A_{CCL,Pt}^{100\%RH}$ and $i_{0,CCL}^{*}$), which don't need to be chosen on an ad-hoc basis, but can be determined from fundamental experiments of catalyst layer structure. These are the two key values used to determine the cathode's superficial exchange current density $I_{0,C}$. The term $i_{0,CCL}^{*}$ (A /cm^2$_{Pt}$), the catalyst-specific exchange current density property for the ORR on the carbon-supported platinum catalyst, at reference partial pressure of 101.3 kPa and 80°C, was taken as 2.0×10^{-8} here, as the value that was determined experimentally. The term $A_{CCL,Pt}^{100\%RH}$ (m^2$_{Pt}$

/g_{Pt}), the cathode catalyst layer's electrochemically available catalyst area, was taken as 53 in this work, as it was measured in the original experiment. Agreement can be judged not only by the agreement seen in the figure, but by the reasonableness of the kinetic parameters needed to get that agreement.

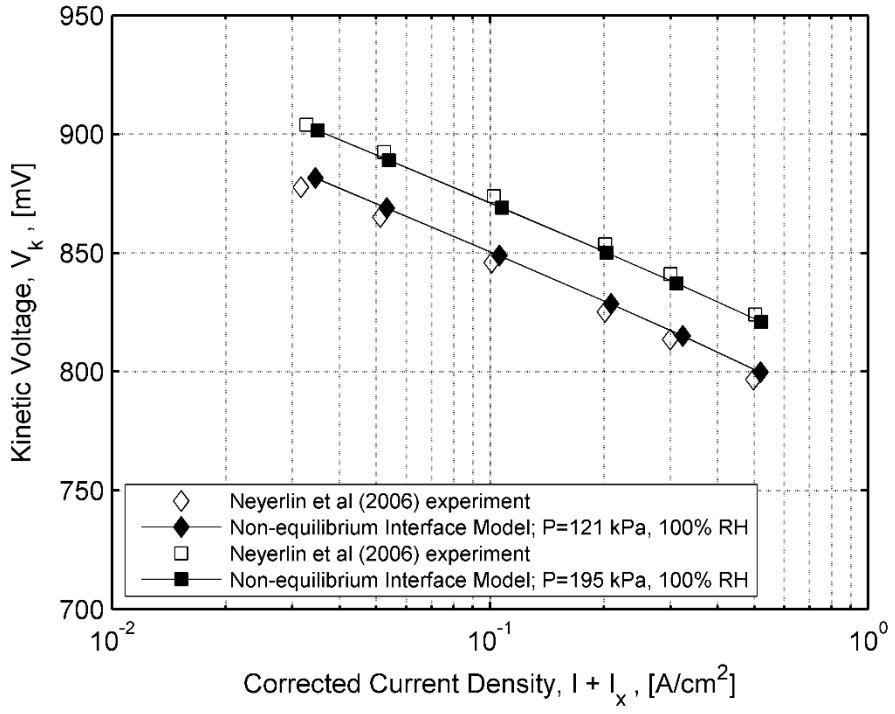

Figure 5.3. Measured and modeled kinetic (iR-free) cell voltage from the non-equilibrium interface model

5.1.3 Concluding Remarks

This validation exercise was done in order to show the open-circuit or 'ideal' voltage, and estimates of cathode kinetic voltage losses. At a very minimum, this involves reproducing the equations for the thermodynamically-determined open-circuit voltage, and kinetic losses of the ORR, occurring in the PEMFC cathode. This is practically trivial; however, the exercise shows that certain other influences were not being erroneously overestimated by the interface model. Diffusional effects, conduction limitations within the catalyst layers, and temperature rise (from heat generation within the MEA), did not visibly impact these iR-free voltage model results.

The precision to be expected when employing these fit relationships can be approximately ascertained. The results, as originally-published, clearly depict ~5 mV discrepancies between measured values and fit estimates of the kinetic, or iR-free, voltage. Slight adjustments (~ 5% or less) to model parameters such as $A_{CCL,Pt}^{100\%RH}$ or $i_{0,ccl}^{*}$ can bring both series of kinetic voltage calculations into precise agreement with experiment (though it is not shown here). It is not known whether this 5-10 mV discrepancy should be considered an issue of slight catalyst layer degradation (with time), a test irreproducibility, or modeling inaccuracy due to the many simplifying assumptions employed in the work.

5.2 Validation of Water Transport and Ohmic Resistance Relationships

The second validation step compares model predictions to experimental data from a differential cell from Neyerlin et al.[20] that was published in 2007. The collection of experiments was performed in order to examine kinetic and conduction losses within the cathode catalyst layer under operating conditions where full 100% catalyst utilization does not occur. A set of measurements from a differential cell were made. The various sources of voltage loss could be concurrently assessed (with catalyst layers of well-defined composition).

The prior verification exercise[19] developed a representation of ORR kinetics for a carbon-supported platinum catalyst (Pt/C). The method of accounting for proton conduction losses within the cathode catalyst layer was limited, in its validity, to cases where there is a small decrease in ionic phase potential across the cathode catalyst layer (CCL). So, full 100% catalyst utilization could be assumed. In a PEMFC, this requires relatively thin, highly-conductive CCL construction, low current densities, and the use of highly-humidified reactant gases to achieve. Conduction losses within the CCL can become more significant with thicker CCL construction, high current density, or low humidity (RH). The second verification exercise examines CCL conduction losses under conditions where full catalyst utilization does not occur. Anode catalyst layer (ACL) losses were also assessed.

For the purposes of developing a useful interface model, a means of estimating the effective protonic conduction resistance within the ACL and CCL under a broader range of operating conditions is needed. This validation step provides a means of checking the model's estimates against relevant experimental data.

The authors explicitly made the assumption that diffusional losses within the differential PEMFC could be neglected, an assumption which sets the gas pressures, temperatures, and mole fractions from the inlet(s) of the anode and cathode as the same as those adjacent to the MEA. Diffusional losses within the catalyst layers are similarly not considered by the experiment. Temperature rise was not considered. Temperature rise and diffusional losses are estimated, however, by the interface model.

The same 3 prior interface models will be evaluated. The benchmark equilibrium interface model of Shimpalee and co-workers is presented. A second model alters the representations of ideal voltage and kinetic losses of that interface, however, to incorporate the forms used here. These are compared against the proposed Non-Equilibrium interface model at the relevant experimental conditions. As heat transfer and diffusional losses aren't considered in the original work, there isn't information available about the experiment to assess these effects. Gas composition data (pressure, temperature, and mole fraction values) from the anode and cathode inlet(s) are again assumed to be those which occur at the outer boundaries of the MEA.

Differences in interface model predictions arise primarily in the handling of water transport and kinetic modeling issues. The models must correctly simulate water transport within the MEA in order to estimate the hydration-dependent (i) membrane and (ii) effective catalyst layer resistances.

The experiment includes voltage and high-frequency resistance (HFR) data as a function of current density. The measured values of HFR, which is hydration-dependent, vary with operating conditions and current density; these have commonly been used to infer changing hydration levels within the MEA. The interface models produce estimates of the various voltage components of the device, which can be compared against the experimental data.

5.2.1 Experimental Conditions

Operating conditions are shown in Table 5.5. Humidified hydrogen and oxygen were used as reactant gases. The gases were 100% humidified and 60% humidified at T=80°C. Hydrogen and oxygen partial pressures were reported as 101 kPa, and hydrogen and oxygen partial pressures were identical. The saturation pressure of water vapor is 47.79 kPa at 80°C, and therefore the total pressures are 149 / 130 kPa for the cases of 100% / 60% RH. Constant gas flow rates of 1050 sccm for hydrogen and 600 sccm for oxygen feeds were used, guaranteeing minimum stoichiometric ratios of 20 (anode) and 23 (cathode) at the largest current density of 1.5 A/cm^2. The uniformly high stoichiometric ratio of the gas flows should create spatially-uniform water and current distribution within the plane of the MEA, creating

the sought-after differential cell flow condition. The pressure drop from inlet to outlet was reported as only 3 kPa or less; it isn't considered further.

The mol fractions of hydrogen/oxygen, water vapor, and inert nitrogen are calculated from their respective partial pressures. The relevant gas pressures and mole fractions settings are shown below in Table 5.6.

The differential PEMFC, with active area of 5 cm^2, was formed by two graphite interdigitated flow fields compressing the respective anode and cathode diffusion media (DM) and MEA between them. A teflon gasket was utilized to seal the perimeter. The diffusion media were carbon fiber paper substrates (Toray, Inc.) subsequently hydrophobized with polytetrafluoroethylene (PTFE) and given an un-described surface treatment. Their thickness and composition isn't further described because that work assumes the absence of oxygen diffusion losses in these DM.

Table 5.5. Operating conditions and parameters from the water transport validation experiment.

Parameter:		Symbol:			Value:
Operating cell voltage		$V_{cell}^{\mathbb{OP}}$			0.87-0.76 V
Average operating cell current density		$I_{cell}^{\mathbb{OP}}$			0.030, 0.044, 0.063, 0.1, 0.2, 0.3, 0.5, 0.75, 1.0, 1.25, 1.5 A cm^{-2}
MEA area (length x width)		A_{MEA}			5 cm^2
Anode:			Cathode:		
Parameter:	Symbol:	Value:	Parameter:	Symbol:	Value:
Operating pressure	$p_A^{\mathbb{OP}}$	case 1: 149.09 kPa case 2: 129.95 kPa	Operating pressure	$p_C^{\mathbb{OP}}$	case 1: 149.09 kPa case 2: 129.95 kPa
Flow inlet area	$A_{A,ch}$	unknown	Flow inlet area	$A_{C,ch}$	unknown
Stoichiometric flow ratio	$\zeta_A^{\mathbb{OP}}$	20.0 (min)	Stoichiometric flow ratio	$\zeta_C^{\mathbb{OP}}$	23.0 (min)
Relative humidity	$\mathbb{RH}_A^{\mathbb{OP}}$	case 1: 100 % case 2: 60 %	Relative Humidity	$\mathbb{RH}_C^{\mathbb{OP}}$	case 1: 100 % case 2: 60 %
Inlet temperature	$T_A^{\mathbb{OP}}$	353.15 K	Inlet temperature	$T_C^{\mathbb{OP}}$	353.15 K
Cell temperature	$T_A^{\mathbb{OP}}$	353.15 K	Cell temperature	$T_C^{\mathbb{OP}}$	353.15 K

Table 5.7 shows the MEA composition. The membrane has 1100 equivalent weight (EW) Nafion ionomer with a nominal thickness of 25 μm which is quoted at 50% RH. For modeling purposes, a dry

thickness of 22 μm is used as that corresponds to a swollen membrane thickness of 25 μm at 50% RH. A crossover current density of 1 mA/cm^2 was assumed here.

The anode catalyst layer (ACL) has platinum loading of 0.35 mg^{Pt}/cm^2 and a thickness of 12 μm. It was made from carbon-supported PT catalyst with 50% Pt/C mass ratio. The ionomer-to-carbon ratio was 1.0, which yielded nearly the given ionomer volume fraction of 0.2. The cathode catalyst layer (CCL) has platinum loading of 0.50 mg$_{Pt}$/cm^2 and a thickness of 18 μm.

Table 5.6. Gas input compositions of anode and cathode from the water transport validation experiment.

Case 1: 80°C temperature 101 kPa reactant partial pressures 100% RH	Anode V_A =0	p_{H_2} =101 kPa	p_{H_2O} =47.79 kPa	p_{N_2} =0 kPa	p_A =149.09 kPa
		$x_{H_2,A}$ =0.679	$x_{H_2O,A}$ =0.320	$x_{N_2,A}$ =0.0	
	Cathode V_C =0.66-0.90	p_{O_2} =101 kPa	p_{H_2O} =47.79 kPa	p_{N_2} =0 kPa	p_C =149.09 kPa
		$x_{O_2,C}$ =0.679	$x_{H_2O,C}$ =0.320	$x_{N_2,C}$ =0.0	
Case 2: 80°C temperature 101 kPa reactant partial pressures 60% RH	Anode V_A =0	p_{H_2} =101 kPa	p_{H_2O} =28.65 kPa	p_{N_2} =0 kPa	p_A =129.95 kPa
		$x_{H_2,A}$ =0.779	$x_{H_2O,A}$ =0.220	$x_{N_2,A}$ =0.0	
	Cathode V_C =0.55-0.89	p_{O_2} =101 kPa	p_{H_2O} =28.65 kPa	p_{N_2} =0 kPa	p_C =129.95 kPa
		$x_{O_2,C}$ =0.779	$x_{H_2O,C}$ =0.220	$x_{N_2,C}$ =0.0	

An estimate of the purely electronic resistances within the differential PEMFC was created experimentally. A dummy cell was created from the differential PEMFC when the MEA was removed and the device reassembled. Electrical resistance measurements of the dummy cell were used to estimate the PEMFC electrical resistances. These consist of various contact resistances between components, as well as bulk electronic conduction losses. The contact resistances between the diffusion media (DM) and flow fields (FF) were said to be an order of magnitude larger than MEA-DM and DM-DM contact resistances. Hence, a single electrical resistance value from the dummy cell is supplied; it is thought a reasonably accurate estimate of the electronic resistance of the PEMFC during all states of operation. The electronic conduction losses are considered constant, independent of temperature and humidity effects. The supplied resistance value (0.030 Ω cm^2) was adjusted upward, slightly, to (0.035 Ω cm^2) compensate

for the contact resistances between the GDL and MEA (missing from the dummy cell's resistance measurement).

Table 5.7. MEA compositions compiled from the water transport validation experiment.

Membrane	Ionomer equivalent weight	EW	1100	g / equiv or g / mol SO3-
	Thickness (dry)	t_{MEM}	$22x10^{-6}$	m
	Crossover current density	I_x	10	A/m^2
Anode Catalyst Layer	Platinum loading	$L_{ACL,Pt}$	0.35	$mgPt / cm^2$
	Pt/C mass ratio	Ptc_{ACL}	50	%
	Ionomer to carbon ratio	IC_{ACL}	1.4	-
	Thickness (dry)	t_{ACL}	$12x10^{-6}$	m
	Available catalyst area	$A_{ACL,Pt}^{100\%RH}$	50	m^2Pt / gPt
	Specific exchange current density	$i_{0,ACL}^{*}$	0.24	A/cm^2Pt
Cathode Catalyst Layer	Platinum loading	$L_{CCL,Pt}$	0.5	$mgPt / cm^2$
	Pt/C mass ratio	Ptc_{CCL}	50	%
	Ionomer to carbon ratio	IC_{CCL}	1.4	-
	Thickness (dry)	t_{CCL}	$18x10^{-6}$	m
	Available catalyst area	$A_{CCL,Pt}^{100\%RH}$	50	m^2Pt / gPt
	Specific exchange current density	$i_{0,CCL}^{*}$	$2x10^{-8}$	A/cm^2Pt
Electronic Resistance	Cell electronic resistance	$R_{cnt}^{e^-}$	0.034	$\Omega\ cm^2$

To compare the differential cell data with the predictions of these interface models, a key adjustment needs to be made. The electronic resistance term $R_{cnt}^{e^-}$, that would ordinarily apply only to the conduction losses within the MEA and contact resistances between the GDL and MEA, now has to incorporate all of the electrical resistances of the differential cell. That is, the electronic resistance term for the MEA is now, for the purposes of this comparison, incorporating electrical resistances from other components of the PEMFC, allowing a comparison.

5.2.2 Comparison of Results

The results produced by the different interface models are compared against the published experimental data. The equilibrium interface model of Shimpalee and co-workers with original kinetics, with modified kinetics, and the developed non-equilibrium interface model can produce estimates of HFR and the various voltage components.

The experimental work reported, for the conditions given, the cell voltage $V_C - V_A$, current density I, exchange current density I_x, high-frequency resistance (HFR) R_Ω, and electronic resistance $R_{cnt}^{e^-}$ measured from an empty "dummy cell". Diffusional resistances anywhere in the cell, whether the GDL or the cathode catalyst layer, were neglected in the work.

The HFR-corrected voltage is the sum of the measured cell voltage and measured cell ohmic losses (from HFR) as in eq. (5.8). The kinetic voltage was found experimentally by adding the HFR-corrected voltage to ohmic corrections accounting for protonic conduction losses in the anode and cathode catalyst layers, in eq. (5.9), where $R_{ACL}^{H^+,\text{eff}}$ and $R_{CCL}^{H^+,\text{eff}}$ are the effective anode and cathode catalyst layer resistances, respectively.

$$V_{HFR-corrected} = V_{cell} + IR_\Omega \tag{5.8}$$

$$V_k = V_{cell} + IR_{Ohm} = V_{cell} + IR_\Omega + IR_{ACL}^{H^+,\text{eff}} + IR_{CCL}^{H^+,\text{eff}} \tag{5.9}$$

The anode effective resistance $R_{ACL}^{H^+,\text{eff}}$ was estimated from separate hydrogen pump experiments. To determine $R_{CCL}^{H^+,\text{eff}}$, they assumed that the average membrane conductivity, measured by the high-frequency resistance measurement, could also be used to describe the average conductivity of the ionomer phase of the cathode catalyst layer. With knowledge of the thickness of each region (t_{CCL} and t_{MEM}), and the ionomer volume fraction of the CCL, $\varepsilon_{CCL,Io}$, the effective cathode catalyst layer resistance is eq. (5.10), where it was assumed in the previous work that the tortuosity of the ionomer conduction network in the CCL electrode is unity. The kinetic voltage becomes eq. (5.11).

$$R_{CCL}^{H^+,\text{eff}} = \left(\frac{1}{3}\right)\frac{R_\Omega - R_{cnt}^{e^-}}{\chi_{CCL}(\theta_{CCL})\varepsilon_{CCL,lo}}\frac{t_{CCL}}{t_{MEM}} \tag{5.10}$$

$$V_k = V_{cell} + I\left[R_\Omega + IR_{ACL}^{H^+,\text{eff}} + \frac{1}{3}\frac{R_\Omega - R_{cnt}^{e^-}}{\varepsilon_{CCL,lo}}\frac{t_{CCL}}{t_{MEM}}\right] \tag{5.11}$$

The interface model makes predictions of current density, ohmic resistances within the MEA, diffusional losses, kinetic losses, and all three voltages. A direct comparison with the measured cell HFR is also sought. The solution of the MEA water content profile allows estimate of the hydration-dependent membrane ionic resistance $R_{MEM}^{H^+}$. The constant electronic resistance $R_{cnt}^{e^-}$ is approximately known from a dummy-cell measurement, and is an input to the interface model. Cell HFR is calculated for comparison to experimental measurement as eq. (5.12)

$$R_\Omega = R_{cnt}^{e^-} + R_{MEM}^{H^+} \tag{5.12}$$

The kinetic voltage is determined with account taken of diffusional losses. It is found as the thermodynamically-estimated reversible voltage minus anode and cathode kinetic losses. It can be determined with either of two equivalent forms as in eq(5.13). In every case, the combined anode overpotential was small in comparison to that of the cathode.

$$V_k = V_{OC} - \eta_C = V_{cell} + IR_{cnt}^{e^-} + IR_{MEM}^{H^+} + IR_{ACL}^{H^+,\text{eff}} + IR_{CCL}^{H^+,\text{eff}} \tag{5.13}$$

The HFR-corrected voltage is calculated by the model when the iterative scheme converges. It can be determined with either of two equivalent forms as in eq. (5.14). It is apparent that differences between the kinetic voltage V_k, and HFR-corrected voltage, $V_{HFR-corrected}$, are due to the sum of the anode and cathode catalyst layer effective resistances; the difference is used to assess correctness of their prediction.

$$V_{HFR-corrected} = V_{OC} - \eta_A - \eta_C - IR_{ACL}^{H^+,\text{eff}} - IR_{CCL}^{H^+,\text{eff}} = V_{cell} + IR_{cnt}^{e^-} + IR_{MEM}^{H^+} \tag{5.14}$$

Cell voltage isn't calculated but taken from the model inputs V_c and V_A. The model validation occurs in the prediction of correct current density in eq. (5.15).

$$V_{cell} = V_C - V_A = V_{OC} - \eta_C - IR_{ACL}^{H^+,\text{eff}} - IR_{CCL}^{H^+,\text{eff}} - IR_{cnt}^{e^-} - IR_{MEM}^{H^+} \quad (5.15)$$

Experimental values were re-created with a plot digitizer software package. Polarization curves were measured at 11 points with current densities of 0.03, 0.045, 0.065, 0.1, 0.2, 0.3, 0.5, 0.75, 1.0, 1.25, 1.5 A/cm^2. Measurements of HFR were performed after each point as well. A separate test estimated the hydration-dependent voltage losses of the anode. Hydrogen pump measurements, performed under identical pressure and humidity operating conditions, provided an estimate of the voltage loss associated with the combined kinetic and conduction losses within the anode of the PEMFC. The voltage losses appeared as almost constant resistances, with the low humidity case presenting, as expected, a greater effective resistance.

The results of the non-equilibrium interface model are shown in Table 5.8. The polarization curves matched the experimental current density values. The individual voltage, current density, water content, and water gain rate values produced by the non-equilibrium interface model are shown. The water gain rate in the MEA, $\partial W / \partial t$, is nearly zero (< 5 x 10^{-5}, or several orders of magnitude lower than the water content), indicating the water content has reached equilibrium. For the 100% RH case, W decreases with current density from anode dryout. In low humidity operation, the model predicts the opposite is predicted to occur.

Table 5.8. Calculated cell voltage, current, and water content of the non-equilibrium interface model.

		V_{cell} (V)	I (A/cm^2)	W (mol/m^2)	$\partial W/\partial t$ (mol s^{-1} m^{-2})
Case 1: 80°C temperature 101 kPa reactant partial pressures 100% RH	1	0.912	0.032	0.8158	0.3 x 10-5
	2	0.900	0.046	0.8147	0.4 x 10-5
	3	0.888	0.065	0.8143	-2.8 x 10-5
	4	0.868	0.111	0.8131	-2.2 x 10-5
	5	0.836	0.222	0.8095	-1.8 x 10-5
	6	0.816	0.324	0.8060	2.0 x 10-5
	7	0.782	0.534	0.7978	-4.1 x 10-5
	8	0.750	0.769	0.7878	4.5 x 10-5
	9	0.722	0.997	0.7775	2.2 x 10-5
	10	0.689	1.280	0.7638	-2.2 x 10-5
	11	0.663	1.517	0.7522	4.8 x 10-5
Case 2: 80°C temperature 101 kPa reactant partial pressures 60% RH	1	0.894	0.027	0.2803	3.9 x 10-5
	2	0.876	0.043	0.2810	4.8 x 10-5
	3	0.860	0.063	0.2818	2.2 x 10-5
	4	0.840	0.097	0.2830	2.9 x 10-5
	5	0.805	0.177	0.2861	4.7 x 10-5
	6	0.772	0.279	0.2898	2.4 x 10-5
	7	0.724	0.469	0.2964	3.7 x 10-5
	8	0.671	0.738	0.3048	-2.4 x 10-5
	9	0.633	0.951	0.3111	-4.7 x 10-5
	10	0.587	1.239	0.3183	3.4 x 10-5
	11	0.545	1.508	0.3228	2.8 x 10-5

HFR measurements are the sum of a constant electronic resistance and the hydration-dependent ionic resistance of the membrane. If the former is known, HFR measurements can be used to infer membrane ionic conductivity and the averaged water content values upon which it depends. HFR results provide an indirect evaluation of the water transport schemes of each interface model.

HFR measurements are compared against the equilibrium interface model Figure 5.4. Experimental results at 60% RH show greater variation with current density than those at 100% RH. Though resistance readings below 0.1 A/cm^2 might be unreliable, HFR measurements at 60% RH show a drop with increasing current density. This equilibrium interface model will necessarily predict a constant resistance level for the differential cell configuration evaluated here; the predictions of R_Ω are flat and

don't reflect dropping resistance levels with increasing current density. The experimental results at 100% RH vary less with current density, where resistance is observed increasing at 1-1.5 A/cm^2. The model once again predicts constant resistance and does not capture the rise in HFR at increased current density. Resistance values are unchanged by the choice of kinetics employed, so the figure applies to both of the equilibrium interface models.

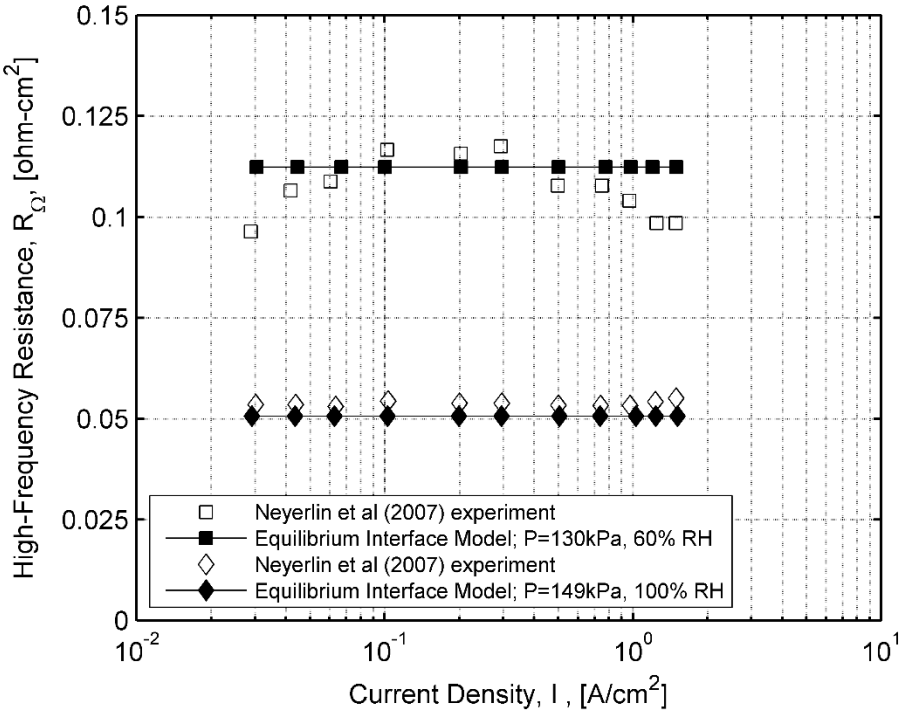

Figure 5.4. Measured HFR and calculations of HFR from the Equilibrium interface model

HFR measurements are compared with predictions from the non-equilibrium interface model in Figure 5.5. The effect of utilizing convective boundary conditions for the treatment of water sorption can be observed: HFR predictions at the lower 60% RH now reflect the experimental data where the resistance levels drop with increasing current density. The HFR predictions at 100% RH now reflect the experimental data where resistance levels increase from 0.053 to 0.055 Ω cm^2 at 1-1.5 A/cm^2.

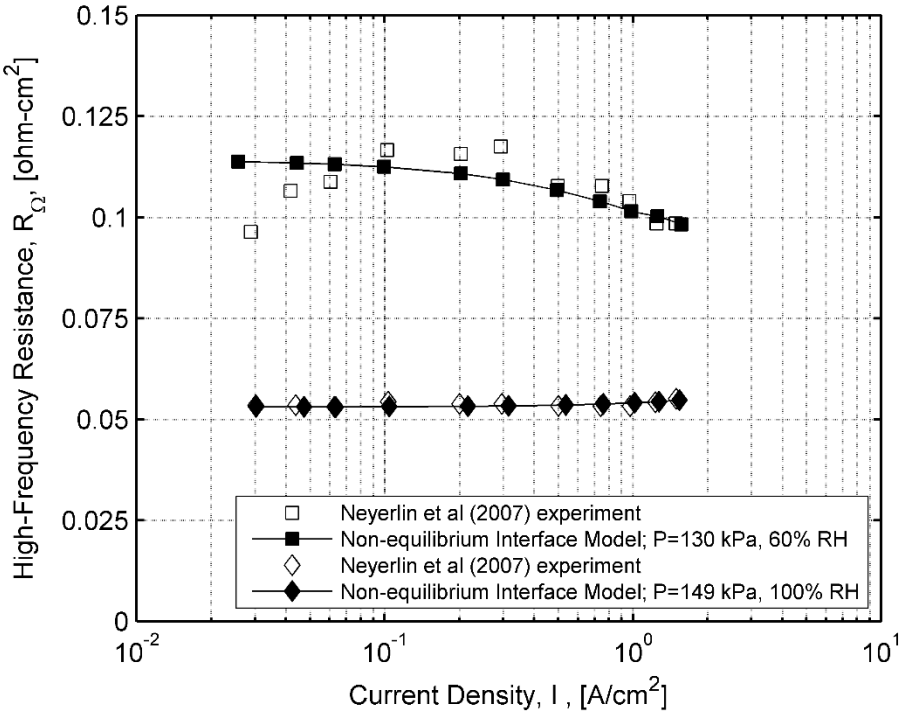

Figure 5.5. Measured HFR and calculations of HFR from the non-equilibrium interface model

Voltage measurements are compared against the equilibrium interface model with original kinetics at 100% humidity conditions in Figure 5.6. The first point was made to match by selecting the cathode exchange current density. The kinetic voltages and the HFR-corrected voltages predicted by this model are identical, as there is no assessment of catalyst layer losses. Kinetic voltages are significantly off from the experimental values, though the first point is matched. Cell voltage levels from the model show significant disagreement with measured values as the current density increases. The obvious source of disagreement is in the kinetic voltage, as described in the prior validation section, where the Tafel slope employed by the interface model was much greater than that found experimentally.

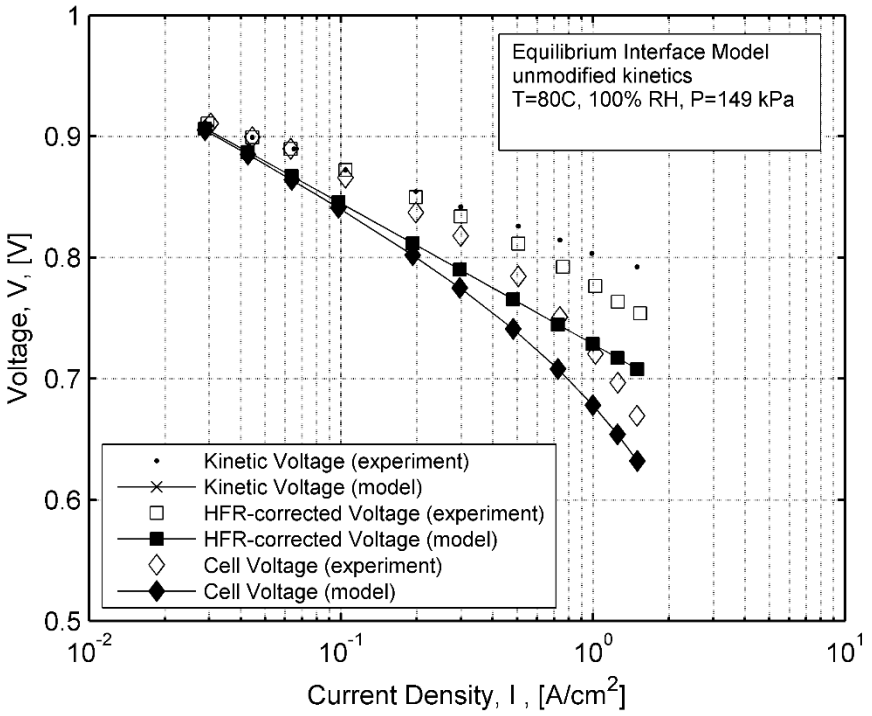

Figure 5.6. Measured and modeled voltages from the equilibrium interface (original kinetics) at 100% RH

Voltage measurements are compared against the equilibrium interface model with original kinetics at 60% humidity conditions in Figure 5.7. The low humidity results are, strangely, producing the appearance of good agreement. The kinetic voltages and the HFR-corrected voltages predicted by this model are identical, as there is no assessment of catalyst layer losses. Kinetic voltages are significantly off from the experimental values. The HFR-corrected voltages match up well, as do the un-compensated cell voltages.

The first experimental work[19] discussed in some detail how this misleading apparent agreement can occur. Un-compensated cathode catalyst layer losses in the physical experiment, not accounted for by the HFR-correction, produce the appearance of a higher-than-expected Tafel slope in the HFR-corrected voltage measurements. Such behavior can be seen to occur in the figure. The experimentally-derived kinetic voltage is greater than any of the experimental readings, with a Tafel slope of only 70 mV/decade.

When the un-measured catalyst layer losses are subtracted from the kinetic voltage, the resulting HFR-corrected voltages appear to have a Tafel slope of 117 mV/decade (in this case). The increased 'apparent' Tafel slope can be caused by mass-transport losses in the gas phase, and / or protonic conduction resistance in the electrolyte phase of the CCL. This model of cathode kinetics, with double the Tafel slope value (140 mV/decade), has been used in many older works which incorporate the interface model of Shimpalee et al. [91, 121]. The slope of 117 mV/decade used here is from a more recent paper describing the model for automotive applications with 75% humidity [112].

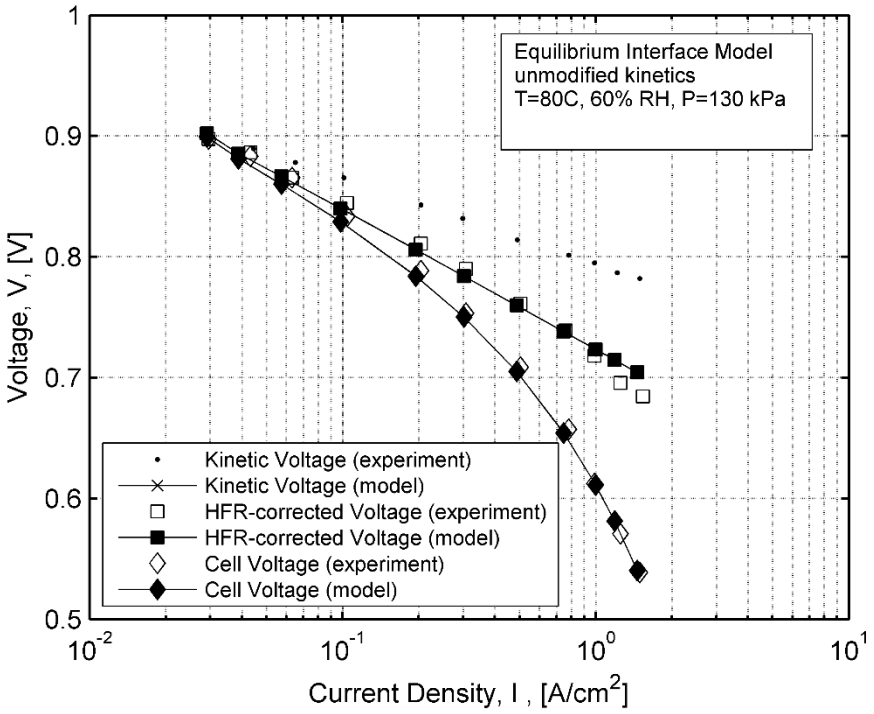

Figure 5.7. Measured and modeled voltages from the equilibrium interface (original kinetics) at 60% RH

The equilibrium interface models appear to have 2 free parameters which can be used to match experimental data. The exchange current density, and additionally the Tafel slope, of the ORR reaction (occurring at the cathode) appear to be treated as model parameters. The increased Tafel slope seen here matches the experimental data well at 60 % RH, but caused substantial disagreement for the prior fully-

humidified case (100 % RH). Therefore, the question arises as to what the results might be if a lower Tafel slope was used to represent the cathode kinetics within the equilibrium interface model.

The equilibrium interface model is also evaluated with 'modified kinetics' where the chosen model of cathode kinetics is utilized. Voltage measurements are compared against the equilibrium interface model with modified kinetics at high-humidity conditions in Figure 5.8. The first point was made to match by adjusting the cathode exchange current density. The kinetic voltages and the HFR-corrected voltages predicted by this model are identical, as there is no assessment of catalyst layer losses. This neglecting of catalyst layer losses is the major source of disagreement. The HFR measurements at 100% RH were approximately correct, hence the vertical gap between cell voltage and the HFR-corrected voltage is equal in both model and experiment. Cell voltage levels from the model show growing disagreement with measured values as the current density increases.

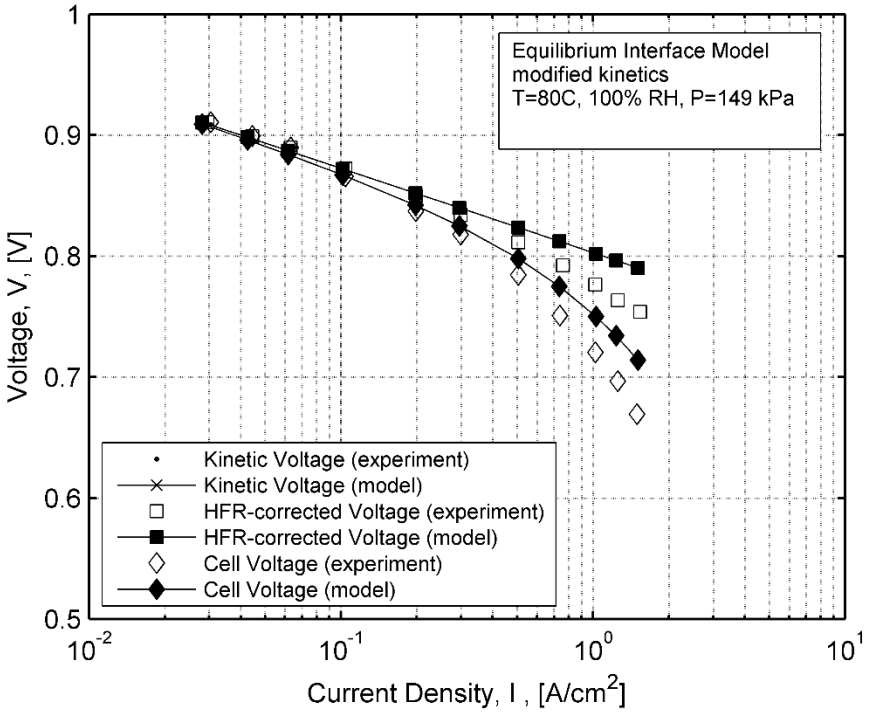

Figure 5.8. Measured and modeled voltages from the equilibrium interface (mod kinetics) at 100% RH

The same data, at 60% RH conditions, is shown in Figure 5.9. Again, the first point was made to match by selecting the cathode exchange current density. The experimental data reflects a larger gap between the kinetic voltage and HFR-corrected values reflecting greater effective catalyst layer, resistance(s). These catalyst layer losses are more substantial at lower humidity and neglecting them leads to greater model-experiment disagreement that is ultimately reflected in the cell voltage. Cell voltage levels show growing disagreement with measured values as the current density increases.

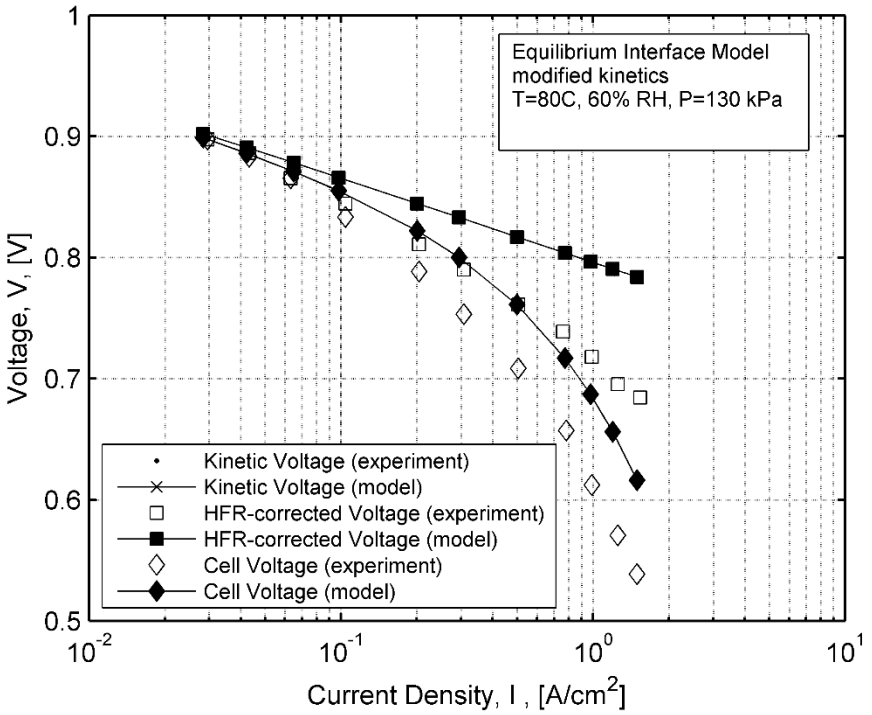

Figure 5.9. Measured and modeled voltages from the equilibrium interface (mod kinetics) at 60% RH

Voltage measurements are compared against the non-equilibrium interface model next. The non-equilibrium interface model was evaluated at both operating conditions; these results showed good agreement with experimental data. Voltage measurements are compared against the non-equilibrium interface model at high-humidity conditions in Figure 5.10. The kinetic voltages predicted by this model were already shown to be correct in the previous validation exercise. The gap between kinetic voltages and HFR-corrected voltages, predicted by this model, indicates a correct assessment of the summed ACL

+ CCL effective resistances. Thus, the non-equilibrium model accounts for the effective catalyst layer resistances correctly. The HFR predictions at 100% RH agreed well with experimental values, hence the gap between cell voltage and the HFR-corrected voltage is also equal in both model and experiment. Cell voltage levels from the interface model show good agreement with measured values.

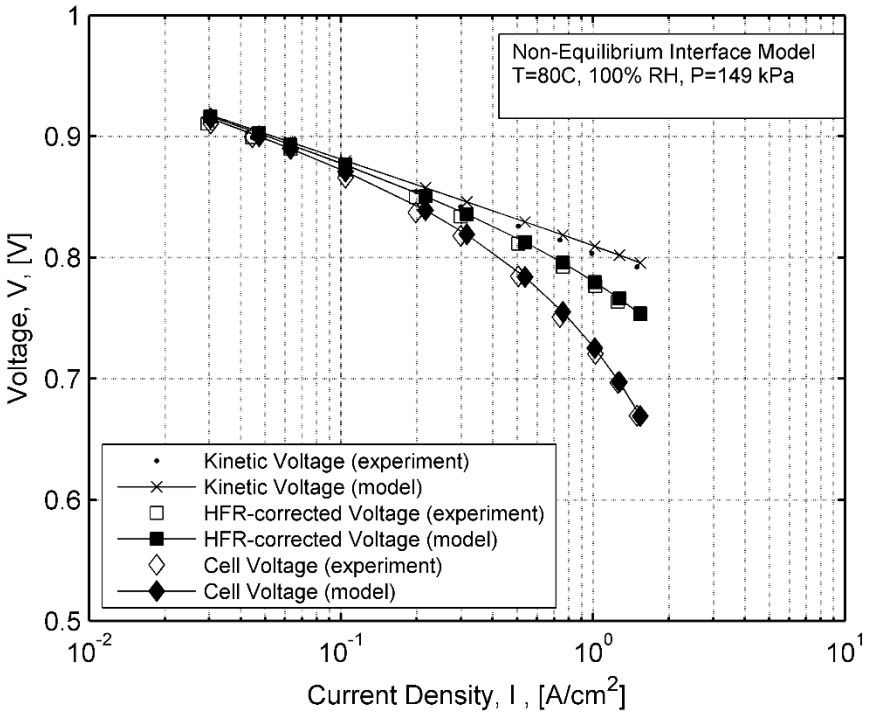

Figure 5.10. Measured and modeled voltages from the non-equilibrium interface at 100% RH

Voltage measurements are compared against the non-equilibrium interface model at low-humidity conditions in Figure 5.11. The kinetic voltages predicted by this model were already shown to be correct in the previous validation exercise. The gap between kinetic voltages and HFR-corrected voltages, predicted by this model, indicates a slight underestimation of the summed ACL + CCL losses.

The HFR predictions at 60% RH agreed well with experimental values, hence the gap between cell voltage and HFR-corrected voltage is also equal between model and experiment. The resulting cell voltage levels from the model are, then, slightly above experimental values due to the slight underestimation of the effective ACL resistance. The differences typically were under 6-10 mV, which is

similar to the amount of scatter found in the testing of the underlying cathode kinetic loss relationships [19].

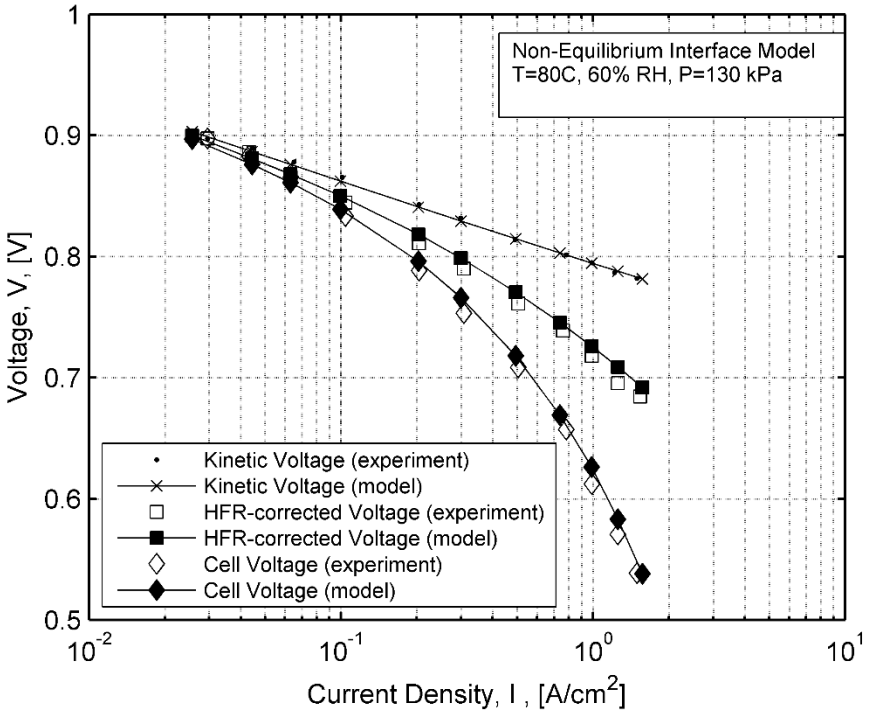

Figure 5.11. Measured and modeled voltages from the non-equilibrium interface at 60% RH

The experiment also reported estimates of the anode voltage loss, through a hydrogen pump test. This yielded what appeared to be constant anode resistance(s) for each of the low and high humidity cases. In the low humidity case, anode losses were reported as 30 mV at 1.5 A/cm^2, or = 0.02 Ω cm^2. Anode losses only reached 5 mV in the high-humidity case. Figure 5.12 shows anode voltage loss data against the predictions of the non-equilibrium interface model. Anode losses of the low-humidity case are correctly assessed, while the very small anode losses of the high-humidity case were predicted as greater than the experimentally-derived values. ACL conduction losses are frequently ignored entirely; this minor disagreement is not deemed critical.

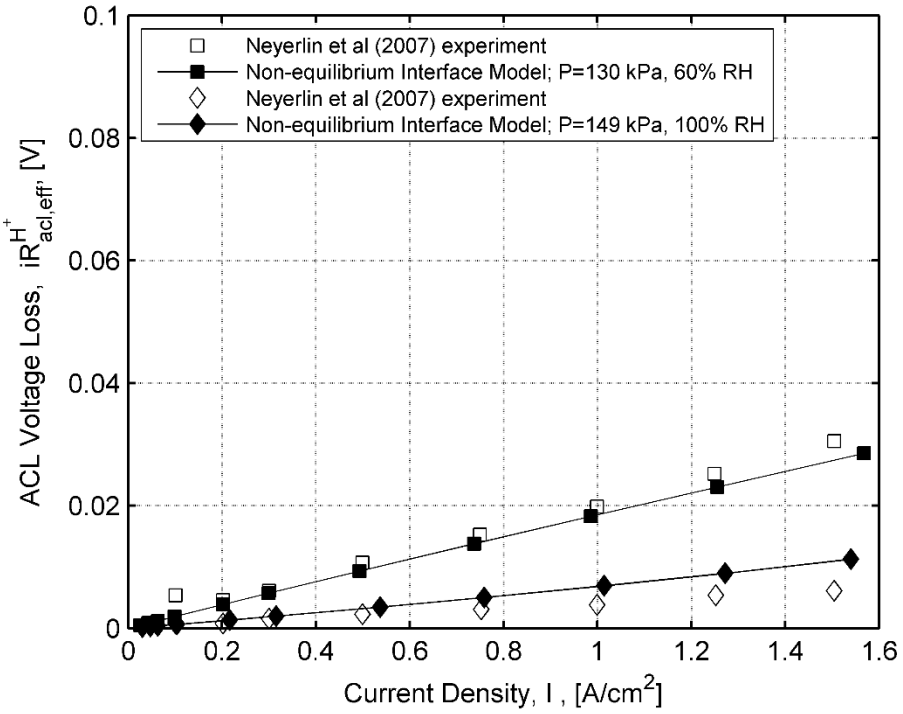

Figure 5.12. Measured and modeled anode losses from the non-equilibrium interface

5.2.3 Concluding Remarks

In conclusion, this validation effort showed that the non-equilibrium interface model could match experimental data produced from a well-defined differential PEMFC of known material composition. It has been already established that ohmic losses within the MEA are determined principally by the solution to a water transport problem. Hence, the interface models were evaluated based upon their ability to match voltage and current measurements at multiple operating conditions, with varying humidity levels. Also important is the ability to do so without resorting to the usage of multiple empirical model parameters, chosen in an ad-hoc manner without analytical basis, to match experimental results. Without a means to viably assess catalyst layer losses, the equilibrium interface models can manipulate their treatment of cathode kinetic losses (Tafel slope and exchange current density) to mimic the observed experimental results.

Neyerlin et al worked to assess the kinetic behavior of the ORR (the kinetic voltage losses occurring in the cathode)[19]. They noted the converse of the problem just described. Limitations of mass transport within the CCL, occurring in either the gaseous phase or as conduction losses within the ionomer, could lead the Tafel slope of the ORR to appear to change. Prior experiments misinterpreted the experimental results as if they indicated a change in ORR kinetics which was occurring as a (nearly) doubling of the Tafel slope of the ORR, which happened in experiments at low humidity.

This non-equilibrium model utilizes convective water transport boundary conditions which allow it to correctly predict the hydration-dependent high-frequency resistance (HFR) as it changes with current level. HFR measurements were not strictly constant with increasing current levels, indicating membrane hydration level changes. Catalyst layer losses can be ascertained once the water contents, and hence ionic conductivities of catalyst layers, are known. The benchmark equilibrium interface models, through their fundamental formulation, produced a constant HFR, unchanging with current density levels. The proposed Non-Equilibrium interface model produced changing levels of HFR (with current) that better match the experimental data. Varying HFR is caused by changing MEA water contents.

Estimates of the various voltage components were compared with experimental values. The crucial estimates of membrane ionic resistance, and the effective anode and cathode catalyst layer resistances, were produced at both low and high-humidity conditions across a range of current densities. The less-important effective anode catalyst layer resistance was estimated correctly at low-humidity conditions but was slightly over-predicted for the high-humidity conditions. The earlier interface models, included for comparison, have tended to ignore both anode and cathode catalyst layer losses. The non-equilibrium interface model thus matched experimentally-derived data for high-frequency resistance (HFR), the various voltage components, and effective anode losses at reactant humidity levels of 60% RH and 100% RH.

The model-experiment agreement was had with a kinetic model whose parameters were determined from fundamental-level physical experiments reported in prior works. That is, the Tafel slope

and exchange current density aren't changed on a case-by-case basis and are separately measurable. One consistent set of kinetic model parameters can produce both the high and low humidity results.

6 PEMFC MODELING – RESULTS

The previous chapter was meant to validate the 1-D (through-plane) non-equilibrium interface model against localized data; i.e. data measured in a differential cell. The current chapter is meant to examine its full 3-dimensional usage.

Spatially resolved current density measurements are desired to validate three-dimensional models because they contain much more information than integral measurements, where perhaps a single cell voltage and average current density are reported. Distributed impedance and temperature distributrion measurements have also been attempted. Segmented fuel cells can be used to gather this data.

6.1 Selection of Test Case

Several considerations were evaluated in selecting the best available experimental data to use. Past and recent validation efforts have been hampered by the lack of reliable and robust input data[122] for validation efforts in the literature. Information coming from experiments was often inadequate for fully describing computational models.

First, the model should include current distribution data. Some works that were ostensibly for validation purposes reported only integral measurements (overall polarization curves). Overall curves were found to be insensitive to modeling errors and could be matched through the judicious selection of a combination of modeling parameters [76]. Overall polarization curves could be matched through the choice of an added ohmic resistance and modified cathode kinetic parameters. These appropriate values have typically been reported in modeling works as parameters, chosen on a case-by-case basis.

Secondly, the ideal test case for this model should involve low humidity operating conditions. The test case shouldn't be excessively dependent on the ability to correctly model the multiphase behavior of liquid water in the porous media of the PEMFC.

Third, it was thought to be important that the experimental case be appropriate to the intentions of the interface model that was described. The interface model is intended for thin membranes; i.e. 1-4 microns in thickness. Several works intended as validation exercises have used thick Nafion 115 or Nafion 117 membranes and so are not the best choice.

It is therefore also desired that the catalyst layer compositions be adequately described in the experimental work. The interface model tries to calculate ACL and CCL losses utilizing detailed information about both catalyst layer compositions. Some of this information was typically missing in every validation oriented work that was examined. Validation works typically presented the catalyst layer information used in the model at hand, rather than a full description (such as those contained within the works of Chapter 5). Complete composition data may have been omitted for additional commercial reasons, as many validation works utilized proprietary, commercially-sourced MEA's.

Validation works have often used composite membranes, which will have noticeably different transport properties than the Nafion. Ionic conductviities of the composite membranes have been reported as being about ½ those of Nafion under saturated conditions, but a comprehensive relationship is not known. The modeling of interfacial absorption / desorption of water vapor was not evaluated with these composite materials. This brings additional sources of uncertainty.

Adequate modeling information is desired in the form of gas compositions, flow rates, material properties, and various boundary conditions. Geometrical simplicity is desired.

The test case of Haknejos et. al [123, 124] will be evaluated because of its simplicity. This work meets some considerations preented above. It lacks fully described catalyst layer compositions, so estimates are used. The composite membrane adds some uncertainties.

6.2 Experimental Conditions

The experiment measured the current distribution in a specially-constructed segmented PEM fuel cell under 3 operating conditions. Low humidity gas inputs were used and the model specifically avoided the consideration of liquid water and condensation effets.

6.2.1 Geometrical and Physical Parameters

The PEMFC under consideration consists of 14 straight and parallel flow channels in both the anode and cathode. These flow fields are graphite. The anode flow field is broken into segments, with 3 segments in the cross-flow direction and 15 segments in the downstream (flow) direction. The setup then 3 rows of 15 segments each. The graphite segments electrically isolated from each other, and are connected to a polysulphone “back-plate” with electrical pins installed; to create a contact block or connector block to allow segmented current measurement.

There are 14 straight 100 mm long parallel channels, with each having a cross secton of 1 mm by 1 mm. The rib width between channels is also 1 mm. Total cell area is reported as 29 cm^2.

The model computational domain consists of only 1 channel, as was done in the original work. Cross-channel effects aren’t considered here; they were also avoided by the original work. The experiment reported averaged data from the 15 segments in the flow direction. The base-case computational domains and mesh are presented in Figure 6.1. Mesh 1 holds 86,366 domain elements and 40,022 boundary elements. The mesh includes the anode domain (bottom) and cathode domain (top). The detached 2-D middle surface is the MEA.

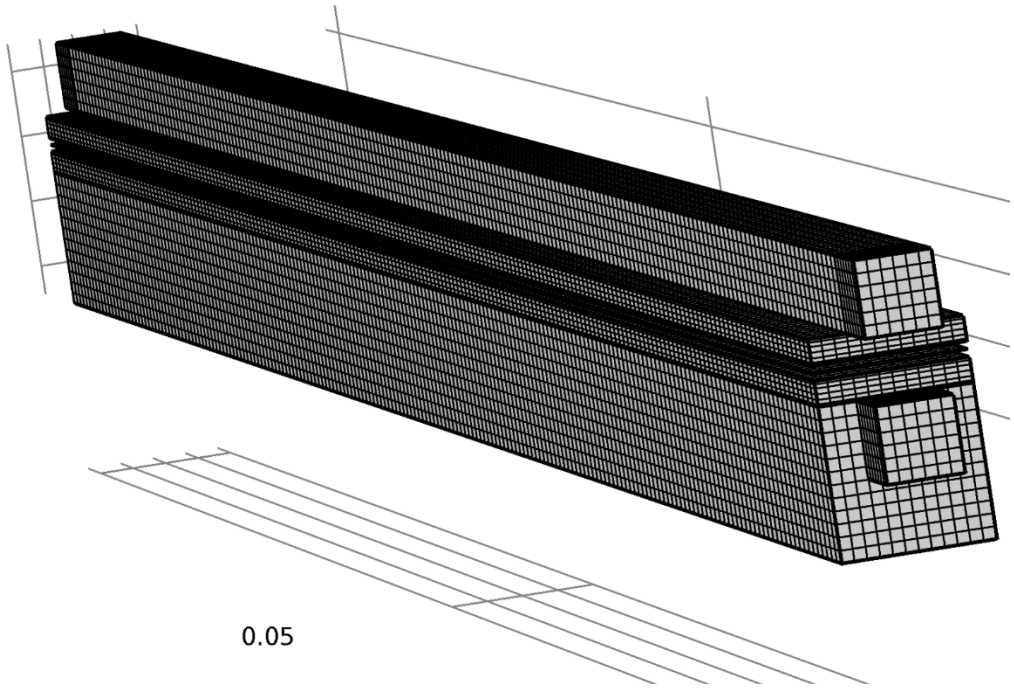

Figure 6.1. View of base case mesh with top collector plate removed

Geometrical and Physical Parameters are reported in Table 6.1. The electrical contact resistances are similar to what was claimed. Material properties come from the original work. The gas diffusion layer (GDL) was reportedly Toray TGP-H-060 (compressed thickness=0.17 mm) in the original work, but was reported as Toray TGP-H-120 (twice the thickness) in the subsequent work.

Table 6.1. Geometrical and Physical Parameters of the experiment.

Gas Channel	Gas channel width (x)	W_{ch}	1.0	mm
	Gas channel height (y)	H_{ch}	1.0	mm
	Fuel cell length (z)	L_{ch}	100	mm
Shoulder	Shoulder width	W_{sh}	0.5	mm
	Shoulder height	H_{sh}	1.0	mm
GDL	thickness	H_{GDL}	330	μm
	density	ρ	1950	kg m^{-3}
	porosity	ε	0.51	-
	permeability	$\overline{\overline{\mathbf{K}}}$	$2x10^{-11}$	m^2
	in-plane thermal conductivity	$k_{GDL,=}$	17	W m^{-1} K^{-1}
	thru-plane thermal conductivity	$k_{GDL,\perp}$	1.7	$(\Omega\ m)^{-1}$
	in-plane electrical conductivity	$\sigma_{e,=}$	10000	$(\Omega\ m)^{-1}$
	thru-plane electrical conductivity	$\sigma_{e,\perp}$	1250	$(\Omega\ m)^{-1}$
Collector Plates	top height	H	2.0	mm
	density	ρ	2100	kg m^{-3}
	thermal conductivity	k_{CL}	20.0	W m^{-1} K^{-1}
	electrical conductivity	σ_e	10,000	$(\Omega\ m)^{-1}$
	thermal contact resistance w/ GDL	R_{cnt}^{T}	$1.5x10^{-4}$	m^2 K^1 W^{-1}
	electrical contact resistance w/ GDL	$R_{cnt}^{e^-}$	4.0	mΩ cm^2
	electrical contact resistance w/ Anode terminal	$R_{cnt}^{e^-}$	800	mΩ cm^2

6.2.2 Operating Conditions and Parameters

Operating conditions and parameters are presented in Table 6.2. The cell voltage was held at 0.5V for all measurements. The anode flow rate into the cell was given as 100 sccm of dry hydrogen, which was humidified to 20% RH at 22 °C prior to entering the cell. The cathode flow rates were reported as 600, 300, and 50 standard cubic centimeters per minute (sccm) of dry air, which was humidified to 80% RH at 22 °C prior to entering the cell. Flow into the 1-channel model is then $1/14^{th}$ of the quoted amounts. The inlet gas flow species mass fractions are given in Table 6.3.

Stoichiometric air flow ratios at the cathode, at these claimed flow rates, were estimated in the original work at $\zeta_C^{\mathbb{OP}}$ =12, 7, and 1.5, respectively, by taking account of the observed average current density. Interestingly, the origininal work's model claimed to predict reversed flow at the gas outlet in

the 50 sccm case. The simulated gas flow rate was reportedly increased to 71 sccm to remedy this problem.

Table 6.2. Operating conditions for single-channel flow simulation.

Parameter:		Symbol:			Value:
Operating cell voltage		$V_{cell}^{\mathbb{OP}}$			0.5 V
Average operating cell current density		$I_{cell}^{\mathbb{OP}}$			(solved for) ~0.2 A/cm^2
MEA area (length x width)		A_{MEA}			29 cm^2
Anode:			Cathode:		
Parameter:	Symbol:	Value:	Parameter:	Symbol:	Value:
Operating pressure	$P_A^{\mathbb{OP}}$	101.3 kPa	Operating pressure	$P_C^{\mathbb{OP}}$	101.3 kPa
Flow inlet area	$A_{A,ch}$	1.0 mm^2	Flow inlet area	$A_{C,ch}$	1.0 mm^2
Gas flow	$Q_A^{\mathbb{OP}}$	105/14 sccm	Gas flow	$Q_C^{\mathbb{OP}}$	1: 1116/14 sccm 2: 608/14 sccm 3: 104/14 sccm
Stoichiometric flow ratio	$\zeta_A^{\mathbb{OP}}$	(estimates) 1: 2.8 2: 3.0 3: 4.2	Stoichiometric flow ratio	$\zeta_C^{\mathbb{OP}}$	(estimates) 1: 12 2: 7 3: 1.5
Relative humidity	$\mathbb{RH}_A^{\mathbb{OP}}$	20 % @ 22 °C	Relative Humidity	$\mathbb{RH}_C^{\mathbb{OP}}$	80 % @ 22 °C
Inlet temperature	$T_A^{\mathbb{OP}}$	295.15 K	Inlet temperature	$T_C^{\mathbb{OP}}$	297.15 K
Anode plate: - htc - ext temperature	$h_A^{\mathbb{OP}}, T_{A,ext}^{\mathbb{OP}}$	10 W/ (m^2 K) 295 K	Cathode Plate: temperature	$T_C^{\mathbb{OP}}$	330.15 K

Table 6.3. Gas input compositions of anode and cathode.

	Anode 101 kPa exit pressure inlet 20% RH @ 22 °C	$\omega_{H_2,A}$ =0.95	$\omega_{H_2O,A}$ =0.05	$\omega_{N_2,A}$ =0.0001	p_A =101.3 kPa
	Cathode 101 kPa exit pressure inlet 80% RH @ 22 °C	$\omega_{O_2,C}$ =0.23	$\omega_{H_2O,C}$ =.014	$\omega_{N_2,C}$ =.756	p_c =101.3 kPa

The mass flow rates of the anode and cathode gas inputs must be discussed. Anode mass flow (kg/s) can be expressed as eq.(6.1) from the standard flowrate and input composition. The mass flow consumed by a current draw can be expressed as (6.2).

$$\dot{m}_A = (M_{H_2} x_{H_2,in} + M_{H_2O} x_{H_2O,in}) \frac{101{,}325\,\text{Pa}}{R\,273.15\,\text{K}} \frac{Q_A(sccm)}{60(s/\text{min})} \left(\frac{.01(m)}{(\text{cm})} \right)^3 \tag{6.1}$$

$$\dot{m}_A = \frac{IA_{MEA}}{2F}\frac{(M_{H_2}x_{H_2,in} + M_{H_2O}x_{H_2O,in})}{x_{H_2,in}} \tag{6.2}$$

Dividing the two yields anode stoichiometry of about 2.8, or nearly 3 for the average current draws which were reported at 100 sccm dry hydrogen reported flow rate. Cathode mass flow can be expressed as eq. (6.3) from the standard flowrate. The mass flow consumed by a current draw can be expressed as eq. (6.4).

$$\dot{m}_C = (M_{O_2}x_{O_2,in} + M_{H_2O}x_{H_2O,in} + M_{N_2}x_{N_2,in})\frac{101{,}325\,\text{Pa}}{R\,273.15\,\text{K}}\frac{Q_C(sccm)}{60(s/\text{min})}\left(\frac{.01(m)}{(\text{cm})}\right)^3 \tag{6.3}$$

$$\dot{m}_C = \frac{IA_{MEA}}{2F}\frac{(M_{O_2}x_{O_2,in} + M_{H_2O}x_{H_2O,in} + M_{N_2}x_{N_2,in})}{x_{O_2,in}} \tag{6.4}$$

Dividing the two yields the approximate cathode stoichiometry which varies with the input flowrate. A full representation is given in Table 6.4. Using standard pressure of 101.3 kPa and standard temperature of 273.15 K, and estimated average experimentally reported reported current density in the right-most column, the anode and cathode stoichiometry for each case are seen. The reported cathode standard flow rates in the middle column would give stoichiometry values lower than what was claimed. The increased standard flow rates in the right column yield stoichiometry values nearly at $\zeta_C^{\mathbb{OP}}$=12, 7, and 1.5 as was claimed in the original work. The original work reported that the model's flow rate in case 3 was increased from 50 sccm to 71.4 sccm to avoid reversed flow at the gas outlet, where the cathode stoichiometry would be less than 1.

Table 6.4. Flow and stoichiometry values for single-channel simulation.

	Anode std flowrate (sccm dry H_2)		Cathode std flowrate (sccm dry air)		Cathode std flowrate (sccm dry air)		I_{avg} (A/cm^2)
Case 1:	100	$\zeta_A^{\mathbb{OP}}$ =2.8	600	$\zeta_C^{\mathbb{OP}}$ =6.7	1100	$\zeta_C^{\mathbb{OP}}$ =12.3	0.19
Case 2:	100	$\zeta_A^{\mathbb{OP}}$ =3	300	$\zeta_C^{\mathbb{OP}}$ =3.5	600	$\zeta_C^{\mathbb{OP}}$ =7.1	0.18
Case 3:	100	$\zeta_A^{\mathbb{OP}}$ =4.2	50	$\zeta_C^{\mathbb{OP}}$ =0.82	100	$\zeta_C^{\mathbb{OP}}$ =1.6	0.13

6.2.3 MEA Composition

The MEA composition is detailed in Table 6.5. The first original work claimed a membrane thickness of 35 μm and 1100 equivalent weight, and claimed a specific, fixed membrane conductivity (that is not used here). Catalyst layer thicknesses were claimed as 10 μm and the ionomer volume fraction in each was claimed as 0.4. The follow-up work claimed the MEA used was a Gore 5510 MEA with platinum catalyst loadings of 0.4 mgPt / cm^2. Full composition data from this MEA could, unfortunately, not be found. Estimates are used.

Table 6.5. MEA compositions used in the single-channel simulation.

Membrane	Ionomer equivalent weight	EW	1100	g / equiv or g / mol SO_3^-
	Thickness (dry)	t_{MEM}	31×10^{-6}	m
	Crossover current density	I_x	10	A / m^2
Anode Catalyst Layer	Platinum loading	$L_{ACL,Pt}$	0.4	mg_{Pt} / cm^2
	Pt/C mass ratio	Ptc_{ACL}	50	%
	Ionomer to carbon ratio	IC_{ACL}	1.4	-
	Thickness (dry)	t_{ACL}	10×10^{-6}	m
	Available catalyst area	$A_{ACL,Pt}^{100\%RH}$	50	m^2_{Pt} / g_{Pt}
	Specific exchange current density	$i_{0,ACL}^{*}$	0.24	A / cm^2_{Pt}
Cathode Catalyst Layer	Platinum loading	$L_{CCL,Pt}$	0.4	mg_{Pt} / cm^2
	Pt/C mass ratio	Ptc_{CCL}	50	%
	Ionomer to carbon ratio	IC_{CCL}	1.4	-
	Thickness (dry)	t_{CCL}	10×10^{-6}	m
	Available catalyst area	$A_{CCL,Pt}^{100\%RH}$	50	m^2 / g_{Pt}
	Specific exchange current density	$i_{0,CCL}^{*}$	2×10^{-8}	A / cm^2_{Pt}
Electronic Resistance	MEA electronic resistance	$R_{cnt}^{e^-}$	0.011	Ω cm^2

6.3 Comparison of Results

Partially converged data from the 600 sccm case in Figure 6.2 shows a comparison between the experimental and model results for the highest flow rate case. Current levels increased in the downstream direction as the solver iterated and humidity levels increased. Unfortunately, un-resolveable errors within the solver prevented its continuing to iterate and produce fully-converged results.

The errors appeared with the switch from 60% RH reactants (in the verification modelsChapter 4) to the present case where nearly dry reactants are being used.

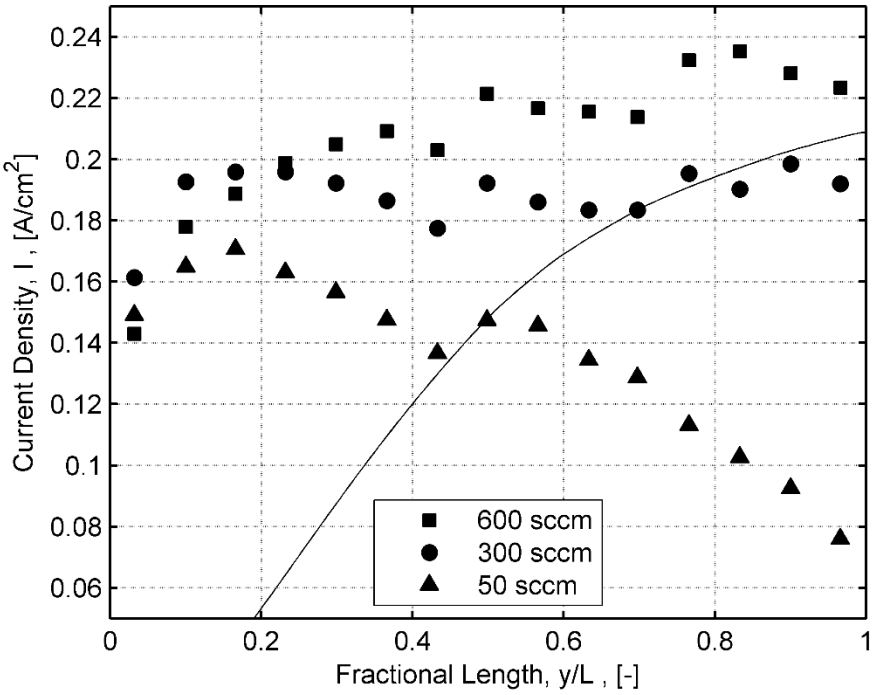

Figure 6.2. Partially-converged model results

6.4 Concluding Remarks

This correlation effort, like many others, is subject to several uncertainties pertaining to the original experiment. The first source of uncertainty in the experiment pertains to the ACL/CCL (catalyst layer) material compositions, which are not precisely available. While the reported information was

utilized with the prior model, the current, proposed, model has more information. Exact composition details might be guarded as a commercial or trade secret. More recent works incorporating the reinforced MEA's do not describe the ACL/CCL material compositions in the same full manner as was done in chapter 5[125, 126].

Most of the published validation works that were considered have involved membranes (MEA) that were not Nafion but were composites. The most reliably seen composite is the microporous stretched PTFE (expanded PTFE sheet) construction. The second source of uncertainty is associated with converting the relevant property data from Nafion into something representative of the performance of these reinforced membranes.

The third source of uncertainty is the large reported electrical contact resistance, $R_{cnt}^{e^-}$, that was included in a table of modeling parameters. Variations in the observed current density were attributed to variability in this contact resistance within the original work. It is unclear how precisely that was known.

Validation without all of the appropriate input data will continue to be challenging.

7 SUMMARY AND CONCLUSIONS

7.1 Summary

This effort was an attempt to develop an improved interface model that could be used with CFD approaches to modeling the PEMFC. The interface model removes the physics of the MEA from the 3-D computational domains of the problem, simiulating its behavior with source terms (fluxes) of the relevant species consumption, heat generation, and current density. The modeling approaches outside of the MEA are well investigated, though significant activity continues in modeling mulriphase behavior related to the treatment of liquid water.

Chapter 2 undertook to re-formulate an interface model to represent the action of the MEA, using newly-available findings from the diverse physics involved. Particular attention was paid to the coupled problems of water transport and current conduction through the Nafion ionomer. By incorporating newly-generated water uptake curves, ionomer expansion effects, and water absorption / desorption effects, better agreement was found with the subsequently-performed validation.

Chapter 4 conducted a verification of the interface model, focused on the 3-point approximate water transport solutions which were developed. Comparisons to 1-D finite-volume solutions showed good agreement with thin (.001”-.002”) membranes when the thru-plane water contents were simulated. Water fluxes and ohmic resistance values were also highly similar between the two techniques.

A 3-dimensional model was solved. Grid convergence studies showed consistency in the solutions with increased mesh refinement. Species balance checks also indicated sufficient mass conservation performance.

Chapter 5 undertook validation of this interface model against experimental data from differential cell measurements. It was seen that the hydration-dependent membrane resistances were correctly

predicted at moderate and high humidities. More so, the variations in resistance attributable to changes in current density were also captured by the model. The prior-art interface models necessarilhy predict a flat response: resistance unchanging with current density.

Evaluation of catalyst layer losses under these conditions was also successful. Prior published works were utilized where the catalyst layer ionomer conductivities were assumed to be known. By accounting for additional water transport physics, the conductivity estimates, and hence catalyst layer losses, were more accurately estimated.

Chapter 6 intended to show agreement with distributed current density measurements from a prior validation effort. Unfortunately, convergence problems combined with uncertainty over some of the input data prevented a good comparison.

7.2 Future work Suggestions

This work focused on assembling various research from homogeneous Nafion membranes. Superior durability of ePTFE (expanded PTFE) micro-reinforced composite membranes has made them a popular choice in more recent validation works with PEMFC's[126]. Nafion is typically the ionomer component of these membranes; however it is not clear how a similar model of water transport might be resolved when applied to these composite membranes.

Models typically incorporate some treatment of liquid water (multiphase) effects, however this appear to be an area of ongoing refinement. A number of approaches exist, and it is not clear which is most accurate.

Validation efforts are also challenged by the lack of reliable input data. This was a primary conclusion of one recent study[122]. The description of catalyst layer compositions incorporated herein was typically not available.

REFERENCES

1. Wang, Y., et al., *A review of polymer electrolyte membrane fuel cells: Technology, applications, and needs on fundamental research.* Applied Energy, 2011. **88**(4): p. 981-1007.
2. Guvelioglu, G.H. and H.G. Stenger, *Computational fluid dynamics modeling of polymer electrolyte membrane fuel cells.* Journal of Power Sources, 2005. **147**(1-2): p. 95-106.
3. Larminie, J. and A. Dicks, *Fuel cell systems explained*. 2nd ed. 2003, West Sussex: John Wiley & Sons Ltd. 406.
4. Mench, M., *Fuel cell engines*. 2008: John Wiley & Sons, Inc.
5. Wood, D.L., J.S. Yi, and T.V. Nguyen, *Effect of direct liquid water injection and interdigitated flow field on the performance of proton exchange membrane fuel cells.* Electrochimica Acta, 1998. **43**(24): p. 3795-3809.
6. Laurencelle, F., et al., *Characterization of a Ballard MK5-E Proton Exchange Membrane Fuel Cell Stack.* Fuel Cells, 2001. **1**(1): p. 66-71.
7. Cooper, K.R., et al., *Experimental Methods and Data Analyses for Polymer Electrolyte Fuel Cells*, I. Scribner Associates, Editor. 2007, Scribner Associates, Inc.
8. Ju, H. and C.-Y. Wang, *Experimental Validation of a PEM Fuel Cell Model by Current Distribution Data.* Journal of The Electrochemical Society, 2004. **151**(11): p. A1954-A1960.
9. Mench, M.M., C.Y. Wang, and M. Ishikawa, *In Situ Current Distribution Measurements in Polymer Electrolyte Fuel Cells.* Journal of The Electrochemical Society, 2003. **150**(8): p. A1052-A1059.
10. Wieser, C., A. Helmbold, and E. Gülzow, *A new technique for two-dimensional current distribution measurements in electrochemical cells.* Journal of Applied Electrochemistry, 2000. **30**(7): p. 803-807.
11. Geiger, A.B., et al., *An Approach to Measuring Locally Resolved Currents in Polymer Electrolyte Fuel Cells.* Journal of The Electrochemical Society, 2004. **151**(3): p. A394-A398.
12. Natarajan, D. and T. Van Nguyen, *Current distribution in PEM fuel cells. Part 1: Oxygen and fuel flow rate effects.* AIChE Journal, 2005. **51**(9): p. 2587-2598.
13. Vie, P.J.S. and S. Kjelstrup, *Thermal conductivities from temperature profiles in the polymer electrolyte fuel cell.* Electrochimica Acta, 2004. **49**(7): p. 1069-1077.
14. Mench, M., D.J. Burford, and T.W. Davis, *In Situ Temperature Distribution Measurements in an Operating Polymerm Electrolyte Fuel Cell, Paper No. 42393*, in *Proceedings of the 2003 International Mechanical Engineering conference and Exposition (IMECE)*. 2003, ASME: Washington, DC.
15. Burford, D.J., T.W. Davis, and M.M. Mench, *Heat Transport and Temperature Distribution in PEFCs, IMECEC 2004-59497*, in *Proceedings of the 2004 International Mechanical Engineering conference and Exposition (IMECE)*. 2004: Anaheim, CA.
16. Mench, M.M., Q.L. Dong, and C.Y. Wang, *In situ water distribution measurements in a polymer electrolyte fuel cell.* Journal of Power Sources, 2003. **124**(1): p. 90-98.
17. Dong, Q., J. Kull, and M.M. Mench, *Real-time water distribution in a polymer electrolyte fuel cell.* Journal of Power Sources, 2005. **139**(1–2): p. 106-114.

18. Stevens, D.A. and J.R. Dahn, *Electrochemical Characterization of the Active Surface in Carbon-Supported Platinum Electrocatalysts for PEM Fuel Cells.* Journal of The Electrochemical Society, 2003. **150**(6): p. A770-A775.
19. Neyerlin, K.C., et al., *Determination of Catalyst Unique Parameters for the Oxygen Reduction Reaction in a PEMFC.* Journal of The Electrochemical Society, 2006. **153**(10): p. A1955-A1963.
20. Neyerlin, K.C., et al., *Cathode Catalyst Utilization for the ORR in a PEMFC.* Journal of The Electrochemical Society, 2007. **154**(2): p. B279-B287.
21. Soboleva, T., et al., *PEMFC catalyst layers: the role of micropores and mesopores on water sorption and fuel cell activity.* ACS Appl Mater Interfaces, 2011. **3**(6): p. 1827-37.
22. Cooper, K.R. and M. Smith, *Electrical test methods for on-line fuel cell ohmic resistance measurement.* Journal of Power Sources, 2006. **160**(2): p. 1088-1095.
23. Neyerlin, K.C., et al., *Study of the Exchange Current Density for the Hydrogen Oxidation and Evolution Reactions.* Journal of The Electrochemical Society, 2007. **154**(7): p. B631-B635.
24. Liu, Y., et al., *Proton Conduction and Oxygen Reduction Kinetics in PEM Fuel Cell Cathodes: Effects of Ionomer-to-Carbon Ratio and Relative Humidity.* Journal of The Electrochemical Society, 2009. **156**(8): p. B970-B980.
25. Kulikovsky, A.A., *Introduction*, in *Analytical Modelling of Fuel Cells*, A.A. Kulikovsky, Editor. 2010, Elsevier: Amsterdam. p. xiii-xv.
26. Uchida, M., et al., *Investigation of the Microstructure in the Catalyst Layer and Effects of Both Perfluorosulfonate Ionomer and PTFE-Loaded Carbon on the Catalyst Layer of Polymer Electrolyte Fuel Cells.* Journal of The Electrochemical Society, 1995. **142**(12): p. 4143-4149.
27. Uchida, M., et al., *Effects of Microstructure of Carbon Support in the Catalyst Layer on the Performance of Polymer-Electrolyte Fuel Cells.* Journal of The Electrochemical Society, 1996. **143**(7): p. 2245-2252.
28. Xie, J., et al., *Ionomer Segregation in Composite MEAs and Its Effect on Polymer Electrolyte Fuel Cell Performance.* Journal of The Electrochemical Society, 2004. **151**(7): p. A1084-A1093.
29. Wang, Y. and X. Feng, *Analysis of Reaction Rates in the Cathode Electrode of Polymer Electrolyte Fuel Cell I. Single-Layer Electrodes.* Journal of The Electrochemical Society, 2008. **155**(12): p. B1289-B1295.
30. Wang, Y., *Analysis of the Key Parameters in the Cold Start of Polymer Electrolyte Fuel Cells.* Journal of The Electrochemical Society, 2007. **154**(10): p. B1041-B1048.
31. Stumper, J., H. Haas, and A. Granados, *In Situ Determination of MEA Resistance and Electrode Diffusivity of a Fuel Cell.* Journal of The Electrochemical Society, 2005. **152**(4): p. A837-A844.
32. Yu, Z. and R.N. Carter, *Measurement of effective oxygen diffusivity in electrodes for proton exchange membrane fuel cells.* Journal of Power Sources, 2010. **195**(4): p. 1079-1084.
33. Shen, J., et al., *Measurement of effective gas diffusion coefficients of catalyst layers of PEM fuel cells with a Loschmidt diffusion cell.* Journal of Power Sources, 2011. **196**(2): p. 674-678.
34. Yu, Z., R.N. Carter, and J. Zhang, *Measurements of Pore Size Distribution, Porosity, Effective Oxygen Diffusivity, and Tortuosity of PEM Fuel Cell Electrodes.* Fuel Cells, 2012. **12**(4): p. 557-565.
35. Lange, K.J., P.-C. Sui, and N. Djilali, *Determination of effective transport properties in a PEMFC catalyst layer using different reconstruction algorithms.* Journal of Power Sources, 2012. **208**(0): p. 354-365.
36. Singh, R., et al., *Dual-Beam FIB/SEM Characterization, Statistical Reconstruction, and Pore Scale Modeling of a PEMFC Catalyst Layer.* Journal of The Electrochemical Society, 2014. **161**(4): p. F415-F424.
37. Durst, J., et al., *Hydrogen Oxidation and Evolution Reaction Kinetics on Carbon Supported Pt, Ir, Rh, and Pd Electrocatalysts in Acidic Media.* Journal of The Electrochemical Society, 2015. **162**(1): p. F190-F203.
38. Barbir, F., *PEM fuel cells: theory and practice*. 2013: Academic Press.

39. Gasteiger, H.A., J.E. Panels, and S.G. Yan, *Dependence of PEM fuel cell performance on catalyst loading.* Journal of Power Sources, 2004. **127**(1-2): p. 162-171.
40. Kornyshev, A.A. and A.A. Kulikovsky, *Characteristic length of fuel and oxygen consumption in feed channels of polymer electrolyte fuel cells.* Electrochimica Acta, 2001. **46**(28): p. 4389-4395.
41. Jaouen, F., G. Lindbergh, and G. Sundholm, *Investigation of Mass-Transport Limitations in the Solid Polymer Fuel Cell Cathode.* Journal of The Electrochemical Society, 2002. **149**(4): p. A437-A447.
42. Neyerlin, K.C., et al., *Effect of Relative Humidity on Oxygen Reduction Kinetics in a PEMFC.* Journal of The Electrochemical Society, 2005. **152**(6): p. A1073-A1080.
43. Shimpalee, S., et al., *Experimental and numerical studies of portable PEMFC stack.* Electrochimica Acta, 2009. **54**(10): p. 2899-2911.
44. Bernardi, D.M. and M.W. Verbrugge, *Mathematical model of a gas diffusion electrode bonded to a polymer electrolyte.* AIChE Journal, 1991. **37**(8): p. 1151-1163.
45. Springer, T.E., T.A. Zawodzinski, and S. Gottesfeld, *Polymer electrolyte fuel cell model.* Journal of the Electrochemical Society, 1991. **138**(8): p. 2334-2342.
46. Kamarajugadda, S. and S. Mazumder, *On the implementation of membrane models in computational fluid dynamics calculations of polymer electrolyte membrane fuel cells.* Computers & Chemical Engineering, 2008. **32**(7): p. 1650-1660.
47. Zawodzinski, T.A., et al., *Determination of water diffusion coefficients in perfluorosulfonate ionomeric membranes.* The Journal of Physical Chemistry, 1991. **95**(15): p. 6040-6044.
48. Zawodzinski, J.T.A., et al., *Water Uptake by and Transport Through Nafion[sup [registered sign]] 117 Membranes.* Journal of The Electrochemical Society, 1993. **140**(4): p. 1041-1047.
49. Hinatsu, J.T., M. Mizuhata, and H. Takenaka, *Water Uptake of Perfluorosulfonic Acid Membranes from Liquid Water and Water Vapor.* Journal of The Electrochemical Society, 1994. **141**(6): p. 1493-1498.
50. Jalani, N.H., P. Choi, and R. Datta, *TEOM: A novel technique for investigating sorption in proton-exchange membranes.* Journal of Membrane Science, 2005. **254**(1–2): p. 31-38.
51. Onishi, L.M., J.M. Prausnitz, and J. Newman, *Water−Nafion Equilibria. Absence of Schroeder's Paradox.* The Journal of Physical Chemistry B, 2007. **111**(34): p. 10166-10173.
52. Kusoglu, A., B.L. Kienitz, and A.Z. Weber, *Understanding the Effects of Compression and Constraints on Water Uptake of Fuel-Cell Membranes.* Journal of The Electrochemical Society, 2011. **158**(12): p. B1504-B1514.
53. Halim, J., et al., *Characterization of perfluorosulfonic acid membranes by conductivity measurements and small-angle x-ray scattering.* Electrochimica Acta, 1994. **39**(8-9): p. 1303-1307.
54. Weber, A.Z. and J. Newman, *Transport in Polymer-Electrolyte Membranes: II. Mathematical Model.* Journal of The Electrochemical Society, 2004. **151**(2): p. A311-A325.
55. Motupally, S., A.J. Becker, and J.W. Weidner, *Diffusion of Water in Nafion 115 Membranes.* Journal of The Electrochemical Society, 2000. **147**(9): p. 3171-3177.
56. Ye, X. and C.-Y. Wang, *Measurement of Water Transport Properties Through Membrane-Electrode Assemblies.* Journal of The Electrochemical Society, 2007. **154**(7): p. B676-B682.
57. Ge, S., B. Yi, and P. Ming, *Experimental Determination of Electro-Osmotic Drag Coefficient in Nafion Membrane for Fuel Cells.* Journal of The Electrochemical Society, 2006. **153**(8): p. A1443-A1450.
58. Büchi, F.N. and G.G. Scherer, *In-situ resistance measurements of Nafion® 117 membranes in polymer electrolyte fuel cells.* Journal of Electroanalytical Chemistry, 1996. **404**(1): p. 37-43.
59. Buchi, F.N. and G.G. Scherer, *Investigation of the transversal water profile in nafion membranes in polymer electrolyte fuel cells.* Journal of the Electrochemical Society, 2001. **148**(Copyright 2001, IEE): p. 183-8.
60. Kulikovsky, A.A., *Quasi-3D Modeling of Water Transport in Polymer Electrolyte Fuel Cells.* Journal of The Electrochemical Society, 2003. **150**(11): p. A1432-A1439.

61. Zhang, Z., et al., *Spatial and temporal mapping of water content across Nafion membranes under wetting and drying conditions.* Journal of Magnetic Resonance, 2008. **194**(2): p. 245-253.
62. Gebel, G., et al., *The kinetics of water sorption in Nafion membranes: a small-angle neutron scattering study.* Journal of Physics: Condensed Matter, 2011. **23**(23): p. 234107.
63. Tabuchi, Y., et al., *Analysis of in situ water transport in Nafion® by confocal micro-Raman spectroscopy.* Journal of Power Sources, 2011. **196**(2): p. 652-658.
64. Hara, M., et al., *Temperature dependence of the water distribution inside a Nafion membrane in an operating polymer electrolyte fuel cell. A micro-Raman study.* Electrochimica Acta, 2011. **58**(0): p. 449-455.
65. Hwang, G.S., et al., *Understanding Water Uptake and Transport in Nafion Using X-ray Microtomography.* ACS Macro Letters, 2013. **2**(4): p. 288-291.
66. Tsushima, S., K. Teranishi, and S. Hirai, *Magnetic Resonance Imaging of the Water Distribution within a Polymer Electrolyte Membrane in Fuel Cells.* Electrochemical and Solid-State Letters, 2004. **7**(9): p. A269-A272.
67. Tsushima, S., et al., *Investigation of Water Distribution in a Membrane in an Operating PEMFC by Environmental MRI.* Journal of The Electrochemical Society, 2010. **157**(12): p. B1814-B1818.
68. Chen, F., et al., *Transient behavior of water transport in the membrane of a PEM fuel cell.* Journal of Electroanalytical Chemistry, 2004. **566**(1): p. 85-93.
69. Berg, P., et al., *Water Management in PEM Fuel Cells.* Journal of The Electrochemical Society, 2004. **151**(3): p. A341-A353.
70. Majsztrik, P.W., et al., *Water sorption, desorption and transport in Nafion membranes.* Journal of Membrane Science, 2007. **301**(1–2): p. 93-106.
71. Monroe, C.W., et al., *A vaporization-exchange model for water sorption and flux in Nafion.* Journal of Membrane Science, 2008. **324**(1–2): p. 1-6.
72. Ge, S., et al., *Absorption, Desorption, and Transport of Water in Polymer Electrolyte Membranes for Fuel Cells.* Journal of The Electrochemical Society, 2005. **152**(6): p. A1149-A1157.
73. Adachi, M., *Proton exchange membrane fuel cells: water permeation through Nafion (R) membranes*. 2010, Department of Chemistry-Simon Fraser University.
74. Adachi, M., et al., *Thickness dependence of water permeation through proton exchange membranes.* Journal of Membrane Science, 2010. **364**(1–2): p. 183-193.
75. Adachi, M., et al., *Water Permeation Through Catalyst-Coated Membranes.* Electrochemical and Solid-State Letters, 2010. **13**(6): p. B51-B54.
76. Wang, C.-Y., *Fundamental Models for Fuel Cell Engineering.* Chemical Reviews, 2004. **104**(10): p. 4727-4766.
77. Dutta, S., S. Shimpalee, and J.W. Van Zee, *Numerical prediction of mass-exchange between cathode and anode channels in a PEM fuel cell.* International Journal of Heat and Mass Transfer, 2001. **44**: p. 2029-42.
78. Meng, H. and C.-Y. Wang, *Electron Transport in PEFCs.* Journal of The Electrochemical Society, 2004. **151**(3): p. A358-A367.
79. Meng, H. and C.Y. Wang, *Multidimensional Modelling of Polymer Electrolyte Fuel Cells under a Current Density Boundary Condition.* Fuel Cells, 2005. **5**(4): p. 455-462.
80. Khandelwal, M. and M.M. Mench, *Direct measurement of through-plane thermal conductivity and contact resistance in fuel cell materials.* Journal of Power Sources, 2006. **161**(2): p. 1106-1115.
81. Ramousse, J., et al., *Estimation of the effective thermal conductivity of carbon felts used as PEMFC Gas Diffusion Layers.* International Journal of Thermal Sciences, 2008. **47**(1): p. 1-6.
82. Burheim, O., et al., *Ex situ measurements of through-plane thermal conductivities in a polymer electrolyte fuel cell.* Journal of Power Sources, 2010. **195**(1): p. 249-256.
83. Sadeghi, E., N. Djilali, and M. Bahrami, *Effective thermal conductivity and thermal contact resistance of gas diffusion layers in proton exchange membrane fuel cells. Part 1: Effect of compressive load.* Journal of Power Sources, 2011. **196**(1): p. 246-254.

84. Teertstra, P., G. Karimi, and X. Li, *Measurement of in-plane effective thermal conductivity in PEM fuel cell diffusion media.* Electrochimica Acta, 2011. **56**(3): p. 1670-1675.
85. Ji, M. and Z. Wei, *A Review of Water Management in Polymer Electrolyte Membrane Fuel Cells.* Energies, 2009. **2**(4): p. 1057-1106.
86. Gurau, V., H. Liu, and S. Kakaç, *Two-dimensional model for proton exchange membrane fuel cells.* AIChE Journal, 1998. **44**(11): p. 2410-2422.
87. Zhou, T. and H.T. Liu, *A General Three-Dimensional Model for Proton Exchange Membrane Fuel Cells.* Int. J. Transp. Phenom., 2001. **3**: p. 177–198.
88. You, L. and H. Liu, *A two-phase flow and transport model for the cathode of PEM fuel cells.* International Journal of Heat and Mass Transfer, 2002. **45**(11): p. 2277-2287.
89. You, L. and H. Liu, *A parametric study of the cathode catalyst layer of PEM fuel cells using a pseudo-homogeneous model.* International Journal of Hydrogen Energy, 2001. **26**(9): p. 991-999.
90. Dutta, S., S. Shimpalee, and J.W. Van Zee, *Three-dimensional numerical simulation of straight channel PEM fuel cells.* Journal of Applied Electrochemistry, 2000. **30**: p. 135-46.
91. Shimpalee, S. and S. Dutta, *Numerical Prediction of Temperature Distribution in PEM Fuel Cells.* Numerical Heat Transfer, Part A: Applications, 2000. **38**(2): p. 111-128.
92. Sui, P.C. and N. Djilali, *Analysis of Water Transport in Proton Exchange Membranes Using a Phenomenological Model.* Journal of Fuel Cell Science and Technology, 2005. **2**(3): p. 149-155.
93. Mazumder, S., *A Generalized Phenomenological Model and Database for the Transport of Water and Current in Polymer Electrolyte Membranes.* Journal of The Electrochemical Society, 2005. **152**(8): p. A1633-A1644.
94. Um, S. and C.Y. Wang, *Three Dimensional Analysis of Transport and Reaction in PEMFC*, in *ASME fuel Cell Division*. 2000, ASME: Orlando, FL. p. 19-25.
95. Um, S., C.Y. Wang, and K.S. Chen, *Computational Fluid Dynamics Modeling of Proton Exchange Membrane Fuel Cells.* Journal of The Electrochemical Society, 2000. **147**(12): p. 4485-4493.
96. Um, S. and C.Y. Wang, *Three-dimensional analysis of transport and electrochemical reactions in polymer electrolyte fuel cells.* Journal of Power Sources, 2004. **125**(1): p. 40-51.
97. Wang, Y. and C.-Y. Wang, *Modeling Polymer Electrolyte Fuel Cells with Large Density and Velocity Changes.* Journal of The Electrochemical Society, 2005. **152**(2): p. A445-A453.
98. Bvumbe Tatenda, J., et al., *Review on management, mechanisms and modelling of thermal processes in PEMFC.* Hydrogen and Fuel Cells, 2016. **1**(1): p. 1-20.
99. Berning, T., D.M. Lu, and N. Djilali, *Three-dimensional computational analysis of transport phenomena in a PEM fuel cell.* Journal of Power Sources, 2002. **106**(1-2): p. 284-294.
100. Mazumder, S. and J.V. Cole, *Rigorous 3-D Mathematical Modeling of PEM Fuel Cells.* Journal of The Electrochemical Society, 2003. **150**(11): p. A1503-A1509.
101. Mazumder, S. and J.V. Cole, *Rigorous 3-D Mathematical Modeling of PEM Fuel Cells.* Journal of The Electrochemical Society, 2003. **150**(11): p. A1510-A1517.
102. Grujicic, M. and K.M. Chittajallu, *Design and optimization of polymer electrolyte membrane (PEM) fuel cells.* Applied Surface Science, 2004. **227**(1–4): p. 56-72.
103. Al-Baghdadi, M.A.R.S., *CFD models for analysis and design of PEM fuel cells*. 2008, New York: Nova Science Publishers.
104. Pourmahmoud, N., et al., *Three-dimensional numerical analysis of proton exchange membrane fuel cell.* Journal of Mechanical Science and Technology, 2011. **25**(10): p. 2665-2673.
105. Meng, H. and C.-Y. Wang, *Large-scale simulation of polymer electrolyte fuel cells by parallel computing.* Chemical Engineering Science, 2004. **59**(16): p. 3331-3343.
106. Wu, H., X. Li, and P. Berg, *On the modeling of water transport in polymer electrolyte membrane fuel cells.* Electrochimica Acta, 2009. **54**(27): p. 6913-6927.
107. Schwarz, D.H. and S.B. Beale, *Calculations of transport phenomena and reaction distribution in a polymer electrolyte membrane fuel cell.* International Journal of Heat and Mass Transfer, 2009. **52**(17–18): p. 4074-4081.

108. Strahl, S., A. Husar, and A.A. Franco, *Electrode structure effects on the performance of open-cathode proton exchange membrane fuel cells: A multiscale modeling approach.* International Journal of Hydrogen Energy, 2014. **39**(18): p. 9752-9767.
109. Pharoah, J.G. and O.S. Burheim, *On the temperature distribution in polymer electrolyte fuel cells.* Journal of Power Sources, 2010. **195**(16): p. 5235-5245.
110. Jalani, N.H. and R. Datta, *The effect of equivalent weight, temperature, cationic forms, sorbates, and nanoinorganic additives on the sorption behavior of Nafion®.* Journal of Membrane Science, 2005. **264**(1–2): p. 167-175.
111. Kulikovsky, A.A., *Chapter 2 - Catalyst layer performance*, in *Analytical Modelling of Fuel Cells*, A.A. Kulikovsky, Editor. 2010, Elsevier: Amsterdam. p. 39-82.
112. Shimpalee, S. and J.W. Van Zee, *Numerical studies on rib & channel dimension of flow-field on PEMFC performance.* International Journal of Hydrogen Energy, 2007. **32**(7): p. 842-856.
113. Wu, H., P. Berg, and X. Li, *Steady and unsteady 3D non-isothermal modeling of PEM fuel cells with the effect of non-equilibrium phase transfer.* Applied Energy, 2010. **87**(9): p. 2778-2784.
114. Kandlikar, S.G. and Z. Lu, *Fundamental Research Needs in Combined Water and Thermal Management Within a Proton Exchange Membrane Fuel Cell Stack Under Normal and Cold-Start Conditions.* Journal of Fuel Cell Science and Technology, 2009. **6**(4): p. 044001-044001.
115. Wu, H., P. Berg, and X. Li, *Non-isothermal transient modeling of water transport in PEM fuel cells.* Journal of Power Sources, 2007. **165**(1): p. 232-243.
116. Shimpalee, S., D. Spuckler, and J.W. Van Zee, *Prediction of transient response for a 25-cm2 PEM fuel cell.* Journal of Power Sources, 2007. **167**(1): p. 130-138.
117. COMSOL, *COMSOL Multiphysics Reference Manual*. 2015.
118. Bellows, R.J., et al., *Neutron Imaging Technique for In Situ Measurement of Water Transport Gradients within Nafion in Polymer Electrolyte Fuel Cells.* Journal of The Electrochemical Society, 1999. **146**(3): p. 1099-1103.
119. Oberholzer, P. and P. Boillat, *Local Characterization of PEFCs by Differential Cells: Systematic Variations of Current and Asymmetric Relative Humidity.* Journal of The Electrochemical Society, 2014. **161**(1): p. F139-F152.
120. Lee, W.k., S. Shimpalee, and J.W. Van Zee, *Verifying Predictions of Water and Current Distributions in a Serpentine Flow Field Polymer Electrolyte Membrane Fuel Cell.* Journal of The Electrochemical Society, 2003. **150**(3): p. A341-A348.
121. Shimpalee, S., et al., *Predicting the transient response of a serpentine flow-field PEMFC: I. Excess to normal fuel and air.* Journal of Power Sources, 2006. **156**(2): p. 355-368.
122. Bednarek, T. and G. Tsotridis, *Issues associated with modelling of proton exchange membrane fuel cell by computational fluid dynamics.* Journal of Power Sources, 2017. **343**: p. 550-563.
123. Hakenjos, A., et al., *Characterising PEM Fuel Cell Performance Using a Current Distribution Measurement in Comparison with a CFD Model.* Fuel Cells, 2004. **4**(3): p. 185-189.
124. Hakenjos, A. and C. Hebling, *Spatially resolved measurement of PEM fuel cells.* Journal of Power Sources, 2005. **145**(2): p. 307-311.
125. Shimpalee, S., et al., *Macro-Scale Analysis of Large Scale PEM Fuel Cell Flow-Fields for Automotive Applications.* Journal of The Electrochemical Society, 2017. **164**(11): p. E3073-E3080.
126. Carnes, B., et al., *Validation of a two-phase multidimensional polymer electrolyte membrane fuel cell computational model using current distribution measurements.* Journal of Power Sources, 2013. **236**: p. 126-137.
127. Al-Baghdadi, M.A.R.S. and H.A.K.S. Al-Janabi, *Modeling optimizes PEM fuel cell performance using three-dimensional multi-phase computational fluid dynamics model.* Energy Conversion and Management, 2007. **48**(12): p. 3102-3119.
128. National Institute of Stadards and technology. *Thermophysical Properties of Fluid Systems*. http://webbook.nist.gov/chemistry/fluid/ 2016.

129. Zawodzinski, J.T.A., et al., *A Comparative Study of Water Uptake By and Transport Through Ionomeric Fuel Cell Membranes.* Journal of The Electrochemical Society, 1993. **140**(7): p. 1981-1985.
130. Walsby, N., et al., *Water in different poly(styrene sulfonic acid)-grafted fluoropolymers.* Journal of Applied Polymer Science, 2002. **86**(1): p. 33-42.
131. Choi, P. and R. Datta, *Sorption in Proton-Exchange Membranes: An Explanation of Schroeder's Paradox.* Journal of The Electrochemical Society, 2003. **150**(12): p. E601-E607.
132. Berning, T., A. Olesen, and S.r. Kær, *On the Diffusion Coefficient of Water in Polymer Electrolyte Membranes.* Meeting Abstracts, 2012. **MA2012-02**(13): p. 1556.
133. Shinozaki, K., H. Yamada, and Y. Morimoto, *Pt Utilization Analysis at Low RH Condition.* ECS Transactions, 2010. **33**(1): p. 1217-1227.
134. Ikeda, K., N. Nonoyama, and Y. Ikogi, *Analysis of the Ionomer Coverage of Pt Surface in PEMFC.* ECS Transactions, 2010. **33**(1): p. 1189-1197.
135. Wu, H., X. Li, and P. Berg, *Numerical analysis of dynamic processes in fully humidified PEM fuel cells.* International Journal of Hydrogen Energy, 2007. **32**(12): p. 2022-2031.
136. Kandlikar, S.G. and Z. Lu, *Thermal management issues in a PEMFC stack – A brief review of current status.* Applied Thermal Engineering, 2009. **29**(7): p. 1276-1280.
137. Burheim, O.S., et al., *Study of thermal conductivity of PEM fuel cell catalyst layers.* International Journal of Hydrogen Energy, 2014. **39**(17): p. 9397-9408.
138. Snowdon, M.R., A.K. Mohanty, and M. Misra, *A Study of Carbonized Lignin as an Alternative to Carbon Black.* ACS Sustainable Chemistry & Engineering, 2014. **2**(5): p. 1257-1263.

APPENDICES

Appendix A Governing Equations

Appendix A presents details of the conservation equations of flow and reaction from Chapter 2.

A.1 Basic Gas Mixture Relations

Some explanation of the properties of ideal gas mixtures are given here to facilitate the development of the transport equations subsequently.

The anode stream is comprised of 2 species: hydrogen and water vapor. The cathode stream is comprised of 3 species: oxygen, water vapor, and inert nitrogen. In ideal gas mixtures the total gas pressure p (Pa) of eq.(A.1) is the sum of all the partial pressures:

$$p = \sum_i p_i \quad i = \{H_2, H_2O\} \big| \text{anode} \quad i = \{O_2, H_2O, N_2\} \big| \text{cathode} \tag{A.1}$$

Gas composition is described by a series of mole fractions x_i or mass fractions ω_i of species with molar mass M_i (kg/mol) in eq.(A.2).

$$x_i = \frac{p_i}{p} \quad \omega_i = \frac{x_i M_i}{\sum_j x_j M_j} \quad x_i = \frac{\frac{\omega_i}{M_i}}{\sum_j \frac{\omega_j}{M_j}} \tag{A.2}$$

Fluid density ρ (kg m^{-3}) in ideal gas mixtures varies with pressure, temperature, and gas composition according to eq. (A.3) where M is the mean molar mass (molecular weight of the gas mixture) (kg mol^{-1}), R=8.314 J mol^{-1} K^{-1} is the universal gas constant, and T (K) is the temperature. The mole fractions or mass fractions must sum to unity; i.e. $\sum_i x_i = \sum_i \omega_i = 1$.

$$\rho = \frac{pM}{RT} = \frac{p}{RT \sum_i \frac{\omega_i}{M_i}} = \frac{p}{RT} \sum_i x_i M_i \tag{A.3}$$

Thermal conductivity k (W m^{-1} K^{-1}) of the gas mixture is calculated as a combination of the individual species thermal conductivity values k_i as in eq.(A.4).

$$k = \frac{1}{2} \left[\sum_{i=1} x_i k_i + \left(\sum_{i=1} \frac{x_i}{k_i} \right)^{-1} \right] \tag{A.4}$$

The individual species thermal conductivity values are treated as functions of temperature, and fit polynomials have been used to describe species thermal conductivity in models of the PEM fuel cell[127].

The values vary within only a few percent within the 50-100 °C range. The species thermal conductivities at 80 °C are developed from an online resource provided by the National Institutes of Standards and Technology [128].

The specific heat capacity of the gas mixture, c_p (J kg^{-1} K^{-1}) is calculated in eq. (A.5) as a mass average of the individual species molar heat capacity values $C_{p,i}$ (J mol^{-1} K^{-1}).

$$c_p = \sum_i \omega_i \frac{C_{p,i}}{M_i} \tag{A.5}$$

Fit polynomials based on temperature have been used to describe the species molar heat capacity values in PEM fuel cell models[127]. These values also appear to change little with temperature within 50-100 °C range. Nominal values are reported in Table A.1. Similarly, nominal values of kinematic viscosity from each species around 80 °C are also included in the table. The anticipated changes in composition (mass fractions) of the anode and cathode gas streams do not suggest substantial changes in the mixture viscosity from these small temperature and composition variations. For simplicity, the anode gas stream is given a constant viscosity of 11 μPa s, and the cathode a value of 20 μPa s.

Table A.1. Gas species property data at 80C from webbook.nist.gov/chemistry/fluid/

Species	k_i (W m^{-1} K^{-1})	$C_{p,i}$ (J mol^{-1} K^{-1})	μ_i (μ Pa s)
O2	0.031	29.76	23.4
N2	0.029	29.2	20.2
H2	0.212	29.1	10.0
H2O	0.022	34.3	11.6

Appendix B Interface Model

Appendix B presents varied developments of the physics of the MEA interface model.

B.1 Interface Model: MEA Composition

The MEA consists of the anode catalyst layer, membrane, and cathode catalyst layer, denoted by ACL, MEM, and CCL, respectively.

The membrane consists of solid ionomer which is nearly impervious to gas penetration, except for water vapor. The ionomer is assumed to be Nafion of a constant, selectable equivalent weight EW (g / equiv or g / mol SO_3^-), and density ρ_{lo} (g / cm^3), in both membrane and catalyst layers. Commercially available ionomer equivalent weights range from 800-1200 g / mol SO_3^- (0.8-1.2 kg / mol)[4]. Absorbed water with density ρ_W (g / cm^3) exists within the ionomer of each region. A constant crossover current density, I_x (A/m^2) is assumed: typically 0.5-1 mA/cm^2 (5-10 A/m^2), as a result of slight hydrogen gas permeation through the membrane from anode to cathode. The thicknesses of the three MEA zones, denoted as t_{ACL}, t_{MEM}, and t_{CCL} (m), refer to the dry values; prior to water uptake. Nominal membrane thicknesses refer to values at about 50% RH; hence a 22 μm membrane dry thickness is used to represent the dry thickness of a membrane that is nominally 25 μm in thickness. The transport properties contained within apply to the Nafion ionomer particularly, though other relationships could be substituted for different materials.

The anode and cathode catalyst layers contain carbon black, platinum catalyst nanoparticles, dry ionomer, absorbed water within the ionomer, and void space. To define the composition of the catalyst layers, several densities, molecular weights, and fundamental physical constants are needed. Fundamental values are listed in Table B.1[32].

Table B.1. Densities and molar masses of catalyst layer components.

Densities		(g cm^{-3})	Molar masses:		(g mole^{-1})
ρ_w	Water density	1.0	M_w	Water molar mass	18
ρ_{lo}	Ionomer dry density	2.0	EW	Ionomer equivalent weight	800-1200 (typ)
ρ_C	Carbon black density	2.2	M_{H2}	Hydrogen molar mass	2
ρ_{Pt}	Platinum density	21.0	M_{O2}	Oxygen molar mass	32

PEMFC catalyst layers are porous electrodes: mixtures of platinum catalyst nanoparticles, the carbon support, the ionomer binder, water sorbed within the ionomer, and void space that allows for reactant gas diffusion through the catalyst layers. The material components, their respective functions within the catalyst layer(s), and their transport roles are summarized in Table B.2.

Table B.2. Material components of catalyst layers.

Material component:	Function:	Transport Role:
(Pt) Pt nano-particles	Catalyst particles	Reaction site location
(C) Carbon black	Support	e- conduction to rxn site
(Io) Ionomer (typ. Nafion)	Binder	H+ conduction to rxn site
(W) Sorbed water within ionomer	Enhances conductivity of ionomer	H+ conduction to rxn site
(V) Void space	Allows gaseous reactant access	Gaseous reactant transport to rxn

Catalyst layer composition is assumed to be spatially uniform throughout its thickness. The composition of the anode catalyst layer (ACL) and cathode catalyst layer (CCL) are determined by four parameters: the platinum loading $L_{ACL,Pt}$ (~ 0.1-0.4 mg_{Pt} cm^{-2}), the weight percent Pt/Carbon in the catalyst powder Ptc_{ACL} (~20-60%), the ionomer to carbon ratio IC_{ACL} (~0.5 – 1.5) which is the mass ratio of dry ionomer to carbon within the respective catalyst layer, and its thickness t_{ACL} (~2-12 μm). Once these are known, the composition of the catalyst layer is further described by (B.1) and (B.2) where $L_{ACL,C}$ and $L_{ACL,Io}$ are the carbon and ionomer loading. The basic volume fractions within catalyst layers are of the carbon support (C), ionomer (Io) (i.e. Nafion), and void space (V) are calculated as:

$$L_{ACL,C} = \frac{\left(100 - Ptc_{ACL}\right)}{Ptc_{ACL}} L_{ACL,Pt} \tag{B.1}$$

$$L_{ACL,Io} = L_{ACL,C}\, IC_{ACL} \tag{B.2}$$

$$\varepsilon_{ACL,C} = \frac{L_{ACL,C}}{\rho_C\, t_{ACL}} \tag{B.3}$$

$$\varepsilon_{ACL,Io} = \frac{L_{ACL,Io}}{\rho_{Io}\, t_{ACL}} \tag{B.4}$$

$$\varepsilon_{ACL,V} = 1 - \left[\frac{\left(L_{ACL,Pt} / \rho_{Pt} \right) + \left(L_{ACL,C} / \rho_{C} \right) + \left(L_{ACL,Io} / \rho_{Io} \right)}{t_{ACL}} \right] \quad \text{(B.5)}$$

Several researchers have examined catalyst layer structure. Inside of the catalyst layers, pore size distributions have been examined and found to be bimodal [26, 27]. The small pores (diameter <40 nm), referred to as "primary pores", were observed to maintain their volume with the addition of ionomer, but contributed little to reactant gas transport through the thickness of the catalyst layer. The large pores (diameter > 40 nm), referred to as "secondary pores", are primarily responsible for reactant gaseous transport through the catalyst layers. They tend to fill with the addition of ionomer. Thus, the addition of ionomer content in the catalyst layers alters the overall distribution of pore sizes and volumes within the catalyst layers, and hence MEA performance. This is summarized in the Table B.3. The cited work found peak pore diameters, pore size distributions, and sample porosities by MIP (mercury intrusion porosimetry).

Table B.3. Characteristics of bi-modal pore size distribution of catalyst layers.

Ionomer does not fill these very small primary pores	Small "primary pores" (< 40 nm)	Large "secondary pores" (> 40 nm)	These larger secondary pores will tend to fill with ionomer.
	Not used for gas permeation	Path for gas permeation	
	Small pore volume is constant with ionomer content	Large pore volume decreases with Ionomer content	

Yu et al. [34] studied the composition and structure of catalyst layers formed from amorphous carbon (Pt/V_A) and graphitized carbon (Pt/V_G) electrodes. The mean pore sizes of the secondary pore structures are compared in Table B.4 with simple linear fit values for the volume-averaged mean pore diameter, d_{ACL} or d_{CCL}. For the amorphous carbon electrodes, the mean pore diameter is estimated by $d_{ACL} = 128 - 53IC_{ACL}$ (nm), and for the graphitized carbon electrodes, the mean pore diameter is estimated by $d_{ACL} = 127 - 64IC_{ACL}$ (nm). Pore diameter drops with increasing ionomer content, with no peak pore size observable by MIP when graphitized carbon electrodes were used with the largest ionomer loading

(I/C=1.5). Following the trend established by the first two points, the estimated pore diameter dropped below 40 nm (32.5 nm) at the greatest ionomer loading.

Table B.4. Measured / fit values of catalyst layer mean pore diameter vs. ionomer / carbon ratio.

Pt/V_A:	I/C=0.5	I/C=1.0	I/C=1.5		Pt/V_G:	I/C=0.5	I/C=1.0	I/C=1.5
Mean values (nm)	102 nm	74 nm	49 nm		Mean values (nm)	95 nm	63 nm	40
Fit values (nm)	102 nm	75 nm	49 nm		Fit values (nm)	95 nm	63 nm	31 nm

Porosity and tortuosity values are also needed to estimate diffusional losses for catalyst layers. Porosity, or void space fraction values estimated by densities and thicknesses can and should be corrected to reflect the effective values. The porosity values estimated by densities (void space $\varepsilon_{ACL,V}$ (V)) and those measured by MIP (gas space $\varepsilon_{ACL,Gas}$ (Gas)) are shown in Table B.5. The two values differ by between 25-60% of the total porosity. Singh et al. [36] investigated, computationally, the issue with predictive computational algorithms (characterization techniques). By 2014, this issue was being discussed as the "inaccessible pore volume" or "closed pore volume". Effective transport properties within the catalyst layers were investigated. Gaseous diffusion coefficients are impacted by the formation of inaccessible pores, but electronic and thermal conductivity were not. The differences in porosity between measured values (with MIP) and those estimated from density-based calculations (est) are attributed to isolated pores surrounded by the ionomer phase, or Nafion bubbles.

Table B.5. Estimated and measured values of catalyst layer effective porosity vs. ionomer / carbon ratio.

Pt/V_A:	I/C=0.5	I/C=1.0	I/C=1.5		Pt/V_G:	I/C=0.5	I/C=1.0	I/C=1.5
Porosity (est)	0.6996	0.5996	0.4996		Porosity (est)	0.6996	0.5996	0.4996
Porosity (MIP)	0.498	0.410	0.177		Porosity (MIP)	0.524	0.301	0

The porosity reduction due to inaccessible pores can be estimated through a second-order fit of a porosity correction (cor) which was estimated for amorphous carbon electrodes or graphitized carbon

electrodes by eq.(B.6). These volume fraction corrections are used to get the effective gas porosity as in $\varepsilon_{ACL,\mathrm{Gas}} = \varepsilon_{ACL,\mathrm{V}} + \varepsilon_{\mathrm{ACL},cor}$. Tortuosity values were fit by eq.(B.7) [34].

$$\begin{aligned} \varepsilon_{ACL,cor} &= -0.3586 + 0.459\,IC_{ACL} - 0.29\,IC_{ACL}^{\,2} \quad \text{amorphous} \\ \varepsilon_{ACL,cor} &= -0.09060 + 0.132\,IC_{ACL} - 0.076\,IC_{ACL}^{\,2} \quad \text{graphitized} \end{aligned} \tag{B.6}$$

$$\begin{aligned} \tau_{ACL,Gas} &= -0.5 + 5.2\,IC_{ACL} \quad \text{amorphous} \\ \tau_{ACL,Gas} &= 0.5 + 6.0\,IC_{ACL} \quad \text{graphitized} \end{aligned} \tag{B.7}$$

Porosity, tortuosity, and mean pore size values describe the composition and structure of the catalyst layers within the MEA. These figures are used in a later section to compute the effective diffusion coefficients of the gaseous reactants. The compositions are written as applying to the ACL, but apply to both ACL and CCL.

B.2 Interface Model: Ionomer-phase water uptake

This appendix describes the details of water uptake by perflourosulfonate membranes. The most commonly-used type of membrane is a perflourosulfonate, and the Nafion ® product of EI Dupont de Numours and Company has been the most widely studied of the perflourinated ionomers used in PEM fuel cells. Some discussion of material structure is included as background to explain water transport in the ionomer phase. Empirical formulations have been included that pertain to the Nafion product for use in modeling, because of its widespread use. The formulations apply to all the available equivalent weights of the product.

Perflourinated ionomers are created by chemically modifying the chemically modifying the regular PTFE polytetrafluoroethylene structure by a process known as sulphonation. Sulfonated side chains are added to the chemically inert, repeating PTFE structure which terminate in sulfonic acid groups (SO_3^-), as depicted in Figure B.1.

The modified chemical structure permits water uptake, and when hydrated, $H_3O^+ - SO_3^-$ groups form that enable the motion of protons (H+ ions) through the solid, which forms the ionic current. The membrane contains a mostly inert PTFE 'backbone' that is durable and chemically stable. This structure is hydrophobic and ionically non-conductive. It also holds an ionically-conductive water-absorbing hydrophilic side chain structure with sulfonic acid groups. The relative occurrence of each component is expressed in terms of the number of tetraflouroethylene groups per side chain(γ). Nafion equivalent weight, EW (g / equiv or g / mol SO_3^-) indicates the membrane's water uptake capacity as grams of polymer per equivalent, or grams per mol of sulfonic acid (SO3-) sites according to eq.(B.8). Equivalent weight influences the ionomer water uptake, volumetric swelling, and ionic conductivity.

$$EW = 100\gamma + 446 \tag{B.8}$$

Membranes are typically described as a combination of equivalent weight (first) and thickness (second). Equivalent weights of 800-1200 g / equiv are commonly-used and available. Low equivalent weight ionomers tend to absorb more water on a per-molar mass basis. They typically have less

durability due to a reduced fraction of the durable PTFE backbone structure. The increased fraction of sulfonic acid sites promotes increased ionic conductivity, as well as water uptake and volumetric swelling. Equivalent weight is indicated by a multiple of 100 (i.e. 11 is used to indicate 1100 EW). Thickness is indicated by a multiple of thickness expressed in thousandths of an inch (i.e. 2 represents a thickness of 0.002" or 51 μm). The membrane designation is a combination of the 2 numbers. For example, a Nafion 112 membrane consists of 1100 EW membrane and thickness of 51 μm.

Ionomer water uptake is modeled with reference to water activity, or gas humidity, using the ideal gas mixture relationships. The relative humidity (% RH) or water activity is defined as the ratio of the partial pressure of water in a gas mixture to the saturation pressure of water at that same temperature. Relative humidity is calculated from the operating inputs at both anode(α_A) and cathode (α_C) side adjacent cells as in eq.(B.9), where water vapor saturation pressure $P_{SAT}(T)$ is defined by a fit in eq. (B.10) with temperature (K) recommended by Mench[4].

$$\alpha_A = \frac{X_{H_2O,A}\, P_A}{P_{SAT}(T_A)} \quad \alpha_C = \frac{X_{H_2O,C}\, P_C}{P_{SAT}(T_C)} \tag{B.9}$$

$$P_{SAT}(T) = 2846.4 + 411.24(T - 273.15) - 10.554(T - 273.15)^2 + 0.16636(T - 273.15)^3 \tag{B.10}$$

Water uptake is expressed in the form of a non-dimensional water uptake λ (mol H_20/mol SO_3^-) the number of water molecules per acid site within the ionomer, which normalizes water uptake for any equivalent weight. Water uptake data from the reported experiments of Jalani and Datta [110] show that water uptake from Nafion membranes in contact with liquid water has been observed at $\lambda = 22$ water molecules per acid site, while uptake from the vapor phase ranges from $\lambda = 1 - 2$ (10% RH) to $\lambda = 14 - 16$ (100% RH). Water uptake was affected by temperature and the state of the water (whether from liquid or vapor phase). Water uptake from the liquid phase is known to be faster and larger than that from vapor-phase water. By 2007, Onishi et al. demonstrated water uptake was influenced by the "pretreatment" of the membrane, known as the "thermal history"[51]. Differences in thermal history were thought to be responsible for the many discrepancies existing in the literature containing water uptake data. Various

treatments such as pre-drying and preboiling have been seen to cause micro-structural changes, which then affect water uptake. Onishi et al. demonstrated how many ex-situ Nafion water uptake studies contained biases caused by pretreatment routines that were not representative of the in-situ PEMFC environment. The 1994 water uptake measurements from Hinatsu et al. [49] are embedded in many CFD models, and have been similarly embedded in experiments developing the interfacial resistance to water transport that are used here. Onishi et al. claimed that those measurements, where uptake from the saturated (100% RH) water vapor phase was seen as low as only $\lambda = 8-9$, were biased by an extremely hot/dry pretreatment routine. This work will substitute newer water uptake curves for the older data within the description of water transport.

These uptake studies have presented substantial variation in results. However, Jalani et al. claimed to improve the speed and accuracy of measuring water uptake in Nafion membranes with the tapered element oscillating microbalance (TEOM) technique [50]. Water uptake for this work is from a subsequent publication [110] examining the effect of equivalent weight and temperature on water sorption in Nafion. Water uptake from vapor is fit by fifth-order polynomials and water uptake from the liquid phase is assumed to be equal to $\lambda = 22$, in agreement with several previous authors [129] and [130]. Transition between saturated water vapor and liquid water occurs between water activities of 1 and 3. Figure B.2 shows the fits of water uptake data. The water uptake curves are given by eq. (B.11).

$$
\begin{aligned}
0 \le \alpha \le 1: \quad & \begin{cases}
\lambda_{298K} = 86.6748\alpha^5 - 181.3080\alpha^4 + 145.6883\alpha^3 - 49.0684\alpha^2 + 10.4402\alpha + 1.3892 \\
\lambda_{363K} = 215.0405\alpha^5 - 480.8855\alpha^4 + 393.4794\alpha^3 - 135.9413\alpha^2 + 23.9560\alpha + 0.7797 \\
\lambda(\alpha,T) = \lambda_{298K} + \dfrac{\lambda_{363K} - \lambda_{298K}}{65}(T - 298)
\end{cases} \\
1 < \alpha \le 3: \quad & \begin{cases}
\lambda_{\alpha=1,298} = 13.8161 \quad \lambda_{\alpha=1,363\mathrm{K}} = 16.4288 \\
\lambda(\alpha = 1,T) = \lambda_{\alpha=1,298\mathrm{K}} + \dfrac{\lambda_{\alpha=1,363\mathrm{K}} - \lambda_{\alpha=1,298\mathrm{K}}}{65}(T - 298) \\
\lambda(\alpha,T) = \lambda(\alpha = 1,T) + \dfrac{22 - \lambda(\alpha = 1,T)}{2}(\alpha - 1)
\end{cases} \\
\alpha > 3: \quad & \{\lambda(\alpha,T) = 22
\end{aligned}
$$

(B.11)

Having described water uptake, swelling within the ionomer is described next. The concentration of dissolved water in the ionomer, C_w (mol H_2O m^{-3}), is related to the dimensionless water content λ expressed as (B.12), where c_f is the concentration of fixed charge sites (mol SO_3^- m^{-3}), a constant for a given membrane and independent of water content. The total area-specific water content within the MEA, W (mol m^{-2}), is the sum of the sorbed ionomer-phase water content of the membrane, anode catalyst layer, and cathode catalyst layer. The total area-specific water content within the MEA, W (mol m^{-2}), is the sum of the sorbed ionomer-phase water content of the membrane, anode catalyst layer, and cathode catalyst layer in (B.13) where $\overline{\lambda}$ represents some representative water content average over the ionomer phase in the thru-plane direction. Thickness values refer to dry, unexpanded thicknesses.

$$C_w = c_f \lambda = \frac{\rho_{lo}}{EW}\lambda \tag{B.12}$$

$$W = c_f \overline{\lambda}\left(t_{ACL}\varepsilon_{ACL,lo} + t_{MEM} + t_{CCL}\varepsilon_{CCL,\mathrm{lo}}\right) \tag{B.13}$$

As a result of water sorption, the membrane phase then expands and is considered a mixture of the two phases: dry membrane and water. The volume fraction of water within the ionomer phase is described as the ratio of water volume to the sum of membrane and water volume in the hydrated ionomer as eq. (B.14), where $\mathbb{V}_w$ represents the molar volume of water (m^3 mol^{-1}) and $\mathbb{V}_{lo}$ the molar volume of the ionomer. The corresponding fractional increase in volume of the hydrated ionomer phase, ε_{dV}, compared to the dry volume, is described by eq. (B.15) [24].

$$f_v = \frac{\lambda \mathbb{V}_w}{\mathbb{V}_{lo} + \lambda \mathbb{V}_w} = \frac{\lambda\left(M_w / \rho_w\right)}{(EW / \rho_{lo}) + \lambda\left(M_w / \rho_w\right)} \tag{B.14}$$

$$\varepsilon_{dV} = \frac{\mathbb{V}_w}{\mathbb{V}_{lo}}\lambda = \frac{M_w \rho_{lo}}{EW \rho_w}\lambda \tag{B.15}$$

When the hydrated membrane takes up water, it will increase in thickness. The Nafion water uptake data described here was created from conditions different than that experienced “in-situ” in an

operating PEMFC. Water uptake was measured from unconstrained membranes. The in-situ PEMFC environment applies imperfect constraint and compression to the entire MEA. A focused study has described the in-situ constraint as preventing membrane expansion in-plane [52]. Compression of the membrane, at typical cell assembly pressures of ~2 MPa was found not to substantially decrease the membrane water content under most conditions. Contact resistance effects were expected to be far more significant in impacting performance than anticipated reductions in water uptake due to compression. Therefore, membrane volumetric swelling is treated here as occurring purely in the thru-plane direction (thickness). No account of a reduction in water uptake (due to compression) is made. Therefore, the swollen membrane thickness with known water uptake λ is:

$$t_{MEM}^{\mathbb{S}} = t_{MEM}\left(1+\varepsilon_{dV}\right) = t_{MEM}\left(1+\frac{M_W \rho_{lo}}{EW \rho_W}\lambda\right) \tag{B.16}$$

Most prior mathematical models have tended to ignore membrane volumetric swelling and constraint effects, and treated the membrane as if it has a constant thickness. The efforts to validate this model against experimental high frequency resistance (HFR) measurements have shown this treatment to be necessary in estimating ionic conductivity / ionic resistance. The experimental kinetics investigations of Liu et al.[24] estimated membrane conductivity from a swollen membrane thickness calculated in this way. Though not as obvious, those investigations contemplate a similar expansion in thickness of the cathode catalyst layer.

B.3 Interface Model: Ionomer-Phase Water and Current (Ion) Transport

This appendix gives the details of water and current transport model that is used herein.

Relations for the transport properties n_d, D_W, and σ_{Io} are needed, in addition to a description of absorption / desorption water transport. The relations for these transport parameters follow the approach of Ge et al. [57, 72], except that their incorporation / use of the water uptake curves of Hinatsu et al. [49] from 1994 is replaced with more recent 2005 data from Jalani and Datta [110]. Updated conductivity relations are included as well.

This newer water uptake data is believed to be more representative of the in-situ PEMFC environment. The ionic conductivity of Nafion 11x membrane at 80°C and 100% humidity is known to be around =17 Ω^{-1} m^{-1} [20]. The water uptake curve of Hinatsu et al. [49] predict a water uptake of λ=9 under these conditions; when combined with the popular conductivity relations of Springer et al. [45], give of only 8 Ω^{-1} m^{-1}, creating an obvious discrepancy. Later work by Onishi et al. [51] in 2007 explicitly claimed that the 1994 water uptake data was biased. Examining the presence of "Schroeder's paradox" in Nafion water uptake measurements, they suggested that a pre-drying procedure, at high temperature under vacuum, may have inappropriately influenced the membrane's morphology, and reduced the water sorption of the 1994 test. Therefore, the transport relations used in the prior work of Ge et al. [57, 72] are re-computed incorporating the 2005 water uptake data of Jalani and Datta [110].

B.3.1 Ionic Conductivity

Weber and Newman [54] studied ionic conductivity in the Nafion ionomer. Their work developed a physical model for transport in PEM and describe the changes occurring in the membrane structure as a function of the water content λ. From conductivity measurements, they observed a percolation threshold for the establishment of ionic conductivity at water uptake of about $\lambda \simeq 2$, or a water volume fraction of $f_v \simeq 0.06$. They created eq. (B.17) describing ionic conductivity, as a function of the ionomer water volume fraction and temperature, between the minimum percolation threshold of

0.06 and the saturated level of 0.45 beyond which conductivity levels off. Ionic conductivity is based on a swollen membrane thickness $t_{MEM}^{\mathbb{S}}$.

$$\begin{aligned}
\sigma_{lo}(f_v,T) &= 100\cdot 0.5\cdot(.001)^{1.5}\exp\left[\frac{15000}{R}\left(\frac{1}{303}-\frac{1}{T}\right)\right] && f_v < .061\\
\sigma_{lo}(f_v,T) &= 100\cdot 0.5\cdot(f_v-.06)^{1.5}\exp\left[\frac{15000}{R}\left(\frac{1}{303}-\frac{1}{T}\right)\right] && .061 \le f_v \le .45\\
\sigma_{lo}(f_v,T) &= 100\cdot 0.5\cdot(0.39)^{1.5}\exp\left[\frac{15000}{R}\left(\frac{1}{303}-\frac{1}{T}\right)\right] && f_v > .45
\end{aligned} \tag{B.17}$$

B.3.2 Diffusion Coefficient

The next transport parameter, the diffusion coefficient of water in the ionomer phase D_w, is expressed as related to the spatial gradient of water concentration. It is based upon the un-swollen membrane thickness t_{MEM}.

The work of Choi and Datta [131] showed that diffusive water transport within the Nafion membrane utilizes water-filled pores occurring in its microstructure. As the absorbed water content of the membrane increases, pore size grows and the water diffusion coefficient increases. It was suggested that the size of the pores available for water permeation was linearly related to the volume fraction of water in the membrane f_v. The diffusion coefficient of water, related to the gradient of chemical potential of the water, can be described as eq.(B.18) where the constant a_w was originally reported as 2.72x 10^{-9} m/s [72]. With the larger water uptake curves [110], this work uses the same value. It (D_w) can be expressed as relating to the spatial gradient in water concentration (based on un-expanded membrane coordinates) in eq.(B.19) with additional consideration of the Darken factor.

$$D_\mu(f_v,T) = a_w f_v \exp\left[2416\left(\frac{1}{303}-\frac{1}{T}\right)\right] \tag{B.18}$$

$$\begin{aligned}
D_w &= a_w f_v \frac{\partial(\ln\alpha)}{\partial(\ln\lambda)}\exp\left[2416\left(\frac{1}{303}-\frac{1}{T}\right)\right]\\
D_w &= a_w f_v \frac{\lambda}{\alpha\left(\frac{\partial\lambda}{\partial\alpha}\right)}\exp\left[2416\left(\frac{1}{303}-\frac{1}{T}\right)\right]
\end{aligned} \tag{B.19}$$

The spatial diffusion coefficient D_w incorporates the water uptake isotherm function $\lambda = \lambda(\alpha)$ at fixed temperature. D_w is then a function of water content and temperature; i.e. $D_w(\lambda, \mathrm{T})$; where α is the water activity corresponding to the water content λ through the water uptake isotherms at the temperature of interest. The derivative $\left(\frac{\partial \lambda}{\partial \alpha}\right)$ is found by differentiating the water uptake isotherm's fit polynomial. The equation is valid for water contents in the range of uptake from water vapor, i.e. $\alpha \le 1$.

Saturated water vapor occurs at α=1 and liquid water at α=3. For greater water contents, $\alpha\left(\partial\lambda/\partial\alpha\right)\big|_{\alpha\ge 1} = (1)\,\partial\lambda/\partial\alpha\big|_{\alpha=1}$. At activities below 0.4, a constant value was used for the derivative of the water uptake curve. Polynomial fitting processes tended to produce near-zero slopes at $\lambda \approx 3$, resulting from the distribution of and limited number of experimental points in the dataset at low activities. This fitting artifact will produce a nonphysical spike in the water diffusion coefficient, as was pointed out in 2012 by Berning [132]. Removal of this artifact prevents the diffusion coefficient from introducing numerical difficulties into the higher-level solution process. This work uses the derivative of the water uptake curve as eq.(B.20).

$$\frac{\partial \lambda}{\partial \alpha}(\alpha, T) = \left.\frac{\partial \lambda}{\partial \alpha}\right|_{298} + \left(\left.\frac{\partial \lambda}{\partial \alpha}\right|_{363} - \left.\frac{\partial \lambda}{\partial \alpha}\right|_{298}\right)(T - 298)/65$$

$$\left.\frac{\partial \lambda}{\partial \alpha}\right|_{298} = \begin{cases} 5.7954 & \alpha < 0.4 \\ 10.44 - 98.14\alpha + 437.06\alpha^2 - 725.23\alpha^3 + 433.37\alpha^4 & 0.4 < \alpha \le 1 \\ 57.51 & \alpha > 1 \end{cases} \qquad \text{(B.20)}$$

$$\left.\frac{\partial \lambda}{\partial \alpha}\right|_{363} = \begin{cases} 8.4916 & \alpha < 0.4 \\ 23.96 - 271.88\alpha + 1180.44\alpha^2 - 1923.54\alpha^3 + 1075.20\alpha^4 & 0.4 < \alpha \le 1 \\ 84.17 & \alpha > 1 \end{cases}$$

The diffusion coefficient of water in the Nafion membrane phase is depicted in Figure B.3 as a function of water content for the two temperatures (303 K and 353K) indicated.

B.3.3 Absorption and Desorption Coefficients

Interfacial resistance to water transport must be considered. Water transport into and out of the ionomer phase occurs at the MEA/ GDL boundary at anode and cathode sides of the interface. When the

MEA is in contact with water vapor, an interfacial jump in water content, between the actual membrane water content level, and that which would be determined by applying the equilibrium water uptake curves, develops. The size of the jump in water content relates to the flux of water into / out of the membrane through mass transfer coefficients. Experiments describing absorption / desorption via mass transfer coefficients began to be published around 2004. Chen et al.[68], and Berg et al. [69] introduced constant mass transfer coefficients. Later work by Ge et al. developed mass transfer coefficients that were not constant, but varied linearly with the volume fraction of water in the membrane [57, 72]. Later work by Adachi et al. [74] found that interfacial resistance and diffusion-based bulk resistance to water permeation were comparable for typical membrane thicknesses of 200 μm. When membrane thickness was decreased to 56 μm, Interfacial resistances to water permeation were found dominant [73]. In those experiments, neither the presence of, nor specific composition of catalyst layers, were experimentally found to influence rates of water permeation through Nafion membranes [73, 75]. The effect of catalyst layer presence on water permeation was found to be negligible. Hence, absorption and desorption mass transfer coefficients are presented here as though they apply to all Nafion-based MEA's without consideration of catalyst layer composition, thickness, etc.

Water absorption into the ionomer, and desorption out of the ionomer phase occurs as eq.(B.21) where $J_W = \left|\vec{\mathbf{J}}_W\right|$ is a net normal water flux magnitude. The flux is considered positive when the ionomer gains water and negative for water loss. The terms k_a and k_d represent mass transfer coefficients for the absorption and desorption, respectively, of water to and from the ionomer. They are assumed to be linearly related to the volume fraction of water occurring in the membrane. The term λ represents the local ionomer-phase water content at either the anode or cathode side of the MEA, and λ^{eq} represents the equilibrium water uptake, based on the temperature and water activity α in the adjacent gaseous control volume. It was further assumed that when either side of the MEA is in contact with liquid water, (α=3), then interfacial equilibrium exists, and $\lambda = \lambda^{eq}$. As implemented, the computational approach has been to increase k_a and k_d by 50x in size between a water activity of saturated vapor, $\lambda_{\alpha=1,T}$, and a fully liquid-

equilibrated sate, $\lambda_{\alpha=3,T}=22$. The absorption / desorption mass transfer terms include activation energy terms to model temperature dependence, and take the form of eq.(B.22).

$$\left.\begin{array}{ll} J_W = k_a c_f\left(\lambda^{eq}-\lambda\right) & \lambda^{eq}>\lambda \\ J_W = k_d c_f\left(\lambda^{eq}-\lambda\right) & \lambda^{eq}<\lambda \end{array}\right\} \text{ (water vapor)}$$
$$\lambda = \lambda^{eq} \quad \text{(liquid water)} \tag{B.21}$$

$$\begin{aligned} k_i(f_v,T) &= a_i f_v \exp\left[2416\left(\frac{1}{303}-\frac{1}{T}\right)\right] && \lambda \le \lambda\big|_{\alpha=1,T} \\ k_i(f_v,T) &= k_i\big|_{\alpha=1,T} + 50\,k_i\big|_{\alpha=1,T}\frac{\lambda-\lambda\big|_{\alpha=1,T}}{22-\lambda\big|_{\alpha=1,T}} && \lambda\big|_{\alpha=1,T} < \lambda \le 22 \\ k_i(f_v,T) &= 51\,k_i\big|_{\alpha=1,T} && \lambda > 22 \end{aligned} \tag{B.22}$$

The terms a_a =1.14x 10^{-5} m/s and a_d =4.60x 10^{-5} m/s matched experimental data [72]. When used with the revised, more recent water uptake curves, a value of a_a =1.00x 10^{-5} m/s better agreed with the operating cell data. Figure B.4 shows absorption and desorption mass transfer coefficients from water vapor, for 1100 equivalent weight Nafion at T=353 K, plotted as functions of dimensionless water content.

B.3.4 Electro-osmotic Drag Coefficient

Electro osmotic drag is modeled through a unit-less drag coefficient n_d (-), that also contains water content and temperature dependence. Ge et al. [57] supplied functional forms for a drag coefficient $n_d(\lambda)$ experimentally measured at temperatures of 303 K, 323 K, and 353 K. These forms pre-supposed the water uptake of Hinatsu et al. [49], however. They are re-formulated here to accommodate the water uptake functions of Jalani and Datta [110].

Liquid-equilibrated membranes were found to have a drag coefficient of 1.8 at 288 K, increasing linearly with temperature to 2.7 at 363 K. These values remain unchanged. Vapor-equilibrated values of the electro osmotic drag coefficient vary from about 0.3 at low water content to 1.13 for an MEA in contact with 100 %RH (water contents of 14-16). The drag coefficient measurements were seen to be

temperature invariant when plotted as functions of water activity α, in that work [57]. A third-order fit of drag coefficient with water activity can be seen as eq.(B.23).

$$n_d = 0.2640 + 0.4759\alpha - 0.0645\alpha^2 + 0.4593\alpha^3 \tag{B.23}$$

The combined results and fit are seen in Figure B.5. By combining the water uptake functions and above curve fit, relations describing the electroosmotic drag coefficient as a function of water content can be created for the case of the MEA in contact with water vapor. These results are seen in Figure B.6. At water contents between saturated water vapor, $\lambda_{T,\alpha=1}$, where n_d is 1.13, and $\lambda_{T,\alpha=3} = 22$ where $n_d = n_{d,liq}$, the electroosmotic drag coefficient is found by linear interpolation. The resulting relations are eq.(B.24) and eq.(B.25).

$$\left.\begin{aligned} n_d(\lambda,T) &= n_{d,303K} + (n_{d,353K} - n_{d,303K})\left(\frac{T-303.15}{50}\right) \\ n_{d,303K} &= 0.0367 + 0.1466\lambda - .0049\lambda^2 \\ n_{d,353K} &= 0.0570 + 0.1276\lambda - .0038\lambda^2 \end{aligned}\right\} 0 < \lambda \le \lambda\big|_{\alpha=1,T} \tag{B.24}$$

$$\left.\begin{aligned} n_d(\lambda,T) &= 1.13 + \left(\frac{\lambda - \lambda\big|_{T,\alpha=1}}{22 - \lambda\big|_{T,\alpha=1}}\right)(n_{d,liq} - 1.13) \\ n_{d,liq}(T) &= -1.834 + .0126T \end{aligned}\right\} \lambda\big|_{\alpha=1,T} < \lambda \le 22 \tag{B.25}$$

B.4 Interface Model: Gas-Phase Transport in Catalyst Layers

This appendix gives the details of thru-plane gas transport model that is used herein. The reactant mole fractions at the outer edge of the ACL and CCL, $X_{H_2,A}$ and $X_{O_2,C}$ are adjusted to diffusion-corrected values $X^{\mathbb{D}}_{H_2,A}$ and $X^{\mathbb{D}}_{O_2,C}$ at the effective gas diffusion thickness. To do so, effective diffusion coefficients $D^{\text{eff}}_{H_2,\text{ACL}}$ of the ACL, and $D^{\text{eff}}_{O_2,\text{CCL}}$ of the CCL are needed.

The through-plane gas-phase transport of the reactants occurs due to diffusion; pressure-driven flow isn't considered. The consumption of reactants causes a gradient in the reactant mole fractions between the outer edge of the ACL/CCL and the membrane-catalyst layer interfaces. A simplified approach is employed; it assumes all the reactants to be consumed (by stoichiometric requirements) must diffuse over an effective length. Effective length is treated as a known here, but is determined analytically by conduction effects in a later section.

Gaseous diffusion takes place, on the macro-scale, through the network of secondary pores in each catalyst layer. It is now understood that the mean secondary pore diameter of porous catalyst layers is comparable in size to the mean free path of hydrogen and oxygen molecules. Hence, both molecular diffusion and Knudsen diffusion mechanisms must be accounted for. Porosity and tortuosity effects can be accounted for to produce an effective oxygen or hydrogen diffusivity. A reduction in mole fraction, at the catalyst layer's mean reaction depth, can be calculated given the reactant flux necessary for the given current density.

In the anode, the free space diffusivity of hydrogen into water vapor can be estimated by calculating the harmonic mean of the molecular and Knudsen diffusion coefficients according to (B.26), where $D^{F}_{H_2,ACL}$ represents the free space diffusivity of hydrogen into water vapor ($cm^2\ s^{-1}$), $D^{K}_{H_2,\text{ACL}}$ in eq. (B.27) represents the Knudsen diffusivity of hydrogen from [35], and $D^{M}_{H_2,\text{ACL}}$ in eq. (B.28)represents the binary molecular diffusivity of hydrogen into water vapor from [4]. These diffusional coefficients are

free space values, not taking into account the porosity and tortuosity of the catalyst layer. The empirical formulas return units of ($cm^2\ s^{-1}$), but these will subsequently be referred to in MKS units.

$$D^F_{H_2,ACL} = \frac{D^M_{H_2,\mathrm{ACL}}\, D^K_{H_2,\mathrm{ACL}}}{D^M_{H_2,\mathrm{ACL}} + D^K_{H_2,\mathrm{ACL}}} \tag{B.26}$$

$$D^K_{H_2,\mathrm{ACL}} = 485{,}000\, d_{ACL}\sqrt{\frac{T_A}{2}} \tag{B.27}$$

$$D^M_{H_2,\mathrm{ACL}} = (.0312)(101.3)\frac{T_A^{1.75}}{P_A} \tag{B.28}$$

In the cathode, the free space diffusivity of oxygen into water vapor can be estimated by calculating the harmonic mean of the molecular and Knudsen diffusion coefficients according to (B.29), where $D^F_{O_2,\mathrm{CCL}}$ represents the free space diffusivity of oxygen into water vapor ($cm^2\ s^{-1}$), $D^K_{O_2,\mathrm{CCL}}$ represents the Knudsen diffusivity of oxygen from [35], $D^M_{O_2,\mathrm{CCL}}$ represents the binary molecular diffusivity of oxygen into water vapor from [4]. These diffusional coefficients do not yet take into account the porosity or tortuosity of the catalyst layer.

$$D^F_{O_2,\mathrm{CCL}} = \frac{D^M_{O_2,\mathrm{CCL}}\, D^K_{O_2,\mathrm{CCL}}}{D^M_{O_2,\mathrm{CCL}} + D^K_{O_2,\mathrm{CCL}}} \tag{B.29}$$

$$D^K_{O_2,\mathrm{CCL}} = 485{,}000\, d_{CCL}\sqrt{\frac{T_C}{32}} \tag{B.30}$$

$$D^M_{O_2,\mathrm{CCL}} = (.0425)\frac{T_C^{2.334}}{P_C} \tag{B.31}$$

Effective diffusion coefficients within the ACL/CCL must take into account the porosity and tortuosity of each catalyst layer. The dry ionomer is assumed to occupy volume fractions ($\varepsilon_{ACL,Io}$, $\varepsilon_{CCL,Io}$) based upon the mass of ionomer and catalyst layer thickness. A fraction of inactive pores ($\varepsilon_{ACL,\mathrm{corr}}$, $\varepsilon_{CCL,\mathrm{corr}}$) is assumed to exist within the catalyst layers closed off from gas transport by the ionomer[36].

Additionally, the ionomer within each catalyst layer will swell with water uptake, and this swelling impacts the effective gaseous diffusion coefficient through each catalyst layer.

In the presence of humidity, the pore volume available for gas transport was observed decreasing further as the ionomer swells with water uptake [34] when it is exposed to increasing humidity levels. In those experimental results, no quantitative explanation, or fit, was offered to explain the observed drop in $\varepsilon_{CCL,Gas}$ with increasing humidity. To quickly fit these results, assume that the effective gas porosity $\varepsilon_{\mathrm{CCL},Gas}$ in the dry state is compressed by water uptake within the ionomer phase of each catalyst layer to reach a reduced value $\varepsilon^{\mathbb{S}}_{\mathrm{CCL},Gas}$. Further, the pressure term is considered to be proportional to the water uptake λ within each CL. The fit of eq.(B.32) develops, where the superscript $\mathbb{S}$ refers to the swollen, or humidified, state. The constant -.016 was only chosen to give a fit of the data.

$$\varepsilon^{\mathbb{S}}_{ACL,Gas} = \varepsilon_{\mathrm{ACL},Gas} e^{-.016\lambda_1} \quad \varepsilon^{\mathbb{S}}_{CCL,Gas} = \varepsilon_{\mathrm{CCL},Gas} e^{-.016\lambda_3} \tag{B.32}$$

Multiple measurements of well-defined cathode catalyst layer compositions were made with variations in humidity [34]. The work was augmented with experimental measurements of pore size distribution and porosity. Utilizing the relations developed for the composition of catalyst layers developed earlier, and the water uptake curves explained previously, fits of effective diffusion coefficients are given in eq.(B.33) and eq.(B.34) from that experimental data.

$$D^{\mathrm{eff}}_{H_2,\mathrm{ACL}} = D^{F}_{H_2,\mathrm{ACL}} \frac{\varepsilon^{\mathbb{S}}_{ACL,Gas}}{\tau_{ACL,Gas}} = D^{F}_{H_2,\mathrm{ACL}} \frac{\varepsilon_{\mathrm{ACL},Gas} e^{-.016\lambda_1}}{\tau_{ACL,Gas}} \tag{B.33}$$

$$D^{\mathrm{eff}}_{O_2,\mathrm{CCL}} = D^{F}_{O_2,\mathrm{CCL}} \frac{\varepsilon^{\mathbb{S}}_{CCL,Gas}}{\tau_{CCL,Gas}} = D^{F}_{O_2,\mathrm{CCL}} \frac{\varepsilon_{\mathrm{CCL},Gas} e^{-.016\lambda_3}}{\tau_{CCL,Gas}} \tag{B.34}$$

The second formula for the effective oxygen diffusivity is compared with the available experimental data in Figure B.7. In the figure, λ_3 was found from the previously given water uptake curves, as a function of the given humidity and temperature. The water uptake of the ionomer in the catalyst layer is assumed to be the same as that of a bulk membrane. Tortuosity is assumed to remain unchanged with humidification. The results show good agreement for multiple compositions. The

highest ionomer loadings are problematic where the readings are too small to be discerned. Experimental readings appear to reach a floor near 0.001 $cm^2\ s^{-1}$. Those compositions are not of concern here, however.

Few works were able to correlate estimates of catalyst layer gaseous diffusion coefficients with actual measurements. Yu and Carter [32] found that the previously-widespread Bruggeman correction substantially underestimated tortuosity, and significantly over-predicted the effective CCL diffusivity. Earlier work from 2008, by Wang and Feng [29], had assumed typical effective cathode diffusivity to be 0.1 $cm^2\ s^{-1}$: 5 times larger than what was later found experimentally.

B.5 Interface Model: Superficial Exchange Current Density of Anode (HOR)

This appendix gives the details of formulating the superficial exchange current density for the HOR $I_{0,A}$ (A/m^2), occurring at the anode electrode.

The superficial exchange current density term $I_{0,A}$ is a product of several factors in eq.(B.35); the form attempts to separate out and identify the different influences of temperature, gas concentration, catalyst layer morphology, and platinum loading. The exchange current density is proportional to the mole fraction of hydrogen $X^{\mathbb{D}}_{H_2,A}$ present, at the mean reaction depth, in the anode catalyst layer. The term $i_{0,\mathrm{ACL}}$ (A cm$^{-2}{}_{\mathrm{Pt}}$) refers to the specific exchange current density of the HOR on platinum catalyst, expressed with the basis of the active area of platinum catalyst. The values are reported below in Table B.6 from [37]. It was estimated to be between 0.24 or 0.26 (A cm$^{-2}{}_{\mathrm{Pt}}$) at a temperature of 80 °C, and a temperature dependence was investigated. It is treated as a fundamental physical property, meaning that is doesn't change with catalyst layer structure, humidity, or factors other than temperature. It is not a parameter of the problem to be adjusted matching experimental data. $L_{\mathrm{ACL},Pt}$ (mg$_{\mathrm{Pt}}$ /cm^2) is the anode platinum catalyst loading, known from the catalyst layer composition.

$$I_{0,A} = 100^2\, X^{\mathbb{D}}_{H_2,A}\, i_{0,\mathrm{ACL}}\, L_{\mathrm{ACL},Pt}\, A_{\mathrm{ACL},Pt}\, 10 \tag{B.35}$$

Table B.6. Specific exchange current density reported from experiment at 40 °C and 80 °C from humidified H_2.

Temperature [K]	$i_{0,\mathrm{ACL}}$: Butler-Volmer fit (mA cm$^{-2}{}_{\mathrm{Pt}}$)	$i_{0,\mathrm{ACL}}$: Linear fit (mA cm$^{-2}{}_{\mathrm{Pt}}$)
313	120±40	135±40
353	240±40	260±30

The catalyst-specific exchange current density for the HOR on the carbon-supported platinum catalyst, $i_{0,\mathrm{ACL}}$ (A cm$^{-2}{}_{\mathrm{Pt}}$), has dependencies of temperature and hydrogen partial pressure [37] seen in eq.

(B.36). The term $i^{*}_{0,\mathrm{ACL}}$ represents the value at reference hydrogen partial pressure of 101 kPa and 80°C (353K) of 0.26 A cm^{-2}_{Pt} [23, 37]. The activation energy of the HOR, E_A^{rev} (kJ mol^{-1}), was found to be 16 kJ mol^{-1}. The dependence of anode losses on hydrogen concentration is modeled through the diffusion-corrected hydrogen mole fraction $X^{\mathbb{D}}_{H_2,A}$ present at the mean reaction depth in the ACL. Mass-transport or diffusional losses result when H_2 molecules can't reach the CCL reaction sites to support the desired reaction rate. As $X^{\mathbb{D}}_{H_2,A}$ diminishes due to diffusional losses, superficial exchange current density $I_{0,A}$ decreases and the anode overpotential η_A grows.

$$i_{0,\mathrm{ACL}} = i^{*}_{0,\mathrm{ACL}} \left(\frac{P_A X^{\mathbb{D}}_{H_2,A}}{101{,}300} \right) \exp\left[\left(\frac{-E_A^{rev}}{RT_{CCL}} \right) \left(1 - \frac{T_{ACL}}{353} \right) \right] \qquad \text{(B.36)}$$

The term $A_{\mathrm{ACL},Pt}$ (m^2_{Pt} /g_{Pt}) is the anode catalyst layer's electrochemically available catalyst area, (ESA or ECSA), expressed per gram of catalyst, indicating morphology effects. This represents the surface area of the Pt catalyst that is simultaneously in contact with the reactant gas, the electronic conducting phase, and the proton conducting phase of the catalyst layer. It has been found to be typically 46-60 m^2_{Pt} /g_{Pt} [4, 24] at fully-humidified conditions. This term measures the effectiveness of the catalyst layer microstructure and design in employing the catalyst to create maximum effective active area where the reaction can take place. Experiments with typical catalyst layer structures showed that this area could drop by 50% as humidity decreases from 100%RH to 50%RH [21, 24, 133, 134].

Recent works have shown that the reduction in area $A_{\mathrm{ACL},Pt}$ with reduced humidity can have a significantly different character, depending on the type of carbon black used as the basis for the catalyst layer. Carbon black catalyst powders are available with varying pore-size distributions (PSD) and surface areas. Pores with diameters < 20 nm create catalyst layer water uptake by capillary condensation, conducting protons to the active sites with surface-adsorbed water on the carbon support. The commercially-available product Ketjen Black (Tanaka Kihinzoku Kogyo (TKK)) has such a wide pore size distribution. This approach allows less ionomer to be used in the catalyst layer under fully-

humidified conditions [21], but produces a sharp and unpredictable drop in ECSA with reduced humidity[134]. Carbon supports with larger PSD tend to have higher ionomer coverage [133] of the catalyst sites, and less reliance on surface-adsorbed water for proton conduction within the CL. The commercially-available product Vulcan XC-72 (Cabot Corp) was found to be one example.

For such a carbon black support, the ECSA is treated here as decreasing linearly with local CL water content λ, and not humidity [24], from 0-100 %RH in eq.(B.37). This introduces more non-linearity into the problem of determining the current density and water contents within the MEA.

$$A_{ACL,Pt} = A_{\mathrm{ACL},Pt}^{100\%RH}\left(1-0.9\left(1-\lambda_{ACL}\Big/\lambda\Big|_{\alpha=1,T}\right)\right) \tag{B.37}$$

In summary, this appendix gives the details of formulating the superficial exchange current density for the HOR $i_{0,A}$ (A m^{-2}), occurring at the anode electrode. This is used for formulating purely kinetic losses. Ohmic losses in the ACL have not yet been considered; these can become significant under sub-saturated conditions. The combined ohmic and kinetic losses are needed, and will be addressed subsequently. The purely kinetic losses of the anode are typically small and have been routinely ignored [42] in modeling efforts.

B.6 Interface Model: Superficial Exchange Current Density of Cathode (ORR)

This appendix gives the details of formulating the superficial exchange current density for the ORR $I_{0,C}$ (A/m^2), occurring at the cathode electrode.

The superficial exchange current density term $I_{0,C}$ is a product of several factors in eq.(B.38); this form attempts to separate the different influences of temperature, gas concentration, catalyst layer morphology, and platinum loading. The exchange current density is proportional to the mole fraction of oxygen $X^{\mathbb{D}}_{O_2,C}$ present, at the mean reaction depth, in the anode catalyst layer. The term $i_{0,CCL}$ (A cm$^{-2}{}_{Pt}$) refers to the catalyst-specific exchange current density of the ORR on platinum catalyst,, expressed with the basis of the active area of platinum catalyst. The term $L_{CCL,Pt}$ (mg$_{Pt}$ /cm^2) is the cathode platinum catalyst loading, known from the catalyst layer composition, and $A_{CCL,Pt}$ (m$^2{}_{Pt}$ /g$_{Pt}$) is the cathode catalyst layer's electrochemically available surface area (ECSA), which is as previously discussed for the anode.

$$I_{0,C} = 100^2 \, i_{0,CCL} \, L_{CCL,Pt} \, A_{CCL,Pt} \, 10 \tag{B.38}$$

The catalyst-specific exchange current density for the ORR on the carbon-supported platinum catalyst, $i_{0,CCL}$ (A cm$^{-2}{}_{Pt}$), has dependencies of temperature and oxygen partial pressure in eq. (B.39) where $i^*_{0,CCL}$ represents the value at reference oxygen partial pressure of 101.3 kPa and 80°C (353K). It was found to be 2.5 x 10^{-8} [19] and later 1.5 x 10^{-8} A cm$^{-2}{}_{Pt}$ [24]. The kinetic reaction order, with respect to oxygen partial pressure was found to be 0.54, and E_c^{rev}, the activation energy of the ORR (at zero overpotential / reversible cell potential), was found to be 67 kJ mol^{-1}. The dependence of cathode losses on oxygen concentration is modeled through the diffusion-corrected oxygen mole fraction $X^{\mathbb{D}}_{O_2,C}$ present at the mean reaction depth in the CCL. Mass-transport or diffusional losses result when oxygen molecules can't reach the CCL reaction sites to support the desired reaction rate. As $X^{\mathbb{D}}_{O_2,C}$ diminishes due to diffusional losses, superficial exchange current density $I_{0,C}$ decreases and the cathode overpotential η_c grows.

$$i_{0,CCL} = i^{*}_{0,CCL}\left(\frac{P_C X^{\mathbb{D}}_{O_2,C}}{101,300}\right)^{0.54} \exp\left[\left(\frac{-E^{rev}_c}{RT_{CCL}}\right)\left(1-\frac{T_{CCL}}{353}\right)\right] \quad \text{(B.39)}$$

In summary, this appendix gives the details of formulating the superficial exchange current density for the ORR $I_{0,C}$ (A/m^2), occurring at the cathode electrode. This is used for formulating purely kinetic losses. Cathode kinetic losses can be quite substantial (~ 0.3-0.4 V), and have been the object of tremendous amounts of catalyst research. Ohmic losses in the CCL have not yet been considered; these can become significant under sub-saturated conditions. Combined ohmic and kinetic losses are needed, and will be described subsequently.

B.7 Interface Model: Effective Losses of the CCL

The effective cathode catalyst layer resistance is derived from an analytical solution that was presented somewhat contemporaneously by Wang and Feng [29, 30], as well as Neyerlin et al. [19, 20].

The analytical solution was developed incorporating several simplifying assumptions come into play within the catalyst layers. The spatial distribution of all material phases (volume fractions) within the CL is assumed constant, as is the ionomer water content within the CCL, where there is constant ionic conductivity. Another key assumption of this analytical solution is that the solid phase, or electronic phase, is thought to have constant phase potential through the thickness of the electrode; electrical conduction losses are assumed insignificant. Electrical contact resistances are incorporated at the outer edge of the catalyst layers. Under these conditions, variations in reaction rate within a porous electrode are dependent upon conduction losses and the Tafel slope of the reaction.

The CCL is assumed to be effectively isothermal [29]. The temperature rise created by the catalyst layer's heat generation was estimated to be as small as 0.03°C at 1.0 A cm^{-2} using approximate conductivity properties. This temperature rise was too small to create significant variation in thermodynamic voltage or ORR kinetics within the cathode.

Reactant gaseous concentration levels are assumed to be constant within the variable depth of the catalyst layer, which is also referred to as the absence of O_2 diffusion resistances. Wang and Feng estimated that, in most ranges of fuel cell operation, diffusional losses within the CCL would be insignificant[29]. Detailed numerical analysis of the reaction rate distribution throughout the thickness of a PEMFC catalyst layer has also been performed by modeling. Wu et al. carried out the full analysis numerically, and found that reaction rates located to minimize conduction losses, without noticeable impact from gas concentration losses[135]. This was said to be due to the form of the Butler-Vollmer equation, where the variations in the exponential term (for overpotential) had much more impact on reaction rates than the variations in the linear term (where exchange current density carries a linear

dependence on the gaseous reactant concentration term). The present work utilizes this analytical solution, but with the small diffusional correction of section 2.3.6 applied.

The electrode sheet resistance $R_{CCL}^{H^+,sheet}$ (Ω m^2) in eq. (B.40) expresses the effective protonic conduction resistance through the electrode, assuming all current travels through the entire thickness of the electrode. The sheet resistance calculation assumes that the electrode swells in thickness with water uptake just as the membrane does. The term where t_{CCL} (m) represents the CCL dry thickness, $\varepsilon_{CCL,Io}$ (-) the dry volume fraction of ionomer in the CCL, $\varepsilon_{dV,3}$ (-) the fractional volume swelling with water uptake at the cathode side of the MEA, $\sigma_{Io,3}$ (Ω^{-1} m^{-1}) the ionic conductivity calculated from water content and temperature, and $\tau_{CCL,Io}$ (-) the tortuosity of the ionomer within the CCL.

The tortuosity of the ionomer conduction network within a typical series of CCL constructions, with variable ionomer contents, was measured by Liu and Murphy [24]. Tortuosity values were about unity with sufficient combinations of both ionomer loading and humidity, but increased at low ionomer contents and dry conditions (low humidity). They were able to fit tortuosity as a single function of swollen ionomer volume fraction. The empirical fit of their results is eq.(B.41). A fit of the tortuosity of the ionomer conduction network is shown Figure B.8. For swollen or wet ionomer volume fractions greater than approximately 0.15, the tortuosity was found to be unity. Volume fractions less than 0.06-0.07 produced tortuosity values reaching 10.

$$R_{CCL}^{H^+,sheet} = \frac{t_{CCL}\tau_{CCL,Io}\left(1+\varepsilon_{dV,3}\right)}{\sigma_{Io,3}\varepsilon_{CCL,Io}} \tag{B.40}$$

$$\tau_{CCL,Io} = \begin{cases} 1.1153 - \dfrac{.0772}{\varepsilon_{CCL,Io}^{\mathbb{S}}} - \dfrac{.0028}{\varepsilon_{CCL,Io}^{\mathbb{S}\ 2}} + \dfrac{.0024}{\varepsilon_{CCL,Io}^{\mathbb{S}\ 3}} & \varepsilon_{CCL,Io}^{\mathbb{S}} = \varepsilon_{CCL,Io}\left(1+\varepsilon_{dV,3}\right) < 0.18 \\ 1 & \varepsilon_{CCL,Io}^{\mathbb{S}} = \varepsilon_{CCL,Io}\left(1+\varepsilon_{dV,3}\right) \geq 0.18 \end{cases} \tag{B.41}$$

A Dimensionless performance parameter θ_{CCL} in eq. (B.42) is the ratio of proton conduction resistance to kinetic resistance within the CCL[20]. The numerator includes the sheet resistance and

current density. The denominator is the Tafel slope of the ORR expressed as b in V/decade. It has been found as 70 mV/decade at 80 °C [19].

$$\theta_{CCL} = \frac{I R_{CCL}^{H^+,\text{sheet}}}{2.303 \frac{RT_{CCL}}{1F}} = \frac{R_{CCL}^{H^+,\text{sheet}}}{b/I} = \frac{R_{CCL}^{H^+}}{R_{CCL}^{\eta}} \tag{B.42}$$

When $\theta_{CCL} \ll 1$, catalyst layer conduction losses are not significant. The voltage drop through the thickness of the ccl ionomer becomes negligible (i.e. the potential is constant), and there is a uniform distribution of current, due to the ORR, occurring through the CCL thickness. The CCL catalyst utilization is said to be uniform, or having 100 % utilization. Lowered catalyst utilization of 90% is predicted when θ_{CCL} reaches 0.15. As θ_{CCL} grows larger the ORR reaction distribution within the CCL occurs primarily the membrane/CCL interface, while reaction rate at the outer edge of the catalyst layer is much reduced.

The effective catalyst layer conduction resistance $R_{CCL}^{H^+,\text{eff}}$ (Ω m^2) is then calculated from the sheet resistance $R_{CCL}^{H^+,\text{sheet}}$ and the resistance correction factor as $\chi_{CCL}(\theta_{CCL})$ as eq.(B.43) [20]. The correction factor $\chi_{CCL}(\theta_{CCL})$ dependence on θ_{CCL} grows from a value of $\chi_{CCL}(0) = 1$ to $\chi_{CCL}(1) = 4/3$ to $\chi_{CCL}(30) = 5.908$. The exact analytical formulation would be costly to perform repeatedly, and so the results were fit with an approximate function in eq. valid between 0 and 30. Values below and above that range were limited to 1 and 5.908, respectively.

$$R_{CCL}^{H^+,\text{eff}} = \frac{1}{3} \frac{R_{CCL}^{H^+,\text{sheet}}}{\chi_{CCL}(\theta_{CCL})} \tag{B.43}$$

$$\chi_{CCL}(\theta_{CCL}) = 1.008 + 0.2371\theta_{CCL} - 0.00236\theta_{CCL}^{\ 2} \tag{B.44}$$

The fit function $\chi_{CCL}(\theta_{CCL})$ is compared to exact values in Figure B.9. The agreement is thought to be adequate over the practical range where the relationship must be used.

The thickness of cathode catalyst layer can then be viewed as being split into a conduction and diffusion thickness, as indicated in Figure B.10. The effective conduction length, $t_{CCL}^{\mathbb{C}}$, and the effective

gas diffusion length, $t_{CCL}^{\mathbb{D}}$, are defined by eq. (B.45) and (B.46); they sum to the swollen/expanded cathode catalyst layer thickness $t_{CCL}\left(1+\varepsilon_{dV,3}\right)$. This effective diffusion length is used in section 2.3.6 to ascertain the reduction in reactant mole fractions within the cathode catalyst layer.

$$t_{CCL}^{\mathbb{C}} = t_{CCL}\left(1+\varepsilon_{dV,3}\right)\frac{1}{3\chi_{CCL}(\theta_{CCL})} \tag{B.45}$$

$$t_{CCL}^{\mathbb{D}} = t_{CCL}\left(1+\varepsilon_{dV,3}\right)\left(1-\frac{1}{3\chi_{CCL}(\theta_{CCL})}\right) \tag{B.46}$$

B.8 Interface Model: Effective Losses of the ACL

The voltage drop occurring in the ACL is modeled by an analytical solution which accounts for both kinetic and ohmic losses simultaneously. Kulikovsky[111] developed an analytical solution for anode overpotential, in the absence of gas-phase diffusional losses (assuming ideal oxygen transport), which will be expanded somewhat to account for the swelling effects which were not originally considered.

The ACL overpotential first depends on the ACL electrode sheet resistance, $R_{ACL}^{H^+,\text{sheet}}$ (Ω m^2). The sheet resistance of the anode is the protonic conduction resistance through the electrode, assuming all current travels through the entire thickness of the electrode. The sheet resistance calculation in eq. (B.47) assumes that the ACL swells in thickness with water uptake just as was described for the CCL. The term where t_{ACL} (m) represents the CCL dry thickness, $\varepsilon_{ACL,Io}$ (-) the dry volume fraction of ionomer in the CCL, $\varepsilon_{dV,1}$ (-) the fractional volume swelling with water uptake at the anode side of the MEA, $\sigma_{Io,1}$ (Ω^{-1} m^{-1}) the ionic conductivity calculated from water content and temperature, and $\tau_{\text{ACL},Io}$ (-) the tortuosity of the ionomer within the ACL. The tortuosity of the ACL ionomer conduction network is calculated in the same manner as was done for the CCL.

$$R_{ACL}^{H^+,\text{sheet}} = \frac{t_{ACL}\tau_{\text{ACL},Io}\left(1+\varepsilon_{dV,1}\right)}{\sigma_{Io,1}\varepsilon_{ACL,Io}} \tag{B.47}$$

The thickness of anode catalyst layer can be viewed as being split into a conduction and diffusion thickness, as indicated in Figure B.11. The effective conduction thickness, $t_{ACL}^{\mathbb{C}}$, and the effective gas diffusion thickness, $t_{ACL}^{\mathbb{D}}$, sum to the expanded anode catalyst layer (ACL) thickness in eq. (B.48). The HOR reaction occurs within a thin strip at the membrane side of the ACL, and so the ACL diffusional thickness is essentially the entire catalyst layer thickness. Conduction losses are considered within a different analytical framework, which is to be presented next. This effective diffusion length is used in section 2.3.6 to ascertain the reduction in reactant mole fractions within the anode catalyst layer.

$$t_{ACL}^{\mathbb{C}} \simeq 0 \quad t_{ACL}^{\mathbb{D}} = t_{ACL}\left(1+\varepsilon_{dV,1}\right) \tag{B.48}$$

The anode loss η_A (V) and the operating current density I are related as eq. (B.49), where $\sigma_{ACL}^{\text{eff}}$ is the catalyst layer effective conductivity. The quantity under the radical is made small (<1) by the large superficial exchange current density of the HOR, $I_{0,A}$, making the sinh function nearly linear in character with respect to current density I. To a first approximation, overpotential η_A can vary linearly with current. The term $I_{0,A}$ will drop with diffusional reductions within the ACL , and with reductions in the ACL ionomer-phase water content (due to electroosmotic drag). The ACL conductivity $\sigma_{ACL}^{\text{eff}}$ will also decline with increasing current density for the same reason. Accounting for the thickness expansion of the ACL, this formula can incorporate the effective anode sheet resistance $R_{ACL}^{H^+,\text{sheet}}$ of the ACL as eq. (B.50).

$$\eta_A = \frac{RT_{ACL}}{\upsilon F}\sinh^{-1}\left(I\sqrt{\frac{t_{ACL}^{\mathbb{S}}}{2\left(\frac{RT_{ACL}}{\upsilon F}\right)I_{0,A}\sigma_{ACL}^{\text{eff}}}}\right) \tag{B.49}$$

$$\eta_A = \frac{RT_{ACL}}{\upsilon F}\sinh^{-1}\left[I\sqrt{\frac{R_{ACL}^{H^+,\text{sheet}}}{2\left(\frac{RT_{ACL}}{\upsilon F}\right)I_{0,A}}}\right] \tag{B.50}$$

If a small argument approximation is applied to linearize the arcsinh function, the relation can be re-written to appear explicitly linear as eq. (B.51). The ACL voltage losses have been assessed, experimentally, as being not completely linear with current density in a hydrogen concentration cell [20, 23, 37]. This last linearization is not employed here.

$$\eta_A = I\sqrt{\frac{RT_{ACL}}{2\upsilon F}\frac{}{I_{0,A}}R_{ACL}^{H^+,\text{sheet}}} = I\sqrt{R_{ACL}^{H^+,\text{kinetic}}R_{ACL}^{H^+,\text{sheet}}} \tag{B.51}$$

The effective catalyst layer conduction resistance $R_{ACL}^{H^+,\text{eff}}$ (Ω m^2) is calculated from eq.(B.52), where the combined kinetic and ohmic losses of the ACL in eq. (B.50) are linearized to an effective resistance.

$$R_{ACL}^{H^+,\text{eff}} = \frac{\eta_A}{I} \tag{B.52}$$

Finally, the bounds of validity of this anode loss approximation are addressed. This anode loss relationship was formed using a small argument simplification, described as the low-current approximation. The anode loss estimate has eq. (B.53) as a restriction on its validity.

$$I\sqrt{\frac{R_{ACL}^{H^+,\text{sheet}}}{2\left(\frac{RT_{ACL}}{\upsilon F}\right)I_{0,A}}} < \coth\left(\frac{2I_{0,A}R_{ACL}^{H^+,\text{sheet}}}{\left(\frac{RT_{ACL}}{\upsilon F}\right)}\right) = \sqrt{\frac{R_{ACL}^{H^+,\text{kinetic}}}{R_{ACL}^{H^+,\text{sheet}}}}\frac{IR_{ACL}^{H^+,\text{sheet}}}{\left(\frac{RT_{ACL}}{\upsilon F}\right)} < \coth\left(\frac{R_{ACL}^{H^+,\text{sheet}}}{R_{ACL}^{H^+,\text{kinetic}}}\right) \tag{B.53}$$

With practical ACL compositions, the right-most ratio is significantly greater than 1, and so the coth function produces a result of very nearly unity. This relationship is thus valid when the ratio of ACL kinetic resistance $R_{ACL}^{H^+,\text{kinetic}}$ to ACL sheet resistance $R_{ACL}^{H^+,\text{sheet}}$ is suitably small in relation to the current density. It was noted that the PEMFC anode consistently obeys this low-current approximation, termed as the linear mode[111]. Should ACL catalyst loading be greatly reduced, the validity of this relation needs to be re-assessed in terms of the reduced superficial exchange current density $I_{0,A}$ to be expected[39].

B.9 Interface Model: Temperature Profile

This appendix gives the details of the interface model's calculation of the MEA temperature profile and heat fluxes into the adjacent computational domains. A 1-D temperature profile in the MEA is depicted in Figure 2.5. A general heat transport equation is applied to the MEA. The thermal conductivities and heat generation terms of each region of the MEA are collected. A simultaneous solution of the 7 temperature values (5 unknowns) is developed to produce a steady-state temperature profile and the needed heat fluxes into the anode and cathode flow domains.

Heat transport in the thru-plane direction occurs by conduction, with the thermal conductivity being hydration-dependent. The regions of the MEA are thought to be isotropic, and thermal contact resistances between the layers of the MEA are thought to be negligible[98]. The governing equation of heat transport can be written as (B.54), where κ_i^{eff} refers to the thermal conductivity (W m^{-1} K^{-1}), T the temperature (K), and $\dot{Q}_i$ the superficial heat source (W m^{-2}), and t (m) the layer thickness. The subscript i refers to the three regions of the MEA (i =ACL, MEM, CCL).

$$\vec{\mathbf{J}}_{T,i} = -\kappa_i^{\text{eff}} \nabla T \quad \nabla \bullet \left(-\kappa_i^{eff} \nabla T \right) = \frac{\dot{Q}_i}{t_i} \tag{B.54}$$

The thermal conductivities, κ_i^{eff}, of the MEA regions are needed. The membrane consists of hydrated Nafion. Measurements of the thermal conductivity of dry Nafion were reported with a good deal of uncertainty as being 0.08 [15] or 0.1 W m^{-1} K^{-1} [13], with a fairly-well hydrated membrane reaching 0.18. Khandelwal and Mench found dry thermal conductivity at 65°C of 0.13 W m^{-1} K^{-1} , and proposed that the conductivity of a hydrated membrane could be found by volume averaging, with the well-hydrated membrane reaching 0.3 W m^{-1} K^{-1} at temperature of 65 °C [80]. Burheim et al reported thermal conductivities of 0.18 and 0.25 W m^{-1} K^{-1} for Nafion at the dry and fully hydrated states at 20 °C. The thermal conductivity of Nafion was isotropic, and unchanging with compaction pressure. Modeling works have used thermal conductivity values from 0.1-1 W m^{-1} K^{-1}[136]. Neglecting small variations in conductivity with temperature, the thermal conductivity of hydrated Nafion membrane can be expressed

with volume averaging as eq.(B.55), where κ_{Io} is the dry conductivity of Nafion (0.13 W m^{-1} K^{-1}) and κ_{H_2O} is the conductivity of water (0.66 W m^{-1} K^{-1}).

$$\kappa_{MEM}^{\text{eff}}\left(f_v,T\right)=\left(1-f_v\right)\kappa_{Io}+f_v\kappa_{H_2O} \tag{B.55}$$

The thermal conductivity of catalyst layers is also needed. Published estimates are varied. Measurements of dry catalyst layers were reported as 0.27 +/- 0.05 W m^{-1} K^{-1} [80]. More recent dry measurements showed a tremendous amount of scatter with values of 0.04-.11 W m^{-1} K^{-1}, with the highest readings reflecting typical MEA assembly pressures of ~16 bar[137]. Hydrated catalyst layers showed noticeably increased conductivity only when liquid water filled the pores. Interestingly, the presence of platinum catalyst particles did not increase catalyst layer conductivity: only the scatter of the measurements grew. Nafion content was doubled without impacting the assessed thermal conductivity. Estimates of 0.87 W m^{-1} K^{-1} are presented in some modeling works without explicit attribution, or any link to the CL composition or structure[106, 115].

PEMFC catalyst layers contain a fraction of carbon black, hydrated Nafion, platinum particles, and void space. Thermal conductivities of amorphous carbon black compounds, made from a combination of sp2 and sp3 bonding, were recently said to fall within the range of 0.01-2 W m^{-1} K^{-1}. A measurement of 0.5 W m^{-1} K^{-1} was reported[138]. The presence of platinum nanoparticles present did not appear to influence effective thermal conductivity measurements [137]. Hence an effective thermal conductivity of the catalyst layers has been formulated by volume-averaging as eq.(B.56). This expression yields an effective hydration-dependent thermal conductivity of about 0.12-0.14 W m^{-1} K^{-1} when the volume fractions $\varepsilon_{-CL,Io}$ and $\varepsilon_{-CL,C}$ are each about typically 0.2.

$$\kappa_{-CL}^{\text{eff}}\left(f_v,T\right)=\varepsilon_{-CL,Io}\kappa_{Io}^{\text{eff}}\left(f_v,T\right)+\varepsilon_{-CL,C}\kappa_C \tag{B.56}$$

Estimates of the superficial heat generation, $\dot{Q}_i$, within the regions of the MEA, are available[106, 115]. These are adapted to the current model below. Within the anode catalyst layer, heat generation occurs from irreversible heating sources. The combined kinetic and ohmic ACL losses will

generate heat, in addition to half of the MEA electronic resistance. The anode superficial heat generation is expressed as eq. (B.57). This assumes that the ACL dwells in thickness with water uptake.

$$\dot{Q}_{ACL} = I^2 \left(R_{ACL}^{H^+,\text{eff}} + R_{cnt}^{e^-} / 2 \right) \tag{B.57}$$

Within the membrane, there is only the irreversible heat source of ohmic losses (protonic conduction losses). The membrane superficial heat generation is expressed as eq. (B.58).

$$\dot{Q}_{MEM} = I^2 \left(R_{MEM}^{H^+} \right) \tag{B.58}$$

The cathode catalyst layer has both reversible and irreversible heat sources in eq. (B.59). Reversible heat generation in the CCL stems from the entropy change of the overall reaction, and irreversible heat generation from the cathode activation (kinetic) and ohmic losses. The entropy change of the reaction, dS (=44 J mol^{-1} K^{-1}), assumes that produced water exits the MEA in vapor form [4, 38, 106], and is approximately constant at temperatures below 100 °C. The term η_c represents the purely kinetic losses in the cathode as described earlier. The right-most term represents ohmic heat generation, utilizing the effective cathode resistance and half of the MEA electronic conduction resistance.

$$\dot{Q}_{CCL} = I \frac{T_{CCL}\, dS}{4F} + I\eta_C + I^2 \left(R_{CCL}^{H^+,\text{eff}} + R_{cnt}^{e^-} / 2 \right) \tag{B.59}$$

The temperature profile within the MEA is now to be determined. Referring to Figure 2.5, there are 7 temperature values in the approximate profile, and thermal contact resistances are negligible[98]. The regional heat sources are approximately uniform (within each region). The temperature profile can be expressed as the solution to a system of 5 heat transfer equations with the 5 unknown temperatures.

The conservation of energy equation (B.54) is applied to the anode catalyst layer in eq.(B.60), the membrane in eq. (B.61), and cathode catalyst layer in (B.62).

$$\frac{4\kappa_{ACL}^{\text{eff}}\left(f_v,T\right)}{\left(t_{ACL}\left(1+\varepsilon_{dV,1}\right)\right)^2}\left(T_A-2T_{ACL}+T_1\right)=\frac{-\dot{Q}_{ACL}}{\left(t_{ACL}\left(1+\varepsilon_{dV,1}\right)\right)} \tag{B.60}$$

$$\frac{4\kappa_{MEM}^{\text{eff}}\left(f_v,T\right)}{\left(t_{MEM}\left(1+\varepsilon_{dV,2}\right)\right)^2}\left(T_1-2T_2+T_3\right)=\frac{-\dot{Q}_{MEM}}{\left(t_{MEM}\left(1+\varepsilon_{dV,2}\right)\right)} \tag{B.61}$$

$$\frac{4\kappa_{ccl}^{\text{eff}}\left(f_v,T\right)}{\left(t_{CCL}\left(1+\varepsilon_{dV,3}\right)\right)^2}\left(T_3-2T_{CCL}+T_C\right)=\frac{-\dot{Q}_{CCL}}{\left(t_{CCL}\left(1+\varepsilon_{dV,3}\right)\right)} \tag{B.62}$$

A continuity of heat flux requirement can be applied at the ACL-membrane interface in eq.(B.63) and at the membrane – CCL interface in eq. (B.64).

$$\begin{gathered}-\kappa_{ACL}^{\text{eff}}\left.\nabla T\right|_{ACL}=-\kappa_{Io}^{\text{eff}}\left.\nabla T\right|_{MEM}\\ \frac{\kappa_{ACL}^{\text{eff}}\left(f_v,T\right)}{t_{ACL}\left(1+\varepsilon_{dV,1}\right)}\left(T_A-4T_{ACL}+3T_1\right)=\frac{\kappa_{Io}^{\text{eff}}\left(f_v,T\right)}{t_{MEM}\left(1+\varepsilon_{dV,2}\right)}\left(-3T_1+4T_2-T_3\right)\end{gathered} \tag{B.63}$$

$$\begin{gathered}-\kappa_{Io}^{\text{eff}}\left.\nabla T\right|_{MEM}=-\kappa_{CCL}^{\text{eff}}\left.\nabla T\right|_{CCL}\\ \frac{\kappa_{Io}^{\text{eff}}\left(f_v,T\right)}{t_{MEM}\left(1+\varepsilon_{dV,2}\right)}\left(T_1-4T_2+3T_3\right)=\frac{\kappa_{CCL}^{\text{eff}}\left(f_v,T\right)}{t_{ACL}\left(1+\varepsilon_{dV,3}\right)}\left(-3T_3+4T_{CCL}-3T_C\right)\end{gathered} \tag{B.64}$$

After re-arrangement and simplification, the temperature profile can be expressed as eq. (B.65). The term Θ_{-CL} is the ratio of thermal (conduction) resistance of the catalyst layers to that of the ionomer membrane as eq. (B.66). The boundary heat fluxes into the anode $J_{T,A}$ and cathode $J_{T,\mathrm{C}}$ domains can be solved for in eq. (B.67), again using 3-point approximations to the first derivative of the temperature profile.

$$\begin{bmatrix} 2 & -1 & 0 & 0 & 0 \\ 4 & -3\left(1+\Theta_{ACL}\right) & 4\Theta_{ACL} & -\Theta_{ACL} & 0 \\ 0 & -1 & 2 & -1 & 0 \\ 0 & -\Theta_{CCL} & 4\Theta_{CCL} & -3\left(1+\Theta_{CCL}\right) & 4 \\ 0 & 0 & 0 & -1 & 2 \end{bmatrix} \begin{Bmatrix} T_{ACL} \\ T_1 \\ T_2 \\ T_3 \\ T_{CCL} \end{Bmatrix} = \begin{Bmatrix} T_A + \dfrac{\dot{Q}_{ACL} t_{ACL}\left(1+\varepsilon_{dV,1}\right)}{4\kappa_{ACL}^{\text{eff}}\left(f_v, T\right)} \\ T_A \\ \dfrac{\dot{Q}_{MEM} t_{MEM}\left(1+\varepsilon_{dV,2}\right)}{4\kappa_{lo}^{\text{eff}}\left(f_v, T\right)} \\ T_C \\ T_C + \dfrac{\dot{Q}_{CCL} t_{CCL}\left(1+\varepsilon_{dV,3}\right)}{4\kappa_{CCL}^{\text{eff}}\left(f_v, T\right)} \end{Bmatrix}$$

(B.65)

$$\Theta_{ACL} = \frac{\kappa_{lo}^{\text{eff}} t_{ACL}}{\kappa_{ACL}^{\text{eff}} t_{MEM}} \quad \Theta_{CCL} = \frac{\kappa_{lo}^{\text{eff}} t_{CCL}}{\kappa_{CCL}^{\text{eff}} t_{MEM}} \tag{B.66}$$

$$J_{T,A} = \frac{-\kappa_{ACL}^{\text{eff}}\left(f_v, T\right)}{t_{ACL}\left(1+\varepsilon_{dV,1}\right)}\left(3T_A - 4T_{ACL} + T_1\right) \quad J_{T,\text{C}} = \frac{-\kappa_{CCL}^{\text{eff}}\left(f_v, T\right)}{t_{CCL}\left(1+\varepsilon_{dV,3}\right)}\left(3T_C - 4T_{CCL} + T_3\right) \tag{B.67}$$

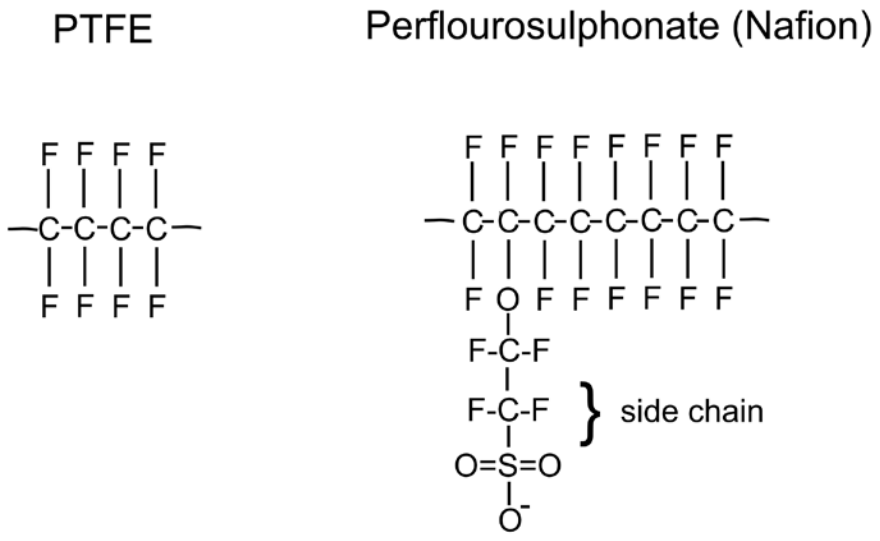

Figure B.1. Perflourosulphonate molecular structure schematic

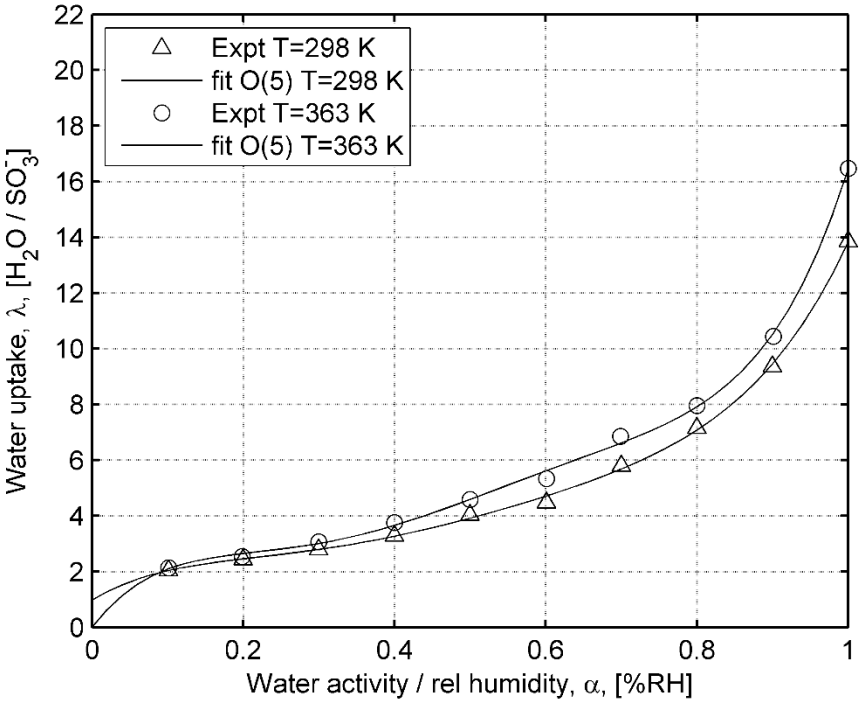

Figure B.2. Fits of water uptake from vapor by Nafion from Jalani and Datta (2005)

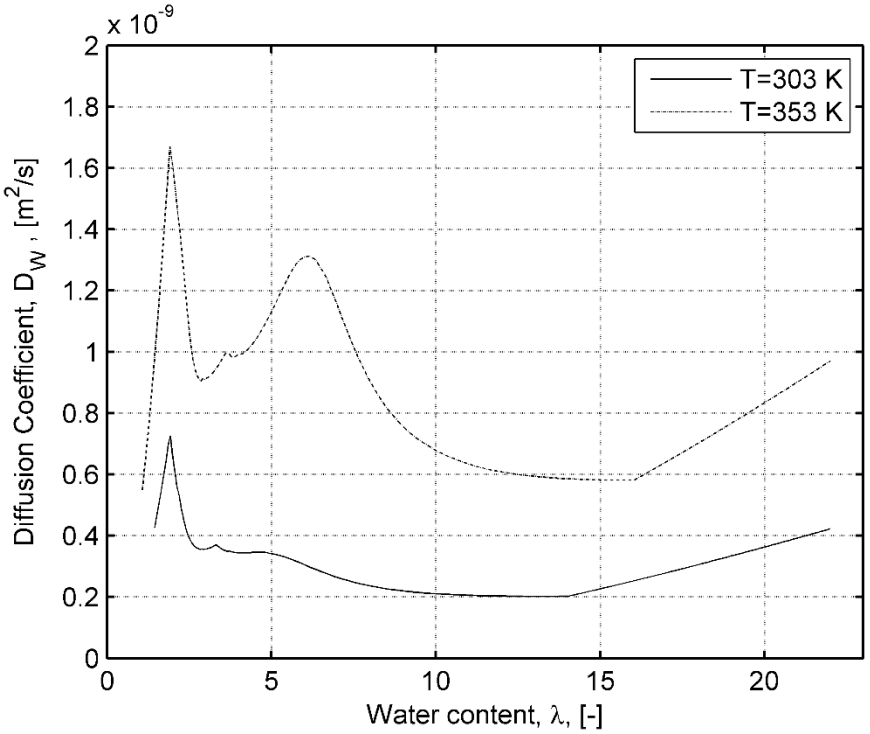

Figure B.3. Diffusion Coefficient Figure B.3in 1100 EW Nafion at 303 K and 353 K

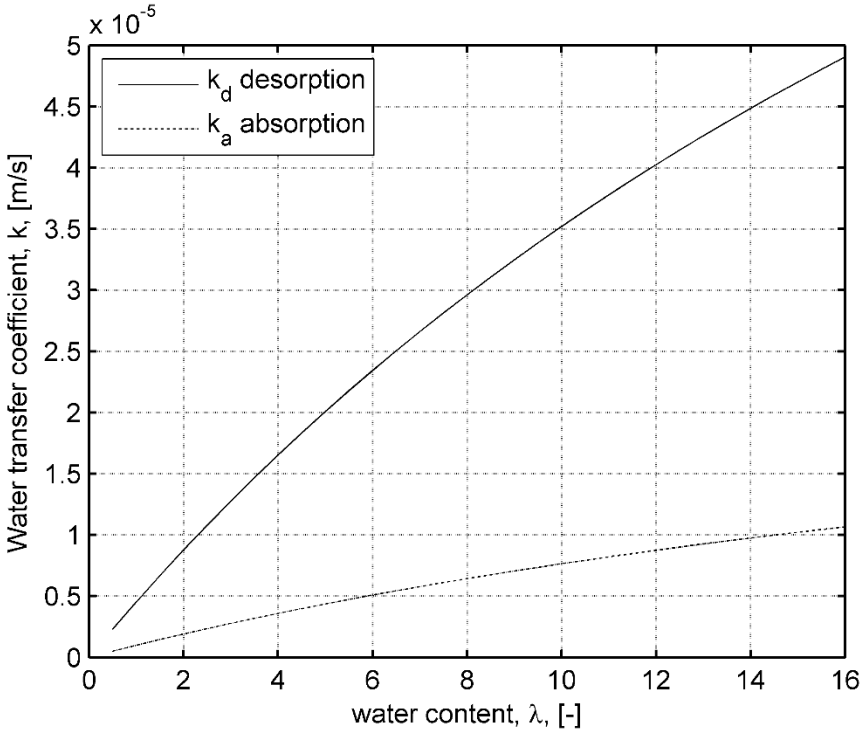

Figure B.4. Water absorption and desorption coefficients for 1100 EW Nafion at 353 K

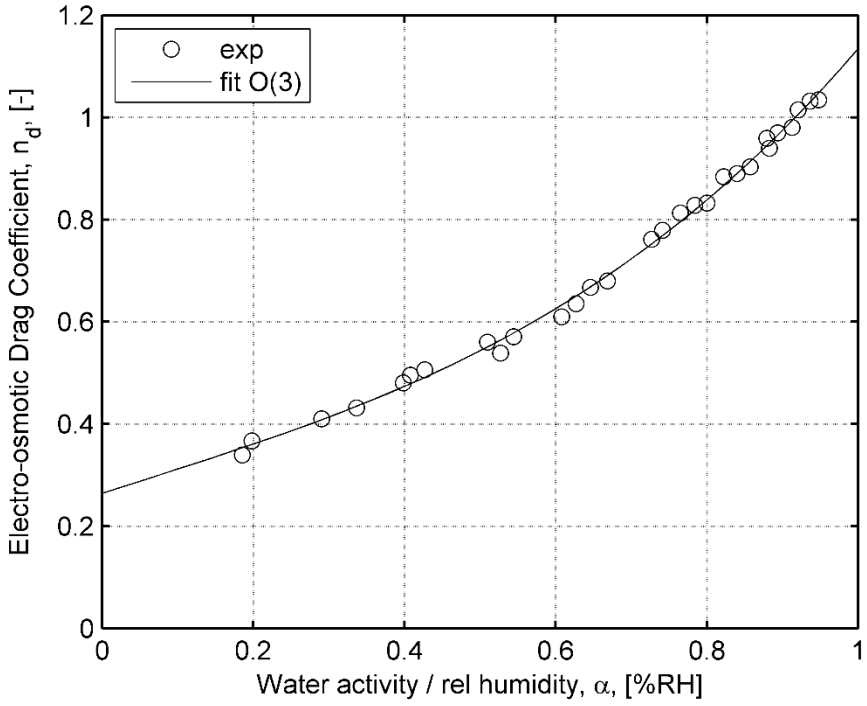

Figure B.5. Drag coefficient vs. humidity in 1100 EW Nafion at 303 K and 353 K

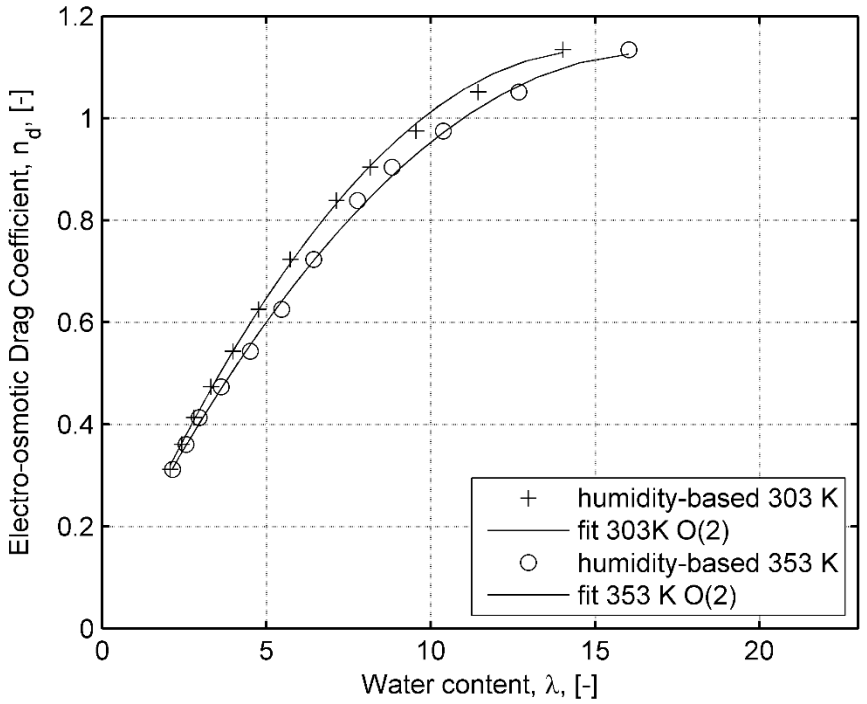

Figure B.6. Drag coefficient vs. water content in 1100 EW Nafion at 303 K and 353 K

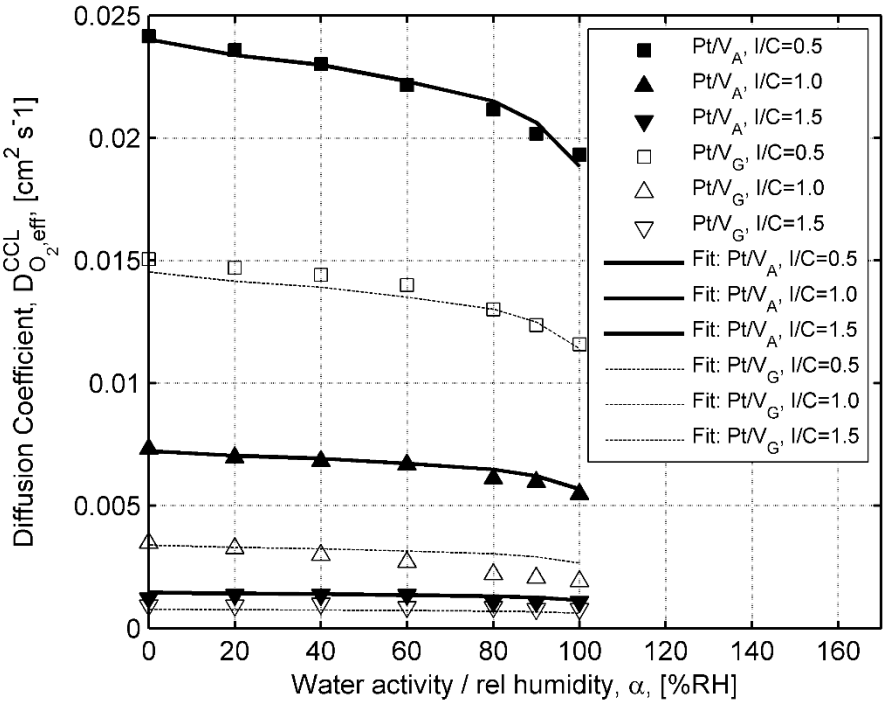

Figure B.7. Measured and fit values of the effective oxygen diffusion coefficient in various CCL compositions

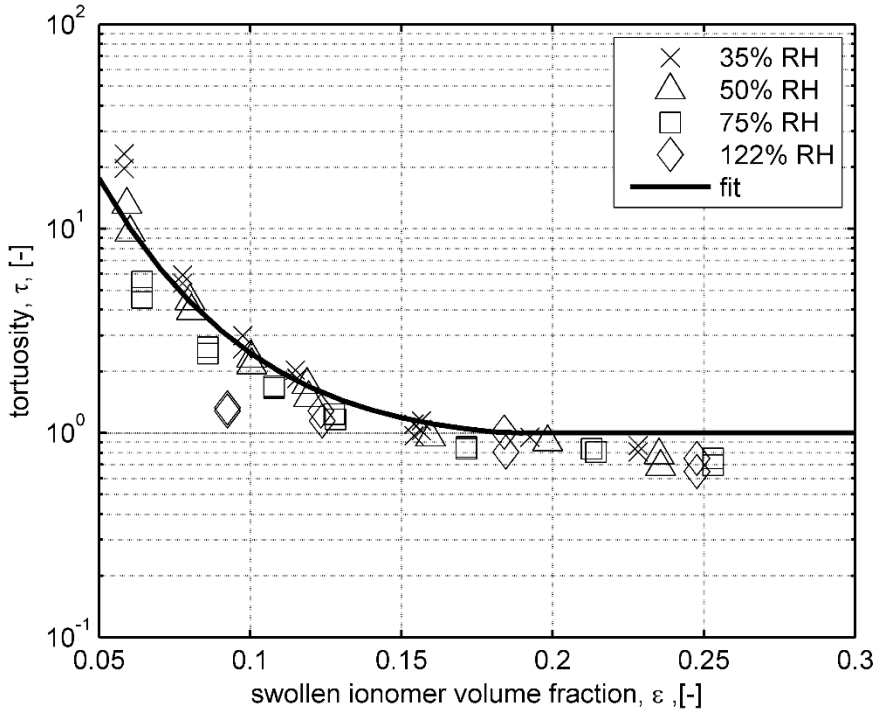

Figure B.8. Tortuosity values and swollen ionomer volume fraction at several humidities

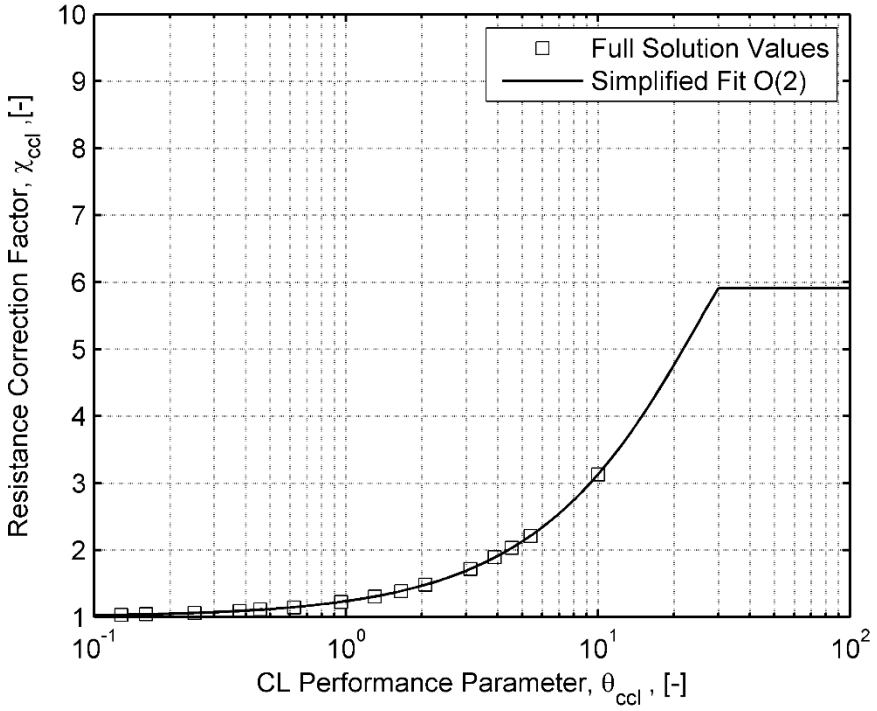

Figure B.9. Resistance correction factor $\chi_{CCL}(\theta_{CCL})$ with limited polynomial fit

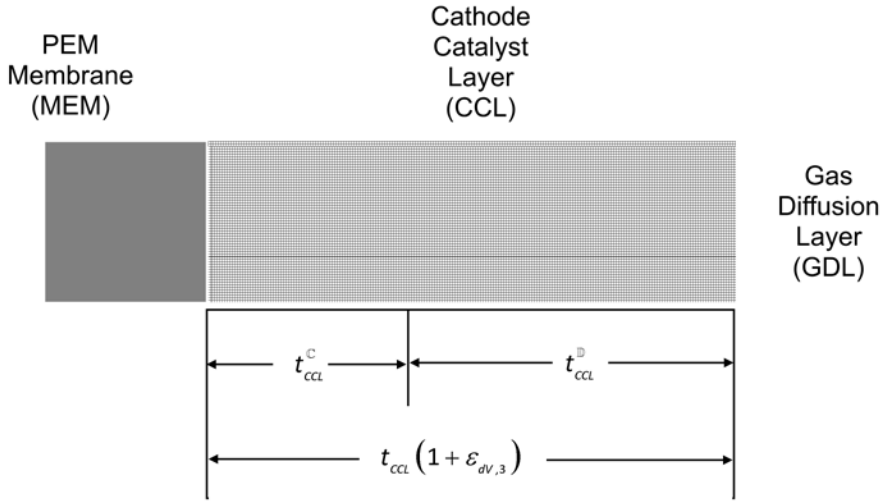

Figure B.10. Effective conduction and diffusion lengths within the CCL

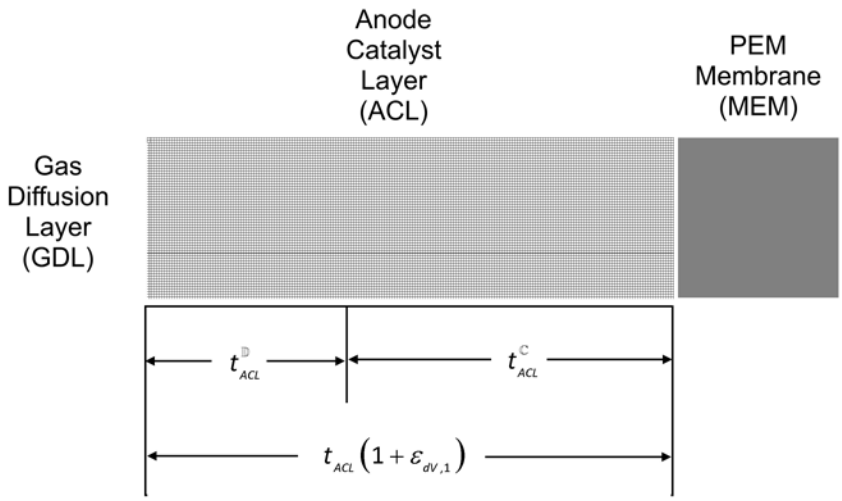

Figure B.11. Effective conduction and diffusion lengths within the ACL

Appendix C Interface Model Code

Appendix C contains the MATLAB code listing for this model. The code listing contains a main script that references several supporting m-file functions.

C.1 Interface Model Code: Main Script

```
%% Test2_P149T80_point09 V=.725
%%2016 Non Equilibrium model v13 (3/07/2016)
% This is the non-Isothermal version of interface model
% v13 (i) Corrects CL gaseous Diffusion coefficient
%     (ii) corrects Anode Kinetics
%     (iii) changes catalytic area redxn(humidity)


% 1. Inputs
% Inputs Electrical contact Resistance Added
R_e=.034/10000; % [Ohm m^2] Electrical resistance 35 mOhm*cm^2

% Inputs Anode side (a)
P_a= 149000; % pressure @ MEA [Pa]
T_a= 80+273.15; % temperature @ MEA [K]
X_wa= 0.32; % mol fraction water
X_h2a= 0.68; %mol fraction H2
V_a=0; % voltage @ anode
A_acv=1; % specific surface area of the anode control volume [m-1]

% Inputs Cathode Side (c)
P_c= 149000; % pressure @ MEA [Pa]
T_c= 80+273.15; % temperature @ MEA [K]
X_wc= 0.32; % mol fraction water
X_O2c= 0.679; %mol fraction O2
V_c=0.725; % voltage @ Cathode
A_ccv=1; % specific surface area of the cathode control volume [m-1]

% Inputs MEA Density and molecular weight values
rho_H2O=1; % [g / cm^3] water density
rho_io=2.0; % [g / cm^3] ionomer density
rho_c=2.2; % [g / cm^3] Carbon density
rho_pt=21.5; % [g / cm^3] Pt (Platinum catalyst) density
EW=1100; % membrane equivalent weight [1100 g/mol] [1100 kg/kmol]
M_w=18;% molecular weight of water [18 g/mol]

% Inputs physical constants
F=96485.33; % [C/mol]
R=8.314; % [J mol-1 K-1] universal gas constant
dS=44; % [J/ (mol K)] Reversible heat generation

% Inputs constituent thermal conductivities
kth_io=0.13; % [W/m/K] thermal conductivity of dry membrane phase @ 65C
kth_H2O=0.65;  %[W/m/K] thermal conductivity of water phase @ 65C
kth_c=0.5; %[W/m/K] thermal conductivity of carbon black

% Inputs MEA-membrane
t_m=22e-6; % dry membrane thickness [m] (25 um @ 50%RH)
aa=1.00E-5;% absorption parameter [m/s]
ad=4.60E-5;% desorption parameter [m/s]
aw=2.60E-9; % the diffusion parameter [m/s]
cf=rho_io*100^3/EW; % fixed concentration [mol SO3-/m^3]
Ix= 10; % Crossover current density [A m-2]= 0.5mA/cm^2
```

```
% MEA-mem phase water content (mol/m^2)
W=18.4*cf*t_m; % [mol/m^2]
% comes from scalae transport equation for W in practice

% Inputs MEA-anode catalyst layers  -> I0_a ~ 500,000 [A / m2] @ 80C
L_acl_pt=0.35; % [mg pt / cm^2] Pt loading
Ptc_acl=50; % wt% Pt/C
IC_acl=1.4; % Ionomer/Carbon ratio 0.5 / 1.0 / 1.5
L_acl_c=((100-Ptc_acl)/(Ptc_acl))*L_acl_pt; % [mg / cm^2] Carbon loading
L_acl_io=L_acl_c*IC_acl; % [mg / cm^2] Ionomer loading
t_acl= 12e-6; % [m] thickness or specific volume(10 um)

eps_acl_c=L_acl_c*0.00001/rho_c/t_acl; % [-] carbonbblack volume fraction
(0.2)
eps_acl_io=L_acl_io*0.00001/rho_io/t_acl; % [-] ionomer volume fraction (0.2)
eps_acl_gas=1-
((L_acl_pt/rho_pt)+(L_acl_c/rho_c)+(L_acl_io/rho_io))/(100000*t_acl); % [-]
porosity vol fraction (0.59)
eps_acl_cor=-0.2900*IC_acl.^2+0.4590.*IC_acl-0.3586;
eps_acl_gas=eps_acl_gas+eps_acl_cor; % porosity reduction f/ ionomer
tau_acl_gas=-0.5+5.2*IC_acl; % tortuosity of acl
d_acl_gas=(128-IC_acl*53)*1E-09; % [m] mean pore diameter of acl
I0_acl=.24; % [A/cm^2 PT] exchange currnet density property) f/[FC_K-5]
Apt_acl= 50; % [m^2 / g pt] EC available surface area/ g Pt
D_acl_K=(485000*d_acl_gas)*sqrt((T_a)/2); % [cm^2 s^-1] Knudsen H2 [FC_K-44]
Lange Table 1;
D_acl_M=101.3*(((T_a)^1.75)/P_a)*0.0312; %[cm^2 s^-1] Molecular H2 [FC_A-1]
Mench p.221 eq 5.34;
D_acl_F=(D_acl_M*D_acl_K)/(D_acl_K+D_acl_M); %[cm^2 s^-1] Free space
Diffusivity

% Inputs MEA-cathode catalyst layer  -> I0_c ~.01 [A/m2] @80C (Barbir 52/66)
L_ccl_pt=0.5; % [mg pt / cm^2] Pt loading
Ptc_ccl=50; % wt% Pt/C
L_ccl_c=((100-Ptc_ccl)/(Ptc_ccl))*L_ccl_pt; % [mg / cm^2] Carbon loading
IC_ccl=1.4; % Ionomer/Carbon ratio 0.5 / 1.0 / 1.5
L_ccl_io=L_ccl_c*IC_ccl; % [mg / cm^2] Ionomer loading
t_ccl=18e-6; % [m] thickness or specific volume(10 um)

eps_ccl_c=L_ccl_c*0.00001/rho_c/t_ccl; % [-] carbonbblack volume fraction
(0.2)
eps_ccl_io=L_ccl_io*0.00001/rho_io/t_ccl; % [-] ionomer volume fraction (0.2)
eps_ccl_gas=1-
((L_ccl_pt/rho_pt)+(L_ccl_c/rho_c)+(L_ccl_io/rho_io))/(100000*t_ccl); % [-]
porosity vol fraction (0.59)
eps_ccl_cor=-0.2900*IC_ccl.^2+0.4590.*IC_ccl-0.3586;
eps_ccl_gas=eps_ccl_gas+eps_ccl_cor; % porosity reduction f/ ionomer
tau_ccl_gas=-0.5+5.2*IC_ccl; % tortuosity of ccl
d_ccl_gas=(128-IC_ccl*53)*1E-09; % [m] mean pore size of ccl
I0_ccl=2e-8; % [A/cm^2 PT] catalyst specific exchange current density
property @ T=80C p=101 kPa) [K-12 table II]
Apt_ccl= 50; % [m^2 / g pt] EC available surface area/ g Pt
D_ccl_K=(485000*d_ccl_gas)*sqrt((T_c)/32); % [cm^2 s^-1] Knudsen O2 [FC_K-44]
Lange Table 1;
```

```
D_ccl_M=.0425*((T_c)^2.334)/P_c; % [cm^2 s^-1] Molecular O2 [FC_A-1] Mench
p.221 eq 5.33;
D_ccl_F=(D_ccl_M*D_ccl_K)/(D_ccl_K+D_ccl_M); % [cm^2 s^-1] Free space
Diffusivity

% 2. Calculate water activities vapor phase
act_a=X_wa*P_a/fnPsat2(T_a); act_a_d=act_a;%anode
[l_a,status]=fnlambda3d(act_a,T_a);l_a_d=l_a;
Apt_acl_hc=Apt_acl*(1-0.9*((1-act_a))); % [m^2 / g pt] humidity-adjusted

act_c=X_wc*P_c/fnPsat2(T_c); act_c_d=act_c;%cathode
[l_c,status]=fnlambda3d(act_c,T_c); l_c_d=l_c;
Apt_ccl_hc=Apt_ccl*(1-0.9*((1-act_c))); % [m^2 / g pt] humidity-adjusted

%3. calculate transport parameters; Diffusion, water content
T_m=0.5*(T_a+T_c); % avg temperature
l_m=W/cf/(eps_acl_io*t_acl+t_m+eps_ccl_io*t_ccl); %l_m=[l_m l_m l_m]; %
average water content (lambda)
molvol_w=M_w/rho_H2O/100^3; % water (liq)molar volume (m^3)/mol
fvm=(l_m*molvol_w)/((1/cf)+l_m*molvol_w); % volume fractions
[s_m,status]=fnsigma_m2(fvm,T_m); % [1/(ohm m)] membrane conductivity


%4. calculate current density
lam=[l_m l_m l_m]; fv=[fvm fvm fvm]; k=[0 0 0]; sg=[s_m s_m s_m]; eps_dv=[0 0
0];
Nwa=0; Nwc=0; Wt=1;
D_w=[0 0 0];nd=[0 0 0];Tvec=[T_a T_a T_a T_a T_c T_c T_c];
V_oc=fnV_oc2(T_c, X_h2a*P_a,X_O2c*P_c,act_c_d); % cell thermodynamic voltage
function
V_loss=V_oc-(V_c-V_a);
I0_a=fnI0_anode(I0_acl,X_h2a*P_a,Tvec(2))*100^2*L_acl_pt*Apt_acl_hc*10; %
adjusted for T, pressure
if (~exist('V_k') || isnan(V_k)) % a starter estimate if I=0
    V_k=0.9*V_loss;
    I=Ix; %(sg(2)/t_m)*(V_oc-(V_c-V_a)-V_k); %current density 1st estimate
end
% clear Wt; % Iteration on I, V terms will converge
while (~exist('Wt'))||(abs(Wt)>5E-5)


    for count=1:10
        fv=(lam*molvol_w)./((1/cf)+lam*molvol_w); % volume fractions
        if lam(1)<l_a_d % anode
            k(1)=fnk_absorption(aa,(1/cf),lam(1),Tvec(2));
        else
            k(1)=fnk_desorption(ad,(1/cf),lam(1),Tvec(2));
        end
        if lam(3)<l_c_d % cathode
            k(3)=fnk_absorption(aa,(1/cf),lam(3),Tvec(6));
        else
            k(3)=fnk_desorption(ad,(1/cf),lam(3),Tvec(6));
        end
        [D_w(1),status]=fnD_w3d(aw,fv(1),lam(1),Tvec(3));% set diffusion
coefficient
```

```
        [D_w(2),status]=fnD_w3d(aw,fv(2),lam(2),Tvec(4));% set diffusion
coefficient
        [D_w(3),status]=fnD_w3d(aw,fv(3),lam(3),Tvec(5));% set diffusion
coefficient

        [nd(1),status]=fnn_d(lam(1),Tvec(3)); %set EO drag coefficient
        [nd(2),status]=fnn_d(lam(2),Tvec(4)); %set EO drag coefficient
        [nd(3),status]=fnn_d(lam(3),Tvec(5)); %set EO drag coefficient


        % [M]{l}={rhs}  2nd order formulation for {d(lam)/dz}
        M=[(3*cf*D_w(1)/t_m) -4*cf*D_w(1)/t_m cf*D_w(1)/t_m;
            cf*t_m+6*cf*eps_acl_io*t_acl 4*cf*t_m
cf*t_m+6*cf*eps_ccl_io*t_ccl;
            cf*D_w(3)/t_m -4*cf*D_w(3)/t_m (3*cf*D_w(3)/t_m)];
        rhs=[(Nwa-nd(1)*I/F); 6*W; (nd(3)+0.5)*I/F-Nwc];
        lam=M\rhs; % Solve lambda profile
        % Nwa=cf*k(1)*(l_a_d-lam(1));
        % Nwc=cf*k(3)*(lam(3)-l_c_d);% Solve water fluxes

        % Calculate resistances
        eps_dv=((M_w*rho_io)/(EW*rho_H2O))*lam; % [-] Ionomer volume swelling
        t_ms=t_m*(1+eps_dv(2)); % [m] calculate swollen membrane thickness
        eps_acl_ios=eps_acl_io*(1+eps_dv(1));
eps_ccl_ios=eps_ccl_io*(1+eps_dv(3));
        % t_acls=t_acl*(1+eps_dv(1)); t_ccls=t_ccl*(1+eps_dv(3));
        [sg(1),status]=fnsigma_m2(fv(1),Tvec(3)); % [1/(ohm m)]
        [sg(2),status]=fnsigma_m2(fv(2),Tvec(4)); % [1/(ohm m)]
        [sg(3),status]=fnsigma_m2(fv(3),Tvec(5)); % [1/(ohm m)]
        R_m=(t_ms/6)*((1/sg(1))+(4/sg(2))+(1/sg(3))); % [ohm m^2] membrane
resistance
        R_a=0.0; % See [FC_K-15] Neyerlin Gasteiger (2005) after eqn 5
        R_a=fnR_anode(I,sg(1),eps_acl_io,t_acl,eps_dv(1),Tvec(2),I0_a); %
anode cl resistance
        R_c=fnR_cathode(I,sg(3),eps_ccl_io,t_ccl,eps_dv(3),Tvec(6)); %
cathode cl resistance
        % Anode linear kinetics, Cathode Tafel kinetics
        R_ohm=(R_e+R_a+R_m+R_c);b=(R*Tvec(6)/F);

        % Calculate Difusional Adjustments
        D_acl_eff=D_acl_F*eps_acl_gas*exp(-.388*eps_dv(1))/tau_acl_gas; %
[cm^2 s^-1] Anode ACL Effective D Coefficient
        D_ccl_eff=D_ccl_F*eps_ccl_gas*exp(-.388*eps_dv(3))/tau_ccl_gas; %
[cm^2 s^-1] Cathode CCL Effective D Coefficient
        % Calculate diffusional length in each acl/ccl
        t_acl_dif=fnL_Diff_a(sg(1),eps_acl_io,t_acl,eps_dv(1),Tvec(2),I0_a);
% Anode diffusional length
        t_ccl_dif=fnL_Diff_c(I,sg(3),eps_ccl_io,t_ccl,eps_dv(3),Tvec(6)); %
Cathode diffusional length
        % -anode
        X_h2a_d=X_h2a-(I/(2*F))*(10000*t_acl_dif/D_acl_eff)*(R*Tvec(2)/P_a);
% [-] mol fraction
        X_wa_d=X_wa; %-(cf*k(1)*(l_a_d-
lam(1)))*(10000*t_acl_dif/D_acl_eff)*(R*T_a/P_a); % [-] mol fraction
        act_a_d=X_wa_d*P_a/fnPsat2(Tvec(2)); %anode
        [l_a_d,status]=fnlambda3d(act_a_d,Tvec(2));
```

```
        Apt_acl_hc=Apt_acl*(1-0.9*(1-lam(1)/fnlambda3d(1,Tvec(2)))); % [m^2 /
g pt] humidity-adjusted

I0_a=fnI0_anode(I0_acl,X_h2a_d*P_a,Tvec(2))*100^2*L_acl_pt*Apt_acl_hc*10; %
adjusted for T, pressure
        % -cathode
        X_O2c_d=X_O2c-(I/(4*F))*(10000*t_ccl_dif/D_ccl_eff)*(R*Tvec(6)/P_c);
% [-] mol fraction
        X_wc_d=X_wc; %+cf*k(3)*(lam(3)-
l_c_d)*(10000*t_ccl_dif/D_ccl_eff)*(R*T_c/P_c); % [-] mol fraction
        act_c_d=X_wc_d*P_c/fnPsat2(Tvec(6)); %cathode
        [l_c_d,status]=fnlambda3d(act_c_d,Tvec(6));
        Apt_ccl_hc=Apt_ccl*(1-0.9*(1-lam(3)/fnlambda3d(1,Tvec(6)))); % [m^2 /
g pt] humidity-adjusted

I0_c=fnI0_cathode(I0_ccl,X_O2c_d*P_c,Tvec(6))*100^2*L_ccl_pt*Apt_ccl_hc*10; %
adjusted for T, pressure
        % -> I0_c ~.01 [A/m2] @80C (Barbir 52/66)

        % Solve for current Newton-Rhapson method
        V_oc=fnV_oc2(Tvec(6), X_h2a_d*P_a,X_O2c_d*P_c,act_c_d); % cell
thermodynamic voltage function
        V_loss=V_oc-(V_c-V_a);
        I2=I+(V_loss-I*R_ohm-b*log((I+Ix)/I0_c))/(R_ohm+(b/(I+Ix)));
        if I2<Ix
            I2=Ix;
        end
        V_k=b*log((I+Ix)/I0_c); %overpotential cathode

        % thermal solver: thermal conductivities [W/m/K]
        kth_acl_io=fnkth_io(kth_io, kth_H2O, fv(1));% [W/m/K] swollen
membrane I get 0.3080
        kth_acl_eff=fnkth_eff(eps_acl_io,kth_acl_io,eps_acl_c,kth_c); %
membrane + carbonblack
        kth_m_eff=fnkth_io(kth_io, kth_H2O, fv(2));% [W/m/K] swollen membrane
I get 0.3080
        kth_ccl_io=fnkth_io(kth_io, kth_H2O, fv(3));% [W/m/K] swollen
membrane I get 0.3080
        kth_ccl_eff=fnkth_eff(eps_ccl_io,kth_ccl_io,eps_ccl_c,kth_c);

        ratacl=(kth_m_eff*t_acl)/(kth_acl_eff*t_m); % 1.31
        ratccl=(kth_m_eff*t_ccl)/(kth_ccl_eff*t_m); % 2.1

        % thermal solver: heat generation terms [W/m^2]
        Qgen=[I^2*(R_a+R_e/2) I^2*(R_m)
(I*Tvec(6)*dS/(4*F))+V_k*I+I^2*(R_c+R_e/2)];
        % 1 is anode acl, 2 is membrane, 3 is cathode ccl
        M2=[1 0 0 0 0 0 0;
            -1 2 -1 0 0 0 0;
            -1 4 -3*(1+ratacl) 4*ratacl -ratacl 0 0;
            0 0 -1 2 -1 0 0;
            0 0 -ratccl 4*ratccl -3*(1+ratccl) 4 -1;
            0 0 0 0 -1 2 -1;
            0 0 0 0 0 0 1];
        rhs2=[T_a;
            (Qgen(1)*t_acl*(1+eps_dv(1)))/(4*kth_acl_eff);
```

```
            0;
            Qgen(2)*t_m*(1+eps_dv(2))/(4*kth_m_eff);
            0;
            (Qgen(3)*t_ccl*(1+eps_dv(3)))/(4*kth_ccl_eff);
            T_c];
        Tvec=M2\rhs2;
        ep=abs((I2-I)/I);

        I=I2;
        % plotting check
        if(~exist('waterplot'))
            waterplot=figure;
        end
        figure(waterplot); plot([-0.1*t_m 0 t_m/2 t_m 1.1*t_m], [l_a lam'
l_c]); hold on;
    end

    disp([V_oc  V_oc-V_k  V_oc-V_k-R_c*I-R_a*I  (V_c-V_a)+I*(R_e+R_m)  (V_c-
V_a)  (I+Ix)/(100^2) (ep)]);
    if(~exist('tempplot'))
       tempplot=figure;
    end
    figure(tempplot); plot([-t_acl -t_acl/2 0 t_m/2 t_m t_m+t_ccl/2
t_m+t_ccl], [Tvec' ]); hold on;


    %5. Sources in adjacent control volumes
    S_1=I*A_acv/(2*F); %
    S_wa=-Nwa*A_acv*.01801; % water at anode [kg / sm^3]
    S_h2a=-S_1*.002; % hydrogen at anode [kg / s m^3]
    S_ma=S_h2a+S_wa; % mass source [kg/ sm^3]

    S_2=I*A_ccv/(2*F);
    S_O2c=(-S_2/2)*.032; % O2 consumption at cathode [kg / m^3]
    S_wc=Nwc*A_ccv*.01801; % water at cathode [kg / m^3]
    S_mc=S_O2c+S_wc; % mass source [kg/m^3]

    %6. Sources in MEA control volume: Thermal
    % S_t=(241818*S_2)-I*(V_c-V_a)*A_ccv; % thermal source [W/ m^3]
    %Water  Gas     H2O     ?241.818 ?Hf (kJ/mol) Standard enthalpy formation
    Sta=-(kth_acl_eff/(t_acl*(1+eps_dv(1))))*(3*Tvec(1)-4*Tvec(2)+Tvec(3));
%[W/m^2] into anode
    Stc=-(kth_ccl_eff/(t_ccl*(1+eps_dv(3))))*(3*Tvec(7)-4*Tvec(6)+Tvec(5));
%[W/m^2] into cathode
    [Sta+Stc sum(Qgen)]; % check heat fluxes = total production


    %7. Time rate of change of water content, W in MEA
    Nwa=Nwa+0.25*(cf*k(1)*(l_a_d-lam(1))-Nwa);
    Nwc=Nwc+0.25*(cf*k(3)*(lam(3)-l_c_d)-Nwc);% Solve water fluxes
    Wt=I/(2*F)+Nwa-Nwc; % dW/dt water content in membrane [mol/(m^2 sec)]
    disp('    W     1 prodn =  2 anode loss  + 3 cathode loss + 4 dW/dt');
    disp([W   I/(2*F) -Nwa  Nwc  Wt]);
    disp('');
    % sum(ans/2)
```

```
    W=W+0.12*Wt; % increment water content in membrane [mol/(m^2)]
end
```

C.2 Interface Model Code: Supporting Functions

```
function [a,status]=fnactivity3d(l,T)
% Function to return the water activity guiven lambda
%Inputs are:-
% l lambda ( the ratio of the number of water molecules to the number of
% charge sites)
% T temperature [K] 303 to 363 C
%Outputs are:-
% a water activity (RH) (0-1 vapor 1-3 liquid)
% later source: [FC_C-3] Springer 1991
% good properties closing in on root for activity <1

al=0 ; au=3 ; evalr=1;
if l>22
    l=22;
end
while abs(evalr) > .01
  evall=fnlambda3d(al,T)-l;
  evalu=fnlambda3d(au,T)-l;
  ar=al-evall*(au-al)/(evalu-evall);
  %[al,au,ar];
  evalr=fnlambda3d(ar,T)-l;

  if evall*evalr <= 0
   au=ar; status=' root bracketed';
  elseif evalr*evalu <= 0
   al=ar; status=' root bracketed';
  else
   status=' Error - root not bracketed ';
   break
  end
  %evalr;
end
a=ar;
if abs(evalr) <0.01
    status=' root OK';
end
```

```
function [D,status]=fnD_w3d(aw,fv,l,T)
% Function D_w3d to return the water diffusion coefficient in membrane phase
% Slope limiter included
% ---Inputs are:-
% aw mass transfer parameter (constant value) [-]
% fv water volume fraction of the membrane [-]
% l lambda (ratio of number of water molecules to the number of charge sites)
% T temperature in [K] (323 K to 353 K)
% ----Outputs are:-
% D Water diffusion coefficient [m^2/s]
% source: [FC_E1-12]

% at a specific temperature, the Darken factor ... is only a function of
% water content of the membrane (lambda).  Dw is a function of (lambda) and
% Temperature.
% limit for supersaturated
TT=exp(2416*((1/303)-(1/T)));
% al water activity (%RH) [-]
[al,status]=fnactivity3d(l,T); % al is matching water activity

%l298=@(a)86.6748*a.^5-181.3080*a.^4+145.6883*a.^3-
49.0684*a.^2+10.4402*a+1.3892;
%l363=@(a)215.0405*a.^5-480.8855*a.^4+393.4794*a.^3-
135.9413*a.^2+23.9560*a+0.7797;

if al<=1 % water vapor
    if al<0.07
        al=0.07;
    end
    if al<0.4
        dl298=5.7954; dl363=8.4916;% dl/da @25C  dl/da @90C
    else
        dl298=(+10.4402-98.1368*al+437.0649*al.^2-
725.2320*al.^3+433.3740*al.^4);% dl/da @25C
        dl363=(+23.9560-271.8826*al+1180.4382*al.^2-
1923.542*al.^3+1075.2025*al.^4);% dl/da @90C
    end
    dlT=dl298+((dl363-dl298)/65)*(T-298);% T C dl/da
    D=aw.*fv.*(l./(al*dlT))*TT; %vapor condition
    status=('vapor');
elseif al>1 % supersaturated vapor (i.e. liquid)
    dl298=57.5103;% dl/da @25C a=1
    dl363=84.1721;% dl/da @90C a=1
    dlT=dl298+((dl363-dl298)/65)*(T-298);% T C dl/da
    D=aw.*fv.*(l./(dlT))*TT;
    %D=10E-10;
    status=('saturated');
else
    status=('problem'); D=1E6;
end

end
```

```
function I0_a=fnI0_anode(I0,PH2,T)
% Function to return cathode exchange current density(T,p) compensated
%Inputs are:-
% I0 exch current density @ 80C, 100 kPa ref conditions [A/m^2]
% PH2 Hydrogen (H2) partial pressure [Pa absolute]
% T temperature [K] Kelvin

%Outputs are:-
% I0_a exchange current density (T, P_H2) [A/m^2]
% Source: [FC_K-1]Neyerlin (2006)
% Source: [FC_K-5] Durst et al (2015)

R=8.314; % [J mol-1 K-1] universal gas constant
Tref=353; % 80C or 353K
Ec=16000; % activation energy of the ORR [J/mol]
% develop sheet resistance
I0_a=I0*(PH2/100000)*exp((-Ec/(R*T))*(1-(T/Tref)));

end


function I0_c=fnI0_cathode(I0,PO2,T)
% Function to return cathode exchange current density(T,p) compensated
%Inputs are:-
% I0 exch current density @ 80C, 101.3 kPa ref conditions [A/m^2]
% PO2 Oxygen (O2) partial pressure [Pa absolute]
% T temperature [K] Kelvin

%Outputs are:-
% I0_c exchange current density (T, P_O2) [A/m^2]
% Source: [FC_K-10] Neyerlin (2006)

R=8.314; % [J mol-1 K-1] universal gas constant
Tref=353; % 80C or 353K
Ec=67000; % activation energy of the ORR [J/mol]
% develop sheet resistance
I0_c=I0*((PO2/101300)^0.54)*exp((-Ec/(R*T))*(1-(T/Tref)));

end
```

```
function [ka,status]=fnk_absorption(aa,Vm,l,T)
% Function k_absorption to return the water aborption mass transfer
coefficient
% in the membrane phase  Inputs are:-
% aa mass transfer parameter (constant value) [-]
% Vm ionomer(membrane) molar volume [m^3/mol]
% l lambda (ratio of # of water molecules / # of charge sites)
% T temperature in [K] (expected 303 K to 353 K)
%Outputs are:-
% ka Water absorption mass transfer coefficient [m/s]
% source: [FC_E1-12], Ge, Yi 2005

molvol_w=1.8E-5; % water (liq)molar volume (m^3)/mol
TT=exp(2416*((1/303)-(1/T)));

if l<1.4
    l=1.4;
end

la1=fnlambda3d(1,T); % lambda @ 100% RH
la3=22; % lambda @ 300% RH ~= liquid equilibrated

% ka=aa*fv*exp(2416*((1/303)-(1/T)));

if l<=la1 % water vapor
    fv=(l*molvol_w)/(Vm+l*molvol_w); % volume fractions
    ka=aa*fv*TT;
    status=('vapor');

elseif l>la1 && l<la3 % supersaturated vapor
    fva1=(la1*molvol_w)/(Vm+la1*molvol_w); % volume fractions
    ka=aa*fva1*TT; % @ 100% RH
    ka=ka+50*ka*((l-la1)/(la3-la1));
    status=('partial liquid');
elseif l>=la3 % liquid immersion
    fva1=(la1*molvol_w)/(Vm+la1*molvol_w); % volume fractions
    ka=51*aa*fva1*TT; % @ 100% RH;
    status='>3 liquid equilibrated';
else
    status=('ka absorption problem'); ka=1E-5;
end
% status=('calculated ka');
end
```

```
function [kd,status]=fnk_desorption(ad,Vm,l,T)
% Function k_desorption to return the water desorption mass transfer
coefficient
% in the membrane phase  Inputs are:-
% ad mass transfer parameter (constant value) [-]
% Vm ionomer(membrane) molar volume [m^3/mol]
% l lambda (ratio of # of water molecules / # of charge sites)
% T temperature in [K] (expected 303 K to 353 K)
%Outputs are:-
% kd Water desorption mass transfer coefficient [m/s]
% source: [FC_E1-12], Ge, Yi 2005

molvol_w=1.8E-5; % water (liq)molar volume (m^3)/mol
TT=exp(2416*((1/303)-(1/T)));

if l<1.4
    l=1.4;
end

la1=fnlambda3d(1,T); % lambda @ 100% RH
la3=22; % lambda @ 300% RH ~= liquid equilibrated

% ka=aa*fv*exp(2416*((1/303)-(1/(T+273))));

if l<=la1 % water vapor
    fv=(l*molvol_w)/(Vm+l*molvol_w); % volume fractions
    kd=ad*fv*TT;
    status=('vapor');

elseif l>la1 && l<la3 % supersaturated vapor
    fva1=(la1*molvol_w)/(Vm+la1*molvol_w); % volume fractions
    kd=ad*fva1*TT; % @ 100% RH
    kd=kd+50*kd*((l-la1)/(la3-la1));
    status=('partial liquid');
elseif l>=la3 % liquid immersion
    fva1=(la1*molvol_w)/(Vm+la1*molvol_w); % volume fractions
    kd=51*ad*fva1*TT; % @ 300% RH;
    status='>3 liquid equilibrated';
else
    status=('kd absorption problem'); kd=4E-5;
end
% status=('calculated kd');
end
```

```
function [k,status]=fnkth_eff(eps_io,kth_io, eps_c, kth_c)
% Function fnkth_eff return effective thermal conductivity of CL
% a catalyst layer by volume averaging
%Inputs are:-
% eps_io [-] ionomer volume fraction (0.2)
% kth_io [W/m/K] thermal conductivity of hydrated membrane phase
% eps_c [-] carbonbblack volume fraction (0.2)
% kth_c [W/m/K] thermal conductivity of carbon black phase
%Outputs are:-
% k thermal conductitiy
% source: [H1-42] Burheim [H1-23] Mench v11 notes(4)

k=(eps_io*kth_io)+(eps_c*kth_c); % hydrated membrane + carbonblack

end

function [k,status]=fnkth_io(kth_io, kth_H2O, fv)
% Function sigma to return the thermal conductivity of hydrated Nafion
% by volume averaging
%Inputs are:-
% kth_io [W/m/K] thermal conductivity of dry membrane phase @ 65C
% kth_H2O [W/m/K] thermal conductivity of membrane water@ 65C
% fv volume fraction of water in the membrane [-]
%Outputs are:-
% k (thermal conduct) [W/m/K]
% source: [E1-1e] Weber Newman 2004 eqn 42
% notes:  threshold volume fraction fv is around 0.06.
% max conductivity reached @ fv 0.45 limit


k=(1-fv)*kth_io+fv(1)*kth_H2O; % thermal conductivity of swollen membrane

end

function delta=fnL_Diff_a(sg,eps,t,dV,T,I0_a)
% Function to return the open-circuit voltage
%Inputs are:-
% sg ionic conductivity of ionomer phase [1/(ohm m)]
% eps dry unswollen volume fraction of ionomer phase [-] (typ 0.2)
% t dry unswollen catalyst layer thickness [m]
% dV (eps_dv) Ionomer volume swelling [-]
% T temperature [K] Kelvin
% I0_a anode exchange current density [A m^-2]

%Outputs are:-
% delta catalyst layer gas diffusion thickness [m]
% Source: [FC_K-1] Neyerlin (2007) (Anode)
% Source: [FC_K-10] Neyerlin (2006)


% makes diffusion lengh the entire thickness
delta=t*(1+dV); % *(1-0.33/correction);

end
```

```
function delta=fnL_Diff_c(I,sg,eps,t,dV,T)
% Function to return
%Inputs are:-
% I current density [A/m^2]
% sg ionic conductivity of ionomer phase [1/(ohm m)]
% eps dry volume fraction of ionomer phase [-] (typ 0.2)
% t catalyst layer thickness [m]
% dV (eps_dv) Ionomer volume swelling [-]
% T temperature [K] Kelvin

%Outputs are:-
% delta catalyst layer gas diffusion length [m]
% Source: [FC_K-11] Neyerlin, Gu (2007) (Cathode)

F=96485.33; % [C/mol]
R=8.314; % [J mol-1 K-1] universal gas constant
% b = Tafel slope of 70 mV/decade for ORR rxn [FC-K-11] (2007) p.B281
% T is in K in  Formula below; convert to K
b=2.303*R*T/(1*F); % [V / decade] [K-11]
epsdv=eps*(1+dV);
% calculate tortuosity [FC_K-12] Lui Murphy (2009)
if epsdv<0.18
    tau=1.1153-.0772./epsdv-.0028./epsdv.^2 +.0024./epsdv.^3;
else
    tau=1;
end

% develop sheet resistance
R_sheet=(t*tau/(sg*eps))*(1+dV); % [ohm m^2]
ratio=I*R_sheet/b; % [-]
if (ratio>30 || ratio<0)
    correction=5.908;
else
    correction=-0.00236*ratio.^2+ 0.2371*ratio+1.0008; % O(2) good fit <30
(green)
end
% correction comes from[FC_K-11] Neyerlin et al (2007) fig. 7a
delta=t*(1+dV)*(1-0.33/correction);

end
```

```
function [l,status]=fnlambda3d(a,T)
% Function to return the membrane water content
%Inputs are:-
% a water activity (RH) (less than 1)
% T temperature [K] 303K to 363K
%Outputs are:-
% l lambda (ratio of the number of water molecules to the number ofcharge
sites)
% Sources:
%Liquid Water: l=22 liq water where (a=3) after in-situ exposure
% [E1-82]Onishi(2007)(fig.4)  [E1-2g]Jalani Choi (2005) [E1-
2h]Jalani,Datta(2005)
% [FC_E1-2] Zawodzinski, Springer  J. Electrochem Soc (1993) (liquid)
% [FC_E1-2f] Walsby Hietala J App Polymer Sci (2002)(liquid)
%Water Vapor: this formula is the improved;
% [FC_E1-2h] Jalani Datta_membr sorption_J Membrane Sci(2005)
% point @ (0) omitted
if a<0
    l=0.02;
    status='out of bounds input';
elseif a>=0 && a<=1
    l298=86.6748*a.^5-181.3080*a.^4+145.6883*a.^3-
49.0684*a.^2+10.4402*a+1.3892;
    l363=215.0405*a.^5-480.8855*a.^4+393.4794*a.^3-
135.9413*a.^2+23.9560*a+0.7797;
    l=l298+((l363-l298)/65)*(T-298);
    status='0-1';
elseif a>1 && a<=3
    l298=13.8161;% 25 C a=1
    l363=16.4288;% 90 C a=1
    l=l298+((l363-l298)/65)*(T-298);
    l=l+((22-l)/2)*(a-1);
    status='>1';
elseif a>3
    l=22.0; % [FC_E1-2] [FC_E1-2f]
    status='>3 super hydrated';
else
    l='error occurred';
    status='cant assign';
end

end
```

```
function [nd,status]=fnn_d(l,T)
% Function sigma to return the eo drag coefficeint
% in the membrane phase
%Inputs are:-
% l lambda (ratio of number of water molecules to the number of charge sites)
% T temperature in [K] (298 K to 353 K)
%Outputs are:-
% nd electroosmotic drag coefficient [-]
%source: [E1-11] Ge, Yi (2006)
% vapor: 3 fits with temp given; then interpolate (T)
% liquid: nd=1.8(@288 K) to 2.7(@358 K)


% first differentiate liquid water vs water vapor
lam_l=13.8161+(2.6127/65)*(T-298); % limit as fn of T

% drag for vapor equilibrated membranes
if l<=lam_l
    nd1=0.0367+0.1466*(l)-0.0049*(l.^2);% membrane T=30C
    nd2=0.0570+0.1276*(l)-0.0038*(l.^2);% membrane T=80C
    nd=nd1+(nd2-nd1)*(T-303.15)/50;status='vapor';
end
% drag for super-saturated cases
if l>lam_l
    ndliq=-1.834+.0126*T; % membrane in contact with liquid water @ l=22
    if l>=22.0
        nd=ndliq;status='liquid';
    else
        nd=1.13+((l-lam_l)/(22.0-lam_l))*(ndliq-1.13);status='supersat
vapor';
    end
end

%status='ok';
end
```

```
function p=fnPsat2(T)
% Function to return the saturation pressure
%Inputs are:-
% T temperature [K] Kelvin
%Outputs are:-
% p saturation pressure of water vapor [Pa]
% value 1 uses the springer equation from CRC handbook

%L1=2.8206+.02953*T-9.1837E-5*T^2+1.4454e-7*T^3;
%p(1)=10.^L1;
%T=T+273;
% August-Roche-Magnus formula
%p=610.94*exp((17.625*T)/(T+243.04));
% [FC_A-1] Mench text p. 93
p=-2846.4+411.24*(T-273.15)-10.554*(T-273.15)^2+.16636*(T-273.15)^3;

end


function Ranode=fnR_anode(I,sg,eps,t,dV,T,I0_a)
% Function to return Anode Resistance Model 13 (5b)
% combined kinetic and ohmic losses
%Inputs are:-
% I current density [A/m^2]
% sg ionic conductivity of ionomer phase [1/(ohm m)]
% eps dry volume fraction of ionomer phase [-] (typ 0.2)
% t dry catalyst layer thickness [m]
% dV (eps_dv) Ionomer volume swelling [-]
% T temperature [K] Kelvin
% I0_a anode exchange current density [A m^-2]

%Outputs are:-
% R catalyst layer resistance [ohm m2]
% Source: [FC_A-8] Kulikovsky (2010) book
% Source: [FC_K-1] Neyerlin (2007) (Anode)
% Source: [FC_K-10] Neyerlin (2006)
F=96485.33; % [C/mol]
R=8.314; % [J mol-1 K-1] universal gas constant
nu=0.5; % transfer coefficient
% b = Tafel slope ~140 mV/decade (@80 C)for HOR rxn [FC-K-5] (2015) p.F197
% T is in K in  Formula below; convert to K
b=R*T/(nu*F); % [V / decade]  [K-11]
epsdv=eps*(1+dV);

% calculate tortuosity [FC_K-12] Lui Murphy (2009)
if epsdv<0.18
    tau=1.1153-.0772./epsdv-.0028./epsdv.^2 +.0024./epsdv.^3;
else
    tau=1;
end

% develop sheet resistance
R_sheet=(t*tau/(sg*eps))*(1+dV); % [ohm m^2]
Vdrop=b*asinh(I*sqrt(R_sheet/(2*b*I0_a))); % [V] voltage drop
Ranode=Vdrop/I; % linearized anode resistance [ohm m2]
```

```
% Ranode=sqrt(((b*R_sheet)/(1*I0_a)));
% Ranode=2E-06; % 60% RH forcing Fig.9
% Ranode=3.3E-07; % 100% RH forcing Fig.9
%tau
end


function [s,status]=fnsigma_m2(fv,T)
% Function sigma to return the ionic conductivity of Nafion
% in the membrane phase
%Inputs are:-
% fv volume fraction of water in the membrane [-]
% T temperature in [K]
%Outputs are:-
% s membrane conductivity [1/(ohm m)]
% source: [E1-1e] Weber Newman 2004 eqn 42
% notes:  threshold volume fraction fv is around 0.06.
% max conductivity reached @ fv 0.45 limit

R=8.314; % [J mol-1 K-1] universal gas constant

if fv<0.061
    fv=0.061;
    status=('overly dry;calculated sm');
end

if fv<0.45
    s=100*0.500*((fv-0.06).^1.5)*exp((15000/R)*((1/303)-(1/T)));
    status=('vapor ;calculated sm');
else
    s=100*0.500*((0.39).^1.5)*exp((15000/R)*((1/303)-(1/T)));
    status=('over-saturated ;calculated sm');
end
end


function V=fnV_oc2(T,P_h2,P_O2,RH)
% Function to return the open-circuit voltage
%Inputs are:-
% T temperature [K] Kelvin
% P_h2 H2 partial pressure [Pa] absolute
% P_O2 O2 partial pressure [Pa] absolute
% RH relatice humidity [-] Expressed as a fraction (0-1)

%Outputs are:-
% V thermodynamic voltage [V]
% Source: [FC_K-10] Neyerlin (2006)
% Source: [FC_K-12] Lui, Murphy (2009) eqn 14

R=8.314; % [J mol-1 K-1] universal gas constant
F=96485.33; % [C/mol]
```

```
V=1.229-0.000846*(T-
298)+((R*T)/(2*F))*log(P_h2/101300)+((R*T)/(4*F))*log(P_O2/101300)-
((R*T)/(2*F))*log(RH);
% above equation uses log base 'e', source uses log base '10'.

end
```

VITA

Russell L. Edwards 1121 Driver Pointe Ct. Suffolk, VA 23435

Education

OLD DOMINION UNIVERSITY, NORFOLK, VA
Ph. D. Mechanical Engineering, 2018

PENNSYLVANIA STATE UNIVERSITY, STATE COLLEGE, PENNSYLVANIA
Master of Engineering, Acoustics, 2005

UNIVERSITY OF CINCINNATI, CINCINNATI, OHIO
B.S., Mechanical Engineering, class of 1993. Graduated Magna cum Laude

Employment

OLD OMINION UNIVERSITY, NORFOLK, VA
Graduate Teaching & Research Assistant, Mechanical Engineering, 2008-2015

LUK USA LLC – PRODUCT DEVELOPMENT, WOOSTER, OHIO
Noise, Vibration, & Harshness Engineer, Engineering Analysis Group, 2006-2007
Performed modeling/simulation of automotive powertrains, emphasis on torsional issues.

LEAR CORPORATION – SEATING SYSTEMS DIVISION, TEST LAB, SOUTHFIELD, MICHIGAN
Sr. Engineer, Sound Quality / Acoustics Group, Test Lab, 2002-2006
Planned, executed, and reviewed acoustical & sound quality tests evaluating automotive seats and interior trim. Directed & trained technicians. Established testing & data processing procedures.

DANA FLUID SYSTEMS – COUPLED PRODUCTS DIVISION, ROCHESTER HILLS, MICHIGAN
NVH Engineer, Sr. NVH Engineer, 1997-2002
Analyzed hydraulic power steering noise, vibration, and durability issues for automotive OEM customers.

Publications

"Correlation of Hydraulic Circuit Dynamic Simulation and Vehicle," at the Steering and Suspension Technology Symposium SAE 2000 World Congress, SAE 2000-01-0811, March 2000, Detroit, MI

"Measurement Uncertainty in Random Incidence Sound Absorption Testing," at the SAE 2007 Noise and Vibration Conference, SAE 2007-01-2227 / 2218, April 2007, St. Charles, IL

"Empirical Study on the Correlation of Random Incidence Sound Absorption Results from Varying Reverberation Room Sizes," at the SAE 2007 Noise and Vibration Conference, SAE 2007-01-2380, April 2007, St. Charles, IL

"Regression analysis of PEM fuel cell transient response," Int J Energy Environ Eng (2016) 7: 329. https://doi.org/10.1007/s40095-016-0209-1